HAL
open science

Laboratory astrophysics with magnetized laser-produced plasmas

Benjamin Khiar

To cite this version:

Benjamin Khiar. Laboratory astrophysics with magnetized laser-produced plasmas. Astrophysics [astro-ph]. Université Pierre et Marie Curie - Paris VI, 2017. English. NNT : 2017PA066310 . tel-01699030v2

HAL Id: tel-01699030

https://theses.hal.science/tel-01699030v2

Submitted on 1 Mar 2018

HAL is a multi-disciplinary open access archive for the deposit and dissemination of scientific research documents, whether they are published or not. The documents may come from teaching and research institutions in France or abroad, or from public or private research centers.

L'archive ouverte pluridisciplinaire **HAL**, est destinée au dépôt et à la diffusion de documents scientifiques de niveau recherche, publiés ou non, émanant des établissements d'enseignement et de recherche français ou étrangers, des laboratoires publics ou privés.

THÈSE DE DOCTORAT

pour obtenir le grade de docteur délivré par

Université Pierre et Marie Curie

École doctorale d'Astronomie et Astrophysique d'Ile-de-France

présentée et soutenue publiquement par

Benjamin KHIAR

le 26 septembre 2017

Laboratory astrophysics with magnetized laser-produced plasmas

Directeur de thèse : **Andrea CIARDI**

Jury

M. Philippe Savoini,	Professeur	Président
M. Petros Tzeferacos,	Research scientist	Rapporteur
M. Emmanuel d'Humières,	Maître de conférences	Rapporteur
Mme. Catherine Dougados,	Directrice de recherche	Examinateur
M. Émeric Falize,	Ingénieur CEA	Examinateur
M. Andrea Ciardi,	Maître de conférences	Directeur de thèse

Contents

Contents iii

1 Introduction 1
1.1 The context: High Energy Density Laboratory Astrophysics (HEDLA) 2
1.2 The thesis environment 3
1.3 What you will see in this manuscript 5
1.4 Bibliography 6

2 MagnetoHydroDynamic 9
2.1 Introduction 10
2.2 Fluid equations from the kinetic theory 12
2.2.1 Zero-order moment: the mass conservation equation 12
2.2.2 First-order moment: the momentum conservation equation 13
2.2.3 Second-order moment: the energy conservation equation 16
2.3 MagnetoHydroDynamic (MHD) reduction 16
2.3.1 Summary of the multi-species fluid equations 16
2.3.2 Expression of the collisional heating term 18
2.3.3 The conservation energy for multi-species fluid equations 19
2.3.4 The bi-temperature MHD model 20
2.3.5 MHD mass conservation equation 21
2.3.6 MHD momentum conservation equation 21
2.3.7 MHD internal energy conservation equation 24
2.3.8 The generalized Ohm's law 25
2.3.9 The displacement current in the Maxwell-Ampere equation 30
2.3.10 Relative importance of the various electric field terms in the generalized Ohm's law 31
2.3.11 The induction equation 35
2.3.12 The quasi-neutrality assumption 36
2.3.13 Conservation of the total energy in the MHD model 36
2.4 The GORGON 3D resistive, bi-temperature MHD code 39
2.4.1 Introduction 39
2.4.2 Implemented equations 40
2.4.3 Localization of the physical quantities in the GORGON grid 40
2.5 Implementation of a laser module in the GORGON code 41
2.5.1 Introduction 41
2.5.2 Electromagnetic Wave propagation equation in a (unmagnetized) plasma 42
2.5.3 Effect of electron-ion collisions on the propagation of light waves in homogeneous plasmas 45
2.5.4 Geometric optic approximation and the eikonal equation 46

2.5.5 Implementing the laser deposition module in the three-dimensional, resistive MHD code GORGON . . . 47
2.5.6 Validation test for the laser module . . . 50
2.6 Implementation of the Biermann battery effect in the GORGON code . . . 52
2.6.1 General description . . . 52
2.6.2 Details of the numerical implementation . . . 53
2.6.3 Simulation tests . . . 54
2.7 Bibliography . . . 57

3 The physics of laser-solid target interaction 61
3.1 Introduction . . . 62
3.2 The ablation process . . . 63
3.2.1 Material removal by laser energy . . . 63
3.2.2 The mediating effect of the ablated material . . . 64
3.2.3 General picture of a solid target illuminated by a laser pulse . . . 65
3.2.4 Temperatures reached in laser-produced plasmas . . . 70
3.2.5 Scaling laws for laser-produced plasmas parameters . . . 71
3.3 Dynamics of laser-produced expanding plasmas . . . 71
3.3.1 Introduction . . . 71
3.3.2 Adiabatic self-similar 1D plasma expansion . . . 72
3.3.3 Isothermal self-similar 1D plasma expansion . . . 80
3.3.4 A new potential 1D description of laser-produced plasmas expanding at supersonic/hypersonic speeds . . . 81
3.4 Bibliography . . . 88

4 Physics of supersonic jets and shocks 93
4.1 Introduction . . . 94
4.2 A little bit of history about supersonic jets and shocks . . . 94
4.3 The propagation of unmagnetized supersonic jets in an external background . . . 97
4.4 Stability of unmagnetized supersonic jets . . . 100
4.5 GORGON simulations of supersonic jets . . . 103
4.5.1 General description of a pressure-matched supersonic jet . . . 103
4.5.2 Effects of the Mach number on jet propagation . . . 109
4.5.3 Influence of an axial magnetic field on the dynamic of a supersonic jet . . . 111
4.5.4 Supersonic jets propagating in a magnetized vacuum . . . 115
4.6 Bibliography . . . 116

5 Generation of astrophysically-relevant jets in the laboratory 119
5.1 Introduction . . . 120
5.2 Experimental production of magnetically collimated jets . . . 120
5.3 Initial numerical setup and laser parameters . . . 123
5.4 General plasma dynamics . . . 124
5.4.1 Velocity profiles . . . 126
5.4.2 Density profiles . . . 127
5.5 Cavity formation and evolution . . . 129
5.6 Jet structure and dynamics . . . 133
5.7 Jet 3D instabilities . . . 134
5.8 Jet structure dependence with different parameters . . . 138

5.9 Influence of a gas background and mitigation of the Rayleigh-Taylor instability . . . 142
5.10 Frequency resolved radiations imaging . . . 144
5.11 Influence of the spatial resolution on the jet 3D structure . . . 145
5.12 Bibliography . . . 147

6 Toward controlling the temporal properties of laser-produced plasma jets 151
6.1 Introduction . . . 152
6.2 Experimental and numerical setup . . . 152
6.3 Results . . . 153
6.4 Bibliography . . . 158

7 Generation of unstable supersonic plasma pancakes in strong transverse magnetic fields 161
7.1 Introduction . . . 162
7.2 Initial setup and lasers parameters . . . 162
7.3 General 3D dynamic . . . 163
7.4 Three-dimensional stability of the produced plasma pancake . . . 165
7.4.1 Rayleigh-Taylor instability in the MHD regime . . . 168
7.5 The effects of the plasma beta on the instability . . . 169
7.6 Experimental results . . . 171
7.7 Bibliography . . . 173

8 Accretion physics 177
8.1 Current picture of magnetospheric accretion onto young stars (T Tauri stars) 178
8.2 The accretion shock . . . 182
8.3 State of the art of numerical simulations of accretion shocks. . . . 186
8.4 Bibliography . . . 191

9 Magnetized accretion in the laboratory 195
9.1 Introduction . . . 196
9.2 Experimental results . . . 196
9.3 Numerical setup . . . 199
9.4 Generation and characterization of the accretion column . . . 201
9.5 Accretion shock 3D structure . . . 203
9.6 Temperatures and emission in the laboratory accretion process . . . 206
9.7 On the importance of the obstacle ablation . . . 210
9.8 Influence of the orientation . . . 212
9.9 Bibliography . . . 214

10 Conclusion and future prospects 219

A Waves and instabilities I
A.1 General formulation from the ideal MHD equations . . . II
A.2 The case of motionless homogeneous unmagnetized compressible plasma: sound waves . . . V
A.3 The case of motionless homogeneous magnetized compressible plasma: Alfven, slow and fast magnetoacoustic waves . . . V
A.4 The case of discontinuously stratified plasma without magnetic field: the Raileygh-Taylor instability . . . VIII

A.5 The case of a discontinuisly sheared velocity unmagnetized compressible plasma: the Kelvin-Helmoltz instability XIV
A.6 The case of a single magnetic stable interface XVII
A.7 The case of a magnetic slab XX

List of Figures **XXVII**

List of Tables **XXXVII**

Chapter 1

Introduction

Sommaire

1.1 The context: High Energy Density Laboratory Astrophysics (HEDLA) . . 2

1.2 The thesis environment 3

1.3 What you will see in this manuscript 5

1.4 Bibliography 6

1.1 The context: High Energy Density Laboratory Astrophysics (HEDLA)

This thesis represents one contribution to the growing field of "laboratory astrophysics" and more particularly to the area of high energy density laboratory astrophysics. First, the origin of the term laboratory astrophysics comes from the possibility to investigate astrophysical processes using human-made tools "on terra firma". This, of course, encompasses a very large panel of different disciplines ranging from atomic/molecular physics [1; 2] and condensed matter [3] to nuclear [4] and particle physics [5] For example, the fundamental question of the origins of life has been addressed in the laboratory in order to assess the possibility of a life being "seeded" by organic chemicals and water brought by cometary impacts [6]. Indeed, experiments have simulated the composition of comets and interstellar ice grains and shown that upon sufficient radiation heating and vaporization of these materials, it is possible to produce the building blocks of life [7]. Plasma physics is another major area relevant for astrophysical studies. Indeed, it is now well established that the vast majority of the visible matter in the universe (so excluding the hypothetical dark matter) is in the state called "plasma". Often qualified as the fourth state of matter, it is observed when the energy present in a given system is sufficiently high to ionize the atoms. This state has been "officially" first reported as "radiant matter" in 1879 by Sir William Crookes and since then, the field has undergone an impressive number of discoveries and breakthroughs. These works have been driven notably by the "quest" aiming to mastering nuclear fusion reactions, in a controlled way, in order to produce energy. In parallel, plasma physics has been very early recognized as the good framework to study a very large number of astrophysical processes. However, it is only until recently that the human technology has reached a point where it is possible to produce, in the laboratory, matters in states or regimes relevant to astrophysical phenomena occurring at high energy densities. This field is often called "High Energy Density Laboratory Astrophysics" (HEDLA). The lasers have a special place in this field since their invention in the 1960's. They are indeed an amazing tool to focus (electromagnetic) energy on small spatial scales and short periods allowing the generation of hot and dense materials. The foundations of HEDLA lies in the famous and relatively intuitive "nerdy" proverb: "same equations → same solutions". The mathematical translation of this sentence is called the "scaling" and consists simply to say that if two systems, for example one in the vacuum chamber of a Parisian laboratory and the other localized around the shock wave propagating in the interstellar medium as the result of the death of a star, obey the exact same set of equations, then their evolution will be strictly equivalent under the condition that the initial and boundary conditions are the same. Of course, the passage from one scale to another is done using certain scaling parameters and one should not be surprised to see somewhere some sentences such that "1 nanosecond of evolution of this system represents one year of this system" or "1 millimeter of this system represents one solar radius of this one". This, of course, has to be understood as being a pure mathematical assertion but which can be useful from a physical point of view. One of the first topic being studied in the laboratory using lasers has been the propagation of bow shocks (in magnetopsheres, interstellar mediums, supernovae...) in the early 1990s. In this case the scaling was hydrodynamical and possible because the physical regimes (quantified by dimensionless parameters such the Reynolds number, Peclet number...) were similar. In mathematical language it is equivalent to say that both systems obey to the Euler equations (Navier-Stokes equations without viscosity and thermal conduction). Later, near the beginning of the new century, Ryutov introduced the same reasoning but

in the case where a magnetic field is present. In this case, he demonstrated the possibility to perform a strict mathematical scaling in the framework of the "ideal magnetohydrodynamic" (MHD), even in the presence of shocks. The MHD is the model describing the behavior of neutral fluids within which electrical currents can flow (because the fluid is ionized) and thus couple to the magnetic fields. Ideal MHD is somehow, for MHD, the equivalent of the Euler equations for the Naviers-Stockes equations. The idea behind the restriction of the scaling to these "simplified" set of equations lies in the fact that dissipative processes tend to break the scaling. It should however be noted that more recently a consequent work has been done to include in the scaling the possibility for the systems to be non adiabatic through the loss of energy by radiations [8]. The work published by Ryutov [9], beginning to be called the "Ryotov scaling", has been the starting point of a whole new generation of magnetized experiments aiming to study the behavior of flow when the fields are sufficiently strong to influence the plasma dynamics. One of the most studied topic in this area concerns the study of magnetized flows observed around young stars at times during which they are still accreting material from the environing medium, notably their accretion disk. Indeed, it has been discovered in the 1980s that these stars (called "T Tauri Stars" or TTS) often exhibit large outflows which can be, in some cases, highly collimated [10]. It was rapidly supposed that magnetic fields observed on these systems could be involved in the formation of these jets/winds [**?**] and now it is considered to be true with a high degree of certainty. Very early in the 2000's, the plasma physics group of Imperial College pioneered the production of magnetized laboratory jets using the high pulsed power facility MAGPIE [12; 13]. They used a setup producing a toroidal magnetic field pushing and collimating hypersonic radiative jets. This configuration was astrophysically-relevant in the sense that it was similar to the topology of the "magnetic tower" model of astrophysical jets [14]. In these experiments the plasma is generated by the sublimation of solid wires through mega-ampere currents delivered by capacitors in very short times ($\sim \mu s$). The magnetic field generated by these currents exerts a pressure such that the flow is accelerated and highly collimated. Roughly at the same time, Bellan and his team developed a platform at Caltech to study MHD jet launching using a planar magnetized coaxial plasma gun [15; 16]. Their work showed strong instabilities (especially "kinks") of the jets in this configuration. In these previous works, the magnetic field was always self-produced by the currents flowing inside the plasma. In 2013, the collaboration within which this thesis was realized demonstrated for the first time the production of astrophysically-relevant magnetized jets using external magnetic fields as well as lasers [17; 18]. The difficulty to experimentally produce homogeneous and stationary (on the hydrodynamic scale) strong magnetic fields ($> 10\,\mathrm{T}$) had for a long time prevented the use of laser-produced plasmas at high intensities (necessary to obtain the "good" astrophysical regimes) to produce magnetized jets. The work demonstrated the possibility to collimate a diverging plasma flow into a highly collimated stable jets using a poloidal field. As we are going to see in the next sections, these laser-produced jets are somehow the "row material" of the work performed in this thesis where novels configurations using the same setup as in 2013 ([19]) are presented both numerically and experimentally.

1.2 The thesis environment

The work presented in this manuscript has been carried out during my three PhD years within the team "Plasmas stellaires et astrophysique de laboratoire" inside the LERMA (UMR8112) laboratory. A small team of a dozen of people, we cover an interesting panel of subjects related to the laboratory astrophysics field presented above. For example, the

use of laser pulses as "pistons" to drive shocks inside gas tubes, in a regime called "radiative shocks", is a topic which has been studied for several years by the team (Chantal Stehlé, Raj Laxmi Singh, Uddhab Chaulagain). The experiences are mainly conducted on the PALS laser facility [20]. Still about the "shock" topic, during a PhD work and within a collaboration with the "Osservatorio Astronomico di Palermo", Lionel de Sa has studied the effect of radiative transfer on the physics of the still not-fully-understood accretion shocks occurring on the surface of T Tauri stars (one of the subjects addressed in this manuscript). Another very important and well developed field for laboratory astrophysics concerns the generation of opacity datas, especially in the context of star internal structures since there radiative transfer plays a dominant role. On this subject, Franck Delahaye is member of the international Opacity Project (OP) and actively participate to its development. Opacities are also the "raw materials" for radiative transfer codes which can be coupled with (magneto-)hydrodynamic codes, either "in line" or as a post-treatment of the generated datas. Three codes are actively developed in our team. One of them is the IRIS3D code, led by Laurent Ibgui, which is dedicated to the generation of synthetic spectra by performing radiative transfer using as an input, thermodynamic quantities (density, temperature...) from other hydrodynamic codes, both for astrophysical and laboratory situations. Very recently, the project PHARE was initiated in collaboration with the Laboratoire de Physique des Plasmas (LPP, UMR-7648). This 3D parallelized hybrid code (ions are treated like particles whereas electrons serve as a neutralizing fluid) is partially developed by two members of the team (Mathieu Drouin, Andrea Ciardi) and is aiming at simulating laboratory experiments in which the hydrodynamic description is not enough/valid. One of the first objective of this code is to model recent or imminent experiments studying the process of magnetic reconnection using laser-produced plasmas (for example at the Laser MegaJoule facility). Another topic studied using an hybrid code (HECKLE) is the streaming instability, potentially suspected to be involved in the star formation process. Loïc Nicolas has been working on this instability during its PhD conducted in parallel with mine. He was particularly interested about the effect of collisions between particles on the evolution of the instability. Finally, for my part, I have been working on GORGON, the third code developed in our team. GORGON is described in 2.4 of this manuscript. This parallelized 3D resistive magnetohydrodynamic code has been initially developed (and is still developed) at Imperial London College within the Blackett Laboratory, especially by my thesis supervisor, Andrea Ciardi. This code was developed first for modelling z-pinches experiments on the MAGPIE facility in London [21]. As an important feature necessary to correctly reproduce these experiments, the handling of "vacuum" regions in this code makes it very adapted for laboratory astrophysics simulations. As mentioned in the previous context introduction, this code has been used to study the astrophysically-relevant production of magnetized jets in z-pinches configurations (magnetic towers...). For a few years now, thanks in particular to a strong collaboration with the team of Julien Fuchs at the LULI laboratory, we have refocused the GORGON code toward the modeling of laser experiments. My work falls within this framework, as it will be detailed just below. In the following years, this work will be expanded, especially toward the capability to inject "particles" in GORGON. Indeed, Julien Guyot, presently a first year PhD student, aims to implement in GORGON a module allowing the treatment of small populations of macro-particles (as in Particle-In-Cell codes) "feedbacking", through electromagnetic fields, the bulk "MHD fluid".

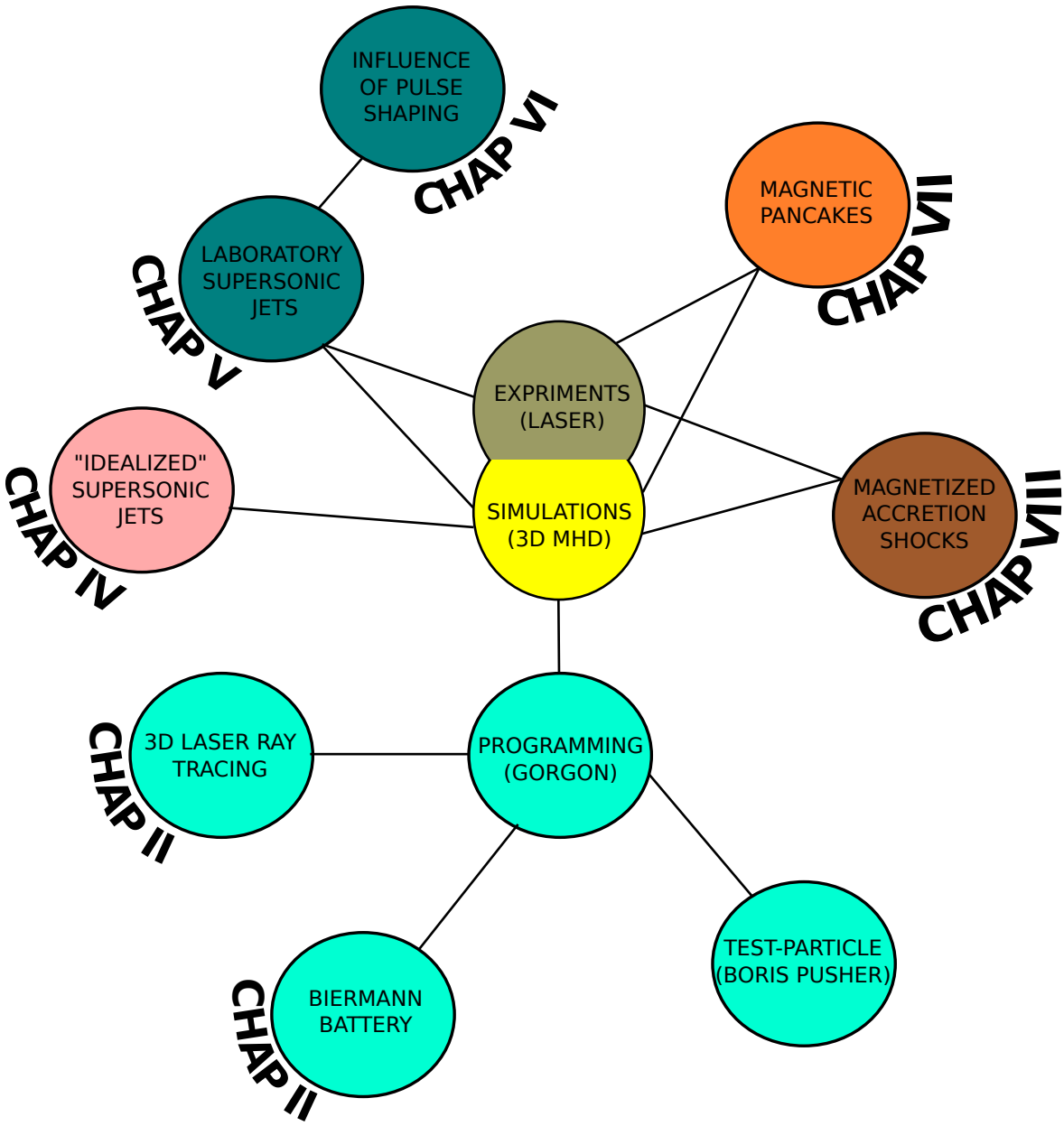

Figure 1.1: Schematic representation of the main addressed topics in this manuscript.

1.3 What you will see in this manuscript

The work I present in this manuscript is represented schematically in fig.1.1. Omitted in this schema are the first part of chapter II where the bi-temperature magnetohydrodynamic (MHD) model is derived (2) and the GORGON code is presented (2.4). Also omitted is chapter III (3) which can be considered as a (very) small review of the physics of laser-solid-plasma interaction at, what could called "hydrodynamic" intensities. These intensities correspond to regimes such that the distribution functions (a notion defined in chapter II) are not departing "too far" from the maxwellian distribution under the laser action. In the last part of this chapter, emphasis is placed on the dynamic of the plasma plume generated by the laser and expanding away from the solid target. A review of the well-known one-dimensional, self-similar adiabatic and isothermal expansions is given, as well as an original (but preliminary) treatment of the hypersonic regions of the plume by using a solution of the inviscid Burger's equation (i.e the "pressureless" Euler equa-

tion). In chapter IV (4) we introduce the topic of supersonic/hypersonic jets by studying both theoretically and numerically some fundamental properties of these objects. To do so, we use an idealized numerical setup where the jet enters, using boundary conditions, one side of the simulation domain which is filled with a background composed of plasma or/and magnetic field. We address especially the aspect of the stability of these jets by looking at the potentially disruptive effect of the Kelvin-Helmholtz instability and the stabilizing effect of the magnetic field. The chapter ends with the case of a supersonic jet propagating in a magnetized vacuum. We show that this configuration is extremely stable and represents the perfect introduction for the fifth chapter. Indeed, in chapter V (5) we present an in-depth study of the production, in the laboratory, of magnetically collimated jets. The "source" of the jet in this setup the laser-produced plasma expanding in front of a solid target. In the following chapter VI (6) we address, both experimentally et numerically, the potential possibility to introduce variability in the source of the jets by adding a second pulse to the previous setup. In particular we vary the delay between the two pulses and observe the resulting changes in the internal structures of the collimated flow. In chapter VII (7) we investigate the case where the magnetic field is rotated by 90° such that it is parallel to the target surface. We show, strongly supported by experimental results, that the magnetic field action on the plasma dynamic results in the formation of what can be identified as magnetic slabs or "magnetic pancakes". It is also shown that these pancakes are largely structured by MHD instabilities. We suggest the potential interest of this configuration in the context of magnetic structuring of stellar atmospheres. Finally, in chapter VIII (8) and IX (9) we treat the topic that should be considered as been the "raison d'être" of this thesis, that is the three-dimensional study of magnetized accretion dynamic in the laboratory. The setup makes use of the previously studied jets in order to use them as "accretion columns" impacting on solid obstacles. First are presented briefly some very recent experimental results obtained at the LULI laboratory and then we expand the study using our 3D simulations to infer several fundamental features present in this type of experiment. In particular, we look at the asymmetric aspects of the developed structures as well as the importance correctly modeling the column-obstacle interaction. We highlight an important characteristic of the laboratory accretion shocks: the shock/postshock region itself is in a non equilibrium state with ions much hotter than electrons. This last point is a fundamental difference with the astrophysical case where the postshock equilibration times are sufficiently small to consider equals temperatures for electrons and ions. In addition to these chapters forming the core of this manuscript, we give in appendix a certain number of theoretical derivations of propagating modes and instabilities in several configurations. We notably derive the dispersion relations for modes propagating in magnetic interfaces or magnetic slabs. These derivations are not essential for the understanding of the core chapters.

1.4 Bibliography

[1] T.R. Kallman and P. Palmeri. Atomic data for x-ray astrophysics. *Reviews of Modern Physics*, 79:79–133, January 2007. 2

[2] E. Herbst and E.F. van Dishoeck. Complex Organic Interstellar Molecules. *araa*, 47:427–480, September 2009. 2

[3] B.T. Draine. Interstellar Dust Grains. *araa*, 41:241–289, 2003. 2

[4] Adelberger et al. Solar fusion cross sections. II. The pp chain and CNO cycles. *Reviews of Modern Physics*, 83:195–246, January 2011. 2

[5] Elena Aprile and Stefano Profumo. Focus on dark matter and particle physics. *New Journal of Physics*, 11(10):105002, 2009. 2

[6] C. N. Matthews and R. D. Minard. Hydrogen cyanide polymers, comets and the origin of life. *Faraday Discussions*, 133:393, 2006. 2

[7] Michel Nuevo, Stefanie N Milam, Scott A Sandford, Jamie E Elsila, and Jason P Dworkin. Formation of uracil from the ultraviolet photo-irradiation of pyrimidine in pure h2o ices. *Astrobiology*, 9(7):683–695, 2009. 2

[8] Emeric Falize, Serge Bouquet, and Claire Michaut. Radiation hydrodynamics scaling laws in high energy density physics and laboratory astrophysics. In *Journal of Physics: Conference Series*, volume 112, page 042016. IOP Publishing, 2008. 3

[9] DD Ryutov, RP Drake, and BA Remington. Criteria for scaled laboratory simulations of astrophysical mhd phenomena. *The Astrophysical Journal Supplement Series*, 127(2):465, 2000. 3

[10] A. Frank, T. P. Ray, S. Cabrit, P. Hartigan, H. G. Arce, F. Bacciotti, J. Bally, M. Benisty, J. Eislöffel, M. Güdel, S. Lebedev, B. Nisini, and A. Raga. Jets and Outflows from Star to Cloud: Observations Confront Theory. *Protostars and Planets VI*, pages 451–474, 2014. 3

[11] J. Kwan and E. Tademaru. Jets from T Tauri stars - Spectroscopic evidence and collimation mechanism. *ApJL*, 332:L41–L44, September 1988.

[12] S. V. Lebedev, A. Ciardi, D. J. Ampleford, S. N. Bland, S. C. Bott, J. P. Chittenden, G. N. Hall, J. Rapley, C. A. Jennings, A. Frank, E. G. Blackman, and T. Lery. Magnetic tower outflows from a radial wire array Z-pinch. *mnras*, 361:97–108, July 2005. 3

[13] A. Ciardi, S. V. Lebedev, A. Frank, E. G. Blackman, D. J. Ampleford, C. A. Jennings, J. P. Chittenden, T. Lery, S. N. Bland, S. C. Bott, G. N. Hall, J. Rapley, F. A. S. Vidal, and A. Marocchino. 3D MHD Simulations of Laboratory Plasma Jets. *apss*, 307:17–22, January 2007. 3

[14] D. Lynden-Bell. Magnetic collimation by accretion discs of quasars and stars. *mnras*, 279:389–401, March 1996. 3

[15] P. M. Bellan, S. You, and S. C. Hsu. Simulating Astrophysical Jets in Laboratory Experiments. *apss*, 298:203–209, July 2005. 3

[16] S. C. Hsu and P. M. Bellan. On the jets, kinks, and spheromaks formed by a planar magnetized coaxial gun. *Physics of Plasmas*, 12(3):032103, March 2005. 3

[17] B. Albertazzi, A. Ciardi, M. Nakatsutsumi, T. Vinci, J. Béard, R. Bonito, J. Billette, M. Borghesi, Z. Burkley, S. N. Chen, T. E. Cowan, T. Herrmannsdörfer, D. P. Higginson, F. Kroll, S. A. Pikuz, K. Naughton, L. Romagnani, C. Riconda, G. Revet, R. Riquier, H.-P. Schlenvoigt, I. Yu. Skobelev, A.Ya. Faenov, A. Soloviev, M. Huarte-Espinosa, A. Frank, O. Portugall, H. Pépin, and J. Fuchs. Laboratory formation of a scaled protostellar jet by coaligned poloidal magnetic field. *Science*, 346(6207):325–328, 2014. 3

[18] A. Ciardi, T. Vinci, J. Fuchs, B. Albertazzi, C. Riconda, H. Pépin, and O. Portugall. *Phys. Rev. Lett.*, 110:025002, 2013. 3

[19] B Albertazzi, J Béard, A Ciardi, T Vinci, J Albrecht, J Billette, T Burris-Mog, SN Chen, D Da Silva, S Dittrich, et al. Production of large volume, strongly magnetized laser-produced plasmas by use of pulsed external magnetic fields. *Review of Scientific Instruments*, 84(4):043505, 2013. 3

[20] B Rus, K Rohlena, J Skála, B Králiková, K Jungwirth, J Ullschmied, KJ Witte, and H Baumhacker. New high-power laser facility pals—prospects for laser–plasma research. *Laser and Particle Beams*, 17(2):179–194, 1999. 4

[21] SV Lebedev, DJ Ampleford, SN Bland, SC Bott, JP Chittenden, J Goyer, C Jennings, MG Haines, GN Hall, DA Hammer, et al. Physics of wire array z-pinch implosions: experiments at imperial college. *Plasma physics and controlled fusion*, 47(5A):A91, 2005. 4

Chapter 2

MagnetoHydroDynamic

Sommaire

2.1 Introduction **10**

2.2 Fluid equations from the kinetic theory **12**

2.2.1 Zero-order moment: the mass conservation equation 12

2.2.2 First-order moment: the momentum conservation equation 13

2.2.3 Second-order moment: the energy conservation equation 16

2.3 MagnetoHydroDynamic (MHD) reduction **16**

2.3.1 Summary of the multi-species fluid equations 16

2.3.2 Expression of the collisional heating term 18

2.3.3 The conservation energy for multi-species fluid equations 19

2.3.4 The bi-temperature MHD model 20

2.3.5 MHD mass conservation equation 21

2.3.6 MHD momentum conservation equation 21

2.3.7 MHD internal energy conservation equation 24

2.3.8 The generalized Ohm's law 25

2.3.9 The displacement current in the Maxwell-Ampere equation 30

2.3.10 Relative importance of the various electric field terms in the generalized Ohm's law 31

2.3.11 The induction equation 35

2.3.12 The quasi-neutrality assumption 36

2.3.13 Conservation of the total energy in the MHD model 36

2.4 The GORGON 3D resistive, bi-temperature MHD code **39**

2.4.1 Introduction 39

2.4.2 Implemented equations 40

2.4.3 Localization of the physical quantities in the GORGON grid 40

2.5 Implementation of a laser module in the GORGON code **41**

2.5.1 Introduction 41

2.5.2 Electromagnetic Wave propagation equation in a (unmagnetized) plasma 42

2.5.3 Effect of electron-ion collisions on the propagation of light waves in homogeneous plasmas 45
2.5.4 Geometric optic approximation and the eikonal equation 46
2.5.5 Implementing the laser deposition module in the three-dimensional, resistive MHD code GORGON 47
2.5.6 Validation test for the laser module 50
2.6 Implementation of the Biermann battery effect in the GORGON code . . 52
2.6.1 General description 52
2.6.2 Details of the numerical implementation 53
2.6.3 Simulation tests 54
2.7 Bibliography 57

2.1 Introduction

In this chapter we present in details the MHD model and code that are the foundation of the work presented in the manuscript. The MHD model equations are derived from first principle, and although the model is well established and the derivation can be found in many excellent books, we have taken particular care to highlight and critically discuss the many assumption that are often made and somewhat overlooked.

In section 2.2 we derive the general fluid equations from the kinetic description. The central mathematical object in the kinetic theory of gas/plasmas is the distribution function, noted $f(\mathbf{r},\mathbf{v},t)$. This function corresponds to the (most probable) number of particles located, at a time t, in a infinitesimal volume $d\mathbf{r}^3 d\mathbf{v}^3$ ($d\mathbf{r}^3 = dxdydz$ and $d\mathbf{v}^3 = v_x v_y v_z$ in Cartesian coordinates) of the phase space around the point $(\mathbf{r},\mathbf{v})$. We will use the definition for the number density of particle $n(\mathbf{r},t)$:

$$n(\mathbf{r},t) = \iiint_{\mathbf{v}} f(\mathbf{r},\mathbf{v},t)\, d\mathbf{v}^3 \tag{2.1}$$

Depending on whether collisions are taken into account or not, the equation describing the evolution of the distribution function is the Vlasov equation (no collisions) or the Boltzmann equation (with collisions). The Boltzmann equation is written as:

$$\frac{\partial f}{\partial t} + (\mathbf{v}\cdot\nabla) f + (\mathbf{a}\cdot\nabla_{\mathbf{v}}) f = \dot{f}_c \tag{2.2}$$

where $\mathbf{a}$ is the acceleration, $\nabla_{\mathbf{v}}$ is nabla operator applied in the velocity space and $\dot{f}_c$ is the term representing the effect of collisions, both intra-species and inter-species. The formulation of this term is generally the trickiest part of the Boltzmann equation and several models exist, one of the most widely used is the Fokker-Planck (FP) equation. The collisionless Vlasov equation is obtained by setting $\dot{f}_c = 0$ in 2.2 (see [1] for a complete derivation and discussion about this equation). The fluid equations, namely the equations describing the conservation of mass, of momentum and of energy are obtained from the Boltzmann equation 2.2 by expressing the first three moments of the distribution function (relative to the variable $\mathbf{v}$). The process by which we obtain these equations is called a "reduction" because of the fact that the system is simplified and described in somewhat less details. Indeed, when integrating on the velocities $\mathbf{v}$ we loose for example all the details about the individual particles speeds which are replaced instead by the mean fluid velocity $\mathbf{u}$:

$$n(\mathbf{r},t)\mathbf{u}(\mathbf{r},t) = \iiint_{\mathbf{v}} \mathbf{v} f(\mathbf{r},\mathbf{v},t)\, d\mathbf{v}^3 \tag{2.3}$$

The relation 2.3 is the 1th-order moment of the distribution function whereas 2.1 is its 0th-order moment. Once the mean velocity (i.e. the fluid velocity) defined, it is useful to introduce the velocity of the particle $\mathbf{w}$ in the frame of the fluid velocity $\mathbf{u}$:

$$\mathbf{w} = \mathbf{v} - \mathbf{u} \tag{2.4}$$

In the vast majority of fluid models, a last third moment is also used and it is obtained by multiplying the Boltzmann equation 2.2 by $m\mathbf{v}\mathbf{v}$ and then by integrating over all velocities. As we shall see (see 2.20), this new equation introduces, when using 2.4, the pressure tensor $\bar{\bar{\mathrm{P}}}$ defined by:

$$\bar{\bar{\mathrm{P}}} = \iiint_{\mathbf{v}} m_\alpha \mathbf{w}\mathbf{w} f(\mathbf{r}, \mathbf{v}, t) d\mathbf{v}^3 \tag{2.5}$$

where we introduced the mass m_α of a particle of the specie α (electrons, ions...). It is important to note that, in general, the pressure is not a scalar but indeed a tensor described by the dyadic product **ww** in 2.5. As we shall see, each equation describing the evolution of a moment involves the knowledge of the next moment of higher order. Thus, ideally, a fourth moment equation (describing the evolution of the heat flux) of the Boltzmann equation would be necessary to express the evolution of the pressure tensor and then a fifth moment equation would be necessary to express the evolution of this fourth moment and so on... Even if some models have been developed to include such higher orders moments equations ([2]), the vast majority of fluid descriptions use only the first three conservation equations and replace the lacking equations by what is called a closure relation. There are two different types of fluid closure schemes. The truncation schemes, where higher order moments are assumed negligible or simply prescribed in terms of lower moments (see [3]), and the asymptotic schemes where assumptions on certain dimensionless parameters allows to infer, from the kinetic theory, expressions for the higher moments involved. For example, the Chapman-Enskog theory of a neutral gas dominated by collisions allows to find simplified expressions for the transport coefficients, see [4]). The description of a complete physical system by the fluid equations will be increasingly precise as the distribution function tends toward a function well described by a decreasing number of moments. The general idea behind is that, to keep the exact same degree of informations between the kinetic description and the fluid description, one would need to compute the evolution of an infinite number of moments. It turns out that in many cases of interest, the distribution function is "simple enough" to be relatively well characterized by a small number of moments. The best example is of course the one temperature Maxwell–Boltzmann distribution:

$$f(\mathbf{r}, \mathbf{v}, t) = n(\mathbf{r}, t) \left(\frac{m_\alpha}{2\pi k_\mathrm{B} \mathrm{T}} \right)^{3/2} \exp\left(-\frac{m_\alpha (\mathbf{v} - \mathbf{u})^2}{2 k_\mathrm{B} \mathrm{T}} \right) \tag{2.6}$$

This distribution function is, as one can see, completely described by the first three moments, namely the density, the mean velocity and the temperature. The Maxwell–Boltzmann distribution is thus the "perfect" function in the framework of the three-moments fluid model. As is well known, it can be shown [4–6] that, in the limit of a collision dominated system (large term $\dot{f}_c$), the Boltzmann equation 2.2 drives the distribution function towards a Maxwell–Boltzmann distribution 2.6. This "relaxation" process is a direct result of the H-theorem of Boltzmann [7]. Therefore, a fluid model will always be more adapted for collisional plasmas (such that the mean free path of a particle is much smaller than the typical size of the system) than for weakly or non-collisional plasmas where the Vlasov equation is required.

In section 2.3 we present an additional simplification to the system of fluid equations obtained in section 2.2. Indeed, the system of equations derived from the moments of the Boltzmann equation (see section 2.2) have to be applied to each species α of the plasma. For each species, the fluid model requires the solution of five equations (one for the mass conservation, three for the momentum conservation and one for the energy conservation). So if N_α is the number of different species composing the plasma, the total number of fluid equations is $5\mathrm{N}_\alpha$, plus the coupled eight maxwell equations. This is a mathematically very demanding system and we highlight the fact that N_α can be very large. Since the

electromagnetic forces depend on the charge state, each ionization state of a given specie needs to be treated separately. The so-called "MHD reduction" that will be described, basically replaces all the different "fluids" by one neutral fluid. One central assumption, among others, is that the time scales of interests are sufficiently large compared to the time scale where charge separation occurs. In such case the net charge density in the plasma can then be set to zero. We will first reduce all ion charge states to a single "heavy" fluid with a mean degree of ionization Z_i^* and then the reduction will be applied the electron (light) and ion (heavy) fluid mass and momentum conservation equations, thus reducing the system to $2 + N_\alpha$ equations.

The remainder of the chapter (section 2.4) will be dedicated to a detailed description of the model used in the code GORGON, which is somewhat a further reduction of the MHD model given in section 2.3, and the implementation of several new physics modules (laser depostion, Biermann battery ,...).

2.2 Fluid equations from the kinetic theory

2.2.1 Zero-order moment: the mass conservation equation

As explained in the introductory section 2.1, the starting point to derive the fluid equations is the Boltzmann equation 2.2. The zero-order moment is obtained by directly integrating this equation over the velocities:

$$\frac{\partial}{\partial t}\left(\iiint_{\mathbf{v}} f d\mathbf{v}^3\right) + \iiint_{\mathbf{v}} (\mathbf{v}\cdot\nabla) f d\mathbf{v}^3 + \iiint_{\mathbf{v}} (\mathbf{a}\cdot\nabla_{\mathbf{v}}) f d\mathbf{v}^3 = \left.\frac{\delta n}{\delta t}\right|_c \tag{2.7}$$

where the right-hand side (RHS),

$$\left.\frac{\delta n}{\delta t}\right|_c = \iiint_{\mathbf{v}} \dot{f}_c d\mathbf{v}^3 \tag{2.8}$$

corresponds to a source term describing, for example, an external injection of matter or nuclear reactions (through collisions). The first term on the left-hand side (LHS) is simply, using 2.1, equal to the partial time derivative of the number density:

$$\frac{\partial}{\partial t}\left(\iiint_{\mathbf{v}} f d\mathbf{v}^3\right) = \frac{\partial n}{\partial t} \tag{2.9}$$

The second term in LHS can be easily rewritten by noticing that the gradient applies only to the variable $\mathbf{r}$: $(\mathbf{v}\cdot\nabla) f = \nabla\cdot(\mathbf{v} f)$, and that the integration is only over the velocities, the gradient can then be removed from the integrals to give:

$$\iiint_{\mathbf{v}} (\mathbf{v}\cdot\nabla) f d\mathbf{v}^3 = \nabla\cdot\left(\iiint_{\mathbf{v}} \mathbf{v} f d\mathbf{v}^3\right) = \nabla\cdot(n\mathbf{u}) \tag{2.10}$$

where we used relation 2.3. This terms corresponds to the divergence of the mass flux. For the last term of the LHS, we need to explicit the expression of the acceleration $\mathbf{a}$. We consider the general case of the Lorentz force $\mathbf{F_{lorentz}} = \mathbf{F_E} + \mathbf{F_B} = q\mathbf{E} + q\mathbf{v}\times\mathbf{B}$ where $\mathbf{E}$ is the local electric field, $\mathbf{B}$ the local magnetic field and q the electric charge of the particle. The electric force does not depend on the velocity and the magnetic force has the particularity

that its component F_{Bi} (i=x,y,z) does not depend on the velocity v_i. The acceleration is related to the force by the Newton's second law: $\mathbf{a} = \mathbf{F_{lorentz}}/m$. Using the index notation (summation over all indices i), we can thus write:

$$\iiint_{\mathbf{v}} (\mathbf{a}\cdot\nabla_{\mathbf{v}}) f\, d\mathbf{v}^3 = \iint_{v_{j\neq i}} a_i \left[\int_{v_i} \partial_{v_i} f\, d v_i\right] d\mathbf{v}^2 = \iint_{v_{j\neq i}} a_i \left[f\right]_{v_i=-\infty}^{v_i=+\infty} d\mathbf{v}^2 = 0 \tag{2.11}$$

where we used the justifiable assumption that the distribution function vanish for $v_i = \pm\infty$ and thus $\left[f\right]_{v_i=-\infty}^{v_i=+\infty} = 0$. Injecting expressions 2.9, 2.10 and 2.11 into 2.7 we get the first fluid equation:

$$\frac{\partial n}{\partial t} + \nabla\cdot(n\mathbf{u}) = \left.\frac{\delta n}{\delta t}\right|_c \tag{2.12}$$

This equation describes the conservation of the quantity of matter or, equivalently by multiplying it by the particle mass m, the conservation of mass.

2.2.2 First-order moment: the momentum conservation equation

The second fluid equation is obtained first multiplying the Boltzmann equation 2.2 by the particle momentum $m\mathbf{v}$ and then by integrating over the velocities:

$$\frac{\partial}{\partial t}\left(\iiint_{\mathbf{v}} m\mathbf{v} f\, d\mathbf{v}^3\right) + \iiint_{\mathbf{v}} m\mathbf{v}(\mathbf{v}\cdot\nabla) f\, d\mathbf{v}^3 + \iiint_{\mathbf{v}} m\mathbf{v}(\mathbf{a}\cdot\nabla_{\mathbf{v}}) f\, d\mathbf{v}^3 = \mathbf{A} \tag{2.13}$$

where:

$$\mathbf{A} = \iiint_{\mathbf{v}} m\mathbf{v}\dot{f}_c d\mathbf{v}^3 \tag{2.14}$$

The first term in the LHS of equation 2.13 is, using 2.3, simply equal to:

$$\frac{\partial}{\partial t}\left(\iiint_{\mathbf{v}} m\mathbf{v} f\, d\mathbf{v}^3\right) = \frac{\partial(\rho\mathbf{u})}{\partial t} \tag{2.15}$$

where $\rho = mn$ is the mass density. The i component of the second term of the LHS can be rewritten using the same argument as for the zero-order moment (i.e. the gradient applies only on $\mathbf{r}$):

$$\left.\iiint_{\mathbf{v}} m\mathbf{v}(\mathbf{v}\cdot\nabla) f\, d\mathbf{v}^3\right|_i = \partial_j\left(\iiint_{\mathbf{v}} m v_i v_j f\, d\mathbf{v}^3\right) \tag{2.16}$$

We can go further by using the previously defined (see 2.4) centered velocity $\mathbf{w}$, for which we recall the expression:

$$\mathbf{w} = \mathbf{v} - \mathbf{u} \tag{2.17}$$

with, by definition:

$$\iiint_{\mathbf{v}} \mathbf{w} f\, d\mathbf{v}^3 = \iiint_{\mathbf{v}} (\mathbf{v}-\mathbf{u}) f\, d\mathbf{v}^3 = n\mathbf{u} - n\mathbf{u} = \mathbf{0} \tag{2.18}$$

Inserting the central moment 2.17 in 2.16 we get:

$$\iiint_{\mathbf{v}} m\mathbf{v}(\mathbf{v}\cdot\nabla) f d\mathbf{v}^3 \Big|_i = \partial_j \left(\iiint_{\mathbf{v}} m(w_i w_j + u_j w_i + u_i w_j + u_i u_j) f d\mathbf{v}^3 \right) \tag{2.19}$$

the first integral in the RHS of 2.19 defines the kinetic pressure tensor $\bar{\bar{\mathrm{P}}}$:

$$\bar{\bar{\mathrm{P}}}_{ij} = \iiint_{\mathbf{w}} m w_i w_j f d\mathbf{w}^3 \tag{2.20}$$

where we used the fact that $d\mathbf{v}^3 = d\mathbf{w}^3$ and the integration bounds are still $\pm\infty$ for each component of the central moment $\mathbf{w}$. The second and third integral of the RHS in 2.19 are zero because of the definition of the central moment 2.18:

$$\iiint_{\mathbf{v}} m u_j w_i f d\mathbf{v}^3 = m u_j \iint_{\mathbf{w_{k\neq i}}} \left(\int_{\mathbf{w_i}} w_i f d w_i \right) d\mathbf{w}^2 = 0 \tag{2.21}$$

and

$$\iiint_{\mathbf{v}} m u_j w_i f d\mathbf{v}^3 = m u_i \iint_{\mathbf{w_{k\neq j}}} \left(\int_{\mathbf{w_j}} w_j f d w_j \right) d\mathbf{w}^2 = 0 \tag{2.22}$$

Finally the third term on the RHS of 2.19 is simply given by:

$$\partial_j \left(\iiint_{\mathbf{v}} m u_i u_j f d\mathbf{v}^3 \right) = \partial_j(\rho u_i u_j) = \rho(u_j \partial_j) u_i + u_i \partial_j(\rho u_j) \tag{2.23}$$

then, by inserting all terms 2.20, 2.21,2.22 and 2.23 in 2.19 we get:

$$\iiint_{\mathbf{v}} m\mathbf{v}(\mathbf{v}\cdot\nabla) f d\mathbf{v}^3 = \nabla\cdot\bar{\bar{\mathrm{P}}} + \rho(\mathbf{u}\cdot\nabla)\mathbf{u} + \mathbf{u}(\nabla\cdot(\rho\mathbf{u})) \tag{2.24}$$

and by summing the first (2.15) and second term (2.24) of the first-order moment equation 2.13 we find:

$$\frac{\partial}{\partial t}\left(\iiint_{\mathbf{v}} m\mathbf{v} f d\mathbf{v}^3 \right) + \iiint_{\mathbf{v}} m\mathbf{v}(\mathbf{v}\cdot\nabla) f d\mathbf{v}^3 = \rho\frac{d\mathbf{u}}{dt} + \nabla\cdot\bar{\bar{\mathrm{P}}} + m\mathbf{u}\,\frac{\delta n}{\delta t}\Big|_c \tag{2.25}$$

where $d\mathbf{u}/dt = \partial\mathbf{u}/\partial t + (\mathbf{u}\cdot\nabla)\mathbf{u}$ is the Lagrangian (or total) derivative and where we used the first fluid equation 2.12.

Now we derive the expression of the third term of the LHS of 2.13. We use again the fact that a component a_i of the particle acceleration does not depend on the component v_i of the particle velocity. We can thus write:

$$\iiint_{\mathbf{v}} m\mathbf{v}(\mathbf{a}\cdot\nabla_{\mathbf{v}}) f d\mathbf{v}^3 \Big|_i = \iiint_{\mathbf{v}} m v_i \partial_{v_j}(a_j f) d\mathbf{v}^3 \tag{2.26}$$

We consider two possibilities: first, if $j = i$, we can write:

$$\iiint_{\mathbf{v}} m v_i \partial_{v_i}(a_i f) d\mathbf{v}^3 = \iint_{v_j \neq v_i} m a_i \left(\int_{v_i} v_i \partial_{v_i} f \right) d\mathbf{v}^2 \tag{2.27}$$

and with:

$$\int_{v_i} v_i \partial_{v_i} f = [v_i f]_{v_i=-\infty}^{v_i=+\infty} - \int_{v_i} f d v_i = -\int_{v_i} f d v_i \tag{2.28}$$

we have

$$\iiint_{\mathbf{v}} m v_i \partial_{v_i}(a_i f) d\mathbf{v}^3 = -\iint_{v_j \neq v_i} m a_i \left(\int_{v_i} f d v_i \right) d\mathbf{v}^2 \tag{2.29}$$

using the index notation, we can write the particle acceleration as:

$$a_i = \frac{q}{m} \mathrm{E}_i + \frac{q}{m} \epsilon_{ijk} v_j \mathrm{B}_k \tag{2.30}$$

and inserting 2.30 in 2.29 we get:

$$-\iint_{v_j \neq v_i} m a_i \left(\int_{v_i} f d v_i \right) d\mathbf{v}^2 = -q \mathrm{E}_i \iiint_{\mathbf{v}} f d\mathbf{v}^3 - q \epsilon_{ijk} \mathrm{B}_k \iiint_{\mathbf{v}} v_j f d\mathbf{v}^3 \tag{2.31}$$

An finally, using 2.1 and 2.3, we obtain:

$$\iiint_{\mathbf{v}} m v_i \partial_{v_i}(a_i f) d\mathbf{v}^3 = -qn\mathrm{E}_i - qnu_i \mathrm{B}_i \tag{2.32}$$

If we now suppose that in relation 2.26 we have $j \neq i$ the result in simply:

$$\iiint_{\mathbf{v}} m v_i \partial_{v_j}(a_j f) d\mathbf{v}^3 = \iint_{v_k \neq v_j} m a_j v_i \left(\int_{v_j} \partial_{v_j} f d v_j \right) d\mathbf{v}^2 = 0 \tag{2.33}$$

because the distribution function is zero for $v = \pm\infty$. We can finally express the third term in the LHS of equation 2.13 as

$$\iiint_{\mathbf{v}} m\mathbf{v}(\mathbf{a} \cdot \nabla_{\mathbf{v}}) f d\mathbf{v}^3 = -qn\mathbf{E} - qn\mathbf{u} \times \mathbf{B} \tag{2.34}$$

and assembling all the term of the first-order moment equation (2.25 and 2.34 we find the second fluid equation:

$$\rho \frac{d\mathbf{u}}{dt} = -\nabla \cdot \bar{\bar{\mathrm{P}}} + qn\mathbf{E} + qn\mathbf{u} \times \mathbf{B} + \mathbf{A} - m\mathbf{u} \left. \frac{\delta n}{\delta t} \right|_c \tag{2.35}$$

2.2.3 Second-order moment: the energy conservation equation

By multiplying the Boltzmann equation 2.2 by **vv** (the dyadic product) one would obtain the equation describing the evolution of the pressure tensor $\bar{\bar{\mathrm{P}}}$ and involving the heat flux tensor $\bar{\bar{\mathrm{Q}}}_{\mathrm{T}}$ (tensor of order 3) defined by:

$$\bar{\bar{\mathrm{Q}}}_{\mathrm{T}} = \iiint_{\mathbf{w}} m\mathbf{www} f d\mathbf{w}^3 \tag{2.36}$$

This equation is quite complicated and not very useful since almost never used in this form. The process to obtain it is however very similar to the one used for the two previous moments. Here we present a simplified form obtained under the assumption that the heat flux can be expressed as a vector defined by:

$$\mathbf{q} = \frac{1}{2}\iiint_{\mathbf{w}} m w^2 \mathbf{w} f d\mathbf{w}^3 \tag{2.37}$$

and valid if the velocity anisotropies are small. If furthermore the non-diagonal terms of the pressure tensor are also neglected (also true for small anisotropies) then the pressure can be simplified as:

$$p = \frac{1}{3}\iiint_{\mathbf{w}} m w^2 f d\mathbf{w}^3 = \frac{1}{3}\mathrm{T}r(\bar{\bar{\mathrm{P}}}) \tag{2.38}$$

where $\mathrm{T}r(\bar{\bar{\mathrm{P}}})$ is the trace of the pressure tensor. In this case, equation obtained from the second-order moment can be written:

$$\frac{\partial}{\partial t}\left(\frac{3}{2}p + \frac{1}{2}\rho u^2\right) + \nabla\cdot\left[\mathbf{q} + \left(\frac{5}{2}p + \frac{1}{2}\rho u^2\right)\mathbf{u}\right] = qn\mathbf{u}\cdot\mathbf{E} + \mathrm{K} - \mathbf{u}\cdot\mathbf{A} + \frac{1}{2}mu^2\left.\frac{\delta n}{\delta t}\right|_c \tag{2.39}$$

where:

$$\mathrm{K} = \iiint_{\mathbf{v}} \frac{mv^2}{2}\dot{f}_c d\mathbf{v}^3 \tag{2.40}$$

With the internal energy density defined as $\epsilon = p/(\gamma - 1)$ we clearly see that equation 2.39 corresponds to the energy fluid equation for a population with an adiabatic index $\gamma = 5/3$.

2.3 MagnetoHydroDynamic (MHD) reduction

2.3.1 Summary of the multi-species fluid equations

We now derive the complete MHD model with, as starting point the multi fluid equations derived in the previous section. In the following, the index α is used to identify a given population (electrons, ions).

I) The conservation of matter, obtained by multiplying equation 2.12 by $m\alpha$:

$$\frac{\partial \rho_\alpha}{\partial t} + \nabla\cdot(\rho_\alpha \mathbf{u}) = \mathrm{S}_\alpha \tag{2.41}$$

where S is a source term (nuclear reactions, external source...). We can write this equation using the the lagrangian derivative $d/dt = \partial/\partial t + \mathbf{u}_\alpha\cdot\nabla$:

$$\frac{d\rho_\alpha}{dt} = -\rho_\alpha \nabla \cdot \mathbf{u}_\alpha \tag{2.42}$$

II) The conservation of momentum (from 2.35):

$$\rho_\alpha \left(\frac{\partial \mathbf{u}_\alpha}{\partial t} + (\mathbf{u}_\alpha \cdot \nabla)\mathbf{u}_\alpha \right) = -\nabla p_\alpha + q_\alpha n_\alpha \mathbf{E} + q_\alpha n_\alpha \mathbf{u}_\alpha \times \mathbf{B} + \mathbf{R}_\alpha - m_\alpha \mathbf{u}_\alpha \mathrm{S} \tag{2.43}$$

where $\mathbf{R}_\alpha$ is the friction force applying on the population α and we considered the reduction of the pressure tensor as a scalar (valid if the time between two collisions is much smaller than the time needed by a particle to make a complete magnetized gyration).

III) The conservation of internal energy:

$$\frac{\partial \epsilon_\alpha}{\partial t} + \nabla \cdot (\epsilon_\alpha \mathbf{u}_\alpha) = -p_\alpha \nabla \cdot \mathbf{u}_\alpha - \nabla \cdot \mathbf{q}_\alpha + \mathrm{Q}^c_\alpha + \mathrm{H}_\alpha \tag{2.44}$$

where Q^c_α is the heat transfer because of collisions and H_α is a energy source term (laser heating...). We also have the important relation:

$$\sum_\alpha \mathrm{Q}^c_\alpha + \sum_\alpha \mathbf{u}_\alpha \cdot \mathbf{R}_\alpha = 0 \tag{2.45}$$

This last equality, contrary to what one might think, does not mean that $\mathrm{Q}^c_\alpha = -\mathbf{u}_\alpha \cdot \mathbf{R}_\alpha$. This is because the frictional heating is only one component of the total heating Q^c_α due to the collisions (see 2.3.2 for more details).

IV) Maxwell's equations also need to be included in the system to describe the time evolution of the electromagnetic fields:

$$\nabla \cdot \mathbf{E} = \frac{\rho_q}{\epsilon_0} \tag{2.46}$$

$$\nabla \cdot \mathbf{B} = 0 \tag{2.47}$$

$$\frac{\partial \mathbf{B}}{\partial t} = -\nabla \times \mathbf{E} \tag{2.48}$$

$$\nabla \times \mathbf{B} = \mu_0 \mathbf{j} + \frac{1}{c^2}\frac{\partial \mathbf{E}}{\partial t} \tag{2.49}$$

with ρ_q the net charge density and:

$$\rho_q = \sum_\alpha q_\alpha n_\alpha \tag{2.50}$$

$\mathbf{j}$ the electrical current obtained from sum of the currents of each population:

$$\mathbf{j} = \sum_\alpha q_\alpha n_\alpha \mathbf{u}_\alpha \tag{2.51}$$

and ϵ_0 is the vacuum permittivity whereas μ_0 is the vacuum permeability.

In writing all the equations 2.41-2.51 we get a very complex system of equations where the only assumption having been made concerns basically the fact that the distribution function for each species, f_α, can be relatively well described by the first three moments. Which is generally valid when the mean free path of the particles is much smaller than the characteristic size of the system because in this case the distribution function tends towards a Maxwellian.

2.3.2 Expression of the collisional heating term

Frictional heating

In equation 2.44 we have introduced the term Q_α^c where several different terms are "hidden". First, the work of the frictional forces $\mathbf{R}_\alpha$ acting on each population α is the source of heat production (conversion of ordered kinetic energy into thermal energy). A simple way to describe how this heating is distributed among each component of the plasma has been given by Woods [8]. Let us suppose that the population α is heated, because of a frictional force with the population β, at rate $\phi_{\alpha\leftarrow\beta}$, and similarly for the population β. Then we have:

$$Q_{Fric} = \phi_{\alpha\leftarrow\beta} + \phi_{\beta\leftarrow\alpha} = -\mathbf{u}_\alpha \cdot \mathbf{R}_\alpha - \mathbf{u}_\beta \cdot \mathbf{R}_\beta \tag{2.52}$$

where Q_{Fric} is the total frictional heating in the plasma. By virtue of the Newton's third law (action-reaction law), the frictional momentum transfer from α to β must be equal to the opposite of the momentum transfer from β to α, that is: $\mathbf{R}_\alpha = -\mathbf{R}_\beta$. With this relation we can write the total frictional heating 2.52 as:

$$Q_{Fric} = \mathbf{R}_\alpha \cdot (\mathbf{u}_\beta - \mathbf{u}_\alpha) = \mathbf{R}_\beta \cdot (\mathbf{u}_\alpha - \mathbf{u}_\beta) \tag{2.53}$$

It is now necessary to determine how this total frictional heating is distributed among the populations. The simplest way, is to consider the case of isotropic elastic collisions where the energy after a collision α/β is distributed inversely to the particle masses:

$$\frac{\phi_{\alpha\leftarrow\beta}}{\phi_{\beta\leftarrow\alpha}} = \frac{m_\beta}{m_\alpha} \tag{2.54}$$

Inserting 2.54 in 2.52 we find:

$$\phi_{\alpha\leftarrow\beta} = \frac{m_\beta}{m_\alpha + m_\beta} Q_{Fric} \tag{2.55}$$

For example, for ions with mass m_i and electrons with mass $m_e << m_i$, it is easy to see that the frictional heating will go mainly into the lightest population, that is, the electrons. This is the reason why, in many two-temperature (MHD) models, the frictional heating is neglected for the ions.

Thermal equilibration

Another important term included in the heating Q_α^c is related to the fact that if two different populations, say electrons and ions, have different temperatures ($T_e \neq T_i$) then, because of collisions, they will tend to "correct" this deviation on a time scale of the order of the time between two collisions (or equivalently on a spatial scale of the order of the mean free path). The expression for this *thermal equilibration* process (first derived by Landau in 1937 [9]) is given by:

$$Q_{ei} = -3\frac{m_e}{m_i} n_e \nu_{ei} k_B (T_e - T_i) \tag{2.56}$$

where ν_{ei} is the electron-ion collision frequency [10]. We shall refer to Q_{ei} as the rate of heat exchange from electrons toward ions and note that the relation $Q_{ei} = -Q_{ie}$ holds.

In summary, using eq.2.53, 2.55, 2.56, and the fact that $\mathbf{R_i} = -\mathbf{R_e}$, the collisional heating term Q_α^c can be written for the electrons and ions as:

$$Q_e^c = \frac{m_i}{m_e + m_i}\mathbf{R_e}\cdot(\mathbf{u_i} - \mathbf{u_e}) - 3\frac{m_e}{m_i}n_e\nu_{ei}k_B(T_e - T_i) \tag{2.57}$$

$$Q_i^c = \frac{m_e}{m_e + m_i}\mathbf{R_e}\cdot(\mathbf{u_i} - \mathbf{u_e}) + 3\frac{m_e}{m_i}n_e\nu_{ei}k_B(T_e - T_i) \tag{2.58}$$

2.3.3 The conservation energy for multi-species fluid equations

The system of fluid equations summarized in 2.3.1 is completely self-consistent in terms of energy conservation. It can be seen by, first, identifying all forms of energy:

1. Kinetic energy: $\epsilon^{kin} = 1/2\rho u^2$
2. Internal energy: ϵ
3. Electromagnetic energy: $\epsilon^{EM} = \epsilon_0 E^2/2 + B^2/2\mu_0$

For each form of energy, there is a corresponding conservation equation. The internal energy conservation equation has already been derived (see eq. 2.44), the conservation of kinetic energy is obtained by multiplying the momentum equation 2.43 by $\mathbf{u}_\alpha$, and finally, the conservation of electromagnetic energy (Poynting's theorem) is obtained by multiplying eq. 2.48 by $\mathbf{B}$ and then using eq. 2.49. The system of equations is then given by:

Energy	Conservation equation
Kinetic	$\frac{\partial \epsilon_\alpha^{kin}}{\partial t} + \nabla\cdot(\epsilon_\alpha^{kin}\mathbf{u}_\alpha) = -\mathbf{u}_\alpha\cdot\nabla\cdot p_\alpha + q_\alpha n_\alpha \mathbf{u}_\alpha\cdot\mathbf{E} + \mathbf{u}_\alpha\cdot\mathbf{R}_\alpha$
Internal	$\frac{\partial \epsilon_\alpha}{\partial t} + \nabla\cdot(\epsilon_\alpha\mathbf{u}_\alpha) = -p_\alpha\nabla\cdot\mathbf{u}_\alpha - \nabla\cdot\mathbf{q}_\alpha + Q_\alpha^c + H_\alpha$
Electromagnetic	$\frac{\partial \epsilon^{EM}}{\partial t} + \nabla\cdot\left(\frac{\mathbf{E}\times\mathbf{B}}{\mu_0}\right) = -\mathbf{E}\cdot\mathbf{j}$

The RHS of the kinetic equation is composed of three terms: the work of pressure forces, the work of the electric field (no work from the magnetic field) and the work of the frictional force. The RHS of the internal equation is composed of the compressional term, the heat transfer term, the frictional heating term as well as all possible external source terms (laser, radiative emission...). Concerning the electromagnetic energy, the "transport" term $\Pi_{\mathbf{EM}} = \mathbf{E}\times\mathbf{B}/\mu_0$ is the Poynting vector and represents the directional energy flux density (W.m^{-2}) of the electromagnetic field. The RHS of this equation represents the electromagnetic energy losses/gains realized through the work the electric field is doing on the fluid particles. The conservation of the total energy is given by the sum of the three conservation equations, for all the species α composing the plasma:

$$\frac{\partial \epsilon^{tot}}{\partial t} + \nabla\cdot\left(\Pi_{\mathbf{EM}} + \sum_\alpha\left[\left(\epsilon_\alpha^{kin} + \epsilon_\alpha + p_\alpha\right)\mathbf{u}_\alpha + \mathbf{q}_\alpha\right]\right) = \sum_\alpha H_\alpha \tag{2.59}$$

where we have used relation 2.45as well as relation 2.51 to write $\sum_\alpha q_\alpha n_\alpha \mathbf{u}_\alpha\cdot\mathbf{E} = \mathbf{j}\cdot\mathbf{E}$ and ϵ^{tot} is the total energy density:

$$\epsilon^{tot} = \epsilon^{EM} + \sum_\alpha\left(\epsilon_\alpha^{kin} + \epsilon_\alpha\right) \tag{2.60}$$

Equation 2.60 describes the strict conservation of the total energy. It can be seen that in the absence of external heating ($\sum_\alpha H_\alpha = 0$) the total energy is only transported with the flux:

$$\mathbf{F^{tot}} = \Pi_{\mathbf{EM}} + \sum_\alpha \left[\left(\epsilon_\alpha^{kin} + \epsilon_\alpha + p_\alpha \right) \mathbf{u}_\alpha + \mathbf{q}_\alpha \right] \tag{2.61}$$

This flux can also be written in terms of the enthalpy density h_α of each species α:

$$h_\alpha = \epsilon_\alpha + p_\alpha \tag{2.62}$$

giving:

$$\mathbf{F^{tot}} = \Pi_{\mathbf{EM}} + \sum_\alpha \left[\left(\epsilon_\alpha^{kin} + h_\alpha \right) \mathbf{u}_\alpha + \mathbf{q}_\alpha \right] \tag{2.63}$$

The reason for discussing in some details the conservation of total energy is because it will be, when deriving the MHD model in the next section, particularly important when interpreting the meaning of what we shall call the "MHD energy".

2.3.4 The bi-temperature MHD model

The first step to derive the full system of equation is to consider the plasma to be composed of electrons ($\alpha = e$) of mass m_e and charge $q_e = -e$ and only one species of ion ($\alpha = i$) of mass m_i and charge $q_i = eZ^*$, where Z^* is the average degree of ionization. Both of these species obey equations 2.41-2.43-2.44 and are coupled with the Maxwell's equations 2.46-2.47-2.48-2.49.
We first define the total mass density of the plasma:

$$\rho = m_e n_e + m_i n_i = \rho_e + \rho_i \tag{2.64}$$

then the velocity $\mathbf{u}$ of the center of mass of the plasma:

$$\rho \mathbf{u} = \rho_e \mathbf{u_e} + \rho_i \mathbf{u_i} \tag{2.65}$$

and the total electrical current density:

$$\mathbf{j} = eZ^* n_i \mathbf{u_i} - e n_e \mathbf{u_e} \tag{2.66}$$

From 2.65 and 2.66 we can write $\mathbf{u_e}$ and $\mathbf{u_i}$ as functions of $\mathbf{u}$ and $\mathbf{j}$:

$$\mathbf{u_i} = \frac{\rho}{\rho^*}\mathbf{u} + \frac{m_e}{e\rho^*}\mathbf{j} \tag{2.67}$$

$$\mathbf{u_e} = \frac{Z^* n_i}{n_e}\frac{\rho}{\rho^*}\mathbf{u} - \frac{n_i}{n_e}\frac{m_i}{e\rho^*}\mathbf{j} \tag{2.68}$$

where:

$$\rho^* = \rho_i + \frac{Z^* n_i}{n_e}\rho_e \tag{2.69}$$

We see that up to this point, we have made no extra assumptions compared to the multi-species system described previously; we are just adding or averaging the previous quantities. We shall make further assumptions on spatial or temporal scales, as late as possible in our MHD derivation.

2.3.5 MHD mass conservation equation

As in the case of the multi-species fluid system, the first MHD equation describes the conservation of the "MHD mass density". It is obtained by directly summing the mass conservation equation for both species 2.41:

$$\frac{\partial(\rho_e+\rho_i)}{\partial t}+\nabla\cdot(\rho_e\mathbf{u_e}+\rho_i\mathbf{u_i})=0 \tag{2.70}$$

and, using, 2.64 2.65:

$$\frac{\partial\rho}{\partial t}+\nabla\cdot(\rho\mathbf{u})=0 \tag{2.71}$$

Equation 2.71 is the conservation equation for the mass density of the reduced MHD single-fluid.

2.3.6 MHD momentum conservation equation

An equation for the single-fluid momentum can be obtained from:

$$\frac{d(\rho\mathbf{u})}{dt}=\rho\frac{d\mathbf{u}}{dt}+\mathbf{u}\frac{d\rho}{dt}=\frac{d(\rho_e\mathbf{u_e})}{dt}+\frac{d(\rho_i\mathbf{u_i})}{dt}=\rho_e\frac{d\mathbf{u_e}}{dt}+\rho_i\frac{d\mathbf{u_i}}{dt}+\mathbf{u_e}\frac{d\rho_e}{dt}+\mathbf{u_i}\frac{d\rho_i}{dt} \tag{2.72}$$

and thus:

$$\rho\frac{d\mathbf{u}}{dt}=\rho_e\frac{d\mathbf{u_e}}{dt}+\rho_i\frac{d\mathbf{u_i}}{dt}+\frac{d\rho_e}{dt}(\mathbf{u_e}-\mathbf{u})+\frac{d\rho_i}{dt}(\mathbf{u_i}-\mathbf{u}) \tag{2.73}$$

From now, one has to be very cautious by the meaning of the total derivative d/dt used in the previous equations. Indeed, when writing these equations we have considered the problem in the frame of the velocity $\mathbf{u}$ of the center of mass defined by 2.65. Thus we have the important relation:

$$\frac{d}{dt}=\frac{\partial}{\partial t}+(\mathbf{u}\cdot\nabla) \tag{2.74}$$

This precision is important because we can't just insert directly the electron and ion momentum equations (given by 2.43) in 2.73 since with our notation:

$$\frac{d\mathbf{u_i}}{dt}\neq\frac{\partial\mathbf{u_i}}{\partial t}+(\mathbf{u_i}\cdot\nabla)\mathbf{u_i} \tag{2.75}$$

and same for electrons. As we will see, the problem will be easily solved using the expressions for the electron and ion velocities 2.68 and 2.67 provided the plasma is assumed to be neutral (see below).

Before to treat this problem, let's look at the last two terms of the RHS of equation 2.73 which can be rewritten using the expressions for the electron and ion velocity in terms of single-fluid velocity and electrical current density (eq. 2.67 and 2.68):

$$\frac{d\rho_e}{dt}(\mathbf{u_e}-\mathbf{u})=\left[\frac{Z^*n_i\rho-n_e\rho^*}{n_e\rho^*}\mathbf{u}-\frac{n_i}{n_e}\frac{m_i}{e\rho^*}\mathbf{j}\right]\frac{d\rho_e}{dt} \tag{2.76}$$

$$\frac{d\rho_i}{dt}(\mathbf{u_i}-\mathbf{u})=\left[\frac{\rho-\rho^*}{\rho^*}\mathbf{u}+\frac{m_e}{e\rho^*}\mathbf{j}\right]\frac{d\rho_i}{dt} \tag{2.77}$$

From here, we clearly see that it is impossible to remove all the dependencies in n_e and n_i without additional assumption. The terms in eq. 2.76 and 2.77 are corrective terms that take into account the fact that the single-fluid velocity is not equal to the velocity of both electrons and ions.

To proceed further, we make one of the main assumptions of the MHD model, namely that the single-fluid is considered as globally neutral. This is the quasi-neutrality of the plasma and it corresponds to the equality:

$$n_e = Z^* n_i \tag{2.78}$$

The assumption quasi-neutrality of the plasma is strong, in the sense that it corresponds to the suppression of all physical processes related to charge separation. We will discuss in details the domain of validity of the MHD model, but let's say for now that equation 2.78 acts as a sort of low-pass filter, by filtering all the dynamic occurring on the electron time scale (ω_{pe}^{-1}). With the assumption of quasi-neutrality (eq. 2.78), we see from eq. 2.69 that $\rho^* = \rho_e + \rho_i = \rho$ and thus the sum of equations 2.76 and 2.77 leads to:

$$\frac{d\rho_e}{dt}(\mathbf{u_e} - \mathbf{u}) + \frac{d\rho_i}{dt}(\mathbf{u_i} - \mathbf{u}) = \frac{m_e m_i}{e\rho}\mathbf{j}\left[\frac{dn_i}{dt} - \frac{1}{Z^*}\frac{dn_e}{dt}\right] = -\frac{m_e}{eZ^*}\frac{\rho_i}{\rho}\frac{dZ^*}{dt}\mathbf{j} \tag{2.79}$$

Furthermore, with our quasi-neutrality assumption, we can rewrite the electron ($\alpha = e$, 2.68) and ion velocities ($\alpha = i$, 2.67) as:

$$\mathbf{u}_\alpha = \mathbf{u} + \gamma_\alpha \mathbf{j} \tag{2.80}$$

where, from 2.96 and 2.97, the factors γ_α are given by:

$$\gamma_e = -\frac{m_i}{eZ^*\rho} \tag{2.81}$$

$$\gamma_i = \frac{m_e}{e\rho} \tag{2.82}$$

With these notations, the first two terms of the RHS of 2.73 writes:

$$\rho_\alpha \frac{d\mathbf{u}_\alpha}{dt} = \rho_\alpha\left(\frac{\partial \mathbf{u}_\alpha}{\partial t} + (\mathbf{u}_\alpha \cdot \nabla)\mathbf{u}_\alpha\right) - \gamma_\alpha \rho_\alpha (\mathbf{j}\cdot\nabla)\mathbf{u}_\alpha \tag{2.83}$$

In this expression we recognize in the first and second term of the RHS the "correct" (i.e. in the correct frame) lagrangian derivative given by equation 2.43. Injecting these expressions and using the fact that $\gamma_e\rho_e = -\gamma_i\rho_i$ and $\gamma_e - \gamma_i = -1/en_e$ (from 2.81 and 2.82), the sum of eq.2.83 of electrons and ions can be written as (with the term source $S = 0$):

$$\rho_e \frac{d\mathbf{u_e}}{dt} + \rho_i \frac{d\mathbf{u_i}}{dt} = -\nabla(p_e + p_i) + \mathbf{j}\times\mathbf{B} - \frac{m_e}{e}\frac{\rho_i}{\rho}(\mathbf{j}\cdot\nabla)\left(\frac{\mathbf{j}}{en_e}\right) \tag{2.84}$$

In writing equation 2.84 we have used the definition of the total electrical current density (eq. 2.66), as well as the fact that $\mathbf{R_e} = -\mathbf{R_i}$ by virtue of the Newton's third law (action-reaction law). This last point is specific to the MHD model: indeed, for the center of mass, the friction forces vanish. It is important to note that this is not related at all to the fact that the plasma has to be inviscid or infinitely conducting; as we shall see later, its just a consequence of the mathematical construction of the MHD reduction. Also, we see that the electric field has completely vanished as a consequence of the plasma neutrality (2.78)

Finally, by summing eq. 2.84 and 2.79, we can finally write the complete MHD momentum equation (eq. 2.73) as:

$$\rho\frac{d\mathbf{u}}{dt} = -\nabla(p_e + p_i) + \mathbf{j}\times\mathbf{B} - \frac{m_e}{e}\frac{\rho_i}{\rho}\left[\frac{1}{Z^*}\frac{dZ^*}{dt}\mathbf{j} + (\mathbf{j}\cdot\nabla)\left(\frac{\mathbf{j}}{en_e}\right)\right] \tag{2.85}$$

Equation 2.85 is the most general MHD momentum equation of a bi-temperature plasma with non constant ionization. The last two terms in the RHS in this equation are often neglected in MHD models because they are proportional to m_e, the electron mass and thus they are in some way a "reminiscence" of the fact that the MHD models includes the electron fluid equations. Let's call the first of these term $\mathbf{F_{io}}$:

$$\mathbf{F_{io}} = -\frac{m_e}{e}\frac{\rho_i}{\rho}\frac{1}{Z^*}\frac{dZ^*}{dt}\mathbf{j} \tag{2.86}$$

In order to quantify the importance of this force we can first remark that this force is always directed perpendicular to the $\mathbf{j}\times\mathbf{B}$ force so these two component will not compete against each other. Therefore, to evaluate its importance we must instead make the comparison with the pressure forces. Supposing that the characteristic time scale of ionization is given by electron-ion collisions, we can write $dZ^*/dt \sim Z^*\nu_{ei}$ (ν_{ei} is the electron-ion collision frequency) and then using the estimation $j \sim B/\mu_0 L$ (L is the characteristic scale of the macroscopic gradients, see 2.129 for details), we find:

$$\frac{|\nabla(p)|}{|\mathbf{F_{io}}|} \sim \frac{\frac{m_e}{e}L\nu_{ei}j}{p} \sim \frac{\nu_{ei}}{eB/m_e}\frac{B^2/\mu_0}{p} \approx \frac{\nu_{ei}}{\omega_{ce}}\beta^{-1} \tag{2.87}$$

where β is the ratio of the magnetic pressure $B^2/2\mu_0$ to the thermal pressure p (here $p = p_e + p_i$ is the total pressure). $\omega_{ce} = eB/m_e$ is the electron cyclotron frequency. Thus, the "ionization" force will be negligible if:

$$\frac{\nu_{ei}}{\omega_{ce}} \ll \beta \tag{2.88}$$

One can see that if the plasma beta is close to unity then condition 2.88 is equivalent to say that the "ionization" force will be negligible if electrons are strongly magnetized. There is another case where this force is also negligible: if the energy density in the plasma is such that atoms are and remain fully ionized (as it is often the case in "HEDLA" plasmas), then we simply have $dZ^*/dt \to 0$ and therefore $\mathbf{F_{io}} \to 0$. The second reminiscent term that we will call the inertial force $\mathbf{F_{Iner}}$:

$$\mathbf{F_{Iner}} = -\frac{m_e}{e}\frac{\rho_i}{\rho}(\mathbf{j}\cdot\nabla)\left(\frac{\mathbf{j}}{en_e}\right) \tag{2.89}$$

This force, also almost always neglected, has been studied by other authors who have observed that it was needed in order to conserve the total energy in the MHD system (a question treated in this chapter, see 2.3.13). They notably studied its effect on the Grad-Shafranov equation used to describes equilibrium state in a torus (see [11; 12]). This force reflects the fact that electrons have actually a finite inertia. As we will see in the section concerning the derivation of the generalized Ohm's law (2.3.8), this inertial force is associated to an inertial electric field (as it is the case for "ionization" force). In order to facilitate this future link, we can note that the sum of the two non-trivial terms can be expressed (after "some" calculations):

$$\mathbf{F_{Io}} + \mathbf{F_{Iner}} = -\nabla\cdot\left(\frac{m_e}{e}\frac{\rho_i}{\rho}\frac{\mathbf{jj}}{en_e}\right) \tag{2.90}$$

because:

$$\mathbf{F_{Io}} = -\frac{\mathbf{j}}{en_e}(\mathbf{j}\cdot\nabla)\left(\frac{m_e}{e}\frac{\rho_i}{\rho}\right) \tag{2.91}$$

and

$$\mathbf{F_{Iner}} = -\frac{m_e}{e}\frac{\rho_i}{\rho}\nabla\cdot\left(\frac{\mathbf{jj}}{en_e}\right) \tag{2.92}$$

where **jj** refers to the dyadic product. In the very usual case where the these non-trivial terms are negligible we find the well-known "classic" (or "non-extended") MHD momentum equation:

$$\rho\frac{d\mathbf{u}}{dt} = -\nabla(p_e + p_i) + \mathbf{j}\times\mathbf{B} \tag{2.93}$$

At this point, we stress that the first MHD equation that we derived, the mass conservation equation 2.71, is exact (no approximations), whereas the second MHD equations (eq.2.85 and2.93) have been obtained assuming that the plasma is quasi-neutral on the concerned time scale. However, in eq.2.85, no hypothesis on the relative importance of the electron and ion masses has been made.

2.3.7 MHD internal energy conservation equation

As in the previous cases of mass and momentum conservation, we could sum the multi-species energy equations 2.44 to obtain a reduced equation for the single-fluid and thus reduce even more the complexity of the system. However, the system of equation would not be applicable to a very large number of physical situations where a separate description of the energy conservation for electrons and ions is needed. For example, in the presence of shocks, it is the massive particles that are preferentially heated (heating proportional to m_α). In such cases, being able to model ion and electron populations with different temperature can be important, particularly if the time needed for the equilibration is comparable or even greater than the typical time scale of the general dynamic. Another case that will interest us, concerns the implementation of a laser energy source term in the system. Indeed, we will see that it is the electrons that are preferentially heated by a laser pulse (2.5). In the case of high-intensity lasers ($I \gtrsim 10^{13}\,\mathrm{W}.cm^{-2}$), the temperatures reached are greater than $100\,e$V, which lead to electron-ion collision frequencies sufficiently low to allow the plasma to stay in a non-equilibrium state for times generally longer than the laser duration. A correct description of the laser-plasma interaction is thus possible only if we keep the energy equations separate, but allow them to be coupled through a term depending on the collision rate. In any case, we highlight the fact that considering the plasma as being quasi-neutral (eq. 2.78), and thus removing all charge separation effects, does not imply that all the physics associated with the electrons is removed.

In the MHD model described here, we shall therefore keep separate the internal energy conservation equations for electrons and ions (eq. 2.44). The internal energy equation for this "bi-temperature" MHD model are:

$$\frac{\partial\epsilon_e}{\partial t} + \nabla(\epsilon_e\mathbf{u_e}) + p_e\nabla\cdot\mathbf{u_e} + \nabla\cdot\mathbf{q_e} = \mathrm{Q}_e^c + \mathrm{H}_e \tag{2.94}$$

$$\frac{\partial \epsilon_i}{\partial t} + \nabla(\epsilon_i \mathbf{u_i}) + p_i \nabla \cdot \mathbf{u_i} + \nabla \cdot \mathbf{q_i} = Q_i^c + H_i \tag{2.95}$$

These equations contain both the electron and the ion velocities. In order to have a fully self-consistent MHD model, which only involves the total mass density ρ and the single-fluid velocity $\mathbf{u}$, we replace these velocities by the expressions given in eq. 2.67 and 2.68. For the case of a quasi-neutral plasma (eq. 2.78 and with $\rho^* = \rho$), the ion and electron velocities can be written respectively as:

$$\mathbf{u_i} = \mathbf{u} + \frac{m_e}{e\rho}\mathbf{j} \tag{2.96}$$

$$\mathbf{u_e} = \mathbf{u} - \frac{m_i}{eZ^*\rho}\mathbf{j} \tag{2.97}$$

Replacing those expressions in eq. 2.94 and 2.95, we arrive at:

$$\frac{\partial \epsilon_e}{\partial t} + \nabla(\epsilon_e \mathbf{u}) + p_e \nabla \cdot \mathbf{u} + \nabla \cdot \mathbf{q_e} = \frac{m_i}{eZ^*\rho}(\mathbf{j} \cdot \nabla)\epsilon_e + (\epsilon_e + p_e)\nabla \cdot \left(\frac{m_i}{eZ^*\rho}\mathbf{j}\right) + Q_e^c + H_e \tag{2.98}$$

$$\frac{\partial \epsilon_i}{\partial t} + \nabla(\epsilon_i \mathbf{u}) + p_i \nabla \cdot \mathbf{u} + \nabla \cdot \mathbf{q_i} = -\frac{m_e}{e\rho}(\mathbf{j} \cdot \nabla)\epsilon_i - (\epsilon_i + p_i)\nabla \cdot \left(\frac{m_e}{e\rho}\mathbf{j}\right) + Q_i^c + H_i \tag{2.99}$$

2.3.8 The generalized Ohm's law

In the MHD model described in the previous three sections, it can be clearly seen that the electric field $\mathbf{E}$ has been somehow "removed" from the system of equations. This is a consequence of the simplifying assumption that the plasma is quasi-neutral. However, the electric field is still needed to compute the magnetic field (which has now become the "main" electromagnetic variable) through Maxwell-Faraday equation, eq. 2.48. The Maxwell-Gauss equation (eq. 2.46) is, because of the quasi-neutrality assumption, not useful and may thus be ignored. Furthermore, because in the MHD model we are not resolving both the electron velocity and the ion velocity, the electrical current density (eq. 2.51) is now an unknown variable and needs an equation for itself. The solution is to retrieve it from Maxwell-Ampere equation 2.49:

$$\mathbf{j} = \frac{\nabla \times \mathbf{B}}{\mu_0} - \frac{1}{c^2}\frac{\partial \mathbf{E}}{\partial t} \tag{2.100}$$

The divergence-free equation for the magnetic field (eq. 2.47) can be considered actually as an initial condition equation, and it is not relevant in the MHD model to find an unknown quantity. We now see that if an equation for the electric field can be found, the global MHD system will then be closed because it will be possible to complete both equations 2.48 and 2.100 (even if for the latter, in many cases, the displacement current $1/c^2 \partial \mathbf{E}/\partial t$ is actually neglected, see 2.3.9). Because in the previous sections we have only made one assumption (the plasma neutrality), the derived model up to now is almost exact and one can thus expect a very good equivalence with the multi-species model provided, of course, that the physical processes described are within the validity domain of the model (see 2.3.12). The procedure by which the electric field is obtained is perhaps the biggest "weakness" of the MHD model. It is there, where the strongest assumptions are generally being made.

When deriving the single-fluid momentum equation 2.93, we have essentially transformed six partial differential equations (electron and ion momentum equations) into only three equations. It seems therefore logical that more information should be extracted from these equations. Let us begin from the general multi-fluid model for an arbitrary number of species α. We will then later consider only the electrons and ions of our MHD model. Multiplying equation 2.43 by q_α/m_α and rewriting the non-linear term by using the mass equation 2.41, we can rewrite the momentum equation, using the index notation, as:

$$\frac{\partial(q_\alpha n_\alpha u_{\alpha,l})}{\partial t} + \partial_j(q_\alpha n_\alpha u_{\alpha,j} u_{\alpha,l}) = -\frac{q_\alpha}{m_\alpha}\partial_l p_\alpha + \frac{q_\alpha^2 n_\alpha}{m_\alpha}\left(\mathrm{E}_l + \mathbf{u}_\alpha \times \mathbf{B}|_l\right) + \frac{q_\alpha}{m_\alpha}\mathrm{R}_{\alpha,l} \tag{2.101}$$

Summing over all the species composing the plasma, we find:

$$\begin{aligned}\frac{\partial}{\partial t}\left(\sum_\alpha q_\alpha n_\alpha u_{\alpha,l}\right) + \partial_j\left(\sum_\alpha q_\alpha n_\alpha u_{\alpha,j} u_{\alpha,l}\right) = -\partial_l\left(\sum_\alpha \frac{q_\alpha}{m_\alpha} p_\alpha\right) + \\ \sum_\alpha\left(\frac{q_\alpha^2 n_\alpha}{m_\alpha}\mathrm{E}_l\right) + \sum_\alpha\left(\frac{q_\alpha^2 n_\alpha}{m_\alpha}\mathbf{u}_\alpha \times \mathbf{B}|_l\right) + \sum_\alpha\left(\frac{q_\alpha}{m_\alpha}\mathrm{R}_{\alpha,l}\right)\end{aligned} \tag{2.102}$$

From the definition of the electrical current density, eq. 2.51, we see that the first term represent the time derivative of the electrical current:

$$\frac{\partial}{\partial t}\left(\sum_\alpha q_\alpha n_\alpha u_{\alpha,l}\right) = \frac{\partial j_l}{\partial t} \tag{2.103}$$

Going back to our MHD fluid composed of electrons and only one species of ions with charge state Z^*, and always assuming a quasi-neutral plasma, we can write eq. 2.103 as:

$$\begin{aligned}\frac{\partial j_l}{\partial t} = -\partial_j\left[e n_e(u_{i,j}u_{i,l} - u_{e,j}u_{e,l})\right] + \frac{e}{m_e}\partial_l\left[p_e - \mathrm{Z}^*\frac{m_e}{m_i}p_i\right] + \\ \frac{e^2 n_e}{m_e}\mathrm{E}_l\left[1 + \mathrm{Z}^*\frac{m_e}{m_i}\right] + \frac{e^2 n_e}{m_e}\left[\mathbf{u_e} + \frac{m_e}{m_i}\mathbf{u_i}\right]\times\mathbf{B}\Big|_l - \frac{e}{m_e}\mathrm{R}_{e,l}\left[1 + \mathrm{Z}^*\frac{m_e}{m_i}\right]\end{aligned} \tag{2.104}$$

where we have used the fact that the transfer of momentum from electrons to ions is equal to the transfer of momentum from ions to electrons: $\mathrm{R}_{e,l} = -\mathrm{R}_{i,l}$. Using the expressions for the ion and electron velocities as function of the single-fluid velocity $\mathbf{u}$, and the electrical current density $\mathbf{j}$ (eq.2.96 and 2.97), we can rewrite the expression of the velocity difference in the derivative present in the first term of the RHS of equation 2.104 as:

$$u_{i,j}u_{i,l} - u_{e,j}u_{e,l} = \frac{m_i}{e\mathrm{Z}^*\rho}\left[1 + \mathrm{Z}^*\frac{m_e}{m_i}\right](u_j j_l - j_j u_l) - \frac{m_i^2}{e^2\mathrm{Z}^{*2}\rho^2}\left[1 - \mathrm{Z}^{*2}\frac{m_e^2}{m_i^2}\right] j_j j_l \tag{2.105}$$

Equation 2.104 is the most general form of the generalized Ohm's law [13], and to derive it, we have again only assumed quasi-neutrality. However, in such form this equation is basically never used. First and foremost because of its complexity, but in practice because many of the terms are proportional to the the very small ratio m_e/m_i. Indeed, in the following we shall assume that these terms are negligible. In particular, we will assume that:

$$Z^* \frac{m_e}{m_i} << 1 \tag{2.106}$$

$$\rho = \rho_i \left(1 + Z^* \frac{m_e}{m_i}\right) \approx \rho_i = m_i n_i = m_i \frac{n_e}{Z^*} \tag{2.107}$$

We can then rewrite eq. 2.105 as:

$$u_{i,j} u_{i,l} - u_{e,j} u_{e,l} = \frac{1}{e n_e}(u_j j_l - j_j u_l) - \frac{1}{e^2 n_e^2} j_j j_l \tag{2.108}$$

With this simplification, and neglecting the terms proportional to $\frac{m_e}{m_i}$ in eq. 2.104, we can write Ohm's law (back in vectorial and dyadic notations) as:

$$\mathbf{E} = -\mathbf{u_e} \times \mathbf{B} + \frac{\mathbf{R_e}}{e n_e} - \frac{\nabla p_e}{e n_e} + \frac{m_e}{e^2 n_e}\left[\frac{\partial \mathbf{j}}{\partial t} + \nabla \cdot \left(\mathbf{uj} + \mathbf{ju} - \frac{\mathbf{jj}}{e n_e}\right)\right] \tag{2.109}$$

We recall the divergence of a dyadic product:

$$\nabla \cdot (\mathbf{uj})\big|_l = \partial_j (u_j j_l) \tag{2.110}$$

Equation 2.109 can be simplified even further by replacing the electron velocity $\mathbf{u_e}$ by eq. 2.97 and using eq. 2.106, to give an expression for the electron velocity:

$$\mathbf{u_e} = \mathbf{u} - \frac{\mathbf{j}}{e n_e} \tag{2.111}$$

Using this in eq. 2.109 we finally get the most usual form of the Ohm's law:

$$\mathbf{E} = -\mathbf{u} \times \mathbf{B} + \frac{\mathbf{j} \times \mathbf{B}}{e n_e} + \frac{\mathbf{R_e}}{e n_e} - \frac{\nabla p_e}{e n_e} + \frac{m_e}{e^2 n_e}\left[\frac{\partial \mathbf{j}}{\partial t} + \nabla \cdot \left(\mathbf{uj} + \mathbf{ju} - \frac{\mathbf{jj}}{e n_e}\right)\right] \tag{2.112}$$

We note that the last manipulation has allowed us to introduce the Hall term $\mathbf{j} \times \mathbf{B}/e n_e$. We have shown here the complete derivation of the generalized Ohm's law by starting from both the electron and the ion momentum equations. Many of the derivations found in the literature arrive at eq. 2.112 directly from the electron momentum equation by taking the limit of $m_e \to 0$. The problem with such derivations is that it is not clear to which other quantity the inertia of the electrons is compared to. By keeping the terms involving the ion dynamics, we see clearly and rigorously from eq.2.104 that the usual Ohm's law is valid in the limit $m_e/m_i << 1$.

We now describe in more details Ohm's law. We begin by writing the RHS of eq. 2.112 as the sum of five electric fields, namely

$$\mathbf{E} = \mathbf{E_{Ind}} + \mathbf{E_{Hall}} + \mathbf{E_{Fric}} + \mathbf{E_{Biermann}} + \mathbf{E_{Iner}} \tag{2.113}$$

1. The first term is the inductive electric field:

$$\mathbf{E_{Ind}} = -\mathbf{u} \times \mathbf{B} \tag{2.114}$$

It represents the electric field created by the charge separation induced by the $q_\alpha \mathbf{v}_\alpha \times \mathbf{B}$ force being exerted in opposite directions for ions and electrons. It can be easily seen that the field $\mathbf{E_{ind}}$ is the one needed for the microscopic particles to drift across the magnetic field with the fluid velocity $\mathbf{u}$. Indeed, a microscopic particle moving in the electromagnetic field ($\mathbf{E_{ind}}$,$\mathbf{B}$) will have the drift velocity:

$$\mathbf{V_{drift}} = \frac{\mathbf{E_{ind}} \times \mathbf{B}}{B^2} = \mathbf{u} - (\mathbf{u} \cdot \mathbf{B})\frac{\mathbf{B}}{B} = u_\parallel \mathbf{b} + \mathbf{u}_\perp - u_\parallel \mathbf{b} = \mathbf{u}_\perp \tag{2.115}$$

where $\mathbf{b}$ is the unitary vector pointing in the direction of $\mathbf{B}$ and $\parallel$ (resp. $\perp$) designates the B-parallel (resp. the B-perpendicular) component of a vector field (here the velocities). So we see clearly that $\mathbf{E_{ind}}$ exists only to "justify" the existence of a perpendicular component of the single-fluid velocity. In the case where the MHD fluid is flowing purely along the magnetic field lines ($\mathbf{u}\parallel\mathbf{B}$) the inductive field is null because no charge separation is induced at the microscopic scale.

2. The second term describes the velocity shear between electrons and ions:

$$\mathbf{E_{Hall}} = \frac{\mathbf{j}\times\mathbf{B}}{en_e} \tag{2.116}$$

It is a corrective term which indicates that the electrons are not flowing with the same speed as ions (see eq. 2.97). Here again, it is associated to the electric field caused by the tendency of charges to separate under the action of the magnetic field force, but in this case it corresponds to a "surplus" of force on the electrons which is not compensated on the ions which are flowing with a different velocity. This "surplus" is important because it is actually the source of a force on the center of mass of the plasma. Indeed, by multiplying the Hall electric field by the charge density of electrons (or ions) we get:

$$en_e\mathbf{E_{Hall}} = \mathbf{j}\times\mathbf{B} \tag{2.117}$$

We see that this corresponds exactly to the force present in the MHD momentum equation 2.93 (the equation describing the momentum conservation of the center of mass of the plasma). In a non-intuitive way, we will see that even if the Hall field is basically responsible for the "mechanic" action of the field on the plasma, it can be often neglected in Ohm's law.

3. The third term is the field arising because of the collisions between electrons and ions.

$$\mathbf{E_{Fric}} = \frac{\mathbf{R_e}}{en_e} \tag{2.118}$$

$\mathbf{R_e}$ is the rate of momentum transfer from ions to electrons. We have seen that by the Newton's third law, ions are experiencing the same amount of momentum transfer from the electrons, but in the opposite direction thus. We understand that these frictional forces tend to separate the two population and because of the strong tendency of the plasma to stay neutral, this produces an electric field $\mathbf{E_{Fric}}$. Because the electrons have much less inertia, the separation is caused mainly by their dynamics and this is why we have neglected the ion contribution in this field. In the general case, the frictional force $\mathbf{R_e}$ can be decomposed as [10]:

$$\mathbf{R_e} = \mathbf{R_j} + \mathbf{R_T} \tag{2.119}$$

where $\mathbf{R_j}$ is the friction on the electrons due to the existence of a velocity shear with the ions, i.e an electrical current $\mathbf{j} \propto \mathbf{u_e} - \mathbf{u_i}$. This term is responsible for the diffusive effects of the magnetic field and can be written using the plasma resistivity η:

$$\mathbf{R_j} \approx en_e\eta\mathbf{j} \tag{2.120}$$

The electric field associated to this term is the so-called ohmic electric field:

$$\mathbf{E_{Ohm}} = \eta \mathbf{j} \tag{2.121}$$

$\mathbf{R_T}$ is a thermal frictional force due to the existence of gradients in the electron temperature [10].

4. The fourth term is:

$$\mathbf{E_{Biermann}} = -\frac{\nabla p_e}{e n_e} \tag{2.122}$$

Several names for this term are found in the literature. The terminology Biermann battery term, refers to the fact that contrary to all other terms in the generalized Ohm's law (with the exception of $\mathbf{R_T}$), it is independent of the existence of an initial magnetic field. As will shall see in the next section, when injected in the Faraday's law 2.48, it can be, under certain conditions, the source of magnetic field. This terms arises because the electron pressure gradients tend to set in motion the electrons on a much shorter time scale than the ions are being moved by their own temperature gradients (because, again, of their different inertia). This tends to produce a charge separation which is assumed in the MHD model to be compensated by an electric field. It is interesting to remark that the Biermann electric field, $\mathbf{E_{Biermann}}$, is also sort of "hidden" in the MHD momentum equation (as in the Hall term case). Indeed, if we multiply this field by the electron charge density, we get:

$$e n_e \mathbf{E_{Biermann}} = -\nabla p_e \tag{2.123}$$

which is exactly the force present in the MHD momentum equation 2.93. This force can thus be understood as the effect of a polarizing electric field pulling the ions in order for them to stay "stuck" with the electrons which are being pushed by their pressure gradients. This view gives an answer to the possible conflict which can appear in the MHD momentum equation 2.93 in cases where the electron-ion collisions are very low (but ion-ion and electron-electron are sufficiently strong to validate in each population the fluid description). Indeed, the pressure forces have a meaning only if, on the characteristic studied scale, the microscopic particles can transfer part of their momentum through collisions [8] (i.e. particle mean free path smaller than the pressure characteristic gradients scale) thus, if electrons are very weakly collisional with the ions, one could ask how the electron pressure force present in the MHD momentum equation 2.93 could act in order to induce a momentum in the bulk population (ions) described by this single-fluid equation. With the previous discussion about the nature of the Biermann electric field, we understand that this "mechanical" action is realized through the existence of this electric field. In the description of the code GORGON, we shall give more details of this term and the work done within this thesis to implement it in the code.

5. The fifth and last term is:

$$\mathbf{E_{Iner}} = \frac{m_e}{e^2 n_e}\left[\frac{\partial \mathbf{j}}{\partial t} + \nabla \cdot \left(\mathbf{uj} + \mathbf{ju} - \frac{\mathbf{jj}}{e n_e}\right)\right] \tag{2.124}$$

This term is proportional to the electron mass and this is why we call it the inertial electric field. As we shall see, this term can be neglected in the vast majority of situations of interest. However, now we come back to an important point we have mentioned when deriving the (exact) MHD momentum equation 2.85. It was found that two non-trivial forces were present in addition to the classic $-\nabla p$ and $\mathbf{j} \times \mathbf{B}$ forces. In the present section,

in order to obtain the inertial electric field 2.124, we considered two different things: first, to derive 2.101, we assumed the electric charge of the particles α to be constant and thus it is evident that the electric field due to potential ionization effect will not be taken into account here (otherwise we will obtain an electric field associated to the "ionization" force $\mathbf{F_{io}}$). Additionally, we also neglected the electron mass with respect to the ion mass with one of the consequence being $\rho \approx \rho_i$. In this case, it can be seen that the inertial force (2.92) can be written as:

$$\mathbf{F_{Iner}} = -\frac{m_e}{e}\nabla\cdot\left(\frac{\mathbf{jj}}{en_e}\right) \tag{2.125}$$

which is exactly the force one would obtained by multiplying the third term of the inertial electric field $\mathbf{E_{Iner}}$ (2.124) by en_e.

2.3.9 The displacement current in the Maxwell-Ampere equation

Before discussing the relative importance of all electric fields in the generalized Ohm's law, we provide an estimate of the electrical current density $\mathbf{j}$ magnitude, which is actually involved in three of the five electric fields components of this law, namely $\mathbf{E_{Fric}}$, $\mathbf{E_{Hall}}$ and $\mathbf{E_{Ohm}}$. To do so, we shall use Maxwell-Ampere equation (2.100) but let's first evaluate the characteristic ratio of the electric field over the magnetic field, E/B. From Maxwell-Faraday law 2.48 we have:

$$\frac{\partial\mathbf{B}}{\partial t} = -\nabla\times\mathbf{E} \Rightarrow \frac{\mathrm{B}}{\mathrm{T}} \sim \frac{\mathrm{E}}{\mathrm{L}} \Rightarrow \frac{\mathrm{E}}{\mathrm{B}} \sim \frac{\mathrm{L}}{\mathrm{T}} \tag{2.126}$$

where L and T are the characteristic length and time of the problem. Next, to simplify Maxwell-Ampere equation, we estimate the ratio of the displacement current to the inductive current:

$$\frac{\left|\frac{1}{c^2}\frac{\partial\mathbf{E}}{\partial t}\right|}{|\nabla\times\mathbf{B}|} \sim \frac{\frac{1}{c^2}\frac{\mathrm{E}}{\mathrm{T}}}{\frac{\mathrm{B}}{\mathrm{L}}} = \frac{1}{c^2}\frac{\mathrm{L}}{\mathrm{T}}\frac{\mathrm{E}}{\mathrm{B}} \sim \frac{\mathrm{V}^2}{c^2} \tag{2.127}$$

where we used 2.126 and V = L/T is the characteristic speed of the problem. We see that in the non-relativistic limit $\mathrm{V} << c$ the displacement current can be safely neglected in the Maxwell-Ampere equation. We note that it is always possible to keep the displacement current and in fact, when dealing with vacuum regions in simulations as in the case in our code GORGON, this term become essential. We highlight the fact that neglecting the displacement current does not mean that the electric field is constant (and it is not).

For the estimated we will conduct in the next section, we will simply use Maxwell-Ampere equation without the displacement current, namely:

$$\mathbf{j} = \frac{\nabla\times\mathbf{B}}{\mu_0} \tag{2.128}$$

and the associated current density magnitude:

$$j \sim \frac{\mathrm{B}}{\mu_0\mathrm{L}} \tag{2.129}$$

2.3.10 Relative importance of the various electric field terms in the generalized Ohm's law

For the plasmas we are interested in, the dominant term in the Ohm's law 2.112 is generally the inductive term $\mathbf{E_{Ind}}$. For this reason we will compare all the other terms with respect to this one.

The Hall term

The first and simplest condition that must be met in order to neglect the Hall term in the Ohm's law can be derived using the fact that $|\mathbf{j}| \approx en_e|u_e - u_i|$. Then the ration:

$$\frac{|\mathbf{E_{Hall}}|}{|\mathbf{E_{Ind}}|} \sim \frac{\frac{jB}{en_e}}{VB} \sim \frac{|u_e - u_i|}{V} \tag{2.130}$$

gives the condition that to neglect the Hall term the drift velocity between electrons and ions has to be small compared to the characteristic bulk velocity V of the plasma.

The Hall term is thus a "reminiscence" of the fact that the MHD fluid is composed of several species and can be understood as a corrective term on the inductive term $\mathbf{E_{Ind}}$. Physically, it also embodies the fact that in ideal MHD (see below), the magnetic field is effectively "frozen" in the electron population. This can be clearly seen by looking at an earlier version of the Ohm's law. Indeed, before introducing the Hall term in eq. 2.112, we obtained the relation 2.109 where only the electron velocity was involved in the inductive term. It was a translation of the fact that because it is electrons which have the lowest inertia, they respond faster to the electromagnetic fields and are thus mainly responsible for the plasma coupling to the magnetic field dynamics.

Alternatively, we have from equations 2.116, 2.114 and 2.129:

$$\frac{|\mathbf{E_{Hall}}|}{|\mathbf{E_{Ind}}|} \sim \frac{\frac{jB}{en_e}}{VB} \sim \frac{1}{en_e}\frac{B}{\mu_0 LV} \sim \frac{V}{\omega_{ci}}\frac{1}{L}\frac{B^2/\mu_0}{\rho V^2} \tag{2.131}$$

where we used:

$$en_e = eZ^* n_i = \frac{eZ^*\rho}{m_i} = \frac{\rho}{B}\frac{eZ^*B}{m_i} = \frac{\rho}{B}\omega_{ci} \tag{2.132}$$

where $\omega_{ci} = eZ^*B/m_i$ is the ion cyclotron frequency. The characteristic velocity V can be estimated from simple consideration about the relative importance of the thermal pressure P_{th} and magnetic pressure P_B, that is the value of the plasma beta:

$$\beta = \frac{P_{th}}{P_B} \approx \frac{\rho c_s^2}{\frac{B^2}{2\mu_0}} \tag{2.133}$$

1. A fluid particle will be mainly accelerated by the pressure forces if $\beta \gtrsim 1$ and in this case the characteristic pressure forces F_{th} can be estimated by:

$$F_{th} \sim \frac{\rho c_s^2}{L} \tag{2.134}$$

and the fluid particle of mass density ρ will undergone a typical acceleration during the "sonic" time $T = \tau_s$ and the spatial length L close to:

$$\rho \frac{L}{\tau_s^2} \sim F_{th} \sim \frac{\rho c_s^2}{L} \tag{2.135}$$

leading to a characteristic velocity V:

$$V = \sqrt{\frac{L^2}{\tau_s^2}} \sim c_s \tag{2.136}$$

that is, the typical velocity V in the case where the beta is much greater than unity has to be taken as the sound speed of the flow c_s. Now the sound speed of a bi-temperature plasma is actually the speed of ion acoustic wave [14] and thus include a contribution of both the electron and the ion temperatures:

$$c_s^2 \approx \frac{\Upsilon p_e}{\rho} + \frac{\Upsilon p_i}{\rho} \tag{2.137}$$

Being interested by order of magnitude, if we consider the electrons to have the same or a much lower temperature than ions (however, we should note that for $T_e \ll T_i$ Landau damping tends to kill ion acoustic waves [15]), then the sound speed c_s can be approximately taken to be equal to the ion thermal velocity [ref] $V \sim c_s \approx v_{Ti}$ then, by definition of the ion larmor radius r_{Li}, we have:

$$\frac{V}{\omega_{ci}} \sim \frac{v_{Ti}}{\omega_{ci}} = r_{Li} \tag{2.138}$$

Inserting 2.133 and 2.138 in 2.131 we get:

$$\frac{|\mathbf{E_{Hall}}|}{|\mathbf{E_{Ind}}|} \sim \frac{r_{Li}}{L}\frac{1}{\beta} \tag{2.139}$$

The Hall term can thus be ignored if:

$$\frac{r_{Li}}{L} << \beta \tag{2.140}$$

For β not far from unity it means that the ion larmor radius has to be much smaller than the characteristic length L on which quantities varies. However, we see that for high betas this condition is much less constraining. It should also be noted that upon the assumption that electrons are not much hotter than ions, condition 2.140 implies also that $r_{Le}/L << \beta$ since in this case $r_{Le} < r_{Li}$ (larmor radius are proportional to $\sqrt{mT}$ and because $m_e/m_i << 1$, the electron larmor radius is often much smaller than the ion one).

2. In the case where $\beta << 1$, the main responsible for the fluid particle acceleration is the magnetic forces F_B that can be estimated by:

$$F_B \sim \frac{B^2}{\mu_0 L} \tag{2.141}$$

and thus the fluid particle of mass density ρ will undergone a typical acceleration during the "Alfven" time $T = \tau_A$ and the spatial length L of the order of:

$$\rho \frac{L}{\tau_A^2} \sim F_B \sim \frac{B^2}{\mu_0 L} \tag{2.142}$$

leading to a characteristic velocity V:

$$V = \sqrt{\frac{L^2}{\tau_A^2}} \sim \frac{B}{\mu_0 \rho} = v_A \tag{2.143}$$

As we could expect, we recognize the Alfven speed $v_A = B/\mu_0\rho$. Then relation 2.131 can be rewritten:

$$\frac{|\mathbf{E_{Hall}}|}{|\mathbf{E_{Ind}}|} \sim\sim \frac{v_A}{v_{Ti}} \frac{v_{Ti}}{\omega_{ci}} \frac{1}{L} \frac{1}{\beta} \tag{2.144}$$

and with $v_A/v_{Ti} \sim 1/\sqrt{\beta}$, the Hall term will be negligible if:

$$\frac{r_{Li}}{L} << \beta^{3/2} << 1 \tag{2.145}$$

because we are looking at the low beta case. Condition 2.145 is more restrictive by telling us that as soon as the magnetic energy is larger than the thermal energy, the Hall term could be neglected only if the problem is solved at much higher scale than the ion larmor radius (and consequently the electron larmor radius).

The ohmic term

The ratio of the ohmic electric field to the inductive electric field is given by:

$$\frac{|\mathbf{E_{Ohm}}|}{|\mathbf{E_{Ind}}|} \sim \frac{\eta j}{VB} \sim \frac{\eta}{VL\mu_0} = \frac{D_m}{VL} = \frac{1}{R_m} \tag{2.146}$$

where we have introduced the magnetic diffusivity $D_m = \eta/\mu_0$ as well as the important dimensionless parameter, the magnetic Reynolds number:

$$R_m = \frac{VL}{D_m} \tag{2.147}$$

This parameter is equivalent to the classical Reynolds number in the sense that it quantify the relative importance between diffusive and convective processes. The difference between the two numbers is that the magnetic Reynolds number quantify these processes for the magnetic fields whereas the Reynolds number concerns the momentum. Two remarkable possibilities can be seen:

$$R_m >> 1 \tag{2.148}$$

and thus in this case the MHD model is called ideal because dissipative processes for the magnetic field are negligible. At the opposite:

$$R_m << 1 \tag{2.149}$$

and we are in this case dealing with "resistive MHD". In the majority of astrophysical plasmas the ideal MHD is a relatively good approximation (because mainly of the very large scales L, [16]) whereas in the laboratory resistive effects are often present and can not be neglected.

The Biermann term

The ratio of this term to the inductive field is approximately:

$$\frac{|\mathbf{E_{Biermann}}|}{|\mathbf{E_{Ind}}|} \sim \frac{p_e}{en_e \mathrm{LVB}} \sim \frac{k_\mathrm{B}\mathrm{T}_e}{e\mathrm{LVB}} \tag{2.150}$$

where we have used, for sake of simplicity, the perfect gas law $p_e = n_e k_\mathrm{B}\mathrm{T}_e$. With the electron thermal velocity defined by $v_{\mathrm{T}e} = \sqrt{k_\mathrm{B}\mathrm{T}_e/m_e}$ and the electron cyclotron frequency $\omega_{ce} = e\mathrm{B}/m_e = v_{\mathrm{T}e}/r_{\mathrm{L}e}$, eq. 2.150 can be written:

$$\frac{|\mathbf{E_{Biermann}}|}{|\mathbf{E_{Ind}}|} \sim \frac{r_{\mathrm{L}e}}{\mathrm{L}}\frac{v_{\mathrm{T}e}}{\mathrm{V}} \tag{2.151}$$

Let's consider first the case where the plasma beta is close or greater than unity $\beta \gtrsim 1$. In this case $\mathrm{V} \sim v_{\mathrm{T}e}$ (supposing that the total pressure is of the same order of magnitude than the electron pressure):

$$\frac{|\mathbf{E_{Biermann}}|}{|\mathbf{E_{Ind}}|} \sim \frac{r_{\mathrm{L}e}}{\mathrm{L}} \sim \sqrt{\frac{m_e}{m_i}}\frac{r_{\mathrm{L}i}}{\mathrm{L}} \tag{2.152}$$

and thus the Biermann field will be negligible with respect to the inductive field if: $r_{\mathrm{L}e} << \mathrm{L}$ or (if ions and electrons have similar temperatures) $r_{\mathrm{L}i} << \mathrm{L}\sqrt{m_i/m_e}$.

In the case where the plasma beta is much smaller than unity, we have $\mathrm{V} \sim v_\mathrm{A}$ and, using $v_{\mathrm{T}e}/v_\mathrm{A} \approx \sqrt{\beta}$, the Biermann field will be negligible if:

$$\frac{r_{\mathrm{L}e}}{\mathrm{L}} << \frac{1}{\sqrt{\beta}} \tag{2.153}$$

and thus, because the thermal energy is small in front of the magnetic energy, the condition on the electron larmor radius is less binding. It can also be interesting to compare the Biermann field with the Hall field:

$$\frac{|\mathbf{E_{Biermann}}|}{|\mathbf{E_{Hall}}|} \sim \frac{\frac{p_e}{en_e\mathrm{L}}}{\frac{\mathrm{B}^2}{en_e\mu_0\mathrm{L}}} \sim \beta \tag{2.154}$$

Thus we see that for high beta plasmas the Hall term will be negligible in front of the Biermann field whereas for low beta plasmas it is the Hall term which will dominate.

The inertial term

The ratio of the first term in the inertial field (2.124) to the inductive field is given by:

$$\frac{\left|\frac{m_e}{e^2 n_e}\frac{\partial \mathbf{j}}{\partial t}\right|}{|\mathbf{E_{Ind}}|} \sim \frac{m_e}{e^2 n_e}\frac{j}{\mathrm{VBT}} \sim \frac{m_e\epsilon_0}{e^2 n_e}\frac{c^2}{\mathrm{LTV}} \sim \frac{\omega^2}{\omega_{pe}^2}\frac{c^2}{\mathrm{V}^2} \tag{2.155}$$

where $\omega_{pe} = \sqrt{e^2 n_e/m_e\epsilon_0}$ is the plasma electronic pulsation and we used the relation $\mu_0\epsilon_0 c^2$. The pulsation $\omega = 1/\mathrm{T}$ is the characteristic pulsation studied in the problem. In order to neglect this first inertial term, one can see that we must have:

$$\frac{\omega^2}{\omega_{pe}^2} << \frac{\mathrm{V}^2}{c^2} << 1 \tag{2.156}$$

the last inequality ($V^2/c^2 << 1$) is in fact a condition that has to be met in order to assure the validity of the quasi-neutrality 2.78 as we will see later (see 2.3.12). It is possible to demonstrate also that the other terms of $\mathbf{E_{Iner}}$ would give the same condition. Thus, in order to safely neglect the inertial field, we must only consider low frequency (relative to the plasma frequency) processes.

2.3.11 The induction equation

The goal of deriving the generalized Ohm's law has been, as explained before, to obtain an expression for the electric field in order to "close" the system by obtaining an equation for the magnetic field evolution. This law is obtained obviously from the Maxwell-Faraday equation (2.48). In the previous section we have explicitly given the scaling of each fields of the Ohm's law by comparing them with the inductive field. Here we write the *induction equation for the magnetic field* keeping all the individual fields composing the Ohm's law. Later we shall consider some particular cases. Inserting eq, 2.112 in 2.48 we get:

$$\frac{\partial \mathbf{B}}{\partial t} = \nabla \times (\mathbf{u} \times \mathbf{B}) - \nabla \times \left(\frac{\mathbf{j} \times \mathbf{B}}{en_e}\right) - \nabla \times \left(\frac{\mathbf{R_e}}{en_e}\right) + \nabla \times \left(\frac{\nabla p_e}{en_e}\right) - \nabla \times \mathbf{E_{Iner}} \tag{2.157}$$

Following the discussion about the importance of the different terms in the Ohm's law (sec. 2.3.10) we can simplify equation 2.157 as:

1. If $r_{Li}, r_{Le} << L$, $R_m >> 1$, $\omega << \omega_{pe}$ we can write:

$$\frac{\partial \mathbf{B}}{\partial t} = \nabla \times (\mathbf{u} \times \mathbf{B}) \tag{2.158}$$

this relation corresponds to the Ideal MHD induction equation. It corresponds to the case where $\mathbf{E} \approx -\mathbf{u} \times \mathbf{B}$. Interestingly, we can note that in this case, the electric field is null in the frame moving with the plasma velocity $\mathbf{u}$. Indeed, in this frame, the field is (in the non-relativistic limit) $\mathbf{E}' = \mathbf{E} + \mathbf{u} \times \mathbf{B} = \mathbf{0}$.

2. If $r_{Li}, r_{Le} << L$ (Hall and Biermann terms negligible), $\omega << \omega_{pe}$ (Inertial term negligible) but the magnetic Reynolds number has a finite value, we can write:

$$\frac{\partial \mathbf{B}}{\partial t} = \nabla \times (\mathbf{u} \times \mathbf{B}) - \nabla \times \left(\frac{\mathbf{R_e}}{en_e}\right) \approx \nabla \times (\mathbf{u} \times \mathbf{B}) - \nabla \times (\eta \mathbf{j}) \tag{2.159}$$

where we have neglected the thermal friction $\mathbf{R_T}$ and only considered the ohmic field $\mathbf{E_{Ohm}} = \eta \mathbf{j}$. Equation 2.159 is the induction equation for the resistive MHD. It corresponds to an electric field $\mathbf{E} \approx -\mathbf{u} \times \mathbf{B} + \eta \mathbf{j}$. We can also note that it is equivalent to say that the "classical" Ohm's law is valid in the frame of a fluid particle moving with the velocity $\mathbf{u}$. Indeed, we have in this frame $\eta \mathbf{j} = \mathbf{E}' = \mathbf{E} + \mathbf{u} \times \mathbf{B}$. So with resistive effects, the electric field in the particle frame is different from zero and is equal to the resistive field.

3. If $R_m >> 1$ (resistive field negligible), $\omega << \omega_{pe}$ (inertial field negligible), $\beta << 1$ (Biermann field negligible) and the ion larmor radius is not small compared to the characteristic length L, we can write:

$$\frac{\partial \mathbf{B}}{\partial t} = \nabla \times (\mathbf{u} \times \mathbf{B}) - \frac{\mathbf{j} \times \mathbf{B}}{en_e} = \nabla \times (\mathbf{u_e} \times \mathbf{B}) \tag{2.160}$$

where we used relation 2.97. Relation 2.160 is the induction equation for the Hall MHD. It corresponds to the an electric field $\mathbf{E} \approx -\mathbf{u} \times \mathbf{B} + \mathbf{j} \times \mathbf{B}/en_e = -\mathbf{u_e} \times \mathbf{B}$. In this case,

it means that the electric field is null in the frame moving with the electron velocity since in in this frame the field is: $\mathbf{E}' = \mathbf{E} + \mathbf{u_e} \times \mathbf{B} = \mathbf{0}$.

2.3.12 The quasi-neutrality assumption

We now investigate the domain of validity of the quasi-neutrality assumption (2.78). We have up to now assumed that the plasma could be considered as neutral and found that this greatly simplifies the system. In order to quantify the order of magnitude of the net charge density Q_{net} we use the Maxwell-Gauss equation 2.46 which says that $Q_{net} = \epsilon_0 |\nabla \cdot \mathbf{E}|$. Thus, the ratio of this net charge density on the electron charge density is:

$$\frac{Q_{net}}{en_e} \approx \frac{\epsilon_0 |\nabla \cdot \mathbf{E_{Ind}}|}{en_e} \sim \frac{\epsilon_0 VB}{en_e L} \sim \frac{Vj}{en_e c^2} \sim \frac{V(V_e - V_i)}{c^2} << 1 \tag{2.161}$$

where we have assumed that the major contribution of the electric field comes from in inductive field and we have used 2.129 and $\mu_0 \epsilon_0 c^2 = 1$. V_e and V_i are the characteristic electron and ion velocities. Assuming that electron-ion drift is small compared to the speed of light, we see that the quasi-neutrality is equivalent to say that we are looking only at non-relativistic plasma flows. We note that condition 2.161 does not mean that the electron-ion drift has to be small compared to the single-fluid characteristic velocity V and thus the validity of the quasi-neutrality assumption is still valid if the Hall term become important or even grater than the inductive term.

2.3.13 Conservation of the total energy in the MHD model

We now address the important topic of the conservation of *total* energy in the MHD model. We have already given the conservation equation for the internal energy (eq. 2.98 and 2.99), however we have later introduced a new velocity, namely the velocity of the center of mass of the plasma $\mathbf{u}$. We ask now the question of what is the new expression and conservation equation for the kinetic energy in this MHD model. As it is almost always done, one could just consider that $1/2\rho u^2$ is the kinetic energy density of the plasma. By multiplying the MHD momentum equation 2.93 (or more precisely 2.85) by $\mathbf{u}$, one may then obtain an equation identical to the one derived for one specie in section 2.3.3. Then by adding this equation to the unchanged electromagnetic energy equation (also given in section 2.3.3) and the internal energy equations (2.98 and 2.99) we could obtain a relation describing total energy of the plasma. In reality, it can be easily see that by writing such a relation, it is not possible to derive it in a conservative form and thus there is reason to believe that the total energy in the MHD system is not conserved. Of course, because to derive the MHD model we have started from the multi-species system where total energy is conserved, if the derivation is realized correctly we should be able to write an energy relation for the MHD system in a conservative form. The solution to this apparent problem lies in the fact that the plasma kinetic energy is *not* $1/2\rho u^2$. Indeed, the kinetic energy density is obviously still given by the sum of the ion kinetic energy and the electron kinetic energy:

$$\epsilon_{tot}^{kin} = \epsilon_e^{kin} + \epsilon_i^{kin} = \frac{1}{2}\rho_e u_e^2 + \frac{1}{2}\rho_i u_i^2 \tag{2.162}$$

next, assuming the quasi-neutrality of the plasma (2.78), we can use relations 2.96 and 2.97 to find:

$$u_i^2 = u^2 + \frac{m_e^2}{e^2\rho^2} j^2 + \frac{2m_e}{e\rho}\mathbf{u}\cdot\mathbf{j} \tag{2.163}$$

$$u_e^2 = u^2 + \frac{m_i^2}{e^2 Z^{*2}\rho^2} j^2 - \frac{2m_i}{eZ^*\rho}\mathbf{u}\cdot\mathbf{j} \tag{2.164}$$

and still because of the quasi-neutrality, we can write the ion and electron densities as:

$$\rho_i = \frac{\rho}{1+\frac{Z^* m_e}{m_i}} \tag{2.165}$$

$$\rho_e = \frac{\rho}{1+\frac{m_i}{Z^* m_e}} \tag{2.166}$$

then, inserting 2.163, 2.164, 2.165 and 2.166 in 2.162 we get, after some simplifications:

$$\epsilon_{tot}^{kin} = \frac{1}{2}\rho u^2 + \frac{m_i m_e}{2e^2 Z^*\rho} j^2 \tag{2.167}$$

This last relation has been obtained with the only assumption of quasi-neutrality (no simplifications were introduced because of the smallness of the electron-ion mass ratio). It is clear from eq. 2.167 that the plasma kinetic energy density is indeed composed of the expected term $1/2\rho u^2$ but an other corrective term is present, which depends on the electron-ion drift velocity. If no currents are present in the plasma, then the kinetic energy density is indeed given simply (but exactly) by the term involving the single-fluid velocity. In the general case where currents are present, we can evaluate the importance of the term in j^2 by:

$$\frac{\frac{m_i m_e}{2e^2 Z^*\rho} j^2}{\frac{1}{2}\rho u^2} \sim Z^* \frac{m_e}{m_i}\frac{(\mathrm{V}_e - \mathrm{V}_i)^2}{\mathrm{V}^2} \tag{2.168}$$

where we have used the relation $j^2 = e^2 Z^{*2}\rho_i^2(\mathbf{u_e} - \mathbf{u_i})^2/m_i^2$, the fact that $\rho_i \approx \rho$ and $\mathrm{V}_{e/i}$ is the characteristic electron/ion velocity whereas V is the characteristic velocity of the center of mass (and in fact $\mathrm{V} \approx \mathrm{V}_i$). Thus, the term in j^2 may be neglected when evaluating th plasma kinetic energy when:

$$\frac{(\mathrm{V}_e - \mathrm{V}_i)^2}{\mathrm{V}^2} << \frac{m_i}{Z^* m_e} \tag{2.169}$$

which is a condition often respected and is relatively similar to the condition allowing to neglect the Hall term (2.130). However, in this section we are interested in the strict derivation of the total energy equation conservation and thus we must consider this term. So the question is now: what is the equation describing the conservation of the "real" kinetic energy of the plasma but only in terms of the "MHD variables", namely **u** and **j**.

To obtain this equation we are first going to rewrite the kinetic energy equation for one species α (ions ($\alpha = i$) or electrons ($\alpha = e$)) in terms of the MHD variables and then we will sum these equations. But first let's recall the following notations (already defined when deriving the MHD momentum equation 2.3.6):

$$\mathbf{u}_\alpha = \mathbf{u} + \gamma_\alpha \mathbf{j} \tag{2.170}$$

where, from 2.96 and 2.97, the factors γ are given by:

$$\gamma_e = -\frac{m_i}{eZ^*\rho} \tag{2.171}$$

$$\gamma_i = \frac{m_e}{e\rho} \tag{2.172}$$

with these notations, the kinetic energy equation for a given species α can be written as (from section 2.3.3):

$$\frac{\partial \epsilon_\alpha^{kin}}{\partial t} + \nabla\cdot(\epsilon_\alpha^{kin}\mathbf{u} + \gamma_\alpha \epsilon_\alpha^{kin}\mathbf{j}) = -\mathbf{u}\cdot\nabla p_\alpha - \gamma_\alpha \mathbf{j}\cdot\nabla p_\alpha + q_\alpha n_\alpha \mathbf{u}\cdot\mathbf{E} + \gamma_\alpha q_\alpha n_\alpha \mathbf{j}\cdot\mathbf{E} + \mathbf{u}_\alpha\cdot\mathbf{R}_\alpha \tag{2.173}$$

and by summing over all species:

$$\begin{aligned}\frac{\partial}{\partial t}\left(\sum_\alpha \epsilon_\alpha^{kin}\right) + \nabla\cdot\left(\sum_\alpha \epsilon_\alpha^{kin}\mathbf{u} + \sum_\alpha \gamma_\alpha \epsilon_\alpha^{kin}\mathbf{j}\right) = -\mathbf{u}\cdot\nabla\left(\sum_\alpha p_\alpha\right)\\ -\sum_\alpha \gamma_\alpha \mathbf{j}\cdot\nabla p_\alpha + \sum_\alpha q_\alpha n_\alpha \mathbf{u}\cdot\mathbf{E} + \sum_\alpha \gamma_\alpha q_\alpha n_\alpha \mathbf{j}\cdot\mathbf{E} + \sum_\alpha \mathbf{u}_\alpha\cdot\mathbf{R}_\alpha\end{aligned} \tag{2.174}$$

We have the following relations for our neutral electron/ion plasma:

$$\sum_\alpha \epsilon_\alpha^{kin} = \epsilon_{total}^{kin} = \frac{1}{2}\rho u^2 + \frac{m_i m_e}{2e^2 Z^*\rho} j^2 \tag{2.175}$$

from 2.167. From quasi-neutrality we have:

$$\sum_\alpha q_\alpha n_\alpha = 0 \tag{2.176}$$

and (using again the quasi-neutrality $n_e = Z^* n_i$):

$$\sum_\alpha \gamma_\alpha q_\alpha n_\alpha = eZ^* n_i \frac{m_e}{e\rho} + e n_e \frac{m_i}{eZ^*\rho} = \frac{m_e n_e + m_i n_i}{\rho} = \frac{\rho}{\rho} = 1 \tag{2.177}$$

Finally, remarking that, using 2.165, 2.166, 2.171 and 2.172, that we have $\gamma_i\rho_i = -\gamma_e\rho_e = m_e/(e(1+Z^* m_e/m_i))$, we can write:

$$\chi = \sum_\alpha \gamma_\alpha \epsilon_\alpha^{kin} = -\frac{1}{2}\frac{m_e m_i}{e^2 Z^*\rho}\frac{1-\frac{Z^* m_e}{m_i}}{1+\frac{Z^* m_e}{m_i}}\left[\frac{m_i}{eZ^*\rho}\left(1+\frac{Z^* m_e}{m_i}\right)j^2 + 2\mathbf{u}\cdot\mathbf{j}\right] \tag{2.178}$$

With these relations we can write the conservation of kinetic energy as:

$$\begin{aligned}\frac{\partial}{\partial t}\left(\epsilon_{tot}^{kin}\right) + \nabla\cdot\left(\epsilon_{tot}^{kin}\mathbf{u} + \chi\mathbf{j}\right) = -\mathbf{u}\cdot\nabla\left(p_e + p_i\right)\\ -\gamma_e\mathbf{j}\cdot\nabla p_e - \gamma_i\mathbf{j}\cdot\nabla p_i + \mathbf{j}\cdot\mathbf{E} + \mathbf{u_e}\cdot\mathbf{R_e} + \mathbf{u_i}\cdot\mathbf{R_i}\end{aligned} \tag{2.179}$$

Relation 2.179 is the *exact* equation describing the conservation of the total kinetic energy of the plasma. To verify the conservation of the total energy, we use the internal energy equations given (exactly) in 2.98 and 2.99 which, when summed and written using the gamma parameters (2.171 and 2.172), gives:

$$\begin{aligned}\frac{\partial(\epsilon_e+\epsilon_i)}{\partial t} + \nabla\cdot\left[(\epsilon_e+\epsilon_i)\mathbf{u} + (\gamma_e\epsilon_e + \gamma_i\epsilon_i)\mathbf{j} + \mathbf{q_e} + \mathbf{q_i}\right] = -(p_e+p_i)\nabla\cdot\mathbf{u}\\ -p_e\nabla\cdot(\gamma_e\mathbf{j}) - -p_i\nabla\cdot(\gamma_i\mathbf{j}) + Q_e^c + Q_i^c + H_e + H_i\end{aligned} \tag{2.180}$$

and with the electromagnetic energy conservation which is unchanged (from 2.3.3):

$$\frac{\partial \epsilon^{\mathrm{EM}}}{\partial t} + \nabla \cdot (\Pi_{\mathbf{EM}}) = -\mathbf{E} \cdot \mathbf{j} \tag{2.181}$$

with $\Pi_{\mathbf{EM}} = \mathbf{E} \times \mathbf{B}/\mu_0$ the Pointying vector. Finally, by summing relations 2.179, 2.180 and 2.181, we can write the equation for the total plasma energy as:

$$\begin{aligned} \frac{\partial \epsilon^{tot}}{\partial t} + \nabla \cdot [\mathbf{q_e} + \mathbf{q_i} + \Pi_{\mathbf{EM}} + (\epsilon^{kin}_{tot} + \epsilon_e + \epsilon_i + p_e + p_i)\mathbf{u} \\ + (\chi + \gamma_e \epsilon_e + \gamma_i \epsilon_i + \gamma_e p_e + \gamma_i p_i)\mathbf{j}] = \mathrm{H}_e + \mathrm{H}_c \end{aligned} \tag{2.182}$$

where we have used the fact that $\mathrm{Q}^c_e + \mathrm{Q}^c_i = -\mathbf{R_e u_e} - \mathbf{R_i u_i}$ and:

$$\epsilon^{tot} = \epsilon^{\mathrm{EM}} + \epsilon^{kin}_{tot} + \epsilon_e + \epsilon_i \tag{2.183}$$

where $\epsilon^{\mathrm{EM}} = \epsilon_0 \mathrm{E}^2/2 + \mathrm{B}^2/2\mu_0$ is the electromagnetic energy density.

We now have with 2.182 a conservative form of the total energy described only in terms of MHD quantities. We see that if external heating sources are absent then the energy is transported only with the MHD energy flux:

$$\begin{aligned} \mathbf{F^{tot}_{MHD}} = \mathbf{q_e} + \mathbf{q_i} + \Pi_{\mathbf{EM}} + (\epsilon^{kin}_{tot} + \epsilon_e + \epsilon_i + p_e + p_i)\mathbf{u} \\ + (\chi + \gamma_e \epsilon_e + \gamma_i \epsilon_i + \gamma_e p_e + \gamma_i p_i)\mathbf{j} \end{aligned} \tag{2.184}$$

In the vast majority of MHD models effectively used, for example, for numerical simulations, this exact form is not retained because of the fact that the energy flux due to the electrical current is often neglected assuming the electron-ion drift is small compared to the velocity $\mathbf{u}$ (same argument used for neglecting the Hall electric field 2.130). It can be easily seen that if the terms proportional to the current $\mathbf{j}$ are neglected both in the kinetic energy equation 2.179 and in the internal energy equation 2.180 then it is still possible to write a total energy equation in a conservative form but in this case the equation is not describing the "real" conservation of the total energy but instead a approximated value of it. As we shall see, this is what is done in the GORGON code.

As a last point, we want to highlight the fact that when deriving relation 2.182 we didn't consider a specific form of Ohm's law. Thus, the choice of which terms must be kept in this law is not going to "break" the total conservation of energy.

2.4 The GORGON 3D resistive, bi-temperature MHD code

2.4.1 Introduction

In this section we will rapidly describe the GORGON code. Further informations about this code can be found in [17; 18]. The code, originally developed to model Z-pinches, has been widely used to model laboratory astrophysics laser experiments [19] and astrophysical plasmas [20] . The code uses a finite volume scheme on a 3D uniform Cartesian grid. The parallelization is realized using the standardized Message Passing Interface (MPI) communication protocol [21].

From the previous section where the full MHD model was derived we will see that the main approximation done in our code is that the previously mentioned terms proportional to **j** in the internal energy equations (see 2.98 and 2.99) are neglected. Also, the retained Ohm's law in GORGON is initially that of the resistive MHD (no Hall term, no Biermann term, no inertial term as well as no thermal frictional force, see 2.3.10).

2.4.2 Implemented equations

The single-fluid, two-temperature resistive magneto-hydrodynamic equations implemented in the code are:

$$\frac{\partial \rho}{\partial t} + \nabla.(\rho \mathbf{u}) = 0 \tag{2.185}$$

$$\frac{\partial (\rho \mathbf{u})}{\partial t} + \nabla.(\rho \mathbf{u}\mathbf{u}) = -\nabla(p_i + p_e) + (\mathbf{j} \times \mathbf{B}) + \mathbf{F_{visc}} \tag{2.186}$$

$$\frac{\partial \epsilon_e}{\partial t} + \nabla.(\epsilon_e \mathbf{u}) = -p_e \nabla.\mathbf{u} - \nabla.\mathbf{q_e} + \eta j^2 - Q_{ei} - Q_{rad} + Q_{laser} \tag{2.187}$$

$$\frac{\partial \epsilon_i}{\partial t} + \nabla.(\epsilon_i \mathbf{u}) = -p_i \nabla.\mathbf{u} - \nabla.\mathbf{q_i} + Q_{visc} + Q_{ei} \tag{2.188}$$

$$\frac{\partial \mathbf{B}}{\partial t} = \nabla \times (\mathbf{u} \times \mathbf{B}) - \nabla \times (\eta \mathbf{j}) \tag{2.189}$$

where ρ is the mass density, $\mathbf{u}$ is the plasma bulk velocity, $p_{e/i} = n_{e/i} k_B T_{e/i}$ is the electronic/ionic pressure ($n_{e/i}$ is the electron-ion density, $T_{e/i}$ is the electron-ion temperature and k_B is the Boltzmann constant), j is the current density obtained from Ampere's law. The evolution of the electromagnetic fields is followed using a vector potential formalism, with the magnetic induction given by $\mathbf{B} = \nabla \times \mathbf{A}$. Regions with densities below $10^{-7}\, g.cm^{-3}$ (this threshold can be changed but all the simulations presented in this manuscript use this value) are treated numerically as a vacuum, where momentum, mass, energy and current densities are zero. In the vacuum regions, the vacuum form of Maxwell's equations is solved and the displacement current in Ampere's law is retained. Shocks are captured using a Von Neumann artificial viscosity [22], with $\mathbf{F_{visc}}$ and Q_{visc} the volumetric force and heating term respectively. The electron/ion internal energy $\epsilon_{e/i}$ are given by $\epsilon_i = p_i/(\gamma - 1)$ for the ions, and by $\epsilon_e = p_e/(\gamma - 1) + Q(Z)$ for the electrons, where $\gamma = 5/3$ is adiabatic index and $Q(Z)$ the ionization potential energy density which depends on the average ionization charge Z of the plasma. The latter is obtained from an analytical approximation to a LTE Thomas-Fermi model [23]. The thermal fluxes are given by $q_{e/i} = -\kappa_{e/i} \nabla T_{e/i}$, where the isotropic thermal conduction coefficients $\kappa_{e/i}$ are taken from [24] with the addition of a standard flux limiter [25]. The plasma resistivity η is given by Braginskii [10]. The volumetric energy transfer rate, $Q_{e/i}$, between ions and electrons is given by 2.56. The code assume an optically thin plasma with Q_{rad} being the volumetric energy loss rate due to radiation escaping the plasma. This rate is computed assuming recombination (free-bound) and Bremsstrahlung radiation ([23]) with an upper limiter given by the black body radiation rate (Stefan–Boltzmann's law).

2.4.3 Localization of the physical quantities in the GORGON grid

For information, the GORGON quantities used for the numerical resolution of the system presented previously are pictured in fig.2.1 for a given cell.

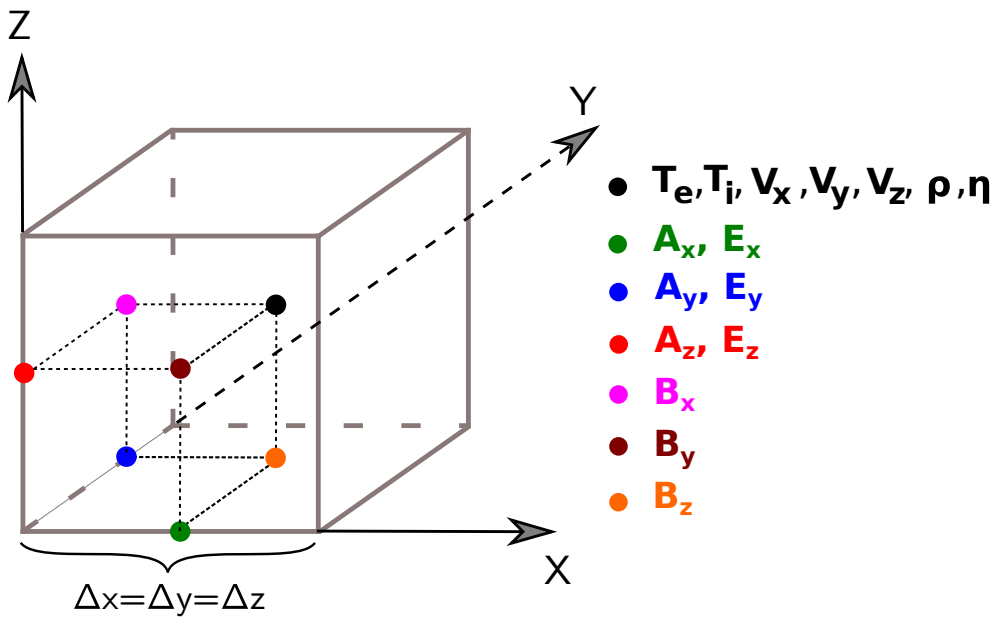

Figure 2.1: Spatial localization of the GORGON variables used to perform the numerical scheme

2.5 Implementation of a laser module in the GORGON code

2.5.1 Introduction

One of the first projects completed during this thesis has been the development of a laser module for the code GORGON described above (see 2.4). Because of an ongoing and strengthening collaboration with experimental teams using lasers in order to produce astrophysically-relevant plasmas, the implementation in our code GORGON of a laser module was necessary to perform simulations on new experiments that have been performed in 2014 (see 6). A large number of hydrodynamic/plasma codes (e.g. DUED [26], PARAX [27], FCI2 [28], CRASH [29], HYADES [30], ALE-AMR [31]...) have already a laser module implemented using different algorithms in different geometries (1D, 2D and 3D) and descriptions (eulerian, lagrangian, geomotrical optics...). Here, because finding a new method for this problem was not the goal, we choose to implement a well-known and tested algorithm of the laser propagation and energy deposition, namely the "Kaiser" algorithm [32]. In order to numerically model a laser we use what is called the "ray tracing" method because the pulse is decomposed in multiples individual rays which obey each to a set of equations describing both their propagation and their absorption.

The implementation presented in this section is similar to the one used in the FLASH code [33]. We do not present here the parallelization aspect which is specific to our module and in common with a test-particle module also developed during this thesis. In this section, we first present the physical equations describing the propagation and absorption processes occurring when a laser pulse propagates in a plasma. We clearly present the validity domain where the geometrical optics approximation used to model the propagation of the rays is valid. We also present the absorption process by which energy transfers from the laser to the plasma. Here we only consider the collisional absorption, also called inverse-Bremsstrahlung absorption, and neglect others possible absorption mech-

anisms that are known to occur in laser-plasma interaction (e.g. resonant absorption at the critical density [34]). Under this assumption, we consider that the laser energy goes into the thermal energy of electrons by increasing the width of the maxwellian (i.e. ~ the temperature) and that non-equilibrium phenomena are absent (e.g. production of supra-thermal electrons [35]...). Finally, we present some benchmark performed using our implement laser module.

2.5.2 Electromagnetic Wave propagation equation in a (unmagnetized) plasma

In order to derive the equations governing the propagation of a laser, the starting point consists to write the full system of Maxwell's equations, including the source terms:

$$\nabla \cdot \mathbf{E} = \frac{\rho_q}{\epsilon_0} \tag{2.190}$$

$$\nabla \cdot \mathbf{B} = 0 \tag{2.191}$$

$$\frac{\partial \mathbf{B}}{\partial t} = -\nabla \times \mathbf{E} \tag{2.192}$$

$$\nabla \times \mathbf{B} = \mu_0 \mathbf{j} + \frac{1}{c^2}\frac{\partial \mathbf{E}}{\partial t} \tag{2.193}$$

Taking the curl of 2.192 and inserting 2.193 we find the equation for the electric field:

$$\Delta \mathbf{E} - \nabla(\nabla \cdot \mathbf{E}) - \frac{1}{c^2}\frac{\partial^2 \mathbf{E}}{\partial t^2} = \mu_0 \frac{\partial \mathbf{j}}{\partial t} \tag{2.194}$$

where we have used the vector identity $\nabla \times (\nabla \times \mathbf{A}) = \nabla(\nabla \cdot \mathbf{A}) - \Delta \mathbf{A}$ and where ϵ_0 and μ_0 respectively the permittivity and the permeability of free space. $\mathbf{j}$ is the total electrical current of the medium. Similarly, the wave equation for the magnetic field can be obtained by taking the curl of 2.192 and the temporal derivative of 2.193 and, using the fact that no magnetic monopole has yet been found:

$$\Delta \mathbf{B} - \frac{1}{c^2}\frac{\partial^2 \mathbf{B}}{\partial t^2} = -\mu_0 \nabla \times \mathbf{j} \tag{2.195}$$

Now, the electrical current induced by the oscillating laser field can be expressed through the conductivity σ of the plasma. We assume here that ions dot not contribute to the total current $\mathbf{j} \approx \mathbf{j_{pol}}$ where $\mathbf{j_{pol}}$ is the current coming from the oscillating movement of the electrons in the laser field. The ions are considered to be immobile over the laser pulsation time scale ($\omega_{pi}^{-1} >> \omega^{-1}$). Thus we can write Ohm's law as:

$$\mathbf{j_{pol}} = \sigma \mathbf{E} \tag{2.196}$$

Furthermore, as long as the electron density spatial variations are smooth, i.e.

$$\lambda << L_c = (|\nabla n_e| / n_e)^{-1} \tag{2.197}$$

holds with L_c the characteristic length of electron density gradients and λ the local laser wavelength, $\nabla \cdot \mathbf{E} = 0$ can be set and eq.2.194 transforms into:

$$\Delta\mathbf{E} - \frac{1}{c^2}\frac{\partial^2\mathbf{E}}{\partial t^2} = \mu_0\frac{\partial(\sigma\mathbf{E})}{\partial t} \tag{2.198}$$

This last equation can be simplified further if we assume that over the laser time scale (ω^{-1}), the only significant contributions to the time derivatives are given by the dependence of the quantities with $e^{-i\omega t}$. In this case we have $\partial/\partial t = -i\omega$ and equation 2.198 transforms into:

$$\Delta \mathrm{E}(\mathbf{r}) + \left(\frac{\omega}{c}\right)^2 n^2 \mathrm{E}(\mathbf{r}) = 0 \tag{2.199}$$

with:

$$n^2 = 1 + i\frac{\sigma}{\epsilon_0\omega} \tag{2.200}$$

n is called the complex refractive index and contains both the parameters for the laser propagation (real part) as well as the wave damping by interaction with the medium (imaginary part). In writing equation 2.199 we have transformed the general vectorial wave equation 2.194 into a stationary equation on the scalar wave field $\mathrm{E}(\mathbf{r})$ by separating the time and space variables. Equation 2.199 is called the Helmholtz equation and is the starting point to analyze the laser propagation (and energy deposition) in the frame of geometrical optics. The same previous development can be applied to the magnetic field from equation 2.195.

Before deriving the equations needed for our ray tracing module, an expression for the plasma conductivity can be derived quite simply using the fluid equation for the conservation of electron momentum (neglecting pressure forces):

$$\rho_e\frac{\partial\mathbf{u_e}}{\partial t} = -en_e\mathbf{E} - m_e n_e \nu_{ei}\mathbf{u_e} \tag{2.201}$$

with ρ_e the electron mass density and ν_{ei} the electron-ion collision frequency. We also neglected the magnetic component of the Lorentz force in this expression because of the relative magnitudes of $\mathbf{E}$ and $u\mathbf{B}$ that can be estimated from 2.192: $\mathrm{E}/u\mathrm{B} \sim \lambda\omega/u \sim c/u >> 1$. We of course reject, in this case, relativistic laser-plasma interaction at high laser intensities ($> 10^{18}\,\mathrm{W}.cm^{-2}$).

Under the laser action, the field quantities are assumed to possess the time dependence associated to the pulse pulsation: $e^{-i\omega t}$ thus $\partial\mathbf{u_e}/\partial t = -i\omega\mathbf{u_e}$. We can then retrieve the polarization current $\mathbf{j_{pol}} = -en_e\mathbf{u_e}$ from 2.201:

$$\mathbf{j_{pol}} = i\epsilon_0\frac{\omega_{pe}^2}{\omega}\frac{1}{1+i\frac{\nu_{ei}}{\omega}}\mathbf{E} \tag{2.202}$$

so we see that in this case the electrical conductivity is given by:

$$\sigma = i\epsilon_0\frac{\omega_{pe}^2}{\omega}\frac{1}{1+i\frac{\nu_{ei}}{\omega}} \tag{2.203}$$

With this expression for the conductivity, the refractive index introduced in 2.200 can be rewritten, assuming we have $\omega >> \nu_{ei}$:

$$n^2 = 1 - \frac{\omega_{pe}^2}{\omega^2} + i\frac{\nu_{ei}\omega_{pe}^2}{\omega^3} + \mathcal{O}\left(\frac{\nu_{ei}^2}{\omega^2}\right) \tag{2.204}$$

In this model, the real part of n^2 is associated to the wave propagation whereas the complex part describes the collisional absorption/damping (inverse Bremsstrahlung) of the wave. We also note that the relative permittivity ϵ of the plasma is connected to the refractive index through $\epsilon = n^2$ and thus:

$$\mathrm{Re}(\epsilon) = 1 - \frac{\omega_{pe}^2}{\omega^2} = 1 - \frac{n_e}{n_c} \tag{2.205}$$

$$\mathrm{Im}(\epsilon) = \frac{\nu_{ei}\omega_{pe}^2}{\omega^3} \tag{2.206}$$

where n_c is defined below (see 2.209).

From equation 2.199, we can obtain the dispersion relation for the propagation of plane waves in a homogeneous, non-collisional ($\nu_{ei} = 0$), unmagnetized plasma. Indeed, for plane waves, the electric field (and the magnetic field) can be written as:

$$\mathrm{E}(\mathbf{r}) = \mathrm{E}_0 exp(i\mathbf{k}\cdot\mathbf{r}) \tag{2.207}$$

where $\mathbf{k}$ is the wavenumber. We have $\Delta\mathrm{E}(\mathbf{r}) = -k^2$ so equation 2.199 in the Fourier space gives the dispersion relation for the propagation of light waves:

$$\omega^2 = k^2c^2 + \omega_{pe}^2 \tag{2.208}$$

One can see that no propagation is allowed if $\omega < \omega_{pe}$ and in this case the wave is reflected at the plasma interface [36]. The equality $\omega = \omega_{pe}$, which defines the frontier where reflection starts, can also be expressed in terms of the electron density:

$$n_e = n_c = \frac{\epsilon_0 m_e \omega^2}{e^2} = \frac{4\pi^2 m_e}{\mu_0 e^2 \lambda^2} \tag{2.209}$$

where we have used the relation between the wave pulsation and the wave wavelength: $\omega = 2\pi/\lambda$ and the relation $\mu_0\epsilon_0 c^2 = 1$. n_c is called the critical density and corresponds to the electron density above which an electromagnetic waves can not propagate. For a given monochromatic wave, the plasma will be called super-critical if $n_e > n_c$ and sub-critical if $n_e < n_c$. For the waves allowed to propagate in the plasma, we can define two different speeds: the phase velocity v_ϕ and the group velocity v_G. The first one is the speed at which the phase ($\mathbf{k}\cdot\mathbf{r} - \omega t$) is "propagating" and is given here by:

$$v_\phi = \frac{\omega}{k} = \frac{c}{\sqrt{1 - \frac{\omega_{pe}^2}{\omega^2}}} = \frac{c}{\sqrt{\mathrm{Re}(\epsilon)}} \tag{2.210}$$

The group velocity is obtained by taking the differential of the dispersion relation 2.208: $\omega d\omega = c^2 k dk$ and then by deducing the ratio $d\omega/dk$:

$$v_G = \frac{d\omega}{dk} = c\sqrt{1 - \frac{\omega_{pe}^2}{\omega^2}} = c\sqrt{\mathrm{Re}(\epsilon)} \tag{2.211}$$

whereas the phase velocity, as it can be seen from eq. 2.210, can be greater than the speed of light, the group velocity is always smaller than c. This last velocity represents actually the speed at which energy is transported and can be interpreted as the speed of the envelope of a packet of monochromatic waves whose frequencies are close and centered around ω. Interestingly, we can easily notice from 2.210 and 2.211 that:

$$v_\phi v_G = c^2 \tag{2.212}$$

2.5.3 Effect of electron-ion collisions on the propagation of light waves in homogeneous plasmas

When deriving the dispersion relation 2.208 we have neglected the collisions by assuming $\nu_{ei} = 0$. If we take into account the electron-ion collisions but still with $\nu_{ei}/\omega << 1$, we derive a corrected dispersion relation for the case of plane waves (2.207). We use 2.199, 2.200 to find:

$$k^2 = \left(\frac{\omega}{c}\right)^2 \left(1 - \frac{\omega_{pe}^2}{\omega^2}\right) + i\frac{\nu_{ei}\omega_{pe}^2}{c^2\omega} \tag{2.213}$$

In the presence of collisions, the wavenumber vector can be decomposed in a real part $\mathrm{R}e(k)$ as well as an imaginary part $\mathrm{I}m(k)$. If we suppose that the wave is propagating in the z-direction, the spatial dependence of the wave electric field (same for the magnetic field) can be written as $\mathrm{E}_0 exp[(i\mathrm{R}e(k) - \mathrm{I}m(k))z]$. Thus, if $\mathrm{I}m(k) > 0$ the electromagnetic wave will be damped as it propagates in the plasma and will deposit its energy via electron-ion collisions (inverse-Bremsstrahlung process). We have $k^2 = \mathrm{R}e(k)^2 - \mathrm{I}m(k)^2 + i2\mathrm{R}e(k)\mathrm{I}m(k)$ so we can equalize both real parts and imaginary parts in equation 2.213 to get:

$$\mathrm{R}e(k)^2 - \mathrm{I}m(k)^2 = \left(\frac{\omega}{c}\right)^2 \left(1 - \frac{\omega_{pe}^2}{\omega^2}\right) \tag{2.214}$$

$$2\mathrm{R}e(k)\mathrm{I}m(k) = \frac{\nu_{ei}\omega_{pe}^2}{c^2\omega} \tag{2.215}$$

As long as $\nu_{ei}/\omega << 1$ holds, this system leads to the following simple expressions for the real and imaginary parts of the wavenumber vector:

$$\mathrm{R}e(k) \approx \left(\frac{\omega}{c}\right)^2 \left(1 - \frac{\omega_{pe}^2}{\omega^2}\right) \tag{2.216}$$

$$\mathrm{I}m(k) \approx \frac{\nu_{ei}\omega_{pe}^2}{2\omega^2 c} \left(1 - \frac{\omega_{pe}^2}{\omega^2}\right)^{-1} \tag{2.217}$$

It can be easily shown that the damping (inverse Bremsstrahlung) rate ν_{IB} of a electromagnetic wave is given by [37]:

$$\nu_{\mathrm{IB}} = 2\mathrm{I}m(k)\, v_G \tag{2.218}$$

Thus, using expressions 2.217 and 2.211 we get:

$$\nu_{\mathrm{IB}} = \frac{\omega_{pe}^2}{\omega^2}\nu_{ei} = \frac{n_e}{n_c}\nu_{ei} \tag{2.219}$$

This last expression is the one we will use in our laser module but, as specified in this section, is valid only if $\nu_{ei} << \omega$.

2.5.4 Geometric optic approximation and the eikonal equation

In the previous section, we have seen several properties of a light wave propagating in a homogeneous plasma. In order to derive the solution needed to implement our laser module in GORGON, we need to investigate the solutions of the (Helmholtz) wave equation 2.194 when the plasma is inhomogeneous. Previously we have considered the solutions to this equation as plane waves so, building on this idea, we consider here waves with small deviations from this previous solution:

$$\mathrm{E}(\mathbf{r}) = \mathrm{A}(\mathbf{r}) exp(i\kappa \mathrm{S}(\mathbf{r})) \tag{2.220}$$

in writing this equation, we assume that the characteristic length of electron density gradients $\mathrm{L}_c = (|\nabla n_e|/n_e)^{-1}$ is large compared to the laser wavelength λ_L. This condition can be formally expressed using the parameter $\kappa = \mathrm{L}_c k_0 = \mathrm{L}_c \omega / c$:

$$\kappa >> 1 \tag{2.221}$$

Equations 2.220 and 2.221 define what is called the Slowly Varying Envelope Approximation (SVEA). If criterion 2.221 is fulfilled, the standard procedure to derive the ray description is to expand the wave amplitude $\mathrm{A}(\mathbf{r})$ as an asymptotic series with respect to integer powers of $(i\kappa)^{-1}$ (Debye expansion, [38]):

$$\mathrm{A}(\mathbf{r}) = \sum_{n=0}^{\infty} \frac{\mathrm{A}_n(\mathbf{r})}{(i\kappa)^n} \tag{2.222}$$

we need then to express the Laplacian of $\mathrm{E}(\mathbf{r})$:

$$\Delta \mathrm{E}(\mathbf{r}) = \left[\Delta \mathrm{A} + i\kappa \mathrm{A} \Delta \mathrm{S} - \kappa^2 \mathrm{A} (\nabla \mathrm{S})^2 + 2i\kappa (\nabla \mathrm{A}) \cdot (\nabla \mathrm{S})\right] exp(i\kappa \mathrm{S}) \tag{2.223}$$

Then, substituting 2.220 and 2.223 into the Helmholtz equation 2.199 we get: (with $n^2 = \mathrm{R}e(\epsilon) + i\mathrm{I}m(\epsilon)$, ϵ being the relative permittivity and $(\omega/c)^2 = (\kappa^2/\mathrm{L}_c^2)$

$$\mathrm{A}\left((\nabla \mathrm{S})^2 - \frac{\mathrm{R}e(\epsilon)}{\mathrm{L}_c^2}\right) + \frac{1}{i\kappa}\left[2(\nabla \mathrm{A}) \cdot (\nabla \mathrm{S}) + \mathrm{A}\Delta \mathrm{S} + \frac{\kappa}{\mathrm{L}_c^2} \mathrm{I}m(\epsilon)\mathrm{A}\right] + \frac{1}{(i\kappa)^2} \Delta \mathrm{A} = 0 \tag{2.224}$$

where we assume that $\mathrm{I}m(\epsilon) << \mathrm{R}e(\epsilon)$ because we use the SVEA. Equation 2.224 can be reduced into one equation if we keep only the dominant term in powers of $(i\kappa)^0$ and consider only the dominant term A_0 in the Debye expansion of $\mathrm{A}(\mathbf{r})$ (see 2.220):

$$(\nabla \mathrm{S})^2 - \frac{\mathrm{R}e(\epsilon)}{\mathrm{L}_c^2} = 0 \tag{2.225}$$

defining a new function ψ such that $\psi = \mathrm{L}_c \mathrm{S}$, we can write 2.225 as:

$$(\nabla \psi)^2 - \mathrm{R}e(\epsilon) = 0 \tag{2.226}$$

this last equation is called the eikonal equation and it describes the so-called eikonal function $\psi(\mathbf{r})$. It is the basis of the geometrical optic model and, for example, one can relatively easily retrieve the well known Snell–Descartes law from this equation.

Equation 2.226 is a partial differential equation of the Hamilton-Jacobi type and as such can be reduced to the Hamiltonian set of ordinal equations:

$$\frac{d\mathbf{r}}{dt} = \frac{\partial \mathrm{H}}{\partial \mathbf{p}} \tag{2.227}$$

$$\frac{d\mathbf{p}}{dt} = -\frac{\partial \mathrm{H}}{\partial \mathbf{r}} \tag{2.228}$$

where the Hamiltonian is given by:

$$\mathrm{H} = \frac{1}{2}\left(\mathbf{p}^2 - c^2 \mathrm{R}e(\epsilon)\right) \tag{2.229}$$

and the ray impulsion is identified to $\mathbf{p} = c\nabla\psi$. The two equations 2.227 and 2.228 can thus be written as

$$\frac{d\mathbf{r}}{dt} = \mathbf{p} \tag{2.230}$$

$$\frac{d\mathbf{p}}{dt} = \frac{c^2}{2}\nabla(\mathrm{R}e(\epsilon)) \tag{2.231}$$

If we use expression 2.205 for the real part of the relative permittivity, we can express the system (eq. 2.230-2.231) using the electron density and the critical density:

$$\frac{d^2\mathbf{r}}{dt^2} = -\frac{c^2}{2n_c}\nabla(n_e) \tag{2.232}$$

As one can see from this last equation, the problem of solving the trajectory of a laser "ray" in a inhomogeneous plasma is similar to solving the motion equation for a particle of mass equal to 1 kg in a potential field equal to $\frac{c^2}{2}\frac{n_e(\mathbf{r})}{n_c}$. Equation 2.232 is the exact form of the eikonal equation we will use in our module for the GORGON code.

2.5.5 Implementing the laser deposition module in the three-dimensional, resistive MHD code GORGON

We implemented the previous model in our 3D MHD code GORGON whose complete description is given in 2.4. We summarize here the results obtained in the previous section concerning the light wave propagation and absorption:

$$\frac{d^2\mathbf{r}}{dt^2} = -\frac{c^2}{2n_c}\nabla(n_e) \tag{2.233}$$

$$\frac{d\mathrm{P}_{ray}}{dt} = -\nu_{\mathrm{IB}}\mathrm{P}_{ray} = -\frac{n_e}{n_c}\nu_{ei}\mathrm{P}_{ray} \tag{2.234}$$

where we have defined the power of one ray P_{ray}. The real laser power P_{laser} at a given instant is related to the ray individual power by $\mathrm{P}_{laser} = \sum \mathrm{P}_{ray}$. It should be noticed that in the geometrical optic approximation the notion of intensity has no meaning for a ray, since it is represented only as an object without volume. As we shall see, the total intensity of the laser can be reconstructed from the sum and spatial distribution of the rays. From equations 2.233 and 2.234 we see that only three MHD variables are needed for the laser deposition module, namely the electronic density n_e, the electronic temperature T_e and the mean degree of ionization $\bar{\mathrm{Z}}$ (the latter being "hidden" in the coulomb logarithm present in the electron-ion collision frequency). The inverse-Bremsstrahlung process, as described in 2.5.3, describes the conversion of the electron kinetic energy coming from their laser-driven ordered oscillatory motion into disorderly thermal energy through collisions with ions. Due to the large mass ratio $m_i/m_e >> 1$, we can reasonably suppose

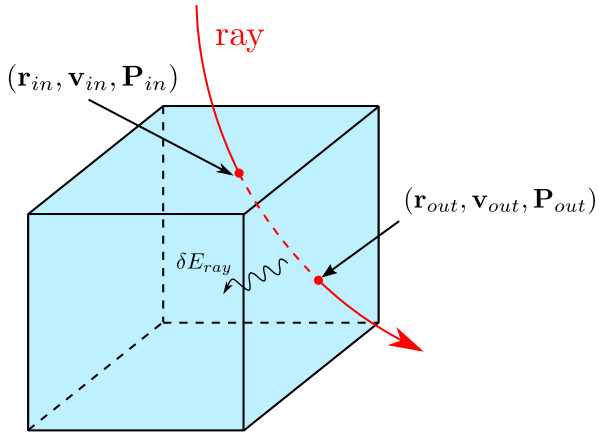

Figure 2.2

that all the laser energy is initially deposited only in the electron population. If furthermore the laser radiation pressure is neglected (see below), the coupling of the laser with the GORGON code is realized only by adding a source term Q_{laser} in the electron energy conservation equation:

$$\frac{\partial \epsilon_e}{\partial t} + \nabla.(\epsilon_e \mathbf{v}) = -p_e \nabla.\mathbf{v} - \nabla.\mathbf{q_e} + \eta j^2 - Q_{ei} - Q_{rad} + Q_{laser} \tag{2.235}$$

Q_{laser} is the laser energy deposition rate per unit of time and volume. The condition necessary to neglect the radiation pressure term can be written $Re(\epsilon)I/c << p_e + p_i$. Since this radiation pressure is effective where the laser is absorbed, i.e not too far from critical density, we have generally there $Re(\epsilon) << 1$ (see 2.205) and thus the condition is usually fulfilled.

We numerically model a laser pulse by decomposing it in multiple rays and solving for each equations 2.234 and 2.233. The implemented ray tracing numerical schema is the Kaiser algorithm [32] where at each time step we transport the rays on a cell-by-cell basis. A useful schematic for this algorithm is given in fig.2.2. For each ray entering in a cell we know its initial position $\mathbf{r_{in}}$, its initial velocity $\mathbf{v_{in}}$ and its initial power P_{in} and we want to determine its exit position $\mathbf{r_{out}}$, its exit velocity $\mathbf{v_{out}}$ and its exit power P_{out}. The exit power will determine the deposited energy in the crossed cell and can be deduced solving equation 2.234:

$$P_{out} = P_{in} \times exp(-\int_{t_{in}}^{t_{out}} \nu_{IB}(t')\,dt') \tag{2.236}$$

where t_{out} is the time needed by the ray to exit the cell. Knowing P_{out} we the deposited energy in the cell is given by:

$$\delta E_{ray} = (P_{in} - P_{out}) \times t_{out} \tag{2.237}$$

The expression for the exit power 2.236 requires to determine the complete trajectory of the ray inside the cell, since the absorption rate ν_{IB} has to be estimated for each time $t' \in [t_{in}, t_{out}]$ at exactly the ray position. Therefore, we first solve equation 2.233 for a small t (we consider, for simplicity, $t_{in} = 0$).

$$\mathbf{v}_{ray}(t) = \mathbf{v}_{in} - \frac{c^2}{2}\nabla_{in}(\frac{n_e}{n_c})t \tag{2.238}$$

$$\mathbf{r}_{ray}(t) = \mathbf{r}_{in} + \mathbf{v}_{in}t - \frac{c^2}{4}\nabla_{in}(\frac{n_e}{n_c})t^2 \tag{2.239}$$

where gradients are computed at the ray initial entrance position $\mathbf{r}_{in}$. The next step is to find the time t_{out}. In the case of a regular orthogonal grid (as in GORGON), we can find t_{out} by solving the equations, for each cell face k, of the intersection of the ray trajectory 2.239 with the plane containing the face k:

$$-\frac{c^2\mathbf{n}_k \cdot \nabla_{in}(n_e)}{4n_c}t_k^2 + \mathbf{n}_k \cdot \mathbf{v}_{in}t_k + \mathbf{n}_k \cdot \mathbf{r}_{in} = d \tag{2.240}$$

and $d = \mathbf{n}_k \cdot \mathbf{r}_{cell,k}$ where $\mathbf{r}_{cell,k}$ is the position of the k cell center and $\mathbf{n}_k$ the unit vector normal to the face k. The final solution t_{out} is the smallest positive one between the twelve solutions t_k corresponding to the six faces. We use this value to compute $\mathbf{v_{out}} = \mathbf{v}_{ray}(t = t_{out})$ and $\mathbf{r_{out}} = \mathbf{r}_{ray}(t = t_{out})$ from equations 2.238 and 2.239. These values will serve as the new $\mathbf{r_{in}}$ and $\mathbf{v_{in}}$ for the next cell crossing.

Now to compute the integral in equation 2.236 we have to find the inverse-Bremsstrahlung absorption rate along the ray trajectory inside the cell

$$\nu_{\mathrm{IB}}(\mathbf{r}_{ray}) = \frac{2.91.10^{-12}}{n_c}\frac{\Lambda(\mathbf{r}_{ray})\bar{\mathrm{Z}}(\mathbf{r_{ray}})n_e^2(\mathbf{r}_{ray})}{\mathrm{T}_e^{\frac{3}{2}}(\mathbf{r}_{ray})} \tag{2.241}$$

Then we expand $n_e(\mathbf{r})$ and $\mathrm{T}e(\mathbf{r})$ at the first order and insert the ray trajectory solution 2.239:

$$n_e(\mathbf{r}(t)) = n_e(\mathbf{r_{in}}) + \nabla_{in} \cdot (\mathbf{r}(t) - \mathbf{r_{in}}) = n_e(\mathbf{r_{in}})\left[1 + at + bt^2\right] \tag{2.242}$$

$$\mathrm{T}_e(\mathbf{r}(t)) = \mathrm{T}_e(\mathbf{r_{in}}) + \nabla_{in} \cdot (\mathbf{r}(t) - \mathbf{r_{in}}) = \mathrm{T}_e(\mathbf{r_{in}})\left[1 + ct + dt^2\right] \tag{2.243}$$

with

$$\begin{aligned} a &= \frac{\nabla_{in}(n_e).\mathbf{v}_{in}}{n_e(\mathbf{r}_{in})} \\ b &= -\frac{c^2(\nabla_{in}(n_e))^2}{4n_c n_e(\mathbf{r}_{in})} \\ c &= \frac{\nabla_{in}(\mathrm{T}_e).\mathbf{v}_{in}}{\mathrm{T}_e(\mathbf{r}_{in})} \\ d &= -\frac{c^2\nabla_{in}(n_e).\nabla_{in}(\mathrm{T}_e)}{4n_c\mathrm{T}_e(\mathbf{r}_{in})} \end{aligned} \tag{2.244}$$

considering Λ and $\bar{\mathrm{Z}}$ constant within the cell, we find the desired expression for the inverse-Bremsstrahlung absorption rate along the ray trajectory for $t \in [t_{in} = 0, t_{out}]$:

$$\nu_{\mathrm{B}rem}(t) = \nu_{\mathrm{B}rem}(\mathbf{r}_{in})\frac{[1 + at + bt^2]^2}{[1 + ct + dt^2]^{3/2}} \tag{2.245}$$

With this formula we can get the integral present in 2.236 using a second order Gaussian quadrature:

$$\int_{t_{in}}^{t_{out}} \nu_{\mathrm{IB}}(t')\,\mathrm{d}t' = \nu_{\mathrm{B}rem}(\mathbf{r}_{in})\frac{t_{out}}{2}\sum_{i=1}^{2}\frac{[1 + at_i + bt_i^2]^2}{[1 + ct_i + dt_i^2]^{3/2}} \tag{2.246}$$

where $t_1 = (1 + 1/\sqrt{3})\,t_{out}/2$ and $t_2 = (1 - 1/\sqrt{3})\,t_{out}/2$.

With expression 2.246 we have everything needed for the laser module: $\mathbf{r_{out}}$, $\mathbf{v_{out}}$, P_{out} and the deposited energy δE_{ray}.

2.5.6 Validation test for the laser module

Here we present a very simple safety check performed in our GORGON code with the implemented module.

Laser propagating in a linearly increasing density

We look at the case where the laser pulse is injected in the box at $z = 0$ and $t = 0$. The density profile depends only on the variable z and is described by:

$$n_e(z) = (1-\alpha)\frac{n_c}{L_z}z + \alpha n_c \tag{2.247}$$

where $\alpha = n_e(0)/n_c$ defines the density at the point where the laser enters the domain. n_c is the critical density and L_z is the total length of the domain in the z direction. We also see that with this profile, the density at the end of the domain is $n_e(L_z) = n_c$, that is the density here is always equal to the critical density.

The position of a ray (among all the rays composing the laser pulse) on the z-axis is $z_r(t)$ and obeys the geometrical optics equation 2.233:

$$\frac{d^2 z_r(t)}{dt^2} = -\frac{c^2}{2n_c}\frac{dn_e}{dz} = -(1-\alpha)\frac{c^2}{2L_z} \tag{2.248}$$

by integrating 2.248 we find the ray velocity $v_{z,r}(t)$ and the ray position:

$$v_{z,r}(t) = \frac{dz_r(t)}{dt} = -(1-\alpha)\frac{c^2}{2L_z}t + v_{z,r}(0) \tag{2.249}$$

where $v_{z,r}(0)$ is the velocity of the ray when entering in the domain (at $z = 0$). For the ray position:

$$z_r(t) = -(1-\alpha)\frac{c^2}{4L_z}t^2 + v_{z,r}(0)\,t \tag{2.250}$$

From these equations, it is easy to see that the density gradient tends to "decelerate" the ray and push it towards the regions of lower densities. The reflection point can be expressed by finding the solution to $v_{z,r}(t) = 0$. Using eq.2.249 we find the time t_{ref} at which the ray is reflected:

$$t_{ref} = \frac{2L_z v_{z,r}(0)}{(1-\alpha)c^2} \tag{2.251}$$

and inserting this time in the solution for the ray position 2.250, we find:

$$z_{ref} = \frac{L_z v_{z,r}^2(0)}{(1-\alpha)c^2} \tag{2.252}$$

Now it is easy to see that if $v_{z,r}(0) = c\sqrt{1-\alpha}$ then, from 2.252, we have $z_{ref} = L_z$. It means that if we effectively have this expression for the initial velocity, the ray is reflected at the end of the domain where the density is equal to the critical density. We have seen that the group velocity, which is the speed at which energy is transported, is given by (2.211): $v_G = c\sqrt{1-n_e/n_c}$. Thus, if we inject the expression for the coefficient α in the

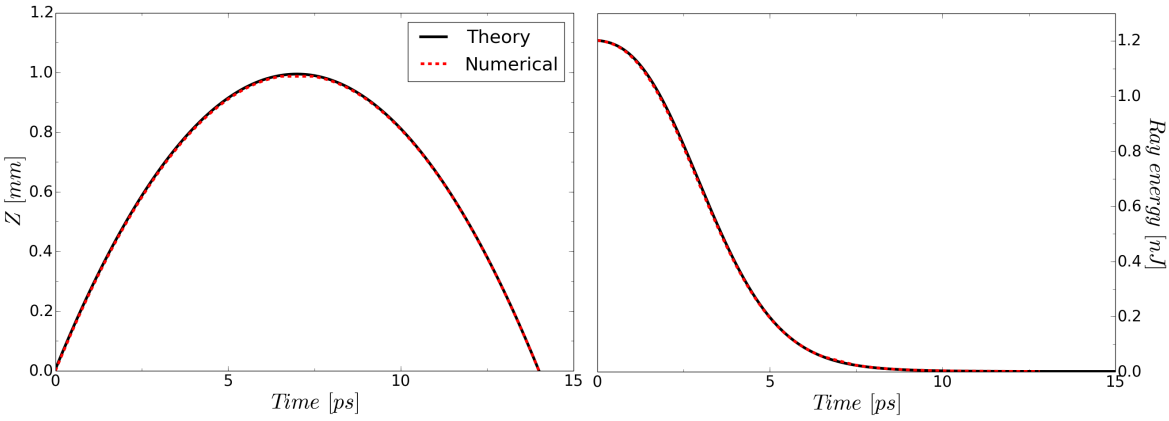

Figure 2.3: Left: Z position of the ray as a function of time. The full black line corresponds to the solution 2.250 whereas the dotted red line corresponds the ray trajectory obtained in GORGON using the model described in the previous section. Right: same as previously but here the plotted quantity is the ray energy as a function of time.

initial velocity, we find: $v_{z,r}(0) = c\sqrt{1 - n_e(0)/n_c}$ which is exactly the group velocity of the wave at the domain entrance. In other words, a ray which enters the domain with the group velocity corresponding to density at this position, will be deflected at the critical density. In fig.2.3 we plot, in the left figure, the position $z_r(t)$ of the ray both from the theoretical relation 2.250 (full black line) and from the implemented module in GORGON (red dotted line) where we initialized the density profile with expression 2.247. We see the good agreement between the two curves. Of course, the trajectory plotted in this graph corresponds to that of one ray among all the other composing the total laser pulse (but since the propagation equation 2.233 does not depend on other thing that the electron density profile and that it is uniform in the plane of the laser beam, all rays have exactly the same trajectory in this case, independently of their energy). Also, the represented ray trajectory is selected during the first "ejection" of rays (the rays are injected in the domain at each MHD time step during the total laser time width).

Now the other important quantity that we must check is the energy/power of one ray as it travels in the simulation domain. Here the equation describing the (collisional) absorption process is given by 2.234. We can rewrite this equation in terms E_r of the ray energy as:

$$\frac{d\mathrm{E}_r}{\mathrm{E}_r} = -\nu_{\mathrm{IB}}\, dt \tag{2.253}$$

In almost every case, it is not possible to find an analytical solution to this equation because ν_{IB} depends on both T_e, n_e in a non-trivial way (see 2.241). However, if we consider the case of a uniform temperature and if we neglect the variation of the coulombian logarithm and consider it as constant (a relatively valid assumption) we can write the inverse-Bremsstrahlung coefficient as (using the density profile 2.247):

$$\nu_{\mathrm{IB}} = \mathrm{K}_0 n_e^2 = \mathrm{K}_0 \left((1-\alpha)^2 \frac{n_c^2}{\mathrm{L}_z^2} z^2 + 2\alpha n_c (1-\alpha) \frac{n_c}{\mathrm{L}_z} z + \alpha^2 n_c^2 \right) \tag{2.254}$$

where K_0 is constant and defined by:

$$K_0 = \frac{2.91.10^{-12}}{n_c} \frac{\Lambda \bar{Z}}{T_e^{\frac{3}{2}}} \tag{2.255}$$

here $\bar{Z}$ is also considered as constant (in the simulation it is imposed). Of course the absorption coefficient has to be evaluated at the ray position, where its energy is absorbed thus the z present in 2.254 is actually equals to $z_r(t)$. So, inserting the expression for the ray position (2.250) in 2.254 we can write the absorption coefficient as:

$$\nu_{IB} = K_0 \left(C_4 t^4 + C_3 t^3 + C_2 t^2 + C_1 t + C_0\right) \tag{2.256}$$

where:

$$C_0 = \alpha^2 n_c^2 \tag{2.257}$$

$$C_1 = 2\alpha(1-\alpha) v_{z,r}(0) \frac{n_c^2}{L_z} \tag{2.258}$$

$$C_2 = (1-\alpha)^2 v_{z,r}^2(0) \frac{n_c^2}{L_z^2} - \alpha(1-\alpha)^2 \frac{n_c^2 c^2}{2L_z^2} \tag{2.259}$$

$$C_3 = -v_{z,r}(0)(1-\alpha)^3 \frac{n_c^2 c^2}{2L_z^3} \tag{2.260}$$

$$C_4 = (1-\alpha)^4 \frac{n_c^2 c^4}{16L_z^4} \tag{2.261}$$

with expression 2.256 for absorption coefficient, we can now integrate relation 2.253 to find the ray energy as a function of time when it is propagating in the plasma:

$$E_r(t) = E_0 \exp\left[-K_0\left(\frac{C_4}{5}t^5 + \frac{C_3}{4}t^4 + \frac{C_2}{3}t^3 + \frac{C_1}{2}t^2 + C_0 t\right)\right] \tag{2.262}$$

This solution is represented, for a 1000 eV plasma, in the right image of fig.2.3 (full black line). The corresponding numerical solution obtained in our laser module in GORGON is plotted in the red dotted line and shows the very good agreement.

2.6 Implementation of the Biermann battery effect in the GORGON code

2.6.1 General description

As we have seen in the section describing the GORGOn code (2.4), Ohm's law implemented in the code is the that of resistive MHD (eq. 2.159). Here we discuss the work done to add the Biermann field $\mathbf{E_{Biermann}}$ in our Ohm's law which will become $\mathbf{E} = \mathbf{E_{Ind}} + \mathbf{E_{Ohm}} + \mathbf{E_{Biermann}}$. See 2.122 for details about the meaning of this term.

This field, because we use ideal gas law for electrons ($p_e = n_e k_B T_e$) in GORGON, can be written as:

$$\mathbf{E_{Biermann}} = -\frac{\nabla p_e}{e n_e} = -\nabla(\frac{k_B T_e}{e}) - \frac{k_B T_e}{e}\nabla(ln(n_e)) \tag{2.263}$$

Of course, in the MHD model, the electric field itself is no explicitly used but instead is used to compute in the Maxwell-Faraday equation (2.48) to compute the magnetic field (i.e. the Maxwell-Ampere equation, see 2.157). Thus if we now express the magnetic field generated by the presence of the Biermann field we have:

$$\left.\frac{\partial \mathbf{B}}{\partial t}\right|_{\mathrm{B}} = -\nabla \times \mathbf{E}_{\mathbf{Biermann}} = \nabla \times \left(\frac{k_{\mathrm{B}}\mathrm{T}_e}{e}\nabla(ln(n_e))\right) = \nabla\left(\frac{k_{\mathrm{B}}\mathrm{T}_e}{e}\right) \times \nabla ln(n_e) \tag{2.264}$$

where we have used the relation $\nabla \times (\nabla(\phi)) = 0$ (where ϕ is any scalar function). The last equality makes it possible to highlight an important characteristic of the self-generation of magnetic field in plasmas: the gradients of $k_{\mathrm{B}}\mathrm{T}_e/e$ and $ln(n_e)$ needs to have a non parallel component in order to generate a non-null magnetic field. This characteristic is assimilated to the notion of baroclinicity which in fluids mechanics is a measure of how misaligned the gradient of pressure is from the gradient of density. In this case we say that a baroclinic fluid is the source of the generation of vorticity [39]. It can be easily understood that the Biermann battery process can be important when a laser impact a solid target. This configuration gives raises to crossed gradients and it has been observed that magnetic field of tens or even hundreds of Teslas can be generated during approximately the pulse duration [40]. The Biermann battery effect is also important in the domain of astrophysics since it is supposed to be involved in the generation of the primordial magnetic field as it was first proposed by Ludwig Biermann in 1950 [41]. Indeed, magnetic fields are widely observed in almost all galaxies, and in galaxy clusters, and the origin of these fields is one of the most fundamental and challenging problems in astrophysics [42; 43]. Without the Biermann field included in the generalized Ohm's law, one can easily see that if the initial magnetic field in zero, then it will remain so as long as the MHD equations are valid.

In GORGON we compute the magnetic field using the potential vector $\mathbf{A}$ related to the magnetic field by: $\mathbf{B} = \nabla \times \mathbf{A}$ (a consequence of the fact that $\nabla \cdot \mathbf{B} = 0$). Thus, the potential vector induced by the Biermann effect will be given by:

$$\left.\frac{\partial \mathbf{A}}{\partial t}\right|_{\mathrm{B}} = \frac{k_{\mathrm{B}}\mathrm{T}_e}{e}\nabla ln(n_e) \tag{2.265}$$

In terms of energy, the self-generated magnetic field through the Biermann battery mechanism induces two contributions: first the electric field acts on the particles and "pump" their energy through the power density:

$$\mathbf{j} \cdot \mathbf{E}_{\mathbf{Biermann}} = -\frac{\nabla p_e}{en_e} \cdot \mathbf{j} = \mathbf{u_e} \cdot \nabla p_e - \mathbf{u_i} \cdot \nabla p_i \tag{2.266}$$

and then the Biermann contribution of the MHD Poynting energy flux is given by:

$$\Pi_{\mathbf{Biermann}} = \frac{\mathbf{E}_{\mathbf{Biermann}} \times \mathbf{B}}{\mu_0} = -\frac{1}{en_e}\frac{\nabla p_e \times \mathbf{B}}{\mu_0} \tag{2.267}$$

2.6.2 Details of the numerical implementation

Quantities noted as f_c represents values at the cell center; Δ is the spatial resolution of the simulation domain; (i,j,k) corresponds to the indices of the cell.

We compute the temperatures at the three points where A_x, A_y and A_z are defined:

$$\mathrm{T}^{ijk}_{e,\mathrm{A}_x} = \frac{\mathrm{T}^{ijk}_{e,c} + \mathrm{T}^{ij(k-1)}_{e,c} + \mathrm{T}^{i(j-1)k}_{e,c} + \mathrm{T}^{i(j-1)(k-1)}_{e,c}}{4} \tag{2.268}$$

$$\mathrm{T}^{ijk}_{e,\mathrm{A}_y} = \frac{\mathrm{T}^{ijk}_{e,c} + \mathrm{T}^{(i-1)jk}_{e,c} + \mathrm{T}^{ij(k-1)}_{e,c} + \mathrm{T}^{(i-1)j(k-1)}_{e,c}}{4} \tag{2.269}$$

$$\mathrm{T}^{ijk}_{e,\mathrm{A}_z} = \frac{\mathrm{T}^{ijk}_{e,c} + \mathrm{T}^{(i-1)jk}_{e,c} + \mathrm{T}^{i(j-1)k}_{e,c} + \mathrm{T}^{(i-1)(j-1)k}_{e,c}}{4} \tag{2.270}$$

and the derivatives of $ln(p_e)$ at these three points:

$$\begin{aligned}\left.\frac{\partial ln(p_e)^{ijk}}{\partial x}\right|_{\mathrm{A}_x} = \frac{1}{8\Delta}[&ln(p_{e,c})^{(i+1)jk} + ln(p_{e,c})^{(i+1)j(k-1)} + ln(p_{e,c})^{(i+1)(j-1)k} + \\ &ln(p_{e,c})^{(i+1)(j-1)(k-1)} - ln(p_{e,c})^{(i-1)jk} - ln(p_{e,c})^{(i-1)j(k-1)} - \\ &ln(p_{e,c})^{(i-1)(j-1)k} - ln(p_{e,c})^{(i-1)(j-1)(k-1)}]\end{aligned} \tag{2.271}$$

$$\begin{aligned}\left.\frac{\partial ln(p_e)^{ijk}}{\partial y}\right|_{\mathrm{A}_y} = \frac{1}{8\Delta}[&ln(p_{e,c})^{i(j+1)k} + ln(p_{e,c})^{(i-1)(j+1)k} + ln(p_{e,c})^{i(j+1)(k-1)} + \\ &ln(p_{e,c})^{(i-1)(j+1)(k-1)} - ln(p_{e,c})^{i(j-1)k} - ln(p_{e,c})^{(i-1)(j-1)k} - \\ &ln(p_{e,c})^{i(j-1)(k-1)} - ln(p_{e,c})^{(i-1)(j-1)(k-1)}]\end{aligned} \tag{2.272}$$

$$\begin{aligned}\left.\frac{\partial ln(p_e)^{ijk}}{\partial z}\right|_{\mathrm{A}_z} = \frac{1}{8\Delta}[&ln(p_{e,c})^{ij(k+1)} + ln(p_{e,c})^{(i-1)j(k+1)} + ln(p_{e,c})^{i(j-1)(k+1)} + \\ &ln(p_{e,c})^{(i-1)(j-1)(k+1)} - ln(p_{e,c})^{ij(k-1)} - ln(p_{e,c})^{(i-1)j(k-1)} - \\ &ln(p_{e,c})^{i(j-1)(k-1)} - ln(p_{e,c})^{(i-1)(j-1)(k-1)}]\end{aligned} \tag{2.273}$$

and now we just have to compute:

$$\left.\frac{\partial \mathrm{A}^{ijk}_x}{\partial t}\right|_{Biermann} = \frac{k_b \mathrm{T}^{ijk}_{e,\mathrm{A}_x}}{e} \left.\frac{\partial ln(p_e)^{ijk}}{\partial x}\right|_{\mathrm{A}_x} \tag{2.274}$$

$$\left.\frac{\partial \mathrm{A}^{ijk}_y}{\partial t}\right|_{Biermann} = \frac{k_b \mathrm{T}^{ijk}_{e,\mathrm{A}_y}}{e} \left.\frac{\partial ln(p_e)^{ijk}}{\partial y}\right|_{\mathrm{A}_y} \tag{2.275}$$

$$\left.\frac{\partial \mathrm{A}^{ijk}_z}{\partial t}\right|_{Biermann} = \frac{k_b \mathrm{T}^{ijk}_{e,\mathrm{A}_z}}{e} \left.\frac{\partial ln(p_e)^{ijk}}{\partial z}\right|_{\mathrm{A}_z} \tag{2.276}$$

2.6.3 Simulation tests

In order to test our implementation of the Biermann battery effect, we performed the following simulations:

1. A plane expansion triggered in a background plasma at rest and of constant density and temperature. The initial temperature profile was perturbed by modifying the temperature (both ionic and electronic) as: $\mathrm{T}_e = \mathrm{T}i = \mathrm{T}_{max} * exp(-z/\mathrm{L}_z)$ where T_{max} was varied from 2 to 100 times the background temperature and L_z is a characteristic length taken to be a small fraction (typically 1/10) of the total length of the domain in the z direction. The self-generated magnetic field should be zero (because of aligned electron pressure and density gradients, see 2.264 and indeed it is what we observed in all our simulations.

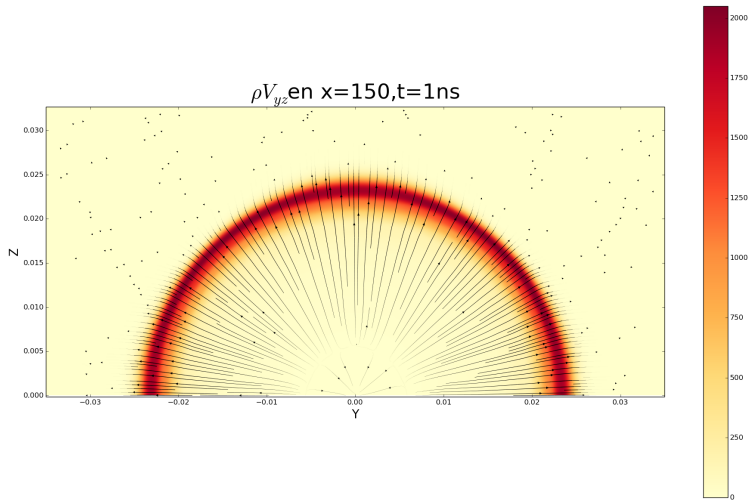

Figure 2.4: Mass flux (in SI units) of a hemispherical blast expansion created by a plasma "ball" of 100 eV with center in (x=0,y=0,z=0). Field lines represents the velocity. Without electronic thermal conduction.

2. Hemispherical expansion of a blast wave triggered by a small hot "ball" of plasma with ion/electron temperature $\approx 10^3$ times greater than the background temperature. The configuration after 1 ns of expansion is shown in fig.2.4 by visualization of the mass flux. The self-generated magnetic field should also be zero in this case (because again of the aligned electron pressure and density gradients). Here it is not entirely the case because the hemispherical expansion is realized in a cartesian grid.

   In fig.2.5 we have represented the maximum total magnetic energy generated in the simulation domain. These maximum occur at the very beginning of the blast expansion ($\approx 0.01\,ns$), when the (electronic) pressure gradients have not yet had time to relax. It can be observed on this figure the "healthy" global behavior of our implementation: as the resolution is increased (decreasing dx) the magnetic energy generated decreases. For a given resolution (here $dx = 0.46\,\mu m$), it can also be seen in fig.2.6 that the value of the temperature initialized to generate the blast has an influence on the maximum generated magnetic energy. This is of course because of the fact that the Biermann generation is proportional to the temperature gradient (see 2.264).

   We must note that we do not observe, in these preliminary results, the "Biermann catastrophe" process that has been described in recent paper from the FLASH team [44]. They have shown that in the presence of strong shocks, the convergence, for "null cases" like the hemispherical blast wave, of the Biermann battery effect is broken and actually worsens when increasing the resolution.

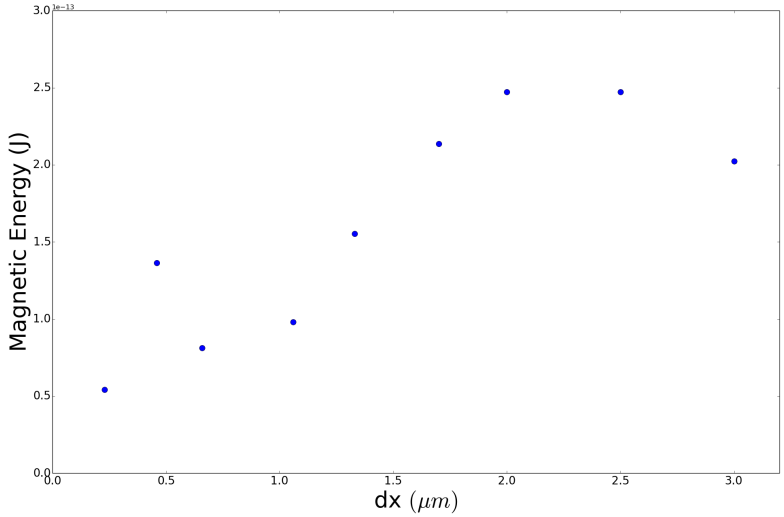

Figure 2.5: Convergence with the spatial resolution of maximal value of the self-generated magnetic field in the case of a hemispherical expansion of a 100 eV plasma blast. Without electronic thermal conduction

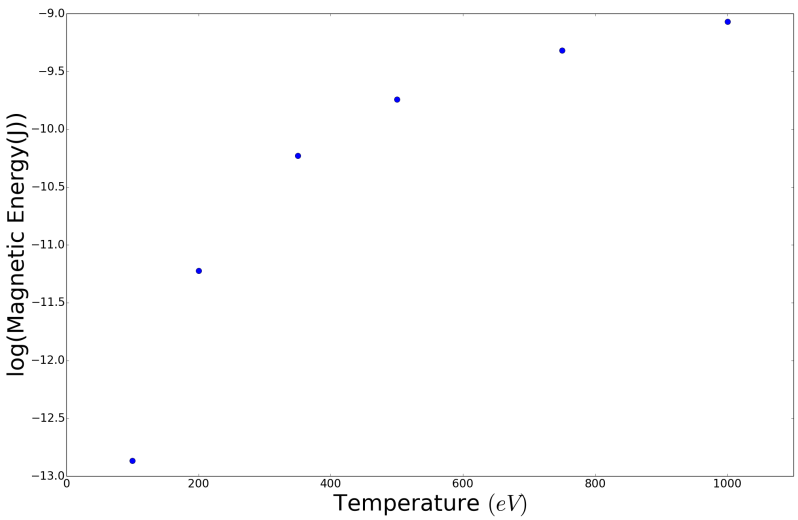

Figure 2.6: For a fixed resolution dx=0.46 um, evolution, as a function of the plasma "ball" temperature, of the maximal value of the self-generated magnetic field in the case of a hemispherical expansion. Without electronic thermal conduction

2.7 Bibliography

[1] H. Hora. D. R. Nicholson, Introduction to Plasma Theory, John Wiley Sons, New York, 1983, XII, 292 pp. *Laser and Particle Beams*, 2:127, 1984. 10

[2] S. Cuperman, I. Weiss, and M. Dryer. Higher order fluid equations for multicomponent nonequilibrium stellar /plasma/ atmospheres and star clusters. *ApJ*, 239:345–359, July 1980. 11

[3] Richard Fitzpatrick. The physics of plasmas. *Texas: The University of Texas at Austin. Ders Notları*, pages 6–7, 2008. 11

[4] Sydney Chapman and Thomas George Cowling. *The mathematical theory of non-uniform gases: an account of the kinetic theory of viscosity, thermal conduction and diffusion in gases.* Cambridge university press, 1970. 11

[5] L.D. Landau and E.M. Lifshitz. *Fluid Mechanics.* Number vol. 6. Elsevier Science, 2013.

[6] A. Sommerfeld. *Partial differential equation in physics.* 1949. 11

[7] Sauro Succi, Iliya V Karlin, and Hudong Chen. Colloquium: Role of the h theorem in lattice boltzmann hydrodynamic simulations. *Reviews of Modern Physics*, 74(4):1203, 2002. 11

[8] Leslie Colin Woods. Principles of magnetoplasma dynamics. 1987. 18, 29

[9] L. D. Landau. The transport equation in the case of coulomb interactions. *ZhETF (J. Exptl. Theoret. Phys. USSR)*, 7(203), 1937. 18

[10] S. I. Braginskii. Transport Processes in a Plasma. *Reviews of Plasma Physics*, 1:205, 1965. 18, 28, 29, 40

[11] Keiji Kimura. On one-fluid mhd models with electron inertia, 2012. 23

[12] M. Lingam, P.J. Morrison, and E. Tassi. Inertial magnetohydrodynamics. *Physics Letters A*, 379(6):570 – 576, 2015. 23

[13] *The Generalized Ohm's Law in Plasma*, pages 193–204. Springer New York, New York, NY, 2007. 26

[14] Naval Research Laboratory. *NRL Plasma Formulary*, 2013. 32

[15] A. Hasegawa. *Electrostatic Ion Acoustic Waves*, pages 425–452. Springer Netherlands, Dordrecht, 1983. 32

[16] DD Ryutov, RP Drake, and BA Remington. Criteria for scaled laboratory simulations of astrophysical mhd phenomena. *The Astrophysical Journal Supplement Series*, 127(2):465, 2000. 33

[17] J P Chittenden, S V Lebedev, C A Jennings, S N Bland, and A Ciardi. X-ray generation mechanisms in three-dimensional simulations of wire array z-pinches. *Plasma Physics and Controlled Fusion*, 46(12B):B457, 2004. 39

[18] A. Ciardi, S. V. Lebedev, A. Frank, E. G. Blackman, D. J. Ampleford, C. A. Jennings, J. P. Chittenden, T. Lery, S. N. Bland, S. C. Bott, G. N. Hall, J. Rapley, F. A. S. Vidal, and A. Marocchino. 3D MHD Simulations of Laboratory Plasma Jets. *apss*, 307:17–22, January 2007. 39

[19] A. Ciardi, T. Vinci, J. Fuchs, B. Albertazzi, C. Riconda, H. Pépin, and O. Portugall. *Phys. Rev. Lett.*, 110:025002, 2013. 39

[20] L. Mejnertsen, J. P. Eastwood, J. P. Chittenden, and A. Masters. Global mhd simulations of neptune's magnetosphere. *Journal of Geophysical Research: Space Physics*, 121(8):7497–7513, 2016. 2015JA022272. 39

[21] Message P Forum. Mpi: A message-passing interface standard. Technical report, Knoxville, TN, USA, 1994. 39

[22] John VonNeumann and Robert D Richtmyer. A method for the numerical calculation of hydrodynamic shocks. *Journal of applied physics*, 21(3):232–237, 1950. 40

[23] D. Salzmann. *Atomic Physics in Hot Plasmas*. International Series of Monographs on Physics. Oxford University Press, 1998. 40

[24] E. M. Epperlein and M. G. Haines. Plasma transport coefficients in a magnetic field by direct numerical solution of the Fokker-Planck equation. *Physics of Fluids*, 29:1029–1041, April 1986. 40

[25] R Paul Drake. *High-energy-density physics: fundamentals, inertial fusion, and experimental astrophysics*. Springer Science & Business Media, 2006. 40

[26] S. Atzeni, A. Schiavi, F. Califano, F. Cattani, F. Cornolti, D. Del Sarto, T. V. Liseykina, A. Macchi, and F. Pegoraro. Fluid and kinetic simulation of inertial confinement fusion plasmas. *Computer Physics Communications*, 169:153–159, July 2005. 41

[27] M. Grech, V. T. Tikhonchuk, G. Riazuelo, and S. Weber. Plasma induced laser beam smoothing below the filamentation threshold. *Physics of Plasmas*, 13(9):093104, 2006. 41

[28] GP Schurtz, Ph D Nicolaï, and M Busquet. A nonlocal electron conduction model for multidimensional radiation hydrodynamics codes. *Physics of plasmas*, 7(10):4238–4249, 2000. 41

[29] B. van der Holst, G. Tóth, I. V. Sokolov, K. G. Powell, J. P. Holloway, E. S. Myra, Q. Stout, M. L. Adams, J. E. Morel, S. Karni, B. Fryxell, and R. P. Drake. Crash: A block-adaptive-mesh code for radiative shock hydrodynamics—implementation and verification. *The Astrophysical Journal Supplement Series*, 194(2):23, 2011. 41

[30] Jon T. Larsen and Stephen M. Lane. Hyades—a plasma hydrodynamics code for dense plasma studies. *Journal of Quantitative Spectroscopy and Radiative Transfer*, 51(1):179 – 186, 1994. Special Issue Radiative Properties of Hot Dense Matter. 41

[31] A E Koniges, N D Masters, A C Fisher, R W Anderson, D C Eder, T B Kaiser, D S Bailey, B Gunney, P Wang, B Brown, K Fisher, F Hansen, B R Maddox, D J Benson, M Meyers, and A Geille. Ale-amr: A new 3d multi-physics code for modeling laser/target effects. *Journal of Physics: Conference Series*, 244(3):032019, 2010. 41

[32] Thomas B. Kaiser. *Phys. Rev. E*, 61:895–905, 2000. 41, 48

[33] B. Fryxell, K. Olson, P. Ricker, F. X. Timmes, M. Zingale, D. Q. Lamb, P. MacNeice, R. Rosner, J. W. Truran, and H. Tufo. Flash: An adaptive mesh hydrodynamics code for modeling astrophysical thermonuclear flashes. *The Astrophysical Journal Supplement Series*, 131(1):273, 2000. 41

[34] J. P. Freidberg, R. W. Mitchell, R. L. Morse, and L. I. Rudsinski. Resonant absorption of laser light by plasma targets. *Phys. Rev. Lett.*, 28:795–799, Mar 1972. 42

[35] V.V. Blazhenkov, A.N. Kirkin, A.V. Kononov, L.P. Kotenko, A.M. Leontovich, G.I. Merzon, A.M. Mozharovsky, and S.D. Zakharov. Evidence of suprathermal electron fluxes in laser-produced plasma from the polarization and anisotropy of x-ray bremsstrahlung emission. *Optics Communications*, 34(2):231 – 234, 1980. 42

[36] IUV AFANASEV, NN Demchenko, ON Krokhin, and VB Rozanov. Absorption and reflection of laser radiation by a dispersing high-temperature plasma. *Zhurnal Eksperimental'noi i Teoreticheskoi Fiziki*, 72:170–179, 1977. 44

[37] Arnaud Colaitis. *Multiscale description of the laser-plasma interaction : application to the physics of shock ignition in inertial confinement fusion.* Theses, Université de Bordeaux, November 2015. 45

[38] G.V. Pereverzev. *Paraxial WKB solution of a scalar wave equation.* IPP, 1993. 46

[39] M. Modestov, V. Bychkov, G. Brodin, M. Marklund, and A. Brandenburg. Evolution of the magnetic field generated by the kelvin-helmholtz instability. *Physics of Plasmas*, 21(7):072126, 2014. 53

[40] MG Haines. Magnetic-field generation in laser fusion and hot-electron transport. *Canadian Journal of Physics*, 64(8):912–919, 1986. 53

[41] L. Biermann. Über den Ursprung der Magnetfelder auf Sternen und im interstellaren Raum (miteinem Anhang von A. Schlüter). *Zeitschrift Naturforschung Teil A*, 5:65, 1950. 53

[42] C. L. Carilli and G. B. Taylor. Cluster Magnetic Fields. *araa*, 40:319–348, 2002. 53

[43] L. M. Widrow. Origin of galactic and extragalactic magnetic fields. *Reviews of Modern Physics*, 74:775–823, 2002. 53

[44] C. Graziani, P. Tzeferacos, D. Lee, D. Q. Lamb, K. Weide, M. Fatenejad, and J. Miller. The Biermann Catastrophe in Numerical Magnetohydrodynamics. *ApJ*, 802:43, March 2015. 55

Chapter 3

The physics of laser-solid target interaction

Sommaire

3.1 Introduction **62**

3.2 The ablation process **63**

3.2.1 Material removal by laser energy 63

3.2.2 The mediating effect of the ablated material 64

3.2.3 General picture of a solid target illuminated by a laser pulse 65

3.2.4 Temperatures reached in laser-produced plasmas 70

3.2.5 Scaling laws for laser-produced plasmas parameters 71

3.3 Dynamics of laser-produced expanding plasmas **71**

3.3.1 Introduction 71

3.3.2 Adiabatic self-similar 1D plasma expansion 72

3.3.3 Isothermal self-similar 1D plasma expansion 80

3.3.4 A new potential 1D description of laser-produced plasmas expanding at supersonic/hypersonic speeds 81

3.4 Bibliography **88**

3.1 Introduction

The chapter we are presenting now aims to give a small overview of the basic aspects of the physics of laser-solid-plasma interaction. This chapter is largely not essential for understanding of the rest of this manuscript. It describes, at least in the first section, physical processes occurring in the region very close to the target while in the following chapters we will be mostly interested in the dynamics far from this region. However, the second section dealing with the description of the plasma expansion is of major interest because it represents our "fundamental tool" with which we will work to perform our astrophysically-relevant simulations.

Since the first laser realized in 1960 by Maiman [1], the uninterrupted progress of optics, electronics, material science have allowed the lasers to reach initially unexpected performances. The most important parameter used to define the class of a laser is the intensity I_L, that is, its energy per unit of time and unit of surface ($[I] = J.cm^2.s^{-1}$). The intensity can be estimated from the laser energy E_L, the pulse duration τ_L as well as the surface of the focal spot ϕ_L: $I_L \approx E_L/\tau_L\phi_L$. Two main trends have been developed since the first millisecond laser of Maiman: on one side, the quest to reach ever more energetic lasers and on the other side the quest to reach the shortest pulse duration possible.

In fig.3.1 the time evolution of focused laser intensity is shown (from [2]) from 1960 to the 2010's. Few years after the first laser, two major breakthrough (Q-switching [3] and mode-locking [4]) have allowed to dramatically increase the peak intensities by compressing the temporal width of the pulse. From there, it was understood early on that above a certain intensity threshold ($\sim 10^8\,W.cm^{-2}$, see 3.2.1) it was possible to ablate and then ionize solid material by focusing the laser pulses onto solid targets. The interest of producing high energy density material states has been at the origin of a strong involvement of military-oriented researchers and a large part of the scientific literature in the sixties and seventies has been carried out in this context [5; 6]. Schematically, for intensities $\lesssim 10^{15}\,W.cm^{-2}$, the pulse durations are generally long enough to induces regimes relatively well described by (radiative) hydrodynamic models. This is mainly because electrons, thanks to their low inertia, have enough time to thermalize the absorbed energy and form a quasi maxwellian distribution function. When the intensity increases, we reach regimes in which electrons receive energy faster than they can "process" through collisions. In these cases, the laser energy goes into non-thermal processes by the generation of instabilities and non-linear mechanisms, such as suprathermal electron accelerations [7], or the effect of the ponderomotive force [8] to name a few. At even higher intensities, the regime become strongly relativistic. Here in this chapter, we will focus on the regime where the intensity is sufficiently low to allow a hydrodynamic description of the plasma. We will first see the general aspects of the ablation process, when a laser impacts a solid planar target. Then we will talk a little bit about the question of the temperatures generated in laser-produced plasmas and finally, because this is an important point for our work, we will discuss the dynamic of the plasma plume expanding in front of the solid target as a result of its heating.

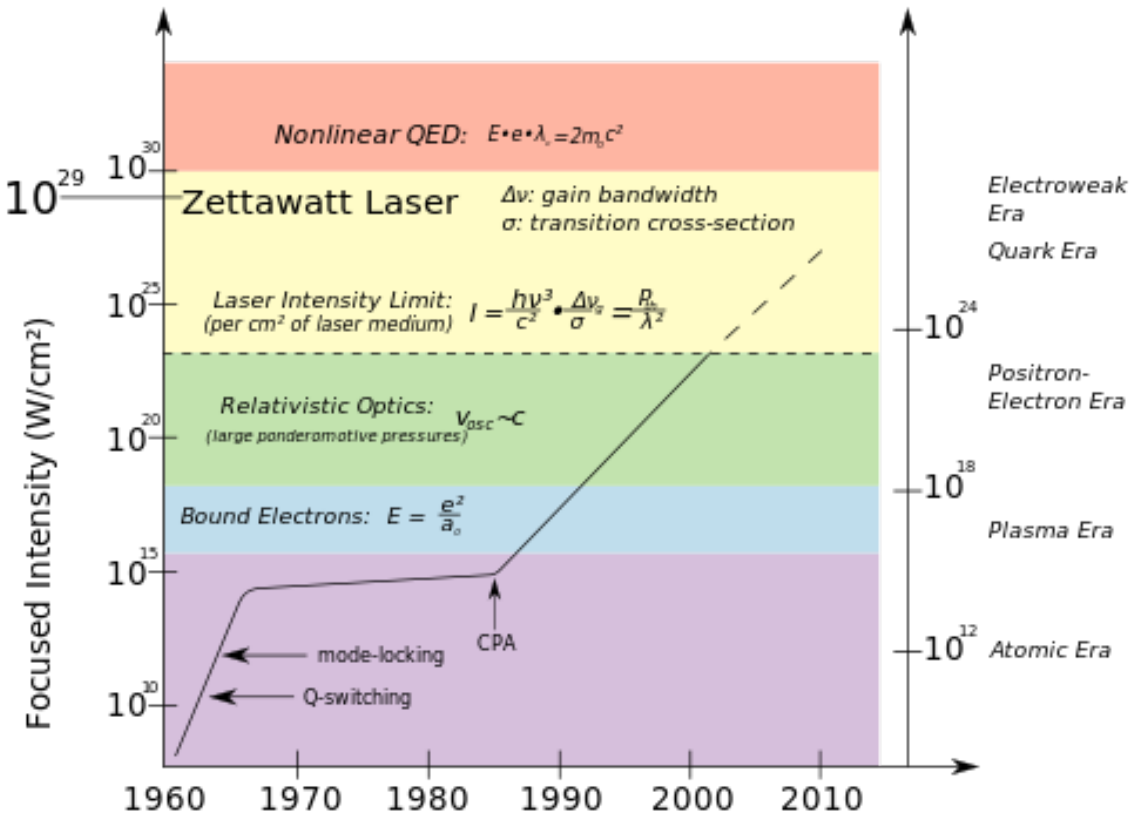

Figure 3.1: Graph showing the history of maximum laser pulse intensity throughout the past 40 years. From [2].

3.2 The ablation process

3.2.1 Material removal by laser energy

When a laser pulse starts to heat the surface of a solid target, the material is very quickly vaporized due to the generally low energy required to vaporize the solid (e.g. sum of specific latent heat of fusion L_f, specific latent heat of vaporization L_v and $C_v(T_v - T_0)$, where C_v is the specific heat capacity, T_v the vaporization temperature and T_0 the initial temperature of the target). This conversion of solid material into gas is called the ablation process. Laser photons are absorbed by free electrons in the solid target through the inverse bremsstrahlung mechanism [9] and, considering good conducting materials, the characteristic time between collisions for the electrons is of the order of $10^{-13} - 10^{-14}\,s$. Thus, electrons will thermalize between themselves and with the lattice phonons on a time scale much shorter than the pulse width. This leads to a regime where the laser energy is essentially turned instantaneously into heat in the absorption volume ϕ/α, where ϕ is the cross section of the laser at the focal point and α is the laser absorption coefficient in the solid phase of the materia(for example, $\alpha \approx 0.1\,nm^{-1}$ for copper and for a wavelength of $1\,\mu m$ [10]). The time t_{vap} needed to start the vaporization of the target material can be estimated by assuming that the laser energy deposited at t_{vap} on the mass $\phi\alpha^{-1}\rho_{solid}$ is equal to the sum of specific latent heat of fusion and specific latent heat of vaporization. The deposited energy at t_{vap} is given by:

$$E_{dep}(t_{vap}) = \int_0^{t_{vap}} P_{laser}(t)\,dt \tag{3.1}$$

In the simplest case of a flat profile, we have $E_{dep}(t_{vap}) = P_{laser}\, t_{vap}$ and thus from $E_{dep}(t_{vap})/(\phi\alpha^{-1}\rho_{solid}) = L_f + L_v + C_v(T_v - T_0)$ we can express the vaporization time:

$$t_{vap} = \frac{\alpha^{-1}\rho_{solid}(L_f + L_v + C_v(T_v - T_0))}{I_{laser}} \tag{3.2}$$

where $I_{laser} = P_{laser}/\phi$ is the laser intensity. For example, for carbon (graphite, $\rho_{solid} \approx 2,267\, g.cm^{-3}$), $L_f \approx 9.7\, kJ.g^{-1}$, $L_v \approx 59\, kJ.g^{-1}$, $C_v \approx 0.709\, J.g^{-1}.K^{-1}$ and $T_v \approx 4098\, K$ and if we suppose that the solid target is initially at room temperature $T_0 = 300\, K$, a laser with an intensity $I_{laser} = 1 \cdot 10^{12}\, W.cm^{-2}$ will vaporize the material at approximately $t_{vap}[s] \approx 1.6 \cdot 10^{-7} \times \alpha^{-1}[cm]$. Even considering a very large value of $\alpha^{-1} = 10\, \mu m = 10^{-4}\, cm$ ("real" values are much less than $1\, \mu m$), we get an vaporization time of $t_{vap} \approx 1.6 \cdot 10^{-11}\, s$ which is generally much smaller than the typical nanosecond lasers that are used for example, for laboratory astrophysics experiments. The conclusion is that we can comfortably consider the generation of gas in front of the solid target to occur instantly after the laser start.

3.2.2 The mediating effect of the ablated material

The principal effect resulting from the presence of the ablated gas is to introduce a intermediate absorbent medium between the laser and the solid target. This expanding gas is responsible mediating the transfer of momentum from the laser towards the target. The second process occurring just after the vaporization is the ionization of the gas. Indeed, after a characteristic very short breakdown time ($< 1\, ps$) [11], the ionization of the vaporized gas under the action of the strong laser field generates an increasing electron density which in turn increases the absorption of the laser photons, mainly through inverse Bremsstrahlung (see 2.5.3). The sudden increase of the electron number density n_e, the so-called "gas breakdown", can be a consequence of "direct" or "indirect" effects (see the pioneering work from Raizer [11]). First, the direct knock-out of the electrons from the atoms by the laser beam is possible mainly through two channels: the tunnel effect and the multiquantum photoeffect (see [12; 13]). The first one can occur if the bounded electrons see a static electric field during their time of flight through the potential barrier of ionization in their atoms. We thus understand that this effect will occur preferably for "low" frequency lasers. The multi-quantum photo-effect is the simultaneous absorption of multiple laser photons by atomic electron, leading to their release in the continuum. It can be shown that the probability for the simultaneous absorption of m photons by an atom is proportional to I_{laser}^m so this ionization mechanism will occur mainly for high intensities lasers [14]. The gas breakdown can also be triggered by indirect processes, i.e. mechanisms by which the laser photons transfer their energy (and momentum) to an intermediary before the atoms are being ionized. The simplest process is the "electron cascade" which is very similar to the electrical breakdown occurring in some technological devices (glow discharge in neon lights, fluorescent lamps, and plasma-screen televisions...) described by the famous Paschen's law [15], which gives the necessary "breakdown voltage". The general idea consists to suppose that there exist initially few free electrons in the gas and that under the action of the laser electric field they will gain enough kinetic energies to collisionally ionize even more atoms. Depending on the gas type and pressure, the "threshold" laser intensity is generally above $\sim 10^8\, W.cm^{-2}$ (depending on the focal spot size and pulse duration) [16]. Once the electron density reaches values close to the critical density (see 2.5.2), a strong laser collisional absorption take place and the laser energy is mainly used to heat the electrons (which can ionize the remaining ions to

higher charge states) whereas the solid target itself is almost shielded from the laser pulse field.

The heating of the electron population triggers a departure of the plasma from thermal equilibrium with ions on a time scale given by the equipartition time:

$$t_{eq}[s] = 3.15 \cdot 10^8 \frac{\mathrm{A}_i \mathrm{T}_e^{3/2}[e\mathrm{V}]}{Z^2 \Lambda n_e [cm^{-3}]} \tag{3.3}$$

where Λ is the coulomb logarithm, typically of the order of 10. Expression 3.3 is an approximation of equation (5.31) of Spitzer)[17]) under the condition that $\mathrm{T}_i/\mathrm{A}_i << \mathrm{T}_e/\mathrm{A}_e$ where A_i is ion the atomic weight and $\mathrm{A}_e \approx 1/1837$ the electron atomic weight. For relatively high intensities ($\mathrm{I} \sim 10^{13}\,\mathrm{W}.cm^{-2}$), we expect temperatures > 100 eV in regions of densities $\sim 10^{19}\,cm^{-3}$ thus, using these values for a carbon plasma (completely ionized), we get $t_{eq} \sim 1\,ns$ which is of the order of typical laser temporal widths we will study in this manuscript. The hypothesis that electrons and ions are at the same temperature can thus be questionable, and indeed our computational models take into account the decoupling of temperatures.

Following this very fast heating, the plasma experiences a rapid free expansion where it converts its thermal energy into bulk kinetic energy. In vacuum, this expansion can be described as a rarefaction wave, which is found to propagates at velocities of the order of the sound speed of the initial ionized and heated gas. The simple case of a one-dimensional free expansion is treated in detail in a dedicated subsection (3.3.2). For a laser generated carbon plasma with an initial temperature of $100\,e$V (see 3.2.4), we thus expect expansion velocities of the order of $100\,km.s^{-1}$.

As a consequence of this rapid expansion, the absorbing plasma medium "spreads" on distances that can be of the order or even greater than the size of the laser focal spot. As it expands, the density decreases as well as the collisional absorption (the absorption rate is proportional to n_e^2, see 2.5.3). Thus the plasma becomes partially transparent to the laser field resulting in a energy deposition profile much more delocalized, and leading globally to lower temperatures. It is interesting to note that this last point has been at the origin of a "quest" to find the optimal laser/material parameters necessary to maximize the temperature of the ablated plasma with the aim to reach fusion-relevant conditions [18; 19] . One of the first solutions envisaged was to use shorter laser pulses to deposit all of the laser energy before any significant expansion. However it was rapidly found that using too short laser pulses ($< ps$) leads to plasma heating which is not "thermal", in the sense that only a small fraction of the electrons (called "suprathermal") are heated, whereas the bulk plasma stays basically "cold" [7].

3.2.3 General picture of a solid target illuminated by a laser pulse

Having described the ablation and the ionization of the material from a solid target irradiated by a laser, we can now draw a general picture of the resulting structure of the whole target+plasma system under the action of a laser.

In fig.3.2, we have represented a schematic view of what is admittedly this structure [20]. We can distinguish four main regions: the unperturbed solid (zone 1), a region of the solid undergoing a shock (zone 2, see below), a (thermal) conductive region (zone 3) and finally the expansion region (zone 4). We now describes all these regions, but not necessarily in this order.

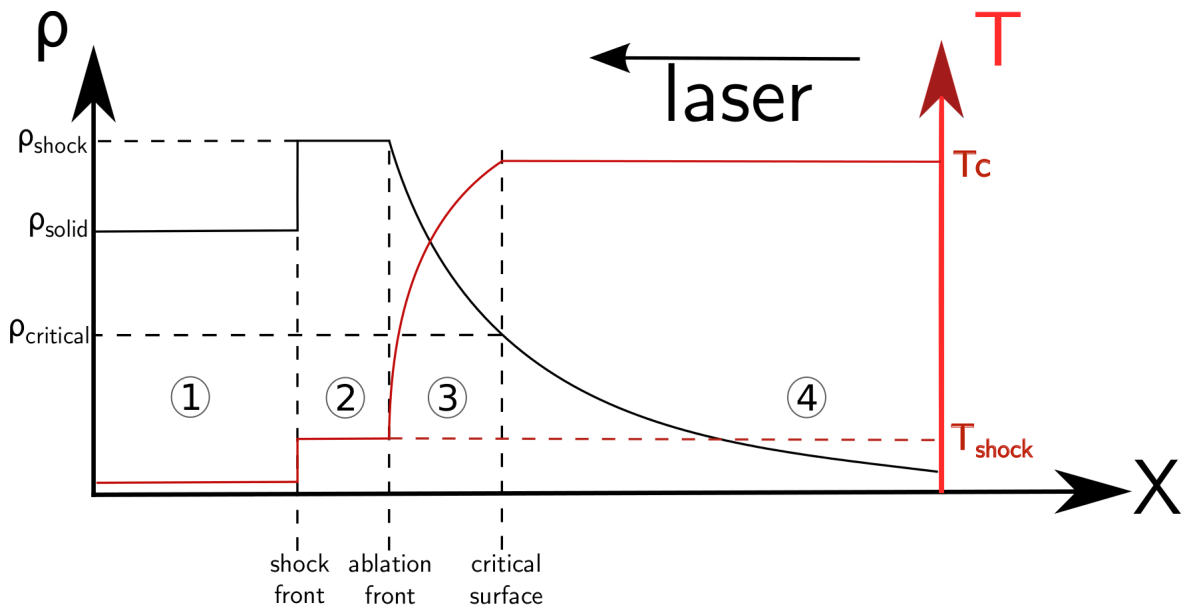

Figure 3.2: Schematic picture of the different regions established during the interaction of a laser pulse with a solid target. Region 1: Unperturbed solid target. Region 2: Part of the solid target been shocked. Region 3: conductive zone, delimited on the left by the ablation front and on the right by the critical surface. The laser energy can not be deposited directly in this region but instead is transported through thermal conduction up to the ablation front. Region 4: Expanding plasma, represented in this schema as been isothermal but, as explained in the main text, in some condition and far form the critical surface, the expansion can be closer to an adiabatic regime.

The conductive zone (zone 3)

As explained in the previous section (3.2.1), as soon as the ablated material breaks down, the collisional absorption rapidly increases. Laser heating then causes the plasma as well as the the critical surface to expand outward and the latter to become "detached" from the solid target. The critical surface is where the electron density is equal to the critical density n_c (2.5.2), see fig.3.2).

Because of "detachment", the region to the left of the critical surface cannot be reached by the laser energy and thus the only way for the energy to be transported towards the target is by thermal conduction, mainly by electrons because of their high mobility [20]. That is the reason this zone (number 3 in fig.3.2) is called the "conductive zone". Inside this region the heat flux Q can be estimated by the harmonic mean [21]:

$$\frac{1}{Q} = \frac{1}{Q_{th}} + \frac{1}{fQ_{lim}} \tag{3.4}$$

where $Q_{th} = -\kappa_0 T_e^{5/2} \frac{dT_e}{dx}$ is a semi-empirical thermal flux proportional to the electronic temperature gradient. In these regimes, the coefficient κ_0 is often taken from SITZER-HARM (where the semi-empirical nature appears, [22]). We point out that because of the steep, positive electron temperature profile in the conductive zone (3), the thermal flux is negative. In general, it is almost always necessary to add a limiter on the thermal flux Q_{lim}, this is because of the perturbation derivation used to derive κ_0 fails at high thermal fluxes [23].

The simplest limited flux corresponds to the flux that one would observe if all electrons are flowing freely with their thermal velocity [21]. The factor f in 3.4 is introduced to take into account all the other mechanisms that can occur during the laser-plasma

interaction (resonant absorption [24], Raman/Brillouin diffusion [25], suprathermal electrons [7]...) and are generally considered as limiting even more the thermal flux. Typical values of $f = 0.03 - 0.1$ have been determined experimentally [26], but large uncertainties exist.

In term of spatial dimension, the scale length L of the conductive zone can be estimated considering that it corresponds to the length over which the transport of energy by conduction is comparable with the transport by convection (with the velocity u). This calculation is carried out in [27] and leads to a length proportional to $\sqrt{A/Z}(1+T_i/ZT_e)^{-3/2}\lambda_e$ where λ_e is the electron mean free path, A the mass number and Z the effective charge state. A more detailed, but similar, estimate of the characteristic length can be found in [28]. The demonstration carried out in this paper assumes the conductive zone to be in a steady state. This hypothesis is valid only if the laser pulse duration τ_L is greater than the time needed to establish the conductive zone. This condition has been derived in [29] and it is given by:

$$\tau_L[ns] \lesssim 25 I_{14} \lambda_L^4[\mu m](A/2Z)^{3/2} \tag{3.5}$$

where I_{14} is expressed in units of $10^{14}\,W.cm^{-2}$ and λ_L is the laser wavelength. As we shall see later (5.3), the characteristic laser parameters we will use in this work are $I_{14} = 7.7\,10^{-2}$ and $\lambda_L = 1.057\,\mu m$ giving, for a carbon target, a value for the right term in 3.5 of $\approx 2.4\,ns$. The typical pulse duration we will use is $\lesssim 1\,ns$ and thus in this case we should be in a non-stationary regime. In fact, with a ($1.057\,\mu m$, $1\,ns$) laser, the intensity threshold above which the conductive zone can not be considered as stationary is $\approx 3\,10^{11}\,W.cm^{-2}$. Because for intensities close or lower than this threshold the plasma would reach relatively "low temperatures" ($\lesssim 10\,eV$) and thus be in a low magnetic Reynolds number regime (2.3.10), this kind of intensities are generally not used for laboratory astrophysics experiments where large magnetic Reynolds number are usually needed [30]. For example, in the case of a $0.35\,\mu m$ laser with the same parameters, the intensity threshold is basically two order of magnitude higher and the ablation process could be considered as stationary during the pulse duration.

The unperturbed/shocked solid target (zones 1-2)

Because of the presence of the conductive zone (zone 3), a thermal wave can propagates towards the solid regions (zones 1-2). If the speed of this wave v_{th} is greater than the sound speed of the solid, a forward shock wave propagates inside the unperturbed target forming the region (3) in fig.3.2. This regime is called the deflagration model [27; 31; 32]. It has been shown that this process occurs almost in all cases, provided the pulse duration is sufficiently short ($\lesssim 10\,ns$) [33]. Typically, for a laser intensity of intensity of $10^{14}\,W.cm^{-2}$, the shock carry $\sim 3\%$ of the laser energy at a wavelength $\lambda = 1.06\,\mu m$ and up to $\sim 10\%$ for a wavelength $\lambda = 0.35\,\mu m$ [34]. The limit between the unperturbed target and the shocked material corresponds to the shock front whereas the limit between shocked material and the conductive zone is called the ablation front (see fig.3.2) .

We have seen in the previous section that the presence of the ablated material in front of the target mediates the direct coupling between the laser and the target. However, this does not mean that the solid material can no longer be ablated since the thermal wave brings a portion of the deposited energy up to the ablation front.

The pressure at the ablation front is called the "ablation pressure" P_a and is one of the variables frequently retrieved from laser experiments. It can be linked to the areal ablative

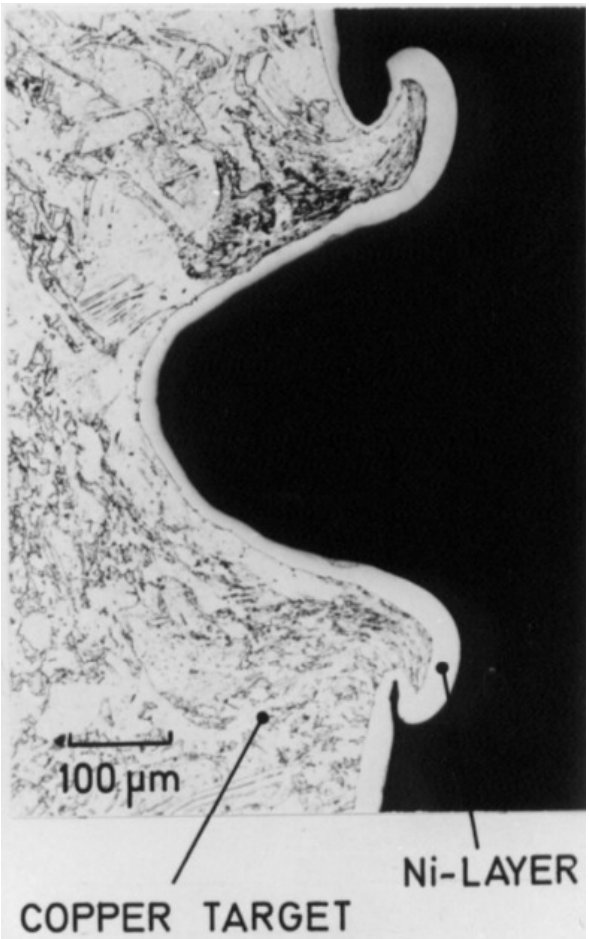

Figure 3.3: Crater produced in copper by a focused Nd laser beam of an energy of 10 J and a duration of 10 ns. From [36]

rate $\dot{m}_a$ through the introduction of the ablation velocity v_a:

$$P_a = \dot{m}_a v_a \tag{3.6}$$

The areal ablative rate is also related to the velocity of the thermal wave front which "digs" into the solid surface with a velocity:

$$v_{th} = \frac{P_a}{v_a \rho_{solid}} \tag{3.7}$$

If we consider that during the laser pulse the areal ablative rate is constant, a very simple way to estimate it, is to measure the crater depth e_{abl} generated after the laser action:

$$e_{abl} = \frac{\tau_L}{\rho_{solid}} \dot{m}_a \tag{3.8}$$

where τ_L is the laser pulse duration. Equivalently, the total ablated mass is simply equal to $M_{abl} = \rho_0 \phi e_{abl}$. A typical crater obtained on a copper target with a 10 J laser pulse of 10 ns is shown in fig.3.3 and the crater depth can be measured, for example, using a white-light interferometric microscope [35].

The other quantity that is often measured in laser experiments is ablation velocity v_a, mentioned earlier. Contrary to what the name might suggest, this is not the velocity at which the target surface is ablated (this velocity is the thermal wave velocity v_{th}). The

ablation velocity is derived from an analogy between the acceleration of laser targets by lasers and the accelerations of rocket by traditional chemical thrusters. The idea is to consider that the ablation of the target surface is equivalent to say that a flow is ejected from the surface with a rate $\dot{m}_a$ and a kind of mean velocity, namely the ablation velocity v_a. This analogy, called the "rocket effect", has been realized for the first time by researchers from the Naval Research Laboratory (NRL) aiming to accelerate planar targets with lasers [37]. Experimentally the ablation velocity is measured using charge collectors to infer the ion velocity spectrum in the emitted plume [38–42]. As an example, for a laser impacting an aluminium target with an intensity of $\sim 10^{14}\,\mathrm{W}.cm^{-2}$ and a wavelength $0.35\,\mu m$, the measured crater depth is $e_{abl} \approx 2.7\,\mu m$, the areal ablation rate $\dot{m}_a \approx 7.28\,10^5\,g.s^{-1}.cm^{-2}$, the ablation pressure $\mathrm{P}_a \approx 27\,\mathrm{M}bar$ and the thermal front velocity $v_{th} \approx 2.7\,10^5\,cm.s^{-1}$ [34]. Also in this same experiment, the conductive zone length (which was in the steady state regime) was estimated to be $\approx 24\,\mu m$.

The expansion region (zone 4)

We come to the last zone, namely the expansion region (zone 4 in fig.3.2). In fact this is the most interesting part in the context of this thesis, since we want to use the expanding plasma to study its dynamic in an externally applied magnetic field of different configurations, and it's interaction with other solid targets.

If we focus (as we have done so far) on times during which the laser pulse is active, two main models exist depending on the absorption regime:

1. At high laser intensities, the temperature of the expanding plasma is such that collisional absorption is negligible and the plasma is almost transparent to the laser pulse. In this case, the laser absorption is almost entirely done at the critical density thanks to non-linear mechanisms (resonant absorption...). The absorbed energy near the critical surface is used to drives both the shock wave described previously and the expansion fan. This is the deflagration model [31; 32]. Depending mainly on the importance of thermal conduction and radiative losses in this region, the expansion can be approximates as isothermal or adiabatic (see 3.3.2). The profile of temperature in zone 4 represented in fig.3.2 shows the case of an isothermal fan at the critical temperature T_c. In fact this profile is not exactly correct. Indeed, if we suppose that the expanding plasma is isothermal, it must exist a heat flux at the critical surface that "feeds" the expansion. This point represents a paradoxical aspect of this model since it would contradicts the isothermal assumption. Several solutions have been proposed to solve this problem [43; 44] and they have shown that there must exist a time-increasing temperature gradient just after the critical surface; however as we look far from this surface, the flow is effectively isothermal.

2. At lower laser intensities, the temperature of the expansion fan is low enough to be in a regime where the underdense expanding region absorbs a large portion of the laser energy through the inverse-Bremsstrahlung mechanism. If the total absorption in the plume reaches values close to 100 % then the energy reaching the critical density can be negligible. Since the temperature in the expanding plasma adjusts itself such that the optical depth of the fan for the laser is approximately unity, this regime is called the "self-regulating model" [45–47]. Here again, the expansion can be considered as isothermal or adiabatic (see 3.3.2).

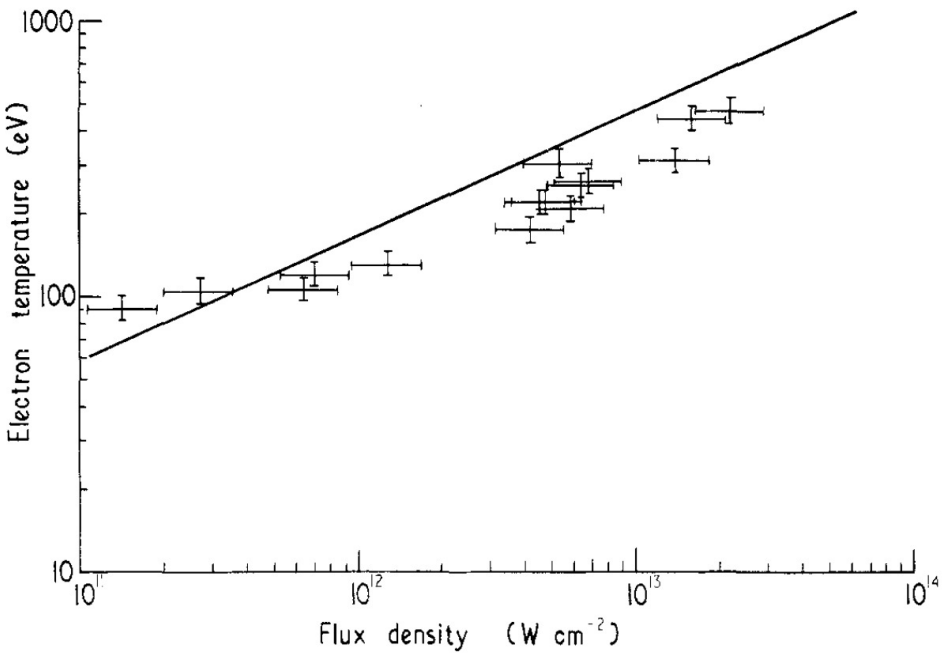

Figure 3.4: Electron temperature of a lucite plasma (C_5,O_2,H_8) as a function of the laser intensity. Temperatures were deduced from soft x-ray continuum. From [51]

3.2.4 Temperatures reached in laser-produced plasmas

The question of the values of temperatures reached during the interaction of the laser pulse with the solid target is a crucial problem when one is seeking to retrieve important plasma dimensioned or dimensionless parameters as the plasma resistivity, thermal conductivity, viscosity, (magnetic) Reynolds number, Peclet number and so one... For high power lasers, the plasma pressure can reach several hundreds of MPa whereas the temperature can reach several tens of millions of Kelvins. Under these conditions, measurements realized in-situ are almost always impossible and we rather rely on emission or absorption diagnostics. A large range of methods are available (see for example [48]), which depend on the materials used, the time and spatial scales of the plasma; but also on more "down to earth" considerations like the available space in the experimental chamber or even the money available to perform the experiments. One of the oldest method used to measure the temperature of a plasma comes from Jahoda, in 1960 [49] where he used, assuming bremsstrahlung dominant radiations, the ratio of X-ray luminosity passed through two different absorbents. This method was relatively inaccurate since it is known that bremsstrahlung radiations are generally dominant for very hot plasmas ($> keV$) when Jahoda was measuring plasmas with temperatures of the order of 250 eV. Now, with the availability of very detailed atomic physics codes and very accurate diagnostic tools we are able to measure plasma temperatures much more accurately. A good review on the topic of laser-produced plasmas temperatures can be found in [50] but here we briefly give some typical values reached in "astrophysically" relevant regimes.

One interesting way to characterize the plasma as a function of the laser parameters is to study the temperature as a function of the laser intensity. In figure 3.4, we present results from [51] where the electron temperature of a lucite plasma (C_5,O_2,H_8) is plotted for laser intensities ranging from I = 10^{11} W.cm^{-2} to I = 10^{14} W.cm^{-2}. The experimental results are indicated by crosses whereas the full black line indicates the theoretical relationship calculated from a stationary hydrodynamic flow model, which corresponds to a temperature proportional to $I^{4/9}$ (assuming the case of the "self-regulating" regime, see next

	Deflagration model	Self-regulating model
T_{max}	$\lambda_L^{4/3} I_L^{2/3}$	$\lambda_L^{4/3} I_L^{4/9}$
P_a	$\lambda_L^{-2/3} I_L^{2/3}$	$\lambda_L^{-2/3} I_L^{7/9}$
$\dot{m}_a$	$\lambda_L^{-4/3} I_L^{1/3}$	$\lambda_L^{-4/3} I_L^{5/9}$

Table 3.1: Scaling laws for the maximum temperature T_{max}, the ablation pressure P_a and the ablation rate $\dot{m}_a$ assuming both the deflagration model and the self-regulating model

section 3.2.5). The temperatures measured should corresponds to the maximum temperatures reached during the laser shot. In the case of the deflagration regime this temperature is the temperature at the critical density T_c. In the case of the "self-regulating" regime (assumed when drawing the full line in fig.3.4), the laser absorption has occurred on a large portion of the expansion fan and the maximum temperature should be located where the absorption is maximum. As one may expect, the electron temperature increases with the intensity with values between $\sim 80\,eV$ and $\sim 100\,eV$ for the lowest intensities ($\sim 10^{11}\,W.cm^{-2}$) and $> 300\,eV$ for intensities above $10^{13}\,W.cm^{-2}$. The important point to note here is that the dependence between the temperature and intensity is not very strong, variation of the intensity on three orders of magnitude results in temperatures values over only one order of magnitude. As explained before, this weak dependence is the result of the mediating effect of the ablated material present in front of the target. Nevertheless, with laboratory astrophysics in mind, this figure shows that in order to obtain sufficiently hot plasmas for the conductivity to be high, laser intensities above $I = 10^{11}\,W.cm^{-2}$ are well adapted.

3.2.5 Scaling laws for laser-produced plasmas parameters

We have reviewed in the previous sections all the parameters that are useful to characterize the laser-target interaction (see 3.2.3). We have also identified two limit regimes: the deflagration model and the self-regulating model. It is always useful to quantify how the plasma parameters will depends on the laser intensity and the laser wavelength. In table 3.1 we give these dependencies for the maximum temperature T_{max}, the ablation pressure P_a and the ablation rate $\dot{m}_a$ for both models. These laws are taken from [31; 32] for the deflagration model and from [52] for the self-regulating model.

It is interesting to remarks the difference in the dependence of the temperature with the laser intensity. The dependence is stronger in the case of the deflagration model because in this case the expanding fan is basically transparent and the laser energy is deposited in very localized volume close to the critical density.

3.3 Dynamics of laser-produced expanding plasmas

3.3.1 Introduction

In the previous sections, we have seen that one of the resulting features of laser-solid-plasma interaction is the generation of an expanding plasma away from the target (see schema 3.2). This plasma is the fundamental "tool" we will use to study astrophysically-relevant configurations in the following chapters. It is thus logical to pay a special attention to the problem of the characterization of hydrodynamical and thermodynami-

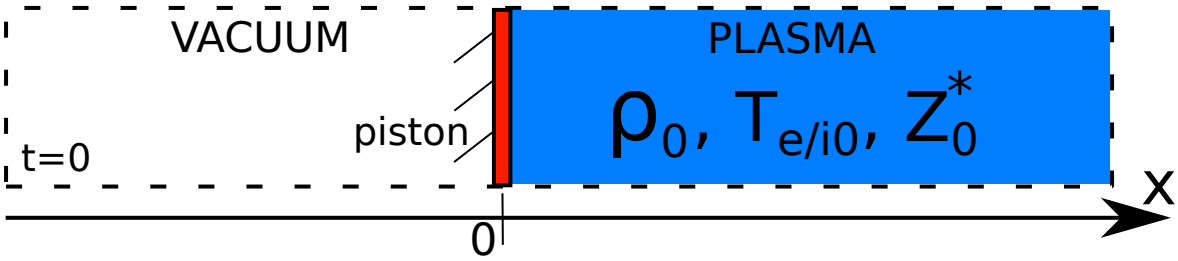

Figure 3.5: Schematic picture of initial configuration studied for the plasma expansion. The region located on the left of piston ($x < 0$) is considered to be vacuum whereas on the right ($x > 0$) we consider a infinite reservoir filled of plasma with mass density ρ_0, electron/ion temperature $T_{e/i0}$ and ionization Z_0^*. At $t = 0$, the piston is pulled back with the constant velocity U_{piston} and an rarefaction wave begins to propagate inside the reservoir.

cal quantities in such freely expanding plasmas. We will extensively use the results presented here and so we find useful, for convenience, to present the complete mathematical derivation of the two limit cases previously mentioned, namely the adiabatic expansion 3.3.2 and the isothermal expansion. In the last subsection of this chapter we will briefly describe our own preliminary attempt to use the hypersonic regime version of the fluid equations (i.e. Burger's equation for the momentum conservation) in order to describe the plasma expansion far from the target, where Mach number are high >~ 3.

3.3.2 Adiabatic self-similar 1D plasma expansion

We address here the basic underlying physics of the free expansion of a heated, laser produced plasma produced in front of the target. This expansion proceeds at high velocities compared to the initial plasma sound speed and over large distances compared to the laser focal spot diameter. We approximate the expansion as being one-dimensional, which is well justified when the laser generated plume is subject to the collimating effect of a strong, externally applied magnetic field. For more details on this aspect, we refer reader to section 5.4. The demonstration presented in this section can be found in the classical physics textbook by [53; 54]. We will, however, present the deviations from the adiabatic solutions when the effect of ionization is taken into account.

The initial state of the gas/plasma is presented schematically in fig.3.5. It consists of a semi-infinite gas/plasma contained by a piston for $x > 0$ whereas on the left side ($x < 0$), we suppose the existence of a strict vacuum ($\rho = 0$). The initial plasma reservoir is at rest. The ion and electron temperatures are allowed to evolve independently, with T_{i0} the initial ion temperature and T_{e0} electron temperature. The initial mass density is ρ_0. From these initial parameters, knowledge of a mean degree of ionization Z_0^* allows one to define the initial total pressure

$$p_0 = \frac{\rho_{i0}}{m_i} k_B (T_{i0} + Z_0^* T_{e0}) \tag{3.9}$$

where ρ_{i0} is ion mass density which, because of the smallness of the electron-proton mass ratio, can be considered to be approximately equal to the total mass density, $\rho_{i0} \approx \rho_0$. The other symbols are the ion mass $m_i = A_i m_p$, the nucleon number A_i and the proton mass m_p. From the pressure p_0 and the density ρ_0 we can then retrieve the initial sound speed:

$$c_0 = \sqrt{\frac{\gamma p_0}{\rho_0}} \tag{3.10}$$

where γ is the adiabatic index (i.e. the ratio of the heat capacity at constant pressure to heat capacity at constant volume.

At $t = 0$, the piston moves to the left with the constant velocity U_{piston}. Here we assume that the piston acquires its speed instantly at $t = 0$. The starting point is to write the MHD equations which, in the absence of magnetic field, reduce to the compressible and adiabatic hydrodynamic equations:

$$\frac{\partial \rho}{\partial t} + \nabla \cdot (\rho \mathbf{u}) = 0 \tag{3.11}$$

$$\rho \frac{\partial \mathbf{u}}{\partial t} + \rho(\mathbf{u} \cdot \nabla)\mathbf{u} = -\nabla p \tag{3.12}$$

$$\frac{dS_{spe}}{dt} = \frac{\partial S_{spe}}{\partial t} + (\mathbf{u} \cdot \nabla)S_{spe} = 0 \tag{3.13}$$

where ρ is the mass density, $\mathbf{u}$ the fluid velocity, $p = p_e + p_i$ the total pressure (electronic + ionic) and $S_{spe} = S_{spe,e} + S_{spe,i}$ the total (electronic + ionic) specific entropy. We should point out that, when taken separately, each species of the plasma can undergo non-adiabatic processes through heat exchanges with the other species, but for the whole plasma all processes are adiabatic, the model does not include effects such as radiative cooling or thermal conduction for example. In the following, we will consider the one-dimensional form of this system of equations. Without loss of generality we take x-direction and we note $u_x(x, t) = u(x, t)$.

Now, from the initial conditions represented in fig.3.5, and from the set of equations, one can clearly see that there exist no characteristic times or distances in this problem. However it exists instead a characteristic speed, the initial sound speed velocity, which suggests that the general solution can only depend on a combination of the time t and space x variables. Such combination, $\xi = x/t$, is called the self-similar variable, and we refer to [53; 54] for a detailed discussion about this point. With this definition, and with the aid of the relations:

$$\frac{\partial}{\partial x} = \frac{1}{t}\frac{d}{d\xi} \tag{3.14}$$

$$\frac{\partial}{\partial t} = -\frac{\xi}{t}\frac{d}{d\xi} \tag{3.15}$$

the system of equations refmassConservFreeExp, 3.12, 3.13) can be expressed entirely in terms of the variable ξ. The hydrodynamic system then takes the form:

$$(u(\xi) - \xi)\frac{d\rho(\xi)}{d\xi} + \rho(\xi)\frac{du(\xi)}{d\xi} = 0 \tag{3.16}$$

$$(u(\xi) - \xi)\frac{du(\xi)}{d\xi} + \frac{1}{\rho(\xi)}\frac{dp(\xi)}{d\xi} = 0 \tag{3.17}$$

$$(u(\xi) - \xi)\frac{dS_{spe}(\xi)}{d\xi} = 0 \tag{3.18}$$

First of all, from equation 3.18 we see that on possible solution of the system could be $u = \xi$. However from equation 3.16, this would imply that $du/d\xi$=0 (since $\rho \neq 0$) and that

$u(\xi) = cste \neq \xi$, which is inconsistent with the initial assumed solution. Therefore, for the specific entropy the correct solution is:

$$\frac{dS_{spe}}{d\xi} = 0 \tag{3.19}$$

which is just the consequence of the adiabatic condition expressed in terms of the self-similar variable ξ.
To proceed further, we can rewrite the momentum equation 3.17 using the fact that a change of pressure inside a fluid element is related, through the sound speed c, to a change of density by

$$dp = c^2 d\rho \tag{3.20}$$

Then

$$\frac{dp}{d\xi} = c^2 \frac{d\rho}{d\xi} \tag{3.21}$$

and inserting this expression in 3.17, we get:

$$(u-\xi)\frac{du}{d\xi} + \frac{c^2}{\rho}\frac{d\rho}{d\xi} = 0 \tag{3.22}$$

Combining 3.16 and 3.22 we retrieve the important relation:

$$c^2 = (u-\xi)^2 \tag{3.23}$$

where two solutions are possible, namely $\xi = u \pm c$. Here we choose:

$$\xi = u + c \tag{3.24}$$

and we will justify later the reasons for this choice. Inserting eq. 3.24 in the mass conservation equation 3.16 allows to make ξ disappear explicitly and to get a equation expressed only in terms of the hydrodynamic/thermodynamic quantities u, ρ and c:

$$c d\rho = \rho du \tag{3.25}$$

where we used the fact that all the quantities depend only on the variable ξ. We can now integrate 3.25 with respect to the density (or the pressure using 3.20:

$$u = \int \frac{c}{\rho} d\rho = \int \frac{1}{\rho c} dp \tag{3.26}$$

This last expression, when solved, gives the complete solution for the free expansion, the steps being: (i) from thermodynamics express $c(\rho)$; (ii) find the velocity u as a function of ρ or c with 3.26; (iii) using 3.24 reintroduce the spatial and temporal dependence (through ξ); (iv) the pressure, the temperature, etc. can then all be expressed as functions of (x,t)

We now derive some basic properties of the solution. The spatial partial derivative can be expressed a density derivative: $\partial/\partial x = (\partial\rho/\partial x) d/d\rho$ and thus, deriving 3.24 with respect to x, we get:

$$t\frac{\partial\rho}{\partial x}\frac{d(u+c)}{d\rho} = 1 \tag{3.27}$$

Using 3.25 and remembering that $dc/d\rho > 0$ in a adiabatic plasma, we arrive at the inequality :

$$\frac{d(u+c)}{d\rho} = \frac{c}{\rho} + \frac{dc}{d\rho} > 0 \tag{3.28}$$

Then, for $t > 0$, we have necessarily that the density gradient is positive :

$$\frac{\partial \rho}{\partial x} > 0 \tag{3.29}$$

A similar constraint on the solution can be found for the velocity u by using the well known relation between pressure and density for an adiabatic plasma:

$$p = K\rho^{\gamma} \tag{3.30}$$

where K is a constant, we have that

$$\partial p/\partial t = c^2 \partial \rho/\partial t \tag{3.31}$$

Coupled with $dp/dt = c^2 d\rho/dt$ (lagrangian derivatives), we find:

$$\frac{\partial p}{\partial x} = c^2 \frac{\partial \rho}{\partial x} > 0 \tag{3.32}$$

and finally, it can be shown that:

$$\frac{\partial u}{\partial x} = \frac{c}{\rho}\frac{\partial \rho}{\partial x} > 0 \tag{3.33}$$

Next, to see the nature of the solution, we can rewrite the fluid equations for mass and momentum conservation 3.11, 3.12 in the Lagrangian form (and 1D):

$$\frac{d\rho}{dt} = -\rho \frac{\partial u}{\partial x} \tag{3.34}$$

$$\frac{du}{dt} = -\frac{1}{\rho}\frac{\partial p}{\partial x} \tag{3.35}$$

thus, with 3.32 and 3.33, we see directly that we must have $d\rho/dt < 0$ and $du/dt < 0$. The first inequality means that as time progresses, the fluid particles experience a decrease of their density, that is a rarefaction process. The second inequality concerning the velocity has to be interpreted carefully, since if u is negative the absolute fluid particle speed actually increases, as one would expect for an expansion in "vacuum".

Now let's develop the entire solution for the case of a perfect adiabatic gas. As mentioned earlier, the first step is to solve 3.26. For such a gas, using 3.30 and $c^2 = \gamma p/\rho$, we can write the mass density as a function of the sound speed c and the initial mass density ρ_0 and sound speed c_0:

$$\rho = \rho_0 \left(\frac{c}{c_0}\right)^{2/\gamma - 1} \tag{3.36}$$

by differentiating this relation, we can retrieve the expression for the mass density variation as a function of the sound speed variation:

$$d\rho = \frac{2}{\gamma - 1}\frac{\rho}{c} dc \tag{3.37}$$

inserting this last expression in 3.26, we get:

$$u(c) = \frac{2}{\gamma - 1}\int dc = \frac{2}{\gamma - 1}(c - c_0) \tag{3.38}$$

Using the fact that $u < 0$ (because, as previously seen, $du/dt < 0$ and initially $u(x, t = 0) = 0$), we can thus express the sound speed of the gas as a function of the absolute velocity $|u|$:

$$c = c_0 - \frac{\gamma - 1}{2}|u| \tag{3.39}$$

since the sound speed of a gas has to be positive, this last relation can be used to retrieve the maximum velocity reached by the expanding gas. Indeed, by setting $c = 0$, the maximum speed $|u_{max}|$ is found to be:

$$|u_{max}| = \frac{2}{\gamma - 1}c_0 \tag{3.40}$$

and if $\gamma = 5/3$, we have $|u_{max}| = 3c_0$, a well-known result which we will frequently use when describing our laser-produced plasmas expanding in vacuum. Now, from 3.36 we can express the density as a function of $|u|$:

$$\rho = \rho_0\left(1 - \frac{\gamma - 1}{2}\frac{|u|}{c_0}\right)^{2/\gamma - 1} \tag{3.41}$$

The plasma total pressure 3.30 can be equivalently expressed as $p = p_0(\frac{\rho}{\rho_0})^\gamma$ and thus, inserting 3.41:

$$p = p_0\left(1 - \frac{\gamma - 1}{2}\frac{|u|}{c_0}\right)^{2\gamma/\gamma - 1} \tag{3.42}$$

For a perfect gas, the pressure can be expressed as:

$$p = \rho\frac{k_B}{m_i}(T_i + Z^* T_e) \tag{3.43}$$

so the modified temperature $T_i + Z^* T_e$ is given by:

$$T_i + Z^* T_e = (T_{i0} + Z_0^* T_{e0})\left(1 - \frac{\gamma - 1}{2}\frac{|u|}{c_0}\right)^2 \tag{3.44}$$

The final step to obtain the complete solution in the (x, t) space can be obtained using the fundamental relation 3.24. Indeed, inserting 3.39 in this relation, we get the value of the absolute velocity as a function of x and t:

$$|u| = \frac{2}{\gamma + 1}\left(c_0 - \frac{x}{t}\right) \tag{3.45}$$

As one can see, with relation 3.45, all the hydrodynamic variables can be expressed as functions of x and t as well as initial parameters ρ_0, T_{i0}, T_{e0}, Z_0^*, p_0 and c_0.

As we have seen in equation 3.40, the maximum expansion velocity is a factor of order unity larger than the initial sound speed. To understand the origin of this limitation, we can insert 3.40 in the density solution 3.41 and we get $\rho(|u| = |u_{max}|) = 0$. It means that because the gas experiences a rarefaction, the fluid particles, when reaching the maximum velocity $|u_{max}|$, become sufficiently "diluted" to be similar to vacuum in terms of their

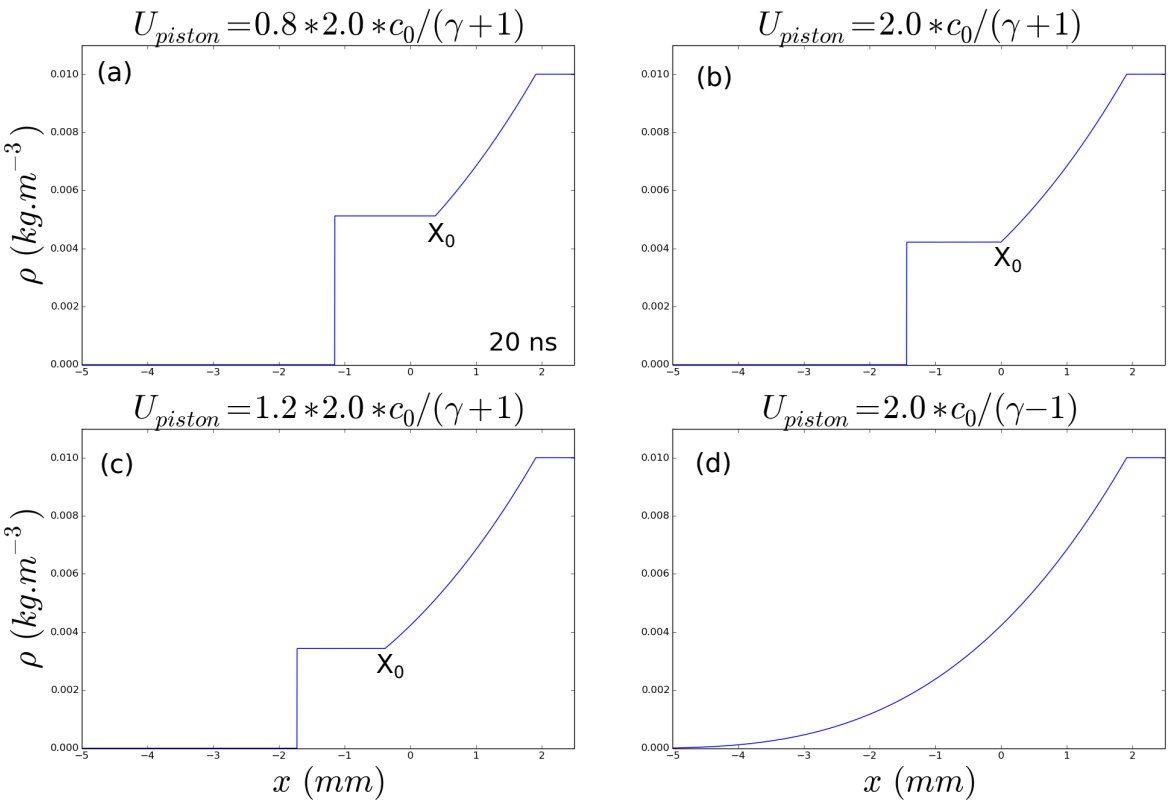

Figure 3.6: Graphs of the mass density at a given time ($t = 20\,ns$) computed using eq.3.41 with four different piston velocity: (a) in this case the piston goes sufficiently slowly such that the characteristic point X_0 (from where the fluid velocity equals the piston velocity) is "pushed" on the right, inside the reservoir. (b) Here the piston has exactly the velocity ($2c_0/(\gamma+1)$) at which the point X_0 is stationary and stay at the initial position of the piston (i.e. $x = 0$). (c) Here the piston goes slightly faster than in the previous case and thus the point X_0 is also pulled back. (c) In the extreme case where the piston has an velocity greater of equal to the maximum adiabatic velocity $|u_{max}| = 2c_0/(\gamma-1)$ then the plasma behaves exactly as if the the piston was absent: this situation is equivalent to a vacuum expansion.

thermodynamic properties.

We now show an example of the solution derived for the adiabatic expansion. In fig.3.6 we plot the density profile for four different piston velocities, 20 ns after the piston was set into motion. The initial reservoir of plasma has the following parameters: $\rho_0 = 10^{-2}\,kg.m^{-3}$ and $T_{e0} = T_{i0} = 100\,eV$ (values corresponding to typical laser-produced plasmas). In our derivation of the different quantities for the adiabatic expansion, we did not have to consider the role of the piston but it is obvious that its presence will impose boundary conditions to the flow. Indeed, if the piston goes slower than the maximum theoretical speed $|u_{max}|$ (3.40) then it will "force" the fluid to acquire, at most, its own velocity U_{piston} (< 0). This velocity is associated to a unique density determined by injecting U_{piston} in 3.41. It means that once a fluid particle reaches this velocity, it keeps a constant value of density (and temperature) and just propagates following the piston. The result is the formation of a uniform slab of plasma behind the piston, clearly seen in the three first images in fig.3.6. Thus, the solution derived previously is valid in a region $x \in [X_0, +\infty]$ whereas for $x \in [U_{piston}t, X_0]$ the density, the velocity and the temperature are constant (it can be seen that such constant quantities are solution of the system of equations 3.16, 3.17 and 3.18). The position X_0 is the point where the absolute velocity of the fluid is equal to the absolute velocity of the piston. Using relation 3.45 to express this equality, we find:

$$X_0 = \left(c_0 - \frac{\gamma+1}{2}|U_{piston}|\right)t \tag{3.46}$$

one can see that if $|U_{piston}| = 2c_0/(\gamma+1)$, we find $X_0 = 0$, that is, the transition point does not move and stay at the initial piston position ($x = 0$). This case is represented in fig.3.6(b). If $|U_{piston}| < 2c_0/(\gamma+1)$ then the transition point move on the right, toward the reservoir (fig.3.6(a)) whereas if $|U_{piston}| > 2c_0/(\gamma+1)$ the transition point move on the left, going away from the reservoir (fig.3.6(c)). Now if the the piston is going so fast that the plasma can't "follow" and adapt itself to its motion, then it is exactly as if the piston was completely removed at $t = 0$. The threshold velocity from which the piston have no effect on the rarefaction wave is obviously the maximum speed $|u_{max}|$ defined above (3.40). This case (shown in fig.3.6(d)) corresponds thus to a free vacuum expansion.

GORGON simulations of plasma vacuum expansions, comparison with the theory

We present here comparisons between the adiabatic self-similar expansion theory presented in the previous section and simulations performed using our GORGON code (disabling all dissipative processes). The results for the density, velocity, temperature and pressure profiles are shown in fig.3.7 with the GORGON results represented with full lines and theoretical predictions with dashed lines. The initial plasma is initialized as follow: $\rho_0 = 10^{-2}\,kg.m^{-3}$ and $T_{e0} = T_{i0} = 100\,eV$ for the red and green lines and $\rho_0 = 10^{-2}\,kg.m^{-3}$, $T_{i0} = 100\,eV$ and $T_{e0} = 0\,eV$ for the blue line. In this case we remove completely the piston from our study and thus we look at the case of vacuum expansions. The difference between the green and the red full lines is that energy going into ionization is neglected for the later. It can be seen that for all three cases the numerical results correspond very well to the model, up to the "head" of the expansion. First we see that, even without having ionization energy taken into account (red and blue lines), a "bump" of density, temperature and pressure appears in this region. The velocity profile is flattened near the head. These are effects resulting from the interaction of our expanding plasma with the "numerical vacuum". Indeed, at the interface, jump relations are not well respected and the

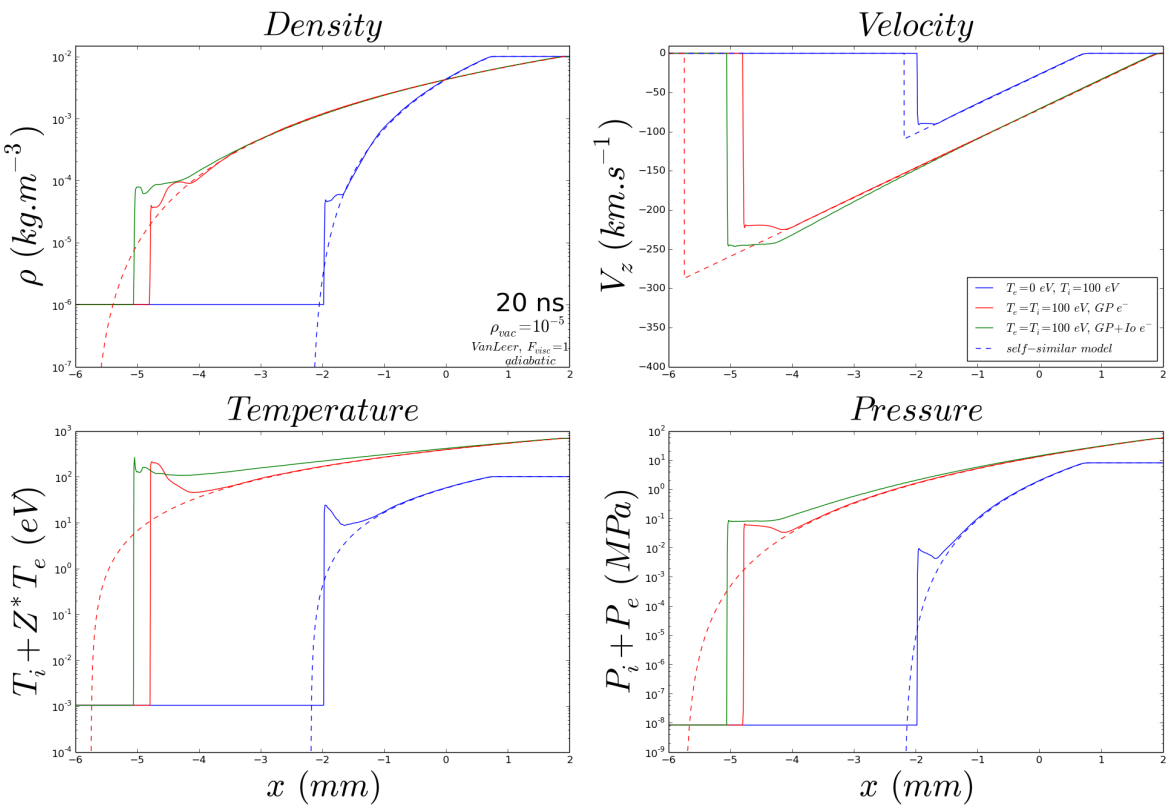

Figure 3.7: Profiles of mass density, velocity, "temperature" and pressure for: (blue) a $T_i = 100\,eV$ plasma with cold electrons ($T_e = 0\,eV$ and no electron-ion energy exchange), (red) a $T_i = T_e = 100\,eV$ plasma with electrons treated as being a perfect gas (no energy going in ionization) and (green) a $T_i = T_e = 100\,eV$ plasma with the ionization energy taken into account in the electron energy.

result is the generation of a strong numerical heating which can be clearly seen in the profiles of temperature. In fact, these peaks are due to the velocity of the plasma/vacuum interface being slightly smaller than the plasma velocity. This gradient generates a compression that is "picked up" by the artificial viscosity, and which then leads to the preferential heating up the ions.

If we now look at the case where the ionization energy is taken into consideration (green line), we see that these features are even more amplified. The most remarkable change concerns the profile of temperature where it can be clearly seen that the green curve is detaching itself from the red ones. In fact this comes from a physical process that is not included in the self-similar adiabatic theory described in the previous section: as the gas expands it cools down but at the same time, the initial energy stocked in the ionization is released in the electronic population increasing thus substantially the plasma temperature. As a consequence, the expansion is "feeded" by this surplus of energy and can reach higher velocities.

3.3.3 Isothermal self-similar 1D plasma expansion

In the previous section we have derived the solution for the adiabatic expansion and explained several features of this limiting case, which is valid when dissipative processes are negligible, such as radiation losses and thermal conduction. On the the other extreme, when thermal conduction is sufficiently strong in the plasma plume, one may consider that it will result in a isothermal expansion fan. In fact, the isothermal assumption is often used in models, at least during the laser pulse duration [27; 29]. This is the case for example, for the deflagration model, where the laser energy is supposed to be deposited almost entirely at the critical density (see 3.2.3). The "engine" of the isothermal expansion in this case is given by the fact that a portion of the laser energy "feeds" the heat flux that must enter in the expansion region at the critical surface (see 3.2) in order to sustain it. It can be shown that this heat flux must be equal to $\rho_c c_0^2$ where ρ_c is the critical mass density and c_0 the sound speed of the isothermal expansion fan [29]. At times greater than the pulse duration, one expects the heat source to become vanishingly small and thus the expansion be much closer to adiabatic conditions.

The solution for the isothermal expansion is actually simpler than the one derived in the previous section. We search again for self-similar solutions for the self-similar variable $\xi = x/t$. The mass and momentum equations are unchanged (3.16 and 3.12) but now the flow is not isentropic. Heat is exchanged during the expansion and equation 3.13 is not valid any longer. As for the adiabatic case we arrive at the equivalent of the momentum equation 3.22:

$$(u-\xi)\frac{du}{d\xi} + \frac{c_0^2}{\rho}\frac{d\rho}{d\xi} = 0 \tag{3.47}$$

however we have now used the relation for the isothermal case:

$$dp = c_0^2 d\rho \tag{3.48}$$

The only difference with 3.22 is that in the present case the sound speed is constant. By combining the mass and momentum equations, we retrieve the relation which link the velocity to the self-similar variable ξ:

$$\xi = u + c_0 \tag{3.49}$$

knowing that $u < 0$. Then, inserting 3.47 in the mass conservation equation 3.16 we find:

$$du = c_0 \frac{d\rho}{\rho} \tag{3.50}$$

The relation 3.50 is actually much simpler than the one for the adiabatic flow (3.25) because here the sound speed is a constant. We just have to integrate this expression to retrieve the velocity:

$$u = c_0 \int \frac{d\rho}{\rho} = c_0 ln(\rho) - c_0 ln(\rho_0) \tag{3.51}$$

where we have used, to find the integration constant, the fact that the velocity is null when the mass density is equal to the initial mass density ρ_0. The reason is being that in this case the rarefaction wave has not yet passed. From 3.51 the solution for the density is simply:

$$\rho = \rho_0 exp\left(\frac{u}{c_0}\right) \tag{3.52}$$

and by inserting the expression for the velocity as function of $\xi = x/t$ (from 3.49):

$$u(x,t) = c_0 \left(\frac{x - c_0 t}{c_0 t}\right) \tag{3.53}$$

we get:

$$\rho(x,t) = \rho_0 exp\left(\frac{x - c_0 t}{c_0 t}\right) \tag{3.54}$$

It can be seen from these solutions that the front of the rarefaction wave (the point where $u = 0$) is propagating at the reservoir sound speed c_0 (as in the case of the adiabatic expansion) and that the density profile decreases exponentially in the isothermal situation. The sonic point (where $u = -c_0$) is always located at $x = 0$ (as in the adiabatic case). However, an important difference with the adiabatic case is that it is not longer possible to derive a maximum velocity of expansion in the isothermal case. This is a consequence of constant sound speed velocity. In the adiabatic case the limit speed was obtained by saying that the local sound speed must be greater than zero. Here, since the isothermal sound speed never goes to zero in the expansion, such argument cannot be made.

3.3.4 A new potential 1D description of laser-produced plasmas expanding at supersonic/hypersonic speeds

We present in this section some preliminary work trying to provide an analytical description of the region of laser-produced plasmas expanding at high Mach number. We warn the reader that this work is very much on-going and it is not yet clear if it is at all relevant to laser produced plasmas. We first present the motivation and the inspiration for the work and finally the model.

Motivation

In section 3.3.2 we presented the "free-reservoir" 1D expansion model. Even if we explained that it should corresponds relatively well to the expansion of laser-produced plasmas, the direct comparison given in 5.4 shows that some deviations with the numerical solution are still present. Among them the modification "by hand" of the initial temperature (i.e. sound speed c_0) is the most worrisome. Such modification was necessary to obtain an agreement of the maximum expansion velocity $|u_{max}|$ (see 3.40) with the numerical simulations. A fact also seen experimentally [55].
As explained, the initial pressure gradients due to the laser deposition are not taken into account in the free-reservoir model and could thus represent a supplementary acceleration leading to velocities greater than the free-reservoir maximum speed. The generation of gradients in the initial plasma reservoir introduces a characteristic length in the problem and thus the self-similar description realized in 3.3.2 is not possible and not analytical expressions for the hydrodynamic variables are available. A large number of experimental papers have reported values of maximum velocities usually between $2-3$ [55] times the free-reservoir adiabatic value $|u_{max}|$ and similarly a large number of theoretical papers have tried to explain this deviation, for example using ionization effects (see our discussion in the previous section). In the model we present here, we are not going to solve this specific problem but instead we want to propose an alternative description for the plasma density and velocity profiles "far" from the target location. We specify "far" because our model will be valid only for flows with high Mach numbers and thus it corresponds generally to plasma regions few millimeters away from the target. The maximum velocity in this model will be considered as an input parameter.

Inspiration

The idea came during a lecture from Alex Raga about the propagation of supersonic jets and more specifically about the time-dependent evolution of highly supersonic jets where the source of these jets is also time-dependent. The work from A.Raga on this topic can be found in [56]. The idea was to explain the presence of more or less regularly spaced bright "knots" observed inside extragalactic and stellar jets. As we explain in (see 4.3), one possibility to explain these knots is the well known structure in shock diamonds observed in supersonic jets propagating in an external gas. The other possibility, introduced first by Rees [57], is that the knots are the results of a time-variability in the outflow source which induces the formation of shock waves traveling along the jets. These shock waves would produce the bright knots through heating and compression of the gas in positions determined by the shape of the curve describing the outflow ejection rate. Kofman and Raga, in an unpublished work, first studied in 1991 the case where the density flow is constant at the source but the velocity is not. Shortly after, in the previously mentioned paper [56], extended their analytical formalism to the case of a variable density flow. The idea of applying this model to the magnetically collimated expansion of laser-produced plasmas is quite straightforward since strong analogies are present. First, as we shall see in the dedicated chapter (5), the addition of a sufficiently strong magnetic field in laser-produced plasmas experiment results in the formation of highly collimated jets along the magnetic field. Thus, in this configuration, the expansion is along the magnetic field direction and sufficiently far from the target surface to be considered 1D, as required by the Raga model. We note that the model allows to take into account the effect of a finite jet radius. Secondly, the laboratory jets are highly supersonic with Mach numbers which can reach potentially values larger than 1000 in the case of an adiabatic jet (in fact, the Mach

number tends toward infinity at the jet head since there the sound speed tends toward zero). This point concerning the presence of high Mach numbers regions in the laser-produced expanding plasma is fundamental in order to apply the Raga model. Finally, the source producing the plasma jet in our experiments is the laser pulse which is of finite duration and thus represents a variable density and velocity flow, as supposed in the astrophysical case of the Raga paper.

The model

The 1D model developed in the Raga papers describes a solution, called the "free-streaming solution", valid only in highly supersonic regimes, i.e. such that $M = u/c >> 1$ (u is the fluid velocity and c the local sound speed). In this case, the momentum equation 3.12 $\rho du/dt = -\partial_x p$ can be simplified. Indeed, the ratio of the convective term in the Lagrangian derivatives ($\rho u \partial_x u$) on the pressure force can be estimated by:

$$\frac{|\rho u \partial_x u|}{|\partial_x p|} \sim \frac{\rho u^2}{p} \sim \frac{\rho u^2}{\rho c^2} = M^2 \tag{3.55}$$

Thus we see that for high Mach numbers, generally hypersonic ($M \gtrsim 5$), the pressure term in the momentum can be neglected. Interestingly, the ratio being proportional to the square of M, one can expect the model to hold reasonably well even for flows that are "only" in the supersonic regimes. So, for $M \gg 1$, we can write:

$$\frac{du}{dt} = \frac{\partial u}{\partial t} + u\frac{\partial u}{\partial x} = 0 \tag{3.56}$$

Equation 3.56 is sometimes called the pressureless Euler equation or, in applied mathematics, the inviscid Burgers' equation [58]. This equation means that a fluid particle ejected from a "source" S at a time τ with a velocity $u_0(\tau)$ will preserve this velocity as it moves away from the source. We can say in a way that the fluid particles are following a Lagrangian ballistic trajectory. The solution of 3.56 for the velocity field is the free-streaming solution and is given by the equation:

$$u(x,t,\tau) = u_0(\tau) = \frac{x - x_s}{t - \tau} \tag{3.57}$$

where x_s is the position of the source S, where the fluid particles are injected with the velocity $u_0(\tau)$ at $t = \tau$, We have assumed that $x > x_s$ and $t > \tau$. Interestingly, as we will see in the chapter dedicated to the propagation of the laboratory supersonic jets (5.4.1), a very good approximation for the velocity profile was found to be x/t. From equation 3.57, we see that it corresponds to the "free-streaming" solution for $t >> \tau$ and $x >> x_s$. In other words, it corresponds to the free-streaming solution when we are looking at late times, compared to laser pulse duration τ_{laser}, and at large distances compared to the accelerating region, which is of the order of $\tau_{laser} c_0$, where c_0 is the initial characteristic sound speed.

Then, concerning the continuity equation 3.11, if we assume for simplicity that the jet has a cross section along its main axis x given by:

$$\sigma(x) = \sigma_0 \left(\frac{x_0}{x + x_0}\right)^p \tag{3.58}$$

where σ_0 is the jet cross section at the source point, p the power that describes the opening angle of the jet and x_0 a constant. Raga showed that the general solution for the density is then determined by:

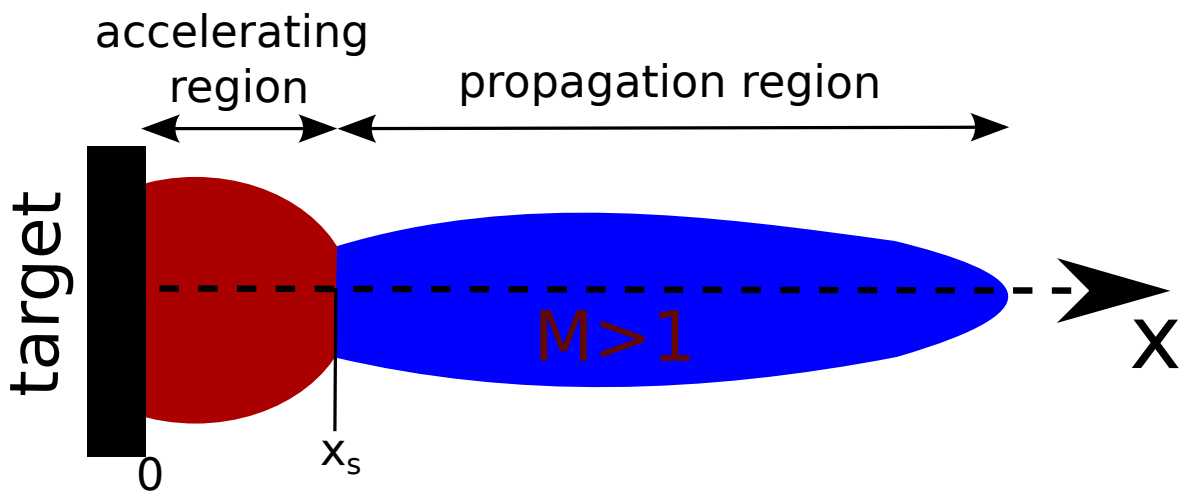

Figure 3.8: Schematic (and very simplified) representation of a laser-produced plasma expanding in front of a solid target (black). We consider two main regions: an accelerating region (in red) where the pressure forces are still important and fluid particles are being accelerated (subsonic flow or weakly supersonic). The second region can be called the "propagation region" (in blue) and is composed of plasma in hypersonic regimes (M $\gtrsim$ 4) where the fluid particles behave as ballistic particles. The two regions are delimited by the important point called x_s which, as shown in the main text, does not correspond to the sonic point (where M = 1)

$$\rho(x,t,\tau) = \rho_0(\tau)\left(\frac{x_0}{x+x_0}\right)^p \left[1-(t-\tau)\frac{d\,ln(u_0)}{d\tau}\right]^{-1} \tag{3.59}$$

This equation introduces a new "input" function, $\rho_0(\tau)$, which corresponds to the mass density of the fluid particle injected at $x = x_s$ and $t = \tau$ with the velocity $u_0(\tau)$.

As one can see, when using the model described here, we need an initial knowledge (as "inputs") of three functions: $\rho_0(\tau)$, $u_0(\tau)$ and $\sigma(x)$. Each function involves several parameters which characterize the physical process "propelling" the supersonic jet at the source S. For an astrophysical system, the density or velocity injected can be, for example, a sinusoidal function involving a star rotation period. For a laser, these functions involve quantities such as the pulse duration τ_{laser}, the pulse intensity I_{laser} or any other parameter related to the laser-solid-plasma interaction. Here lies the real difficulty of applying this model to the laser-produced plasma expansion (and the difficulty is actually the same for astrophysical jets).

Before attempting to derive a solution, we must detail the configuration we consider for our laser-produced plasma. As explained in section 3.2, once the vaporized gas in front of the solid target begin to absorb significantly the laser energy (the "breakdown"), the heated gas starts to expand converting its thermal energy into bulk kinetic energy: here we will suppose that this conversion occurs in what we call the "accelerating region" with a length x_s (from $x = 0$, the target surface position, to $x = x_s$). This region is represented in red in fig.3.8. Just after the accelerating region comes what could be called the "propagating region" or the "inertial region". This region is represented in blue in fig.3.8. In this region, the acceleration of fluid particles is basically negligible because the Mach numbers are sufficiently large (M $\gtrsim$ 3). It is in this region that equation 3.56 is valid and thus that solutions 3.57 for the velocity and 3.59 for the density are applicable.

We now derive a possible solution for the problem pictured in fig.3.8. The general method is to first "guess" the injected velocity function $u_0(\tau)$ in order solve equation 3.57 by finding the expression of $\tau(x,t)$. One has to be very careful when realizing this step since, depending on the form of $u_0(\tau)$, the function $\tau(x,t)$ can be multi-valued. Indeed, finding this function means that we want to known, for a given point x at a given time t, the time τ at which the fluid particle present a this point has been ejected. For example, suppose that at $\tau = 0$, a fluid particle, named "1" has been ejected from $x = x_s$ with a velocity V_0. At a time t this particle will then be at the position $x_1 = V_0 t + x_s$. If an other fluid particle "2" with a velocity $2V_0$ is injected at a time $\tau = t/2$, it will be, at t, at the same position $x_2 = V_0 t + x_s$, i.e. $x_1 = x_2$. In this case, as we can see, it is no possible to properly define the function $\tau(x,t)$. It is nevertheless interesting that the possibility of generating multi-valued τ functions is at the basis of the Raga model for the explanation of the knots in astrophysical jets. Indeed, in fluid theory, the "accumulation" of several fluid particle at the same position (x,t) is the source of shocks and thus brightly emitting regions. More formally, it corresponds to the intersection of "characteristics" of the fluid equations, see [53]. In our case we are looking at a case where there is no reason for the laser-produced plasma to accelerate fluid particles at higher speeds when τ increases. As mentioned at the beginning of this section, the present work is very "embryonic" and not much work has been carried out related to the "input" functions $u_0(\tau)$ and $\rho_0(\tau)$ that would be adapted for the case of laser-produced plasmas. However, as a "proof of concept", we propose here to "join" the adiabatic solution developed in 3.3.2 and the Burger's inviscid solution taken from the Raga model. We can do that because a large portion of the flow in the adiabatic solution is hypersonic. Indeed, since in this model the expanding plasma has a sound speed which tends towards zero at the front propagation (see 3.39), there exist a whole part of the plume which has extremely high Mach numbers (> 100). The idea is then to inject this hypersonic portion of the adiabatic flow as an input in our equations 3.59 and 3.57. From the adiabatic model, we understand that the injection position x_s, from where the flow is basically propagating with negligible effect of pressure acceleration, is a crucial parameter. For example, in the adiabatic theory, the initial position of the interface between the reservoir and the vacuum ($x = 0$) is always the sonic point (M = 1) so it is clear that if we choose this point for our x_s, the free-streaming solutions (3.59 and 3.57) will certainly give a very good agreement since there the pressure forces are still non negligible. So let's keep x_s as a free parameter and we will see later how its choice influence the results. Here we consider the adiabatic solution given in section 3.3.2 for the case where the reservoir is located initially in $x \in [-\infty, 0]$ and the vacuum in $x \in [0, +\infty]$. The piston is supposed to be completely removed at $t = 0$. Thus, the input velocity for our free-streaming solution is given by (from 3.45 and 3.41):

$$u_0(\tau) = \frac{2}{\gamma+1}\left(c_0 + \frac{x_s}{\tau}\right) \tag{3.60}$$

and the input density is:

$$\rho_0(\tau) = \rho_0\left(1 - \frac{\gamma-1}{\gamma+1}\left(1 + \frac{x_s}{c_0\tau}\right)\right)^{2/(\gamma-1)} \tag{3.61}$$

where these input quantities have a meaning only once the adiabatic expanding front propagating at the velocity $|u_{max}| = 2c_0/(\gamma-1)$ is crossing the injecting point $x = x_s$. In other words, we must have $\tau \geq x_s/|u_{max}|$ and the free-streaming solution will be "available" from $t = x_s/|u_{max}|$. Then we must find the expression of $\tau(x,t)$ by solving the equation 3.57:

$$\frac{x - x_s}{t - \tau(x,t)} = \frac{2}{\gamma + 1}\left(c_0 + \frac{x_s}{\tau}\right) \tag{3.62}$$

which can be rewritten as:

$$\tau^2 + \frac{(\gamma - 1)(x - x_s) + 2x_s - 2c_0 t}{2c_0}\tau - \frac{x_s t}{c_0} = 0 \tag{3.63}$$

this equation is a simple second order equation which can be solved by first finding the delta:

$$\Delta = \frac{[(\gamma - 1)(x - x_s) + 2x_s - 2c_0 t]^2 + 16 x_s c_0 t}{4c_0^2} \tag{3.64}$$

One can see that we have $\Delta > 0$ so two solutions are possible:

$$\tau_\pm = \frac{1}{2}\left[\frac{2x_s + 2c_0 t - (\gamma - 1)(x - x_s)}{2c_0} \pm \sqrt{\Delta}\right] \tag{3.65}$$

the solution is identified simply by saying that at $x = x_s$ and $t = x_s/|u_{max}|$ we must have $\tau = x_s/|u_{max}|$. We find that the correct solution is the "+" solution:

$$\tau(x,t) = \frac{1}{2}\left[\frac{2x_s + 2c_0 t - (\gamma - 1)(x - x_s)}{2c_0} + \sqrt{\Delta}\right] \tag{3.66}$$

and finally to obtain all needed terms for the density profile 3.59 we have:

$$\frac{d\,ln(u_0(\tau))}{d\tau} = -\frac{x_s}{c_0\tau^2 + x_s\tau} \tag{3.67}$$

We have now everything to write the density profile (and the velocity profile) as a function of x and t (by inserting the expression for τ 3.66 wherever it is needed).

In fig.3.9 we plot the results for an initial plasma reservoir at $\rho_0 = 10^{-2}\,kg.m^{-3}$, $T_{e0} = T_{i0} = 300\,eV$. The corresponding sound speed is $c_0 \approx 166\,km.s^{-1}$ and the speed of the expanding front is $|u_{max}| = 2c_0/(\gamma - 1) \approx 497\,km.s^{-1}$. We plot the solution at $t = 50\,ns$ for four different injection position (where the adiabatic solution is injected in the free-streaming solution): $x_s = 1, 4, 8, 18\,mm$. One can clearly see that as the injection position is moved to the right, away from the sonic point ($x = 0$), the free-streaming solution effectively tends towards the adiabatic solution. This is because as we shift the injection point on the right, the flow which crosses this position has higher local Mach numbers and thus we are effectively in a regime such that the "complete" momentum equation 3.12 (i.e. with the pressure forces included) can be relatively well approximated by the inviscid Burger's equation 3.56. After this simple example which validates the original idea, one could argue that the free-streaming solution found is actually more complicated than the adiabatic solution but the point is that since this model needs just the two "input" density and velocity functions we don't have to make any assumptions on the equation of states, the acceleration processes, etc. The only condition being that the flow has to have high Mach numbers (in practice $M \gtrsim > 4$). The density profiles obtained from experiments are often non exactly isothermal or adiabatic and thus an interesting empirical idea would be to look for the input functions "needed" to obtain the experimental profiles in regions far from the target. This is a work that remains to be done.

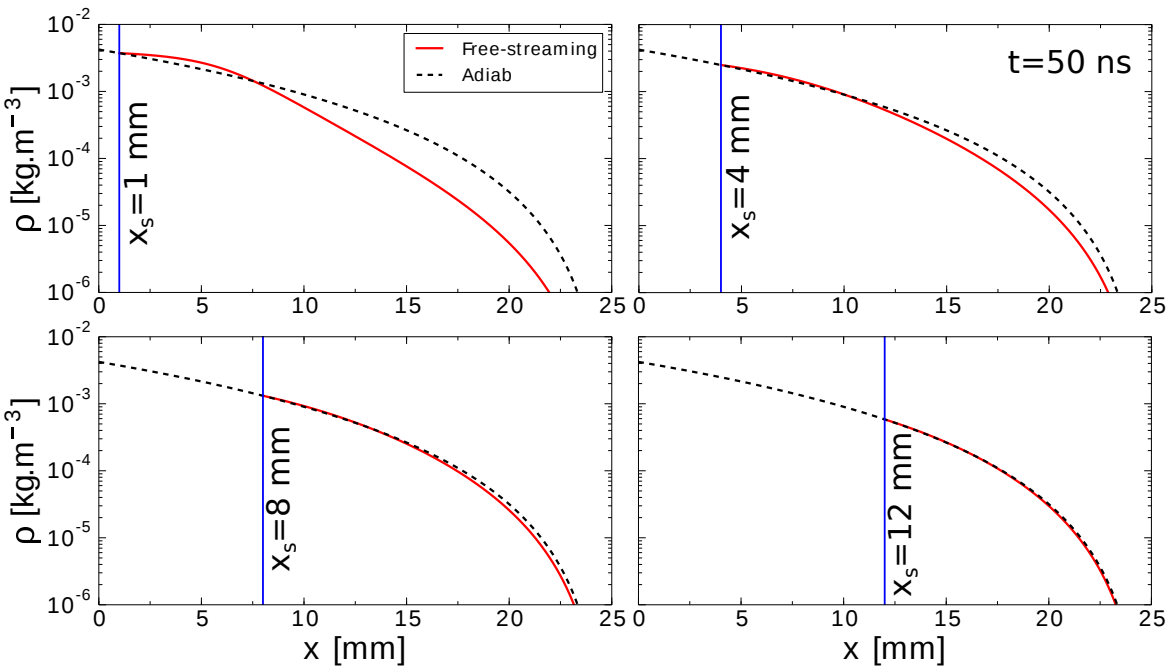

Figure 3.9: Mass density profiles (at $t = 50\,ns$) for both the adiabatic expansion (red full lines) and the free-streaming expansion proposed here (black dotted lines). The adiabatic expansion is supposed to come from the expansion of a plasma reservoir at an ion and electron temperature of 300 eV and a density of $10^{-2}\,kg.m^{-3}$. The join between the adiabatic and the free-streaming solutions is realized at the point x_s which is varied in each of the graphs presented here ($x_s = 1, 4, 8, 12\,mm$). We see that as this point is shifted away from the origin (where the adiabatic flow is sonic, i.e M = 1), the two solution converges because the fluid particles crossing this point have effectively higher Mach numbers and are so well described by the Burger's equation.

3.4 Bibliography

[1] Theodore H Maiman. Stimulated optical radiation in ruby. *nature*, 187(4736):493–494, 1960. 62

[2] Slashme. "graph showing the history of maximum laser pulse intensity throughout the past 40 years. 2010. 62, 63, XXVII

[3] F. J. McClung and R. W. Hellwarth. Giant optical pulsations from ruby. *Journal of Applied Physics*, 33(3):828–829, 1962. 62

[4] Herman A Haus. Mode-locking of lasers. *IEEE Journal of Selected Topics in Quantum Electronics*, 6(6):1173–1185, 2000. 62

[5] CEL-V LASER RESEARCH Group. Twenty-two years of laser-matter work at centre d'etudes de limeil-valenton (cel-v). *Nuclear Fusion*, 25(9):1333, 1985. 62

[6] W.L. Kruer. *The physics of laser plasma interactions*. Addison-Wesley Pub. Co. Inc.,Reading, MA, Jan 1988. 62

[7] V.V. Blazhenkov, A.N. Kirkin, A.V. Kononov, L.P. Kotenko, A.M. Leontovich, G.I. Merzon, A.M. Mozharovsky, and S.D. Zakharov. Evidence of suprathermal electron fluxes in laser-produced plasma from the polarization and anisotropy of x-ray bremsstrahlung emission. *Optics Communications*, 34(2):231 – 234, 1980. 62, 65, 67

[8] G Malka and JL Miquel. Experimental confirmation of ponderomotive-force electrons produced by an ultrarelativistic laser pulse on a solid target. *Physical Review Letters*, 77(1):75, 1996. 62

[9] N. F. Mott and H. Jones. The theory of the properties of metals and alloys. *Dover Publications, Inc., New York*, 1958. 63

[10] Matthew S Brown, Craig B Arnold, et al. Fundamentals of laser-material interaction and application to multiscale surface modification. *Laser precision microfabrication*, 135:91–120, 2010. 63

[11] Yu. P. Raizer. Breakdown and heating of gases under the influence of a laser beam. *Phys. Usp.*, 8(5):650–673, 1966. 64

[12] L. V. Keldysh. Ionization in the field of a strong electromagnetic wave. *Soviet Physics JETP*, 20:1307–1314, May 1965. 64

[13] V. S. Popov. REVIEWS OF TOPICAL PROBLEMS: Tunnel and multiphoton ionization of atoms and ions in a strong laser field (Keldysh theory). *Physics Uspekhi*, 47:855–885, September 2004. 64

[14] Albert Gold and H. Barry Bebb. Theory of multiphoton ionization. *Phys. Rev. Lett.*, 14:60–63, Jan 1965. 64

[15] Friedrich Paschen. Ueber die zum funkenübergang in luft, wasserstoff und kohlensäure bei verschiedenen drucken erforderliche potentialdifferenz. *Annalen der Physik*, 273(5):69–96, 1889. 64

[16] V. A. Volkov, F. V. Grigorev, V. V. Kalinovskii, S. B. Kormer, L. M. Lavrov, I. V. Maslov, V. D. Urlin, and V. P. Chudinov. Dependence of threshold for air breakdown by a focused laser beam on the geometry of the focal region. *Zhurnal Eksperimentalnoi i Teoreticheskoi Fiziki*, 69:115–121, July 1975. 64

[17] Lyman Spitzer Jr. Physics of fully ionized gases. *American Journal of Physics*, 31(11):890–891, 1963. 65

[18] N. G. Basov and O. N. Krokhin. The Conditions of Plasma Heating by the Optical Generator Radiation. In I. Agarbiceanu, A. Agafitei, L. Blanaru, N. Ionescu-Pallas, I. M. Popescu, V. Vasiliu, and V. G. Velculescu, editors, *Quantum Electronics*, page 1373, 1964. 65

[19] John M Dawson. On the production of plasma by giant pulse lasers. *The Physics of Fluids*, 7(7):981–987, 1964. 65

[20] Peter Mulser and Dieter Bauer. *High power laser-matter interaction*. Springer tracts in modern physics. Springer, Berlin, 2010. 65, 66

[21] R. C. Malone, R. L. McCrory, and R. L. Morse. Indications of strongly flux-limited electron thermal conduction in laser-target experiments. *Phys. Rev. Lett.*, 34:721–724, Mar 1975. 66

[22] Lyman Spitzer and Richard Härm. Transport phenomena in a completely ionized gas. *Phys. Rev.*, 89:977–981, Mar 1953. 66

[23] R. L. Morse and C. W. Nielson. Occurrence of highenergy electrons and surface expansion in laserheated target plasmas. *The Physics of Fluids*, 16(6):909–920, 1973. 66

[24] J. P. Freidberg, R. W. Mitchell, R. L. Morse, and L. I. Rudsinski. Resonant absorption of laser light by plasma targets. *Phys. Rev. Lett.*, 28:795–799, Mar 1972. 67

[25] C. Riconda and S. Weber. Raman–brillouin interplay for inertial confinement fusion relevant laser–plasma interaction. *High Power Laser Science and Engineering*, 4, 2016. 67

[26] J.C. Couturaud, P.A. Holstein, M. Louis-Jacquet, B. Meyer, and G. Thiell. Determination of energy transport parameters in flat, layered targets irradiated by picosecond nd-laser pulses. *Nuclear Fusion*, 21(12):1657, 1981. 67

[27] G J Pert. Thermal conduction effects in laser solid target interaction. *Plasma Physics*, 16(11):1019, 1974. 67, 80

[28] W. M. Manheimer, D. G. Colombant, and J. H. Gardner. Steadystate planar ablative flow. *The Physics of Fluids*, 25(9):1644–1652, 1982. 67

[29] Remy Fabbro, Claire Max, and Edouard Fabre. Planar laserdriven ablation: Effect of inhibited electron thermal conduction. *The Physics of Fluids*, 28(5):1463–1481, 1985. 67, 80

[30] DD Ryutov, RP Drake, and BA Remington. Criteria for scaled laboratory simulations of astrophysical mhd phenomena. *The Astrophysical Journal Supplement Series*, 127(2):465, 2000. 67

[31] C. Fauquignon and F. Floux. Hydrodynamic behavior of solid deuterium under laser heating. *The Physics of Fluids*, 13(2):386–391, 1970. 67, 69, 71

[32] J. L. Bobin. Flame propagation and overdense heating in a laser created plasma. *The Physics of Fluids*, 14(11):2341–2354, 1971. 67, 69, 71

[33] J.P. Babuel-Peyrissac, C. Fauquignon, and F. Floux. Effect of powerful laser pulse on low z solid material. *Physics Letters A*, 30(5):290 – 291, 1969. 67

[34] Jean-Paul Watteau et al. Robert Dautray. *La fusion thermonucléaire inertielle par laser*. Eyrolles, 1995. 67, 69

[35] H.C. Liu, X.L. Mao, J.H. Yoo, and R.E. Russo. Early phase laser induced plasma diagnostics and mass removal during single-pulse laser ablation of silicon. *Spectrochimica Acta Part B: Atomic Spectroscopy*, 54(11):1607 – 1624, 1999. 68

[36] K. Eidmann and R. Sigel. Backscatter experiments. In H. J. Schwarz and H. Hora, editors, *Laser Interaction and Related Plasma Phenonema*, pages 667–690, 1974. 68, XXVII

[37] BH Ripin, R Decoste, SP Obenschain, SE Bodner, EA McLean, FC Young, RR Whitlock, CM Armstrong, J Grun, JA Stamper, et al. Laser-plasma interaction and ablative acceleration of thin foils at 1012–1015 w/cm2. *The Physics of Fluids*, 23(5):1012–1030, 1980. 69

[38] T.J. Goldsack, J.D. Kilkenny, B.J. MacGowan, S.A. Veats, P.F. Cunningham, C.L.S. Lewis, M.H. Key, P.T. Rumsby, and W.T. Toner. The variation of mass ablation rate with laser wavelength and target geometry. *Optics Communications*, 42(1):55 – 59, 1982. 69

[39] MH Key, WT Toner, TJ Goldsack, JD Kilkenny, SA Veats, PF Cunningham, and CLS Lewis. A study of ablation by laser irradiation of plane targets at wavelengths 1.05, 0.53, and 0.35 µm. *The Physics of fluids*, 26(7):2011–2026, 1983.

[40] P.D. Gupta, Y.Y. Tsui, R. Popil, R. Fedosejevs, and A.A. Offenberger. Energy transport in gold coated plastic targets irradiated by a krf laser. *Optics Communications*, 63(3):165 – 170, 1987.

[41] JP Anthes, MA Gusinow, and M Keith Matzen. Experimental observation and numerical simulations of laser-driven ablation. *Physical Review Letters*, 41(19):1300, 1978.

[42] 69

[43] B Ahlborn and M H Key. Scaling laws for laser driven exploding pusher targets. *Plasma Physics*, 23(5):435, 1981. 69

[44] Boye Ahlborn and Wolfgang Liese. Heat flux induced wave fronts. *The Physics of Fluids*, 24(11):1955–1966, 1981. 69

[45] H Puell et al. Heating of laser produced plasmas generated at plane solid targets i. theory. *Zeitschrift für Naturforschung A*, 25(12):1807–1815, 1970. 69

[46] A. Caruso, B. Bertotti, and P. Giupponi. Ionization and heating of solid material by means of a laser pulse. *Il Nuovo Cimento B (1965-1970)*, 45(2):176–189, Oct 1966.

[47] A Caruso and R Gratton. Some properties of the plasmas produced by irradiating light solids by laser pulses. *Plasma Physics*, 10(9):867, 1968. 69

[48] Ian H Hutchinson. Principles of plasma diagnostics. *Plasma Physics and Controlled Fusion*, 44(12):2603, 2002. 70

[49] F. C. Jahoda, E. M. Little, W. E. Quinn, G. A. Sawyer, and T. F. Stratton. Continuum radiation in the x ray and visible regions from a magnetically compressed plasma (scylla). *Phys. Rev.*, 119:843–856, Aug 1960. 70

[50] John Ready. *Effects of high-power laser radiation*. Elsevier, 2012. 70

[51] TP Donaldson, RJ Hutcheon, and MH Key. Electron temperature and ionization state in laser produced plasmas. *Journal of Physics B: Atomic and Molecular Physics*, 6(8):1525, 1973. 70, XXVII

[52] B. Meyer and G. Thiell. Experimental scaling laws for ablation parameters in plane target-laser interaction with 1.06 um and 0.35 um laser wavelengths. *Physics of Fluids*, 27:302–311, January 1984. 71

[53] Ya B Zeldovich and Yu P Raizer. Physics of shock waves and high-temperature hydrodynamic phenomena. Technical report, FOREIGN TECHNOLOGY DIV WRIGHT-PATTERSON AFB OH, 1965. 72, 73, 85

[54] L.D. Landau and E.M. Lifshitz. *Fluid Mechanics*. Number vol. 6. Elsevier Science, 2013. 72, 73

[55] K. R. Chen, T. C. King, J. H. Hes, J. N. Leboeuf, D. B. Geohegan, R. F. Wood, A. A. Puretzky, and J. M. Donato. Theory and numerical modeling of the accelerated expansion of laser-ablated materials near a solid surface. *prb*, 60:8373–8382, September 1999. 82

[56] A. C. Raga and L. Kofman. Knots in stellar jets from time-dependent sources. *ApJ*, 386:222–228, February 1992. 82

[57] M. J. Rees. The M87 jet - Internal shocks in a plasma beam. *mnras*, 184:61P–65P, September 1978. 82

[58] Johannes Martinus Burgers. A mathematical model illustrating the theory of turbulence. *Advances in applied mechanics*, 1:171–199, 1948. 83

Chapter 4

Physics of supersonic jets and shocks

Sommaire

4.1 Introduction **94**

4.2 A little bit of history about supersonic jets and shocks **94**

4.3 The propagation of unmagnetized supersonic jets in an external background **97**

4.4 Stability of unmagnetized supersonic jets **100**

4.5 GORGON simulations of supersonic jets **103**

4.5.1 General description of a pressure-matched supersonic jet 103

4.5.2 Effects of the Mach number on jet propagation 109

4.5.3 Influence of an axial magnetic field on the dynamic of a supersonic jet 111

4.5.4 Supersonic jets propagating in a magnetized vacuum 115

4.6 Bibliography **116**

4.1 Introduction

We now turn to a chapter which will serve as an opening discussion about one of the main topic treated in this manuscript: the generation, the propagation and the structure of supersonic jets. In our case we will present, in the next chapter, an in-depth study of laboratory jets produced through the interaction of a laser-produced plasma with an external strong magnetic field. This work we will present find its foundations in more than a century of research on both laboratory and astrophysical supersonic jets. Therefore, in the present chapter, we will first present a small historical introduction (4.2) and then we will present general considerations on the structure 4.3 and stability (4.4) of supersonic jets propagating in mediums. Finally we present idealized numerical studies of supersonic jets using our GORGON code (4.5) to, step by step, introduces the effect of a magnetic field on the propagation of such jets. The general discussion presented in this chapter provide a physical physical basis so that results presented in the next chapter can be better understood.

4.2 A little bit of history about supersonic jets and shocks

The physics of supersonic jets is a topic closely related to the concept of shock waves. Back in the 1880s, physicist like Riemann, Rankine, Rayleigh and Hugoniot were still debating on the theoretical properties of these nonlinear compression waves [1]. One of the main question that was discussed concerned the quantities that must be conserved across the surface of a discontinuity created by a shock front. The question was mainly about whether it is the energy or the entropy that is conserved across a shock. In 1864, Riemann was the first to analyze wave-steepening within the context of ideal gas dynamics but he mistakenly assumed that entropy must be conserved [2]. Later, Rankine, Rayleigh and Hugoniot showed that an adiabatic shock front would violate conservation of energy and therefore demonstrated that shock fronts must be non-adiabatic and irreversible [1]. Now we all know the famous Rankine-Hugoniot relations describing the change of density, velocity and energy across the surface of a discontinuity [3].

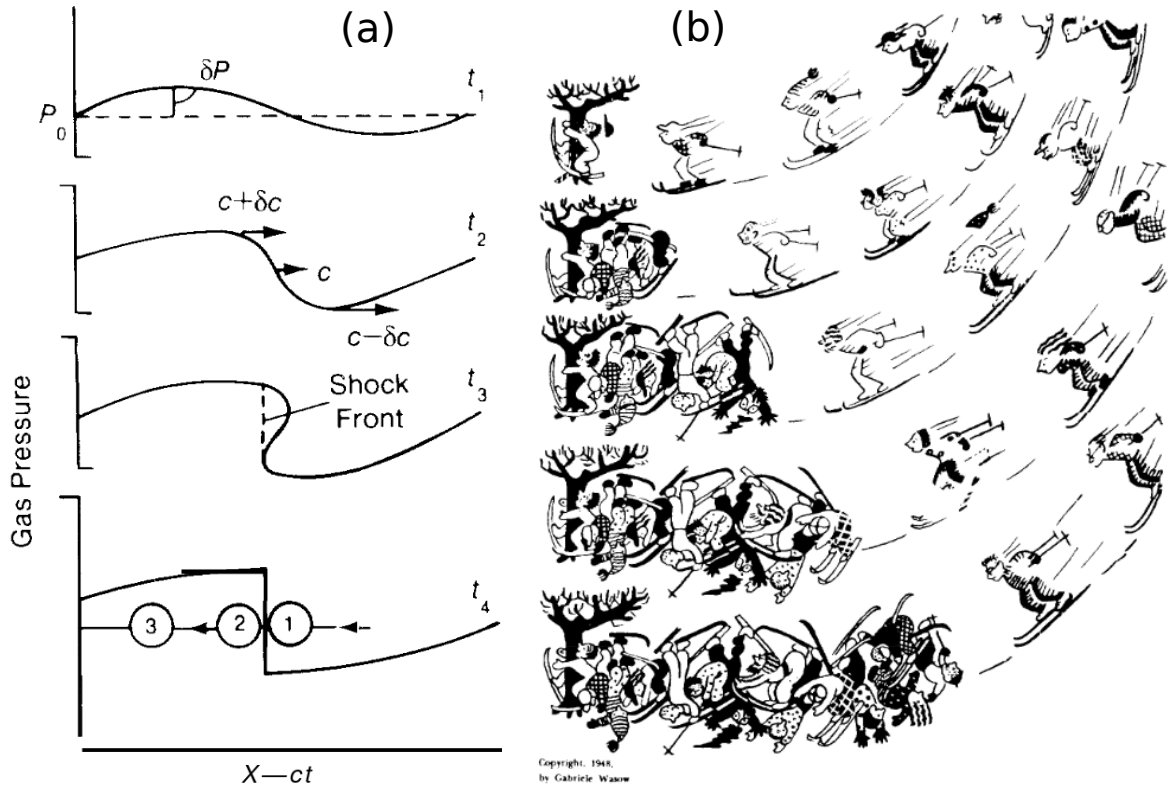

Figure 4.1: (a) Self-steepening of a finite amplitude sound wave. The situation a $t = t_3$ is not physical because of the multi-valued function that the pressure would become. Instead, dissipative processes create the situation represented at $t = t_4$, where the front shock separating the regions 1 and 2 is established on a distance of few mean free path. (b) Cartoon representing the process by which a shock is formed, in this case a receding reverse/accretion) shock. The skiers which are going faster than the speed at which they can receive informations from skiers downstream, just hit the stack in front of them before being able to slow down. From "Supersonic flow and Shock waves", R.Courant and K. O. Friedrichs, 1948 [4].

Shocks are produced when perturbations of pressure δP become of the order of the equilibrium pressure P_0. When the perturbation is small, the medium allows it to propagate at a characteristic speed, the so-called speed of sound. In the case of a magnetoplasma, sound waves are replaced by waves that couple the magnetic field and the compression waves: the fast and slow magnetoacoustic waves (SEE A.3). When the perturbation is too large in amplitude ($\delta P \sim P_0$), the local sound speed can vary strongly spatially, with regions where the pressure is high having high sound speed and regions of lower pressure having lower sound speed. This result in the self-steepening process shown in fig.8.1(a) (taken from [4]).

In the context of supersonic jets and shock physics, the "bow shock" holds a special place. First for historical reasons, because it has been for a long time at the origin of a strange phenomenon observed by gunners during the France-Prussian war: indeed, using the new French army's high-speed bullets, they reported the presence of two "bang" when the projectile was fired at high speed whereas there was only one "boom" at low speeds [2]. The Belgian ballistician Melsens proposed as an explanation that the the first "bang" was, as in the case of a low speed projectile, the sound from the gases escaping from the muzzle of the canon whereas the second bang was due to strongly compressed mass of air in front of the bullet, traveling at high speed (in fact supersonic speed) [5]. Melsens was, in fact, proposing the existence of the "bow shock", that precedes a su-

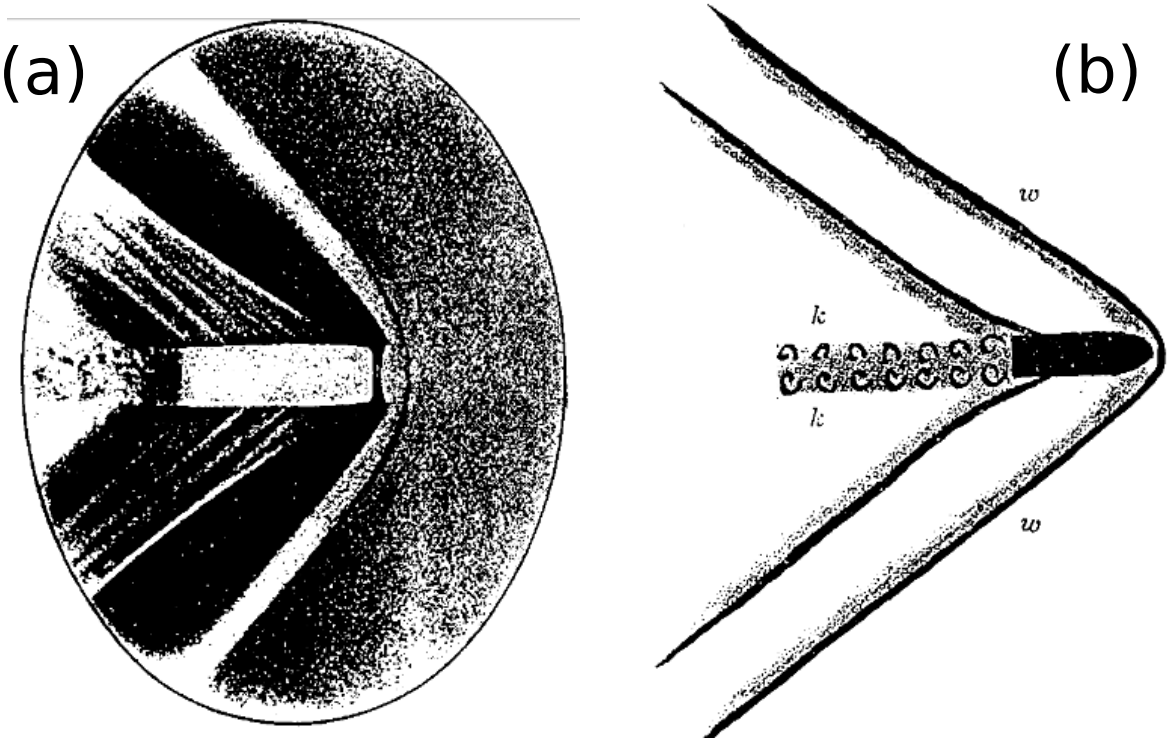

Figure 4.2: (a) Photograpic image of the bow shock in front of a projectile embedded in a supersonic flow. From Ernst Mach, "Uber Erscheinungen an fliegenden Projectilen". 1898. (b) Schematic, from Mach himself, of what he observed in his experiment. In front of the projectile is represented the bow shock whereas at the back turbulence is represented

personic projectile. In 1886, Mach and his colleague Peter Salcher reported for the first time [6], the photographic observations (see fig.8.2(a)) of a bow shock through refraction anomalies caused by abrupt change in density across the shock front. Ernst Mach was also the first to understand the total equivalence between propelling an object in a fluid or propelling air past this object. The supersonic air stream in his experiments was produced by allowing highly compressed air to escape from a reservoir through a collimating De Laval nozzle [7]. This technique is still used nowadays to produce supersonic gas jets in the laboratory or at on larger scales, for example to study the blast produced by strong (nuclear) explosions.

In fact, after his studies centered on the behavior of a flow around a supersonic projectile, Mach realized that the supersonic flow itself was of great interest with many complex internal structures. This work was mainly carried out by Ludwig Mach, his son, as well as Emden [8] and Prandtl [9]. From their research, they uncovered the presence of incident/reflected oblique shocks inside the supersonic jet envelope. These steady-state shocks are schematically represented in fig.4.3. The de Laval nozzle (on the right) allows a high-pressure gas to expand in an ambient gas and the result is the formation of the jet itself through the formation of a modulated boundary with the external medium as well as a network of internal shocks forming a succession of "cold" and "hot" regions. As one can see, the internal shock pattern is not in phase with the pattern corresponding to the interface between the jet and the external medium (the jet boundary). This ambient gas acts somehow as a piston oscillating around a equilibrium position whereas the jet itself undergoes a succession of compression and rarefaction regions [10]. After the pioneering work of Mach, Emden and Prandtl, the topic became more or less obsolete for several decades.

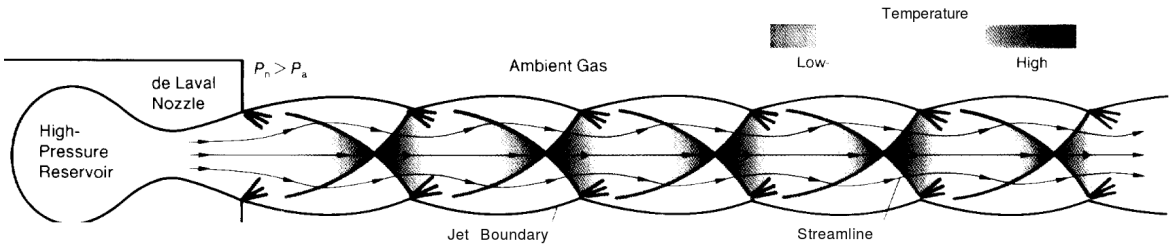

Figure 4.3: From [2]. Idealized supersonic slightly underexpanded jet ($P_{jet} > P_{background}$). Conical shocks are formed at regular steps as a consequence of the action of the background on the jet material.

The revival of interest came only at the beginning of World War II, when the military became very intrigued in a phenomenon known as "gun flash" [11]. Artillery fire in fact revealed a network of strong internal shocks in the exhaust gas, which occurred when the ratio of the emerging exhaust gas pressure to the background pressure at the nozzle was far from unity. They were particularly worried by the occurrence of very strong planar shocks (the so-called "Mach disks", [11]). These stronger shocks emit much more light than oblique shocks and they could potentially reveal the position of a gun to the enemy. As a solution it was found that with a correctly redesigned muzzle, the strong flashes associated with the presence of a Mach disk could be eliminated. Indeed, extending the muzzle wall outward allows the emerging gas to reduce its pressure before reaching the atmosphere and thus the pressure ratio can be reduced to a value close to unity [2].

4.3 The propagation of unmagnetized supersonic jets in an external background

Now we give important general results concerning the propagation of supersonic jets in an external medium. Contrary to the jet pictured in fig.4.3, we investigate here the more complicated case of non-steady jets. Fundamental work on non-steady jets has been done starting from the early 70's because of the observation of astrophysical jets and their very distinct features [13], which are not explained by the theory of steady-state jets (briefly discussed in the previous section). An example of an astrophysical jets is presented in fig.4.4. The jet is fed by material from an accretion disk, which orbits a supermassive black hole at the center of the quasar's host galaxy. The very bright regions at the end of the bipolar jet was investigated by Blandford and Rees in 1974 ([14]) who predicted the existence of a "cocoon" of gas, surrounding the central jet after being "reflected" at the head of the jet (or more precisely at the "working surface").

A schematic of the flow structure near the head of the jet is given in fig.4.5 (from [2]). As the head propagates, the external medium material is compresses through a bow shock. This shocked material is in contact with the jet material at the so-called working surface, which is a contact discontinuity. Behind the working surface we find the "cocoon" which is composed of jet material shocked through the "terminal shock" of the jet, which has the characteristics of a Mach disk whose reflected shocks have been swept back in the cocoon. Thus, the external medium is not directly in contact with the core material of the jet. This model explains the bright region seen in astrophysical jets, like the one seen in fig.4.4. Indeed, what we see is in fact the radiation emitted by the hot material composing the cocoon and the shocked material of the medium after its passage through the bow shock. The scale of the cocoon depends on several parameters including the rate at which the

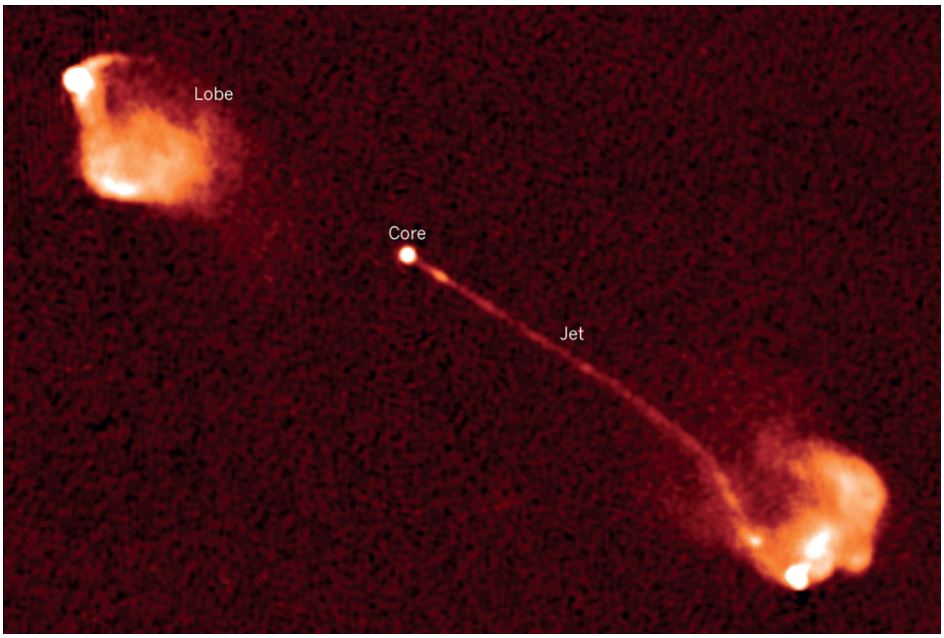

Figure 4.4: Quasar 3C 175 pictured in radio wavelengths. The jet extend far into intergalactic space and its most visible part consists of the head, where there exist the strongest conversion of kinetic energy into thermal energy, re-radiated subsequently. From Brotherton, Nature, (2014) [12]

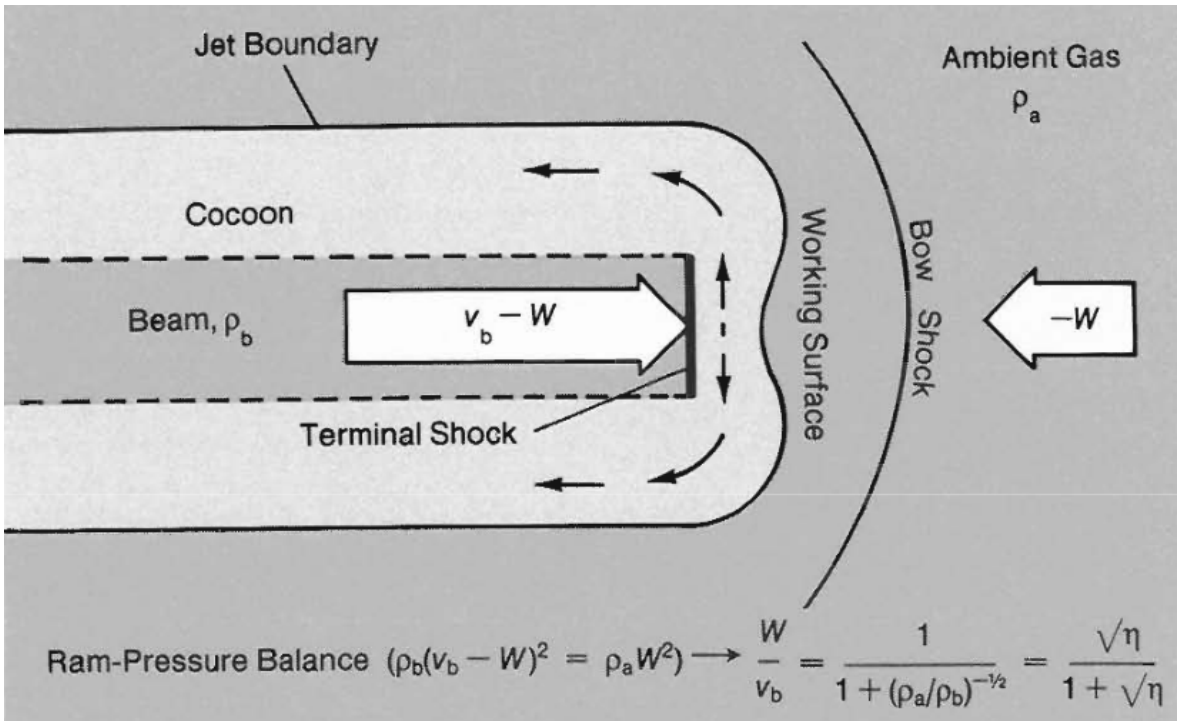

Figure 4.5: Schematic of the head of a supersonic jet expanding in a external medium. From [2]

beam fills up the cocoon and the power of the beam at the terminal shock. To look into the details of theses parameters, we must evaluate first what is the speed of the working surface. This surface is considered in equilibrium with a constant velocity W thus, in its frame, we must have equal ram pressures on both sides of the surface:

$$\rho_{jet}(v_{jet} - W)^2 = \rho_b W^2 \tag{4.1}$$

where ρ_b is the background density. Solving this expression for the velocity W, we get:

$$W = \frac{\sqrt{\eta}}{1+\sqrt{\eta}} v_{jet} \tag{4.2}$$

with the definition

$$\eta = \frac{\rho_{jet}}{\rho_b} \tag{4.3}$$

We see that if the jet density is much higher than the background pressure ($\eta >> 1$) then the working surface velocity is almost the same as the jet velocity ($W \approx v_{jet}$); whereas if the density of the jet is much lower than that of the background ($\eta << 1$) then the speed of the working surface is much lower than the speed of the jet ($W << v_{jet}$) and jet material can efficiently accumulate in the cocoon. Now we can use eq.4.2 to infer some properties of the cocoon, such as its dependency on the density ratio η. The rate at which the core jet material fills the cocoon is proportional to $v_{jet} - W$ thus we see that for $\eta >> 1$, we have $v_{jet} - W \approx 0$ and so almost no cocoon can develop around the jet core. Now, in the opposite case where $\eta << 1$, we have $v_{jet} - W \approx v_{jet}$ and thus large cocoons can develop. An other important parameter relating to the scale of the cocoon is the heating of the jet material at the terminal shock. Strong heating means strong pressure and thus the resulting lateral extension of the cocoon after the terminal shock will be much larger. This heating is related to the square of the Mach number of the jet flow in the frame of the working surface: $M_W = (v_{jet} - W)/c_{s,jet}$. Using equation 4.2, we get:

$$M_W = \frac{M}{1+\sqrt{\eta}} \tag{4.4}$$

One can see from this relation that the smaller is the density ratio η, the more intense will be the heating at the terminal shock. Thus, both the cocoon filling and the plasma heating are enhanced when η decreases.

Another important feature of the supersonic jets propagating in external mediums concerns the network of internal shocks that develop in the jet and which are represented schematically in fig.4.3. This feature has been one of the first theory invoked to explain the observations of bright knots in a large number of extragalactic radio/stellar jets, such for example those shown in fig.4.6. However, it is now known that these internal bright spots are more likely the result of time-variability at the source of these astrophysical supersonic jets [15].

It has been pointed out by M.L. Norman et al.([10]) that the observed knots in astrophysical non-steady jets are in fact different from the knots that can be observed in steady-state supersonic jets on earth, for example in the plume of some rocket engines [16]. Indeed, whereas the internal network of incident and reflected shocks in steady-state jets do not propagate inside the jet core, in the case of non-steady state jets, the pattern flows actually downstream at velocities non-negligible compare to the jet speed. They showed that in this case, the internal shock pattern is actually the manifestation

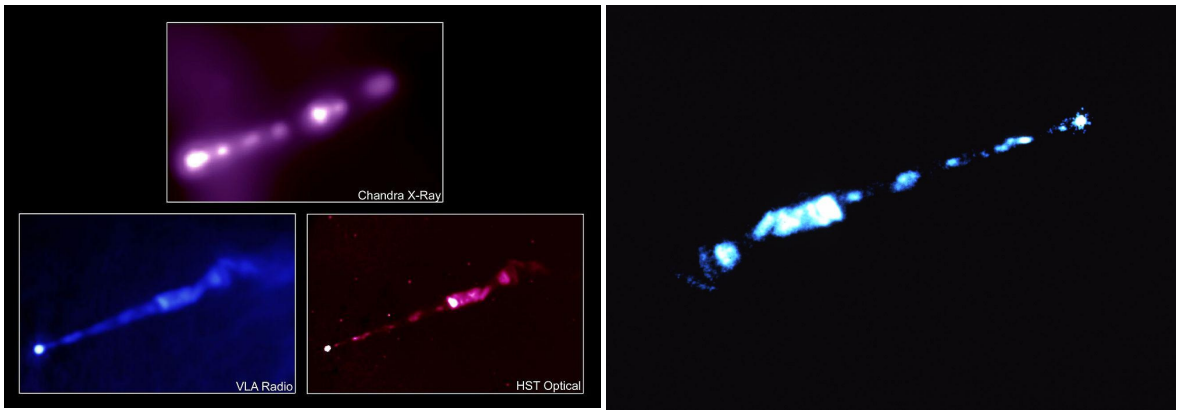

Figure 4.6: Images of the supergiant elliptical galaxy Messier 87 (M87), also known as "the Smoking Gun". Images – X-ray: H. Marshall (MIT), et al., CXC, NASA Radio: F. Zhou, F. Owen (NRAO), J. Biretta (STScI) Optical: E. Perlman (UMBC), et al., STScI, NASA

of the "Kelvin-Helmholtz pinch instability" and more precisely reflections modes of this instability. In the next section we investigate the stability of supersonic jets.

4.4 Stability of unmagnetized supersonic jets

The stability of supersonic jets is a topic of great importance if one wants to understand the observed extraordinary stability of many jets both in laboratory and space. Several instabilities are susceptible to arise in such objects. The main are the Kelvin-Helmholtz instability (A.5), the Reileygh-Taylor instability (A.4) or the Richtmyer–Meshkov instability ([17]) and the firehose/gardenhose instability, with the magnetic field acting like a collimating pipe ([18]). Without performing the complete first order typical mode analysis, we can investigate the stability of jets using simple considerations as it has been done in [2]. To do that, we need to use two relations, in particular the compressible Bernoulli relation that we now briefly derive. The Bernoulli equation states that, along each streamlines, and in a stationary regime, a given quantity is conserved. The simplest way to derive this expression is to write the equations of conservation in the Lagrangian form since it describes the evolution of a quantity associated to a given fluid particle along their streamlines. Since the fluid particles can be (de-)compressed and thus their volume can change, the correct variables to consider for the Bernoulli equation are the specific energies. In a compressible fluid, we must consider the kinetic specific energy $1/2v^2$ and the specific enthalpy $h_{spe} = \epsilon_{spe} + p/\rho$, where ϵ_{spe} is the internal specific energy. The Lagrangian derivatives of the specific kinetic energy is:

$$\frac{\mathrm{D}}{\mathrm{D}t}\left(\frac{v^2}{2}\right) = -\frac{1}{\rho}(\mathbf{v}\cdot\nabla)p \tag{4.5}$$

that of the internal specific energy is given by:

$$\frac{\mathrm{D}\epsilon_{spe}}{\mathrm{D}t} = -\frac{p}{\rho}\nabla\cdot\mathbf{v} \tag{4.6}$$

and finally the Lagrangian derivative of p/ρ is:

$$\frac{\mathrm{D}}{\mathrm{D}t}\left(\frac{p}{\rho}\right) = -(\gamma-1)\frac{p}{\rho}\nabla\cdot\mathbf{v} \tag{4.7}$$

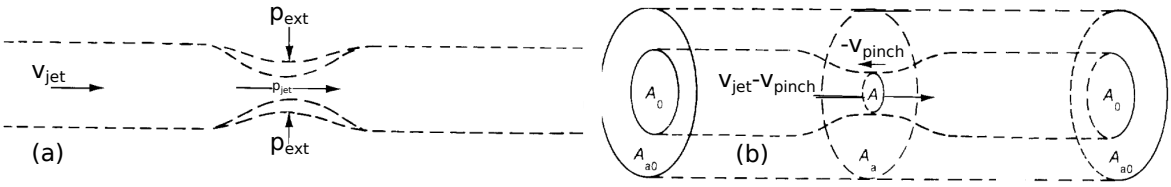

Figure 4.7: Schema showing the configuration at a constriction along the jet, both in the external frame (left) and the frame of the constriction (right). From [2].

By summing all these terms, we get:

$$\frac{\mathrm{D}}{\mathrm{D}t}\left(\frac{v^2}{2}+h_{spe}\right)=-(\mathbf{v}\cdot\nabla)p-\gamma p\nabla\cdot\mathbf{v}=\frac{1}{\rho}\frac{\partial p}{\partial t} \tag{4.8}$$

Since we can relate the internal energy to the gas pressure by $\epsilon = p/(1-\gamma)$, the specific enthalpy can be rewritten:

$$h_{spe}=\frac{\gamma}{\gamma-1}\frac{p}{\rho} \tag{4.9}$$

we can then rewrite eq. 4.8 as:

$$\frac{\mathrm{D}}{\mathrm{D}t}\left(\frac{v^2}{2}+\frac{\gamma}{\gamma-1}\frac{p}{\rho}\right)=\frac{1}{\rho}\frac{\partial p}{\partial t} \tag{4.10}$$

Here, we recall that the Lagrangian derivative is given by $\mathrm{D}/\mathrm{D}t=\partial/\partial t+(\mathbf{v}\cdot\nabla)$. The second term on the right side represents the derivative of the quantity along the streamline thus, if the configuration is stationary ($\partial/\partial t=0$), eq. 4.10 transforms to

$$(\mathbf{v}\cdot\nabla)\left(\frac{v^2}{2}+\frac{\gamma}{\gamma-1}\frac{p}{\rho}\right)=0 \tag{4.11}$$

This last equation is the Bernoulli equation for a stationary compressible gas/plasma and it just says that the sum of the specific kinetic energy and the specific enthalpy is constant along a streamline. To analyze the stability of jets, we need an other equation which describes how the velocity of the fluid in a cylinder (a pipe) varies when the section A of the cylinder changes. The equation describing this relation is given by ([2]):

$$\frac{dv}{v}=\left(\frac{v^2}{c_s^2}-1\right)^{-1}\frac{d\mathrm{A}}{\mathrm{A}} \tag{4.12}$$

This last equation is valid for slowly varying cross section. As one can see, two regimes are possible: (i) if the flow is subsonic ($\mathrm{M}=v/c_s<1$), we retrieve the well known behavior of flow acceleration ($dv>0$) when the section decreases ($d\mathrm{A}<0$); (ii) whereas in the case of a supersonic regime ($\mathrm{M}=v/c_s>1$) the fluid is decelerated ($dv<0$) when the section increases ($d\mathrm{A}>0$). Now we have the tools to understand what happens in term of stability, for both case, subsonic and supersonic regimes.

First, in a subsonic flow and in the incompressible limit, a fluid particle keeps the same mass density ρ along its trajectory on a streamline thus the Bernoulli equation 4.11 just states that if the velocity increases because of decreasing area then the pressure of the jet must decrease. The configuration of an incompressible subsonic jets is given in fig.4.7 (from [2]). If the external medium has a fixed pressure P_{ext} then a initial small perturbation (small pinch) will be amplified since as the section the decreases, the pressure gradient at the interface will also increase. Since the material of the jet advects the growing

perturbation with it, very quickly the interface will develop eddy structures characteristic of the Kelvin-Helmholtz instability. Thus, a subsonic jet in a external medium will always be unstable and therefore its expansion on very large distances is unlikely.

When the flow is supersonic, eq. 4.12 shows that the pressure actually increases in the constriction because from the continuity equation $d\rho \propto -dv$, the mass density also increases. This increase of pressure inside the constricted jet acts to stabilized the perturbed interface, contrary to the subsonic case. One could thus conclude that if the jet flow is supersonic then it would be stable to the pinch instability. However, as noted by Norman et al. (1982) [10], one has to be very cautious of the fact that the pinch perturbation is not motionless and that it is instead a convected perturbation. Therefore, in the frame of this perturbation, the flow can be subsonic. To analyze this situation we must consider two fluxes in the frame of the pinch. Suppose that the pinch is flowing with a velocity v_{pinch} then the velocity of the jet material in this frame is $v_{jet} - v_{pinch}$ and the velocity of the external medium material is $-v_{pinch}$. To obtain an unstable configuration, we must have the following configuration: the pressure of jet material must decrease as the constriction increases whereas the pressure of the external medium must increase. When the constriction increases, the section of the jet decreases while that of the external medium increases (fig.4.7). From eq4.12 written in the pinch frame, we understand that, if the external medium flow is subsonic ($v_{pinch}/c_{s,ext} < 1$) then, since $dA > 0$, we have $dv_{ext} < 0$. The result is that the pressure of the external medium would increase. For the jet itself, we have $dA < 0$ so if in the frame of the pinch the jet flow is subsonic $v_{jet} - v_{pinch}/c_{s,jet} < 1$ then it would accelerate ($dv_{jet} > 0$) and thus, from the Bernoulli equation, the pressure inside the jet would decrease. From this discussion, the conclusion is that, in order to observe pinch-unstable supersonic jets, we must have the two following conditions:

$$\begin{cases} v_{pinch} < v_{s,ext} & (4.13) \\ v_{jet} - v_{pinch} < c_{s,jet} & (4.14) \end{cases}$$

Combining the two previous relations, we get the important condition:

$$v_{jet} < c_{s,jet} + c_{s,ext} \tag{4.15}$$

Thus, in order to see the pinch instability to develops in a supersonic jets, its speed must be less than the sum of the internal and external sound speeds. If we consider the particular case of a pressure-matched jet, $\rho_{jet} c_{s,jet}^2 = \rho_{ext} c_{s,ext}^2$, we can express the external sound speed as a function of the jet sound speed and the important parameter $\eta = \rho_{jet}/\rho_{ext}$, as

$$c_{s,ext} = c_{s,jet}\sqrt{\eta} \tag{4.16}$$

Then the relation 4.15 can be written as:

$$M_{jet} = \frac{v_{jet}}{c_{jet}} < 1 + \sqrt{\eta} \tag{4.17}$$

This last relation shows that, for a fixed Mach number and for a *pressure-matched* supersonic jet, the denser the jet compared to the external medium the larger the unstable domain. We stress to maintain the pressure matching, while increasing the density ratio, implies increasing the external sound speed (see eq. 4.16

As a particular case, some astrophysical jets are actually less dense than the external medium in which they are propagating [19] (not the case for jets from young stars) so in

these cases η will be small before unity and thus not unstable to the fundamental pinch instability ($M_{jet} > 1 + \sqrt{\eta}$).

To return to the previous discussion about the fact that the very long extent of astrophysical jets would mean that they are necessarily supersonic because if not, they would be unstable to the fundamental pinch instability. We can now refine this affirmation by saying that, being supersonic is not a sufficient conditions to be stable, but the jet needs to have a Mach number higher than $1 + \sqrt{\eta}$.

Now, as the reader may have noted, we have used the term "fundamental" to name the pinch instability because it turns out actually that the process by which the jet is pinched is just one possible mode of the pinch instability. Indeed, there exist, as previously mentioned, other "reflection modes", termed the first, second, etc. The transition boundary separating the fundamental mode to the others is precisely given by the curve $1+\sqrt{\eta}$ in the (M, η) space. These reflexion modes have been studied in the early 80's by A.Ferrari et al. ([20]). Contrary to the fundamental mode which is purely longitudinal, the higher order modes also have a transverse component. They derive their name from the property that a sound wave can have when it reflects on a supersonic shear surface (the jet boundary). Indeed, it can be proved ([20]) that, for certain angles of incidence, such a wave can be amplified repeatedly by back and forth reflections between the jet boundary. The reflection modes are in fact at the origin of the network of oblique shock seen in the non-steady jets, however we remind that in steady-state jets the shock pattern is stationary.

4.5 GORGON simulations of supersonic jets

4.5.1 General description of a pressure-matched supersonic jet

We now present 3D numerical simulations of supersonic jets performed with GORGON. Whenever the contrary is not indicated, the simulations of our idealized supersonic jets are performed without including magnetic fields, thermal conduction and radiation losses.

The computational domain is shown in fig.4.8. Before presenting the numerical results, we define several dimensionless parameters of interest (some have been already mentioned, like the density ratio η). In the absence of dissipative processes (viscosity, resistivity, radiation, etc), one can perform a strict scaling between two physical systems described by the Eulerian hydrodynamic equations ([21]). Thus, once the correct dimensionless numbers are properly defined, the dynamic observed in a given simulation will be applicable to every other system with the same dimensionless parameters and where those scaling relations apply.

A given simulation is defined by the three dimensionless parameters:

$$\begin{cases} \eta = \dfrac{\rho_{jet}}{\rho_b} & (4.18) \\ K = \dfrac{P_{jet}}{P_b} & (4.19) \\ M_{jet} = \dfrac{v_{jet}}{c_{s,jet}} & (4.20) \\ \theta & (4.21) \end{cases}$$

K is the ratio of the jet pressure to the background pressure, M_{jet} is internal jet mach number, θ is th opening angle of the jet (see fig.4.8). We notice that we these definitions,

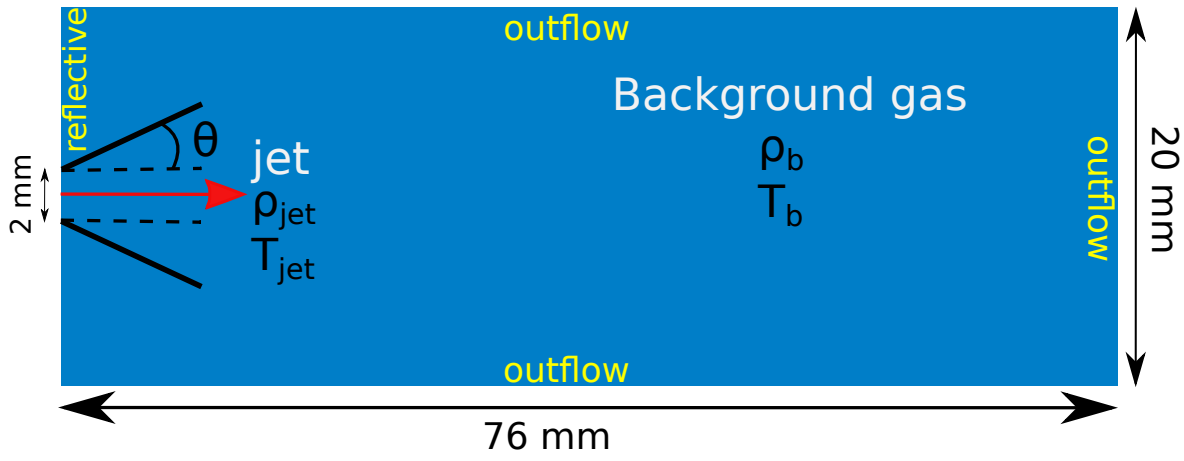

Figure 4.8: Schema of the simulation domain used in the GORGON code to simulate idealized supersonic jets. In all simulations presented in this chapter we will use $\theta = 0°$ meaning that the jet enters in the domain with a null opening angle.

the "external" jet Mach number $M_{jet}^{ext} = v_{jet}/c_{s,b}$ can also be expressed as a function of the other parameters:

$$M_{jet}^{ext} = \sqrt{\frac{K}{\eta}} M_{jet} \tag{4.22}$$

This number is interesting because it determines the development of a bow shock in the simulation. The jet has to be supersonic relative to the sound speed of the background ($M_{jet}^{ext} > 1$) to generate a bow shock. This condition can also be written as a condition on the internal Mach number as:

$$M_{jet} > \sqrt{\frac{\eta}{K}} \tag{4.23}$$

We begin by presenting simulations of a supersonic jet which is under-dense and pressure matched. The flow is inject parallel to z-axis. The relevant parameters are:

$$\begin{cases} \eta = 0.1 & (4.24) \\ K = 1 & (4.25) \\ M_{jet} = 3 & (4.26) \\ \theta = 0 & (4.27) \end{cases}$$

For completeness and to make contact with the realistic simulations presented in later sections, we also give the physical quantities associated with these parameters, which were chosen to correspond to "typical" values of densities and temperatures found in laser-produced plasma jets:

$$\begin{cases} \rho_{jet} = 0.01\, kg.m^{-3} & (4.28) \\ \rho_b = 0.1\, kg.m^{-3} & (4.29) \\ T_{jet} = 100\, eV & (4.30) \\ T_b = 10\, eV & (4.31) \\ R_{jet} = 1\, mm & (4.32) \end{cases}$$

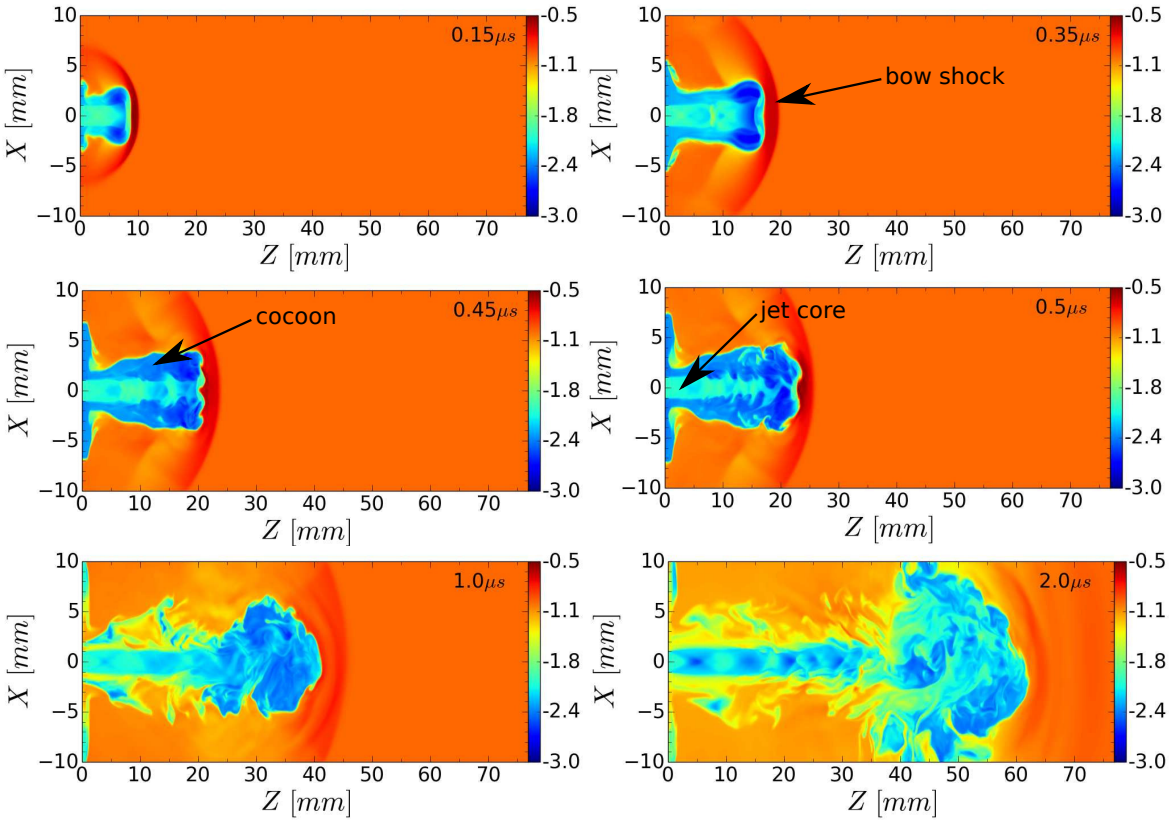

Figure 4.9: 2D maps of the decimal logarithm of the mass density at t=0.15, 0.35, 0.45, 0.5, 1 and 2 μs. The jet is injected at $z = 0$ with a zero opening angle. The internal Mach number of the jet is 3, the density ration η is 0.1 and the jet is pressure-matched with the background. The corresponding ion temperature maps are shown in fig.4.10 and the pressure maps in fig.4.11

Two-dimensional slices of mass density, ion temperature and the total pressure ($p_e + p_i$, are shown respectively in fig.4.9, fig.4.10 and in fig.4.11. The jet is injected constantly on the lef-hand boundary between x=-1 mm and x=1 mm and has a circular cross section. The evolution is followed over $2\,\mu s$. If we apply the Ryutov scaling [21] to this problem, the length scale can defined by the jet diameter ($2\,mm$) and the characteristic velocity by the jet sound speed ($\approx 140\,km.s^{-1}$) and thus in this case the unit time scale is given by: $2\,10^{-3}/140\,10^3 \approx 14\,ns$. Therefore, following our jet dynamic on $2\,\mu s$ is equivalent to say that it is studied on ≈ 143 times the unit time scale. In term of spatial unit, we observe the jet in our simulation over a distance of $76\,mm$ and so it represents 38 times the length scale (the jet diameter).

Here we show six times 0.15, 0.35, 0.45, 0.5, 1 and 2 μs. At early times (0.15 and 0.35 μs), the jet already shows some of features discussed earlier and depicted in fig.4.5. These include the bow shock (dense red region, the cocoon (clearly seen in dark blue above and below the jet head) as well as the jet core itself (in sky blue). The terminal shock is present at the head of jet and can be clearly seen in the ion temperature maps in fig.4.10 as the hotter region. A network of internal shocks can be also observed, most notably trough the 2D slices of the total pressure shown in fig.4.11. Just before its terminal shock, the jet develops a region of low pressure gas which allows the jet core to expand and become under-expanded, thus resulting in the formation of the terminal Mach disk. This self-consistent "termination" mechanism that a supersonic establishes at its propagation front was first studied and discussed in [10]. The low pressure plasma just before the terminal shock can be seen in fig.4.11 at 0.15 and 0.35 μs as the white regions near the jet head. In fact this low pressure region is composed of two distinct parts: the first one, located in the cocoon and seen as lobes sitting above the jet core, is responsible for the existence of the second one, located in the jet just before the terminal shock. Indeed, the low pressure centers of the cocoon sets off the lateral expansion inside the jet head, resulting in a region called the "rarefaction valley". The supersonic jet is thus somehow self-generating an "effective orifice" to allows its propagation.

We now discuss in more details the bow and terminal shocks. As previously seen, in the frame of the working surface (and the bow and terminal shock), we have approximately the equality of ram pressures: $\rho_{jet}(v_{jet} - W)^2 = \rho_b W^2$ and, because we are interested in pressure-matched jets, we also have that $\rho_{jet} c_{s,jet}^2 = \rho_b c_{s,b}^2$. Thus we can write:

$$\left(\frac{v_{jet} - W}{c_{s,jet}}\right)^2 = \left(\frac{W}{c_{s,b}}\right)^2 \tag{4.33}$$

This last relation expresses the equality of the Mach numbers in the frame of the working surface (and of the shocks). For a plasma with $\gamma = 5/3$, the pressure jump across a shock is given by $P'/P = 1/4(5M^2 - 1)$ where P'/P is the ratio of the post-shock pressure to the pre-shock pressure. Thus, because the pressure jump across a shock is only dependent on the Mach number of the flow in the frame of this shock, we can understand from relation 4.33 that the flow crossing the bow shock and the flow crossing the terminal shock have the same Mach number and one would thus expect the pressure jump to be the same for both cases. In fact, this is not the case because of the "rarefaction valley" described earlier. Indeed, since the flow in this region (see label in fig.4.11) experiences a decrease of its pressure and an increase in its local velocity, the local Mach number turns out to be much more important just before the terminal shock than before the bow shock. Thus the jump in pressure across the Mach disk exceeds the jump of pressure across the bow shock by the amount of pressure drop along the rarefaction valley.

We now discuss the next stage of plasma jet evolution, at times when the stability of

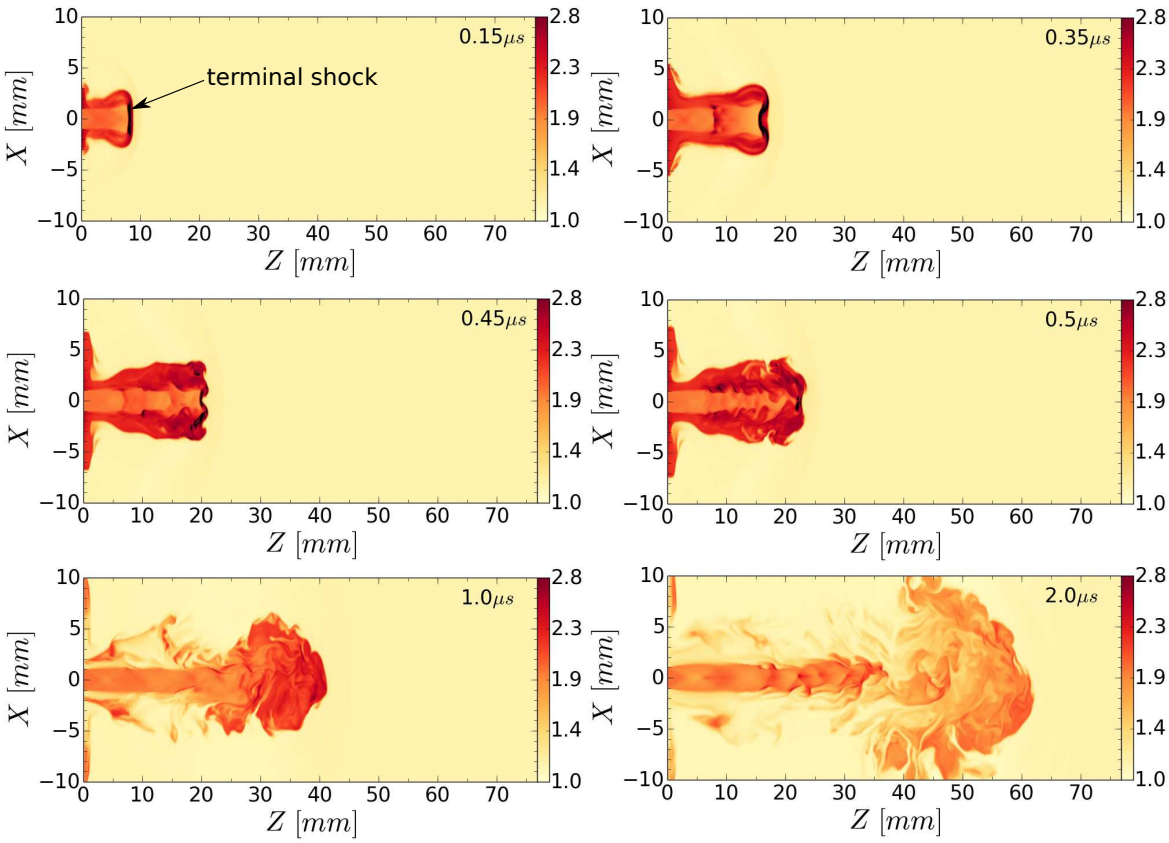

Figure 4.10: 2D maps of the decimal logarithm of the ion temperature at t=0.15, 0.35, 0.45, 0.5, 1 and 2 µs. The jet is injected at $z = 0$ with a zero opening angle. The internal Mach number of the jet is 3, the density ration η is 0.1 and the jet is pressure-matched with the background. The corresponding densities map are shown in fig.4.9 and the pressure maps in fig.4.11

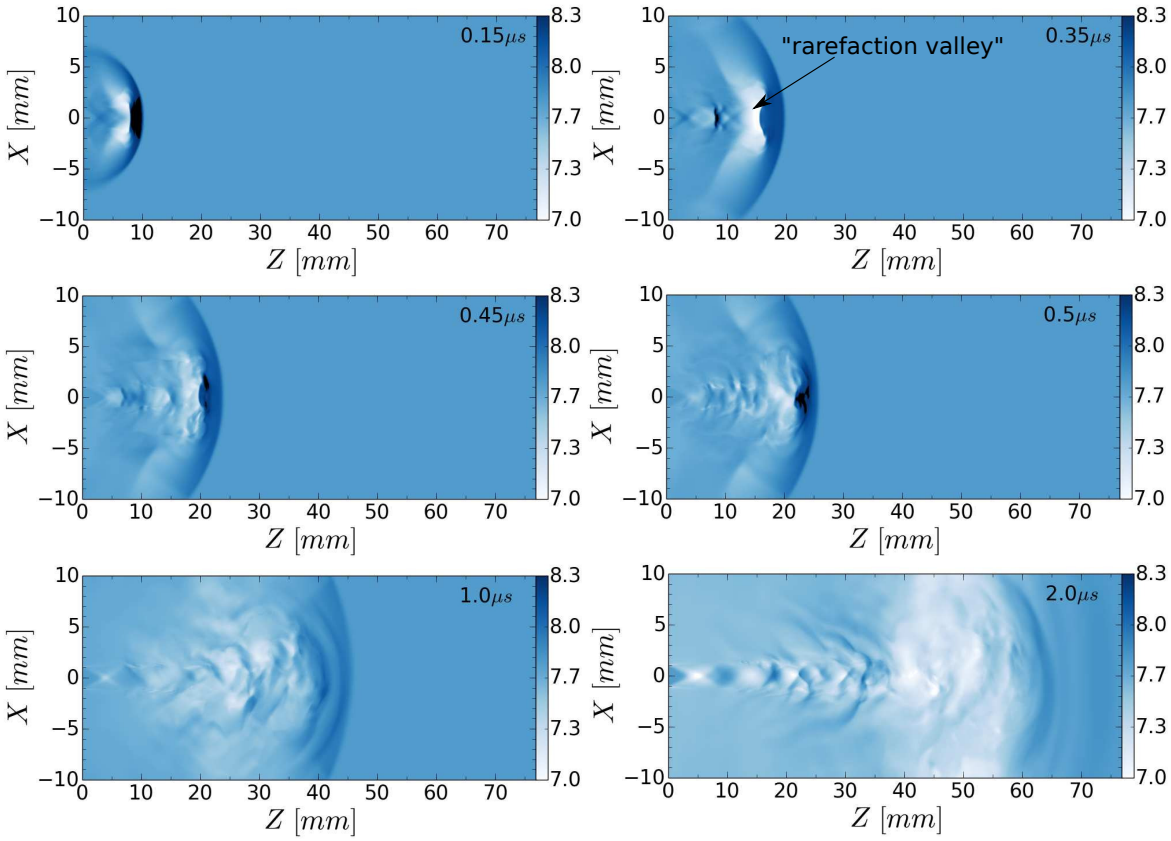

Figure 4.11: 2D maps of the decimal logarithm of the total pressure (ionic + electronic) at t=0.15, 0.35, 0.45, 0.5, 1 and 2 µs. The jet is injected at $z = 0$ with a zero opening angle. The internal Mach number of the jet is 3, the density ration η is 0.1 and the jet is pressure-matched with the background. The corresponding densities map are shown in fig.4.9 and the corresponding ion temperature maps in fig.4.10

the jet is greatly perturbed. We point out that small amplitude perturbation are already present at earlier times too. In fig.4.9, we show the jet at 0.45 and 0.5 μs. In the first one, one can see the pinching of the jet core with a main perturbation at $z \sim 16\,mm$ as well as Kelvin-Helmholtz-like perturbation on the working surface. Regarding the previous discussion, the pinch instability should be seen if $M < 1 + \sqrt{\eta}$. For the parameters used in the simulations, M=3 and $\eta = 0.1$, the inequality is not respected and one would expect the jet to be stable to the pinch instability. However, in the case where a cocoon is established, the external medium is composed of low dense shocked plasma. Thus, relation 4.15 should instead be considered in this configuration. Since the cocoon is flowing with a non negligible velocity (in the laboratory frame, this velocity is in the same direction that of the jet), the relation now becomes:

$$v_{cocoon} - v_{jet} < c_{s,cocoon} - c_{s,jet} \tag{4.34}$$

where v_{cocoon} is the value of the cocoon velocity in the laboratory frame and $c_{s,cocoon}$ its sound speed. As observed in our simulation, the cocoon velocity is always smaller than the jet velocity and the cocoon temperature is also much higher than the jet temperature (because the cocoon is composed of shocked material). Therefore, inequality 4.34 is satisfied. In fact, it highlights the fact that the cocoon is almost always a source of instability for the jet. At t= 0.5 μs, we see the jet core been almost completely broken by the instability on its last ~ 10 millimeters. We also see the advected perturbations on the working surface starting to roll up, dragging with them the external medium. This time corresponds roughly to the time when, thanks to the Kelvin-Helmholtz instability, the jet effectively starts to mix with the ambient material. In the corresponding images of ion temperature in fig.4.10 and total pressure in fig.4.11 we see the now turbulent behavior been fed by the instabilities. As one can see, specifically in the pressures maps (fig.4.11), the surface of the bow shock itself stays, on the contrary, very stable. However, as we shall see just below, the "disassembling" of the jet by the Kelvin-Helmholtz instability signals, in some way, the future "death" of the strong unique bow shock propagating at early times in front of the jet head. Much later in time, at 1 μs, the mixing becomes very efficient with a "mushroom" configuration at the jet head where the material is pouring out in this largely turbulent region. The cocoon previously located at the jet base has almost completely disappeared and thus the jet can propagates stably in this region; whereas the terminal shock is now absent and the conversion of kinetic energy of the jet into thermal energy at the head is done on a much more large volume and in a much more complex way. As can be seen in fig.4.10, the resulting ion temperatures are lower.

From fig.4.11 at 1 μs, the bow shock is now weaker and followed by a succession of "small" shock waves launched almost randomly by the turbulent "mushroom". Interestingly, on this pressure maps, we see at the jet entrance the start of a setting up of a network of conical shocks. In fact, if we look later at 2 μs, still on the pressure map in fig.4.11, the jet has now stabilized itself with a nice shock diamonds pattern, which is characteristic of stationary supersonic jets, like in the exhaust of some rocket engines. The "mushroom" is still present with even larger dimensions and much lower temperatures.

4.5.2 Effects of the Mach number on jet propagation

We discuss now the influence of the Mach number on the dynamic of supersonic jets. In fig.4.12 we show 2D slices of the evolution mass density for three different cases: M=0.5, M=1, M=6 and M=9. In fig.4.13 we show the corresponding ion temperatures.

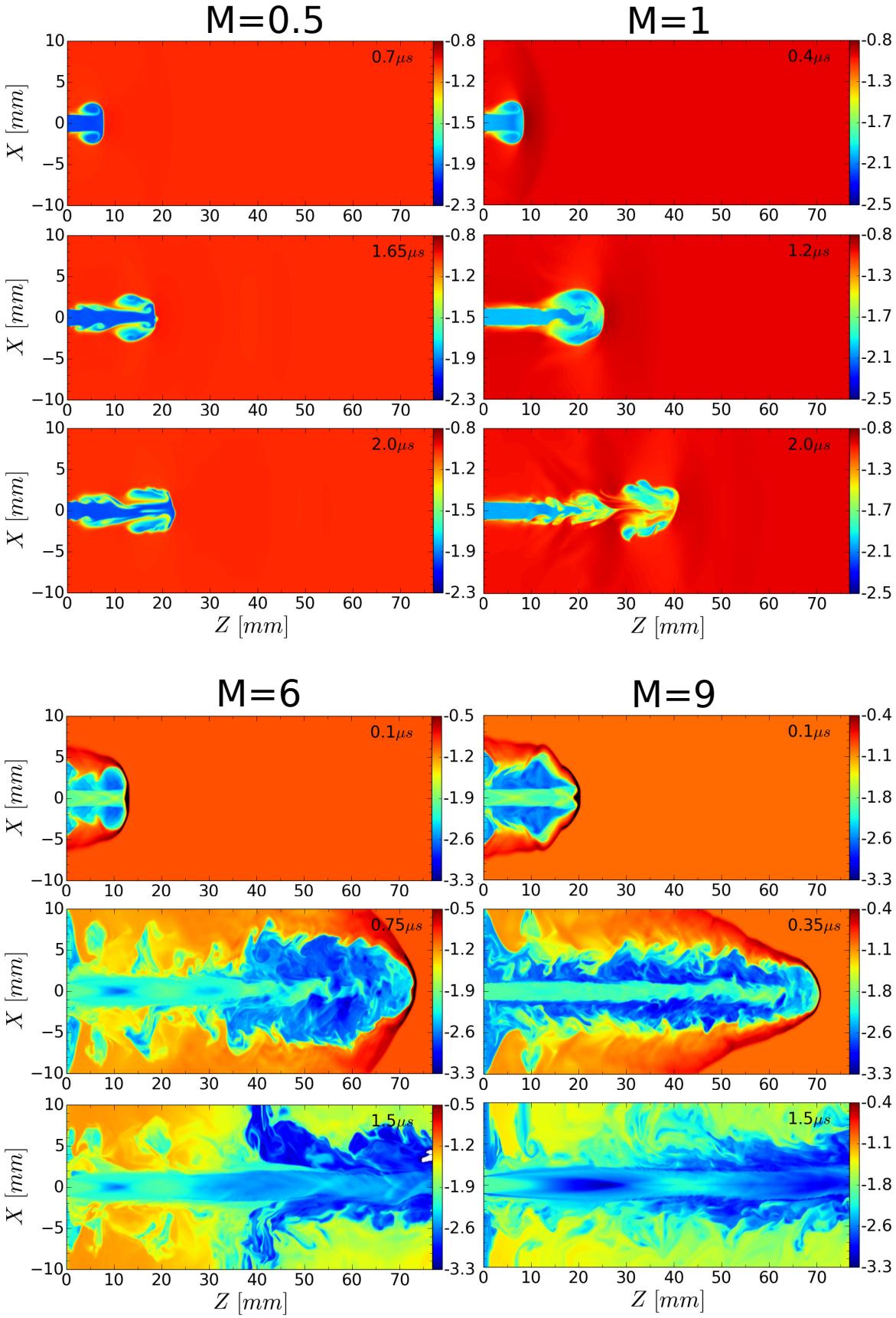

Figure 4.12: 2D maps of the decimal logarithm of the mass density for pressure-matched jets. Are shown four different Mach number jets: M=0.5, M=1, M=6 and M=9. The jets are injected at $z = 0$ with a zero opening angle. The density ratio η is 0.1 for all cases. The corresponding ion temperature maps are shown in fig.4.13.

The first remarks concerns the fact that for low Mach numbers, no cocoon is generated, as predicted in our discussion about the general features of supersonic jets (as a reminder, the cocoon been pressure-driven, a low Mach number is synonymous with no or weak terminal shock and thus a low pressure at the jet head. Furthermore, for subsonic flows, the Kelvin-Helmholtz is so destructive that any "leakage" of material on the jet sides is very rapidly destructured). In the case of high Mach number flows (M=6 and M=9), the cocoon is basically all around the jet core, and over its entire length. Very interestingly, if we look at the temperature maps of theses jets (see fig.4.13 at t=0.75 and 0.35 μs), we see that the cocoon cools down as it travel backward. This cooling is caused by the adiabatic expansion after the terminal shock because. We remind that no thermal conduction or radiative cooling is included in the simulations. The consequence of this spatial inhomogeneity of the ion temperature is crucial, in that the jet core is always much more sensible to the Kelvin-Helmholtz pinch instability near its head, where the cocoon sound speed is higher and thus the unstable condition 4.34 more easily verified. However, we highlight the fact that even if we clearly see the head of jet being quite disturbed (see the density maps of M=6 and M=9 jets at 0.75 and 0.35 μs), the very high Mach number of these flows allows them to stay relatively collimated and to not break over the simulated time-scale.

Noteworthy, the internal shock patterns developing at these same late times seems to clearly increase in scale with the Mach number (see, for example, the difference in the shock spacing between the mass density map at $t = 2\,\mu s$ for the M = 3 case in fig.4.9 and the density map at $t = 1.5\,\mu s$ for the M = 9 case in fig.4.12). From our previous discussion about the reflexion transverse modes in supersonic jets (see section 4.4), these patterns comes from the reflected sound waves amplified on the supersonic velocity shear at the jet core boundaries. Thus, when the Mach number increase, the successive reflexions needed to obtain large amplitude takes place over larger distances. The other important observation also coherent with our previous discussion, is that for low subsonic or low Mach number jets, the pinch instability become very disruptive. For example, for the subsonic jet (M=0.5), the jet is Kelvin-Helmholtz unstable even at small z ($< 10\,mm$, see at t=1.65 μs). These low Mach numbers jets only propagate over a distance typically ≈ 10 times their diameter and are afterward dislocated and mixed with the external medium.

4.5.3 Influence of an axial magnetic field on the dynamic of a supersonic jet

In this subsection we look at the effect of adding a magnetic field to the background, in the same direction as the jet main axis (z-direction). The presence of a magnetic field associated with astrophysical jets is invoked in many cases, for example in the bipolar jets often observed in Young Star Objects (even if in these cases the field is is usually toroidal [22]). As explained in the chapter (5.2) about the state-of-the-art of laboratory astrophysics jets, our collaboration has already demonstrated experimentally the possibility to collimate a laser-produced entirely with a magnetic field (vacuum background). As explained, one of the key parameter necessary to obtain the collimation process is the magnetic Reynolds number because the ideal MHD regime is absolutely required for this collimation. Here we study the "idealized" case used in the previous subsections (see fig.4.8) but we introduce a magnetic field which account for a certain percentage of the total background pressure (thermal + magnetic). We still look at pressure-matched jets thus to stay in this situation, we keep the same parameter described for M=3 jet (see 1.27-1.31) but we decrease the background temperature (and so the background thermal pressure) and compensate the difference with the magnetic field in order to always have: $P_{jet} = P_b + P_B$ where

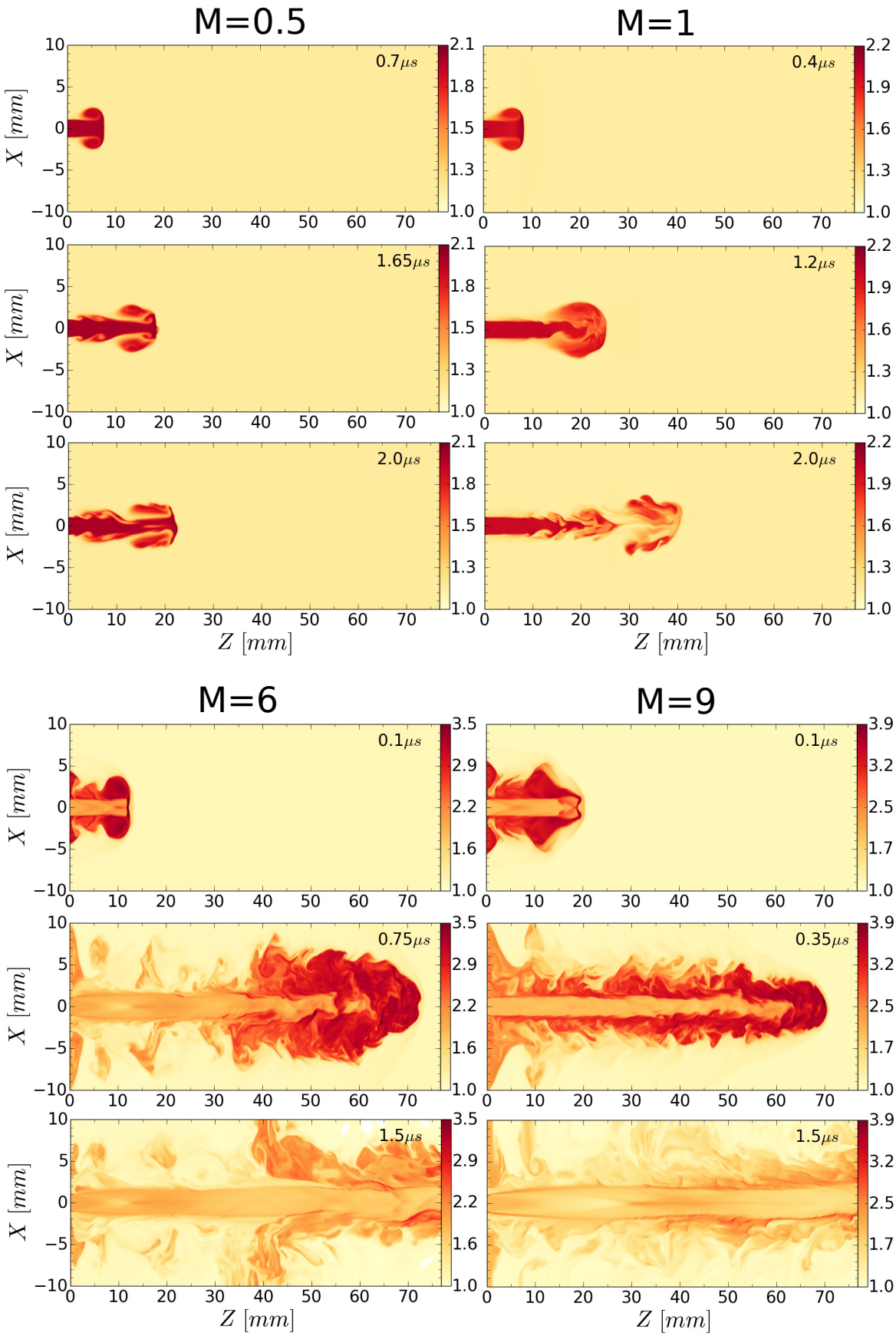

Figure 4.13: 2D maps of the decimal logarithm of the ion temperature for pressure-matched jets. Are shown four different Mach number jets: M=0.5, M=1, M=6 and M=9. The jets are injected at $z = 0$ with a zero opening angle. The density ratio η is 0.1 for all cases. The corresponding mass density maps are shown in fig.

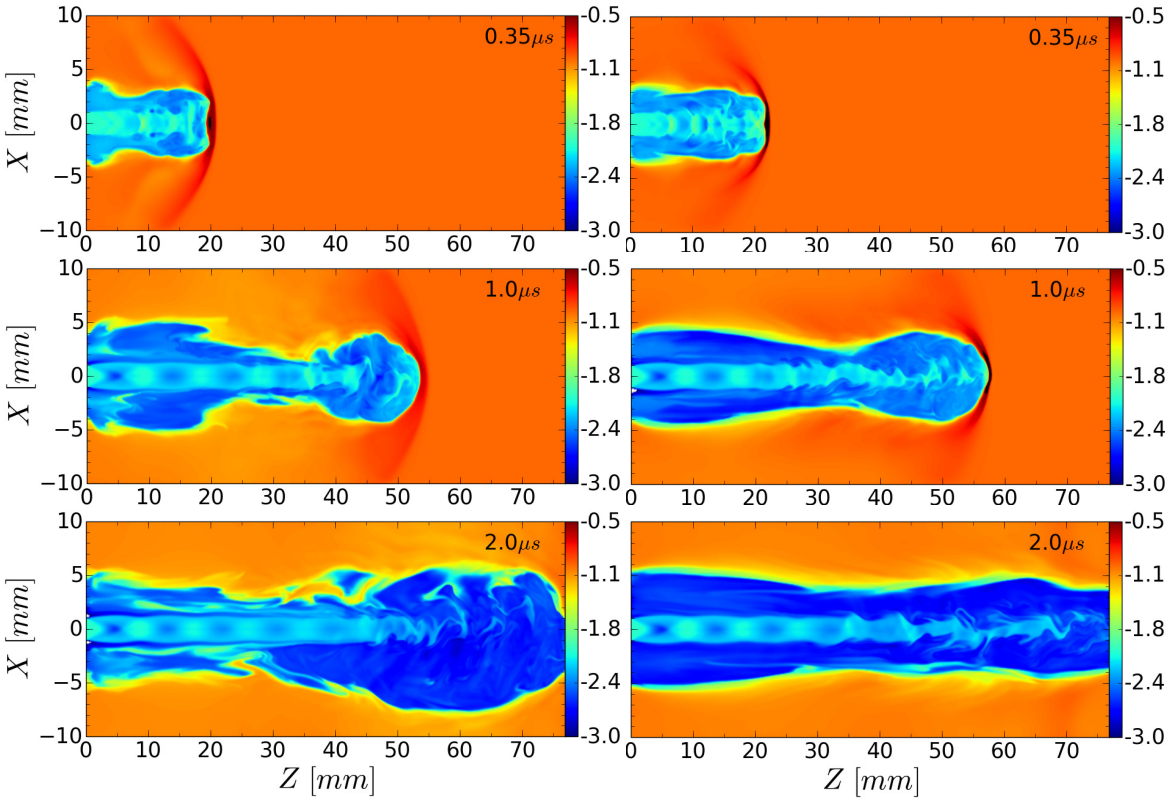

Figure 4.14: 2D maps of the decimal logarithm of the mass density for a pressure-matched jet. The background pressure is the sum of the thermal background pressure and the magnetic pressure. In the left panel, the field ($B_z = 6.97\,T$) accounts for ≈ 35% of the total pressure whereas in the right panel the field ($B_z = 10.23\,T$) accounts for ≈ 75% of the total pressure. The jets are injected in both cases at $z = 0$ with a zero opening angle. The density ratio η is 0.1 in both cases.

$P_B = B^2/2\mu_0$ is the magnetic pressure.

The results are presented in fig.4.14. In the left column we show three times (0.35, 1 and 2 μs) of a simulation with $B_z = 6.97\,T$, which represents $\approx 35\%$ of the total external pressure. In this the case the plasma background is initialized at the temperature $T_e = T_i = 10\,eV$ with a density of $10^{-1}\,kg.m^{-3}$, keeping the same ration density studied before ($\eta = 0.1$). In the right panel, the magnetic field is $B_z = 10.23\,T$ and thus the magnetic pressure represents in this case $\approx 75\%$ of the total external pressure. The temperature is here of 5 eV and we still have $\eta = 0.1$. The images shown in fig.4.14 should be compared to the ones previously presented in fig.4.9, for the same parameters but with an external pressure entirely supplied by the thermal pressure of the plasma background. One can see a remarkable difference at early times ($< 0.35\,\mu s$) concerning the absence of the low dense lobes when the magnetic field is present. In fact in this case the magnetic field tension prevents the lateral expansion of the plasma having passed through the terminal shock. As we already saw, this terminal shock is similar to a Mach disk and thus this region is normally propitious to the generation of vorticity thanks to the slip discontinuity present there. The discontinuity arises because of the differential velocity between plasma having passed through directly the Mach disk and the plasma having passed trough the incident and reflect shock. The presence of a magnetic field interfere with the generation of the previously observed "vortex". At later times ($1-2\,\mu s$), the difference between the magnetized cases and the unmagnetized becomes even more obvious. First the magnetized jets propagate farther and this effect is enhanced when the B-field is increased. For example, at $1\,\mu s$, the "$B_z = 6.97\,T$" jet is $\sim 35\%$ farther than the unmagnetized jet. This result is a consequence of the fact that the Kelvin-Helmholtz instability is greatly attenuated or even suppress in the strong B-field case (at the interface between the external medium and cocoon). However, we can see that near the jet head, the jet core is still relatively unstable, as in the unmagnetized case. The assumption that the magnetic tension stabilizes the Kelvin-Helmholtz instability should thus suggest that in the region of the *jet core head*, weak field should be observed whereas when looking close to the *jet core tail*, stronger fields should be present. In fig.4.15 we show a slice of the magnetic field magnitude for the strong field ($B_z = 10.23\,T$) case. As one can see, the strongest fields are in fact located at the bow shock with increase of ,$\sim 32\%$ compared to the initial field. As predicted, the head of the jet is basically free of magnetic energy with magnitudes $\lesssim 1.5\,T$. Thus inside this diamagnetic cavity, the plasma can develop an turbulent behavior with strong perturbations of the central beam. Closer to the tail, we see that the core is more and more surrounded by a significant magnetic field and thus in this region the jet develops a much more stable behavior. A very important point concerns the boundary conditions for the B-field. Indeed, in these simulations the field lines foots are "fixed" on the +/- z boundaries. The consequence is that the plasma cannot bring the lines too far from their original position since it will implies very strong magnetic tension forces. For the late time $t = 2\,\mu s$, especially for the strong field case, the configuration presents an almost "perfect" picture of the idealized stationary supersonic jet propagating in an ambient medium. Indeed, the shock diamonds pattern is well established on $\sim$ half the size of the box and the jet core is embedded in a hot cocoon. An other important aspect is the effect of the finite dimensions of the box. When the jet head exits the domain, the feeding source of the cocoon, the jet head, is not present anymore thus for these late times, the stable configuration is actually vowed to stay.

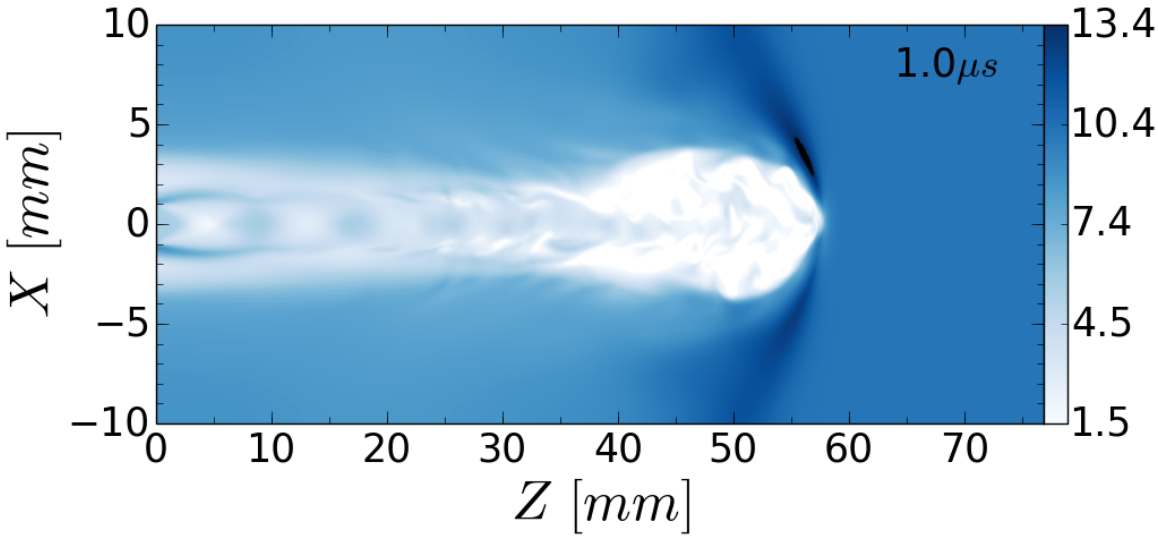

Figure 4.15: 2D maps of the magnetic field magnitude at $t = 1\,\mu s$ for the case where the initial field is of 10.23 T (≈ 35% of the total background pressure). The corresponding mass density maps is the middle one in the right panel of fig.4.14.

4.5.4 Supersonic jets propagating in a magnetized vacuum

For the last point of this study about our idealized supersonic jets, we want to address the case where the background is a vacuum. We still look at the case where the jet is pressure-matched so, in the case of our M = 3, $T_{jet} = 100\,eV$ and $\rho_{jet} = 0.01\,kg.m^{-3}$ jet, the necessary magnetic field is $B_z = 11.77$ T. It is not the purpose of this section to give a detailed description of this specific configuration since we will present an in-depth study of the more "realistic" laboratory jets (propagating similarly in vacuum) in the next chapter. Nevertheless, the idealized case presented here can serve as a perfect introduction for several features we will see later. We have represented in fig.4.16 2D maps of the mass density at t=0.05, 0.15, 0.25 and 2 μs. The first observation is that, even without any material in the background, the collimation of the jet is still possible as a consequence of the lorentz forces applied on the jet material. As we will see in the next chapter, in order to be effective, the magnetic Reynolds of the flow needs to be much larger than unity. This is because if diffusion of the magnetic field is large compared to its advection, the generated lorentz forces are not strong enough in order to collimate the flow. The second important observation from fig.4.16 concerns the extreme stability of the jet as well as the absence of a cocoon. Indeed, there are no disruptive instabilities, most notably the complete absence of the Kelvin-Helmholtz instability makes the propagation of the jet almost "perfect". The cocoon can not develops here because the pressure in front of the jets is basically null (because the magnetic force applies always perpendicularly to the magnetic field direction which is the same as the jet propagation in our case). Interestingly, we still observe an internal shock pattern inside the jet itself. This pattern proves itself to be very stable and steady-state. This is the indication that when the collimation is realized in vacuum through the action of a magnetic field, the previously observed compression and rarefaction regions are still part of the process but, because in this case the jet boundary is very stable, the shock pattern is correspondingly also very stable. Of course, we must highlight from now on that this stationary state can be established only because the source of the jet, that is the flow coming through the left "hole" in our simulation domain, is itself constant. As we shall see in the case of laboratory jets produced using laser pulses, this

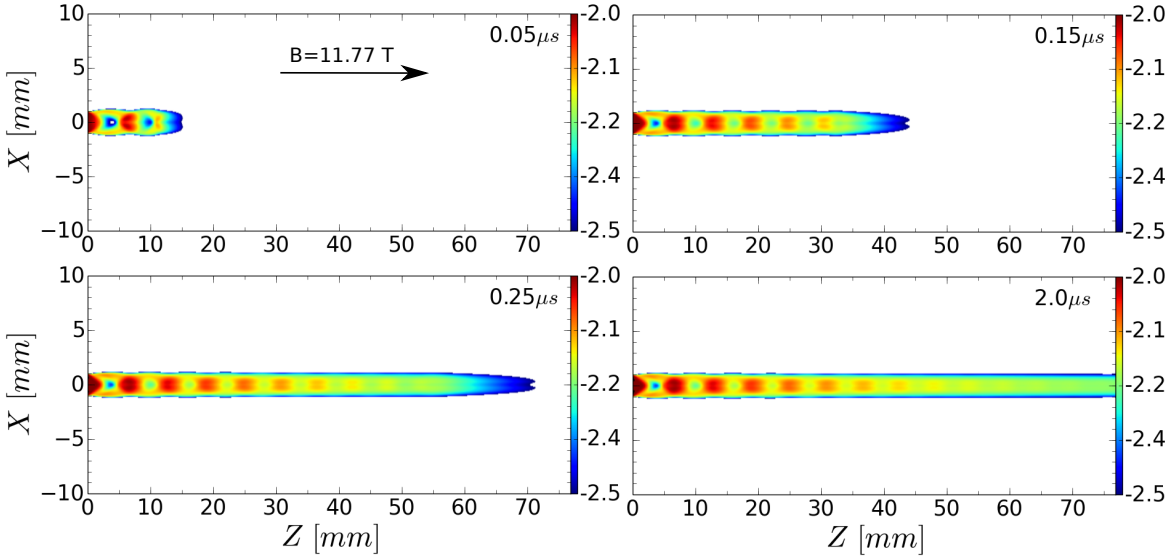

Figure 4.16: 2D maps of the mass density at t=0.05, 0.15, 0.25 and 2 μs for "magnetically" pressure-matched supersonic jets (M = 3, T_{jet} = 100 eV and ρ_{jet} = 0.01 $kg.m^{-3}$). Here the jet is propagating in vacuum.

steady-state character will not be observed because of the strong time-dependent nature of this configuration.

4.6 Bibliography

[1] Rolf Prummer. History of shock waves, explosions and impact – a chronological and biographical reference, peter o. k. krehl. *Propellants, Explosives, Pyrotechnics*, 34(5):458–458, 2009. 94

[2] Winkler Norman. Supersonic jets. *LOS ALAMOS SCIENCE*, 1985. 94, 95, 97, 98, 100, 101, XXIX

[3] Charles E. Needham. *The Rankine–Hugoniot Relations*, pages 9–15. Springer Berlin Heidelberg, Berlin, Heidelberg, 2010. 94

[4] R. Courant and K. O. Friedrichs. *Supersonic flow and shock waves.* 1948. 95, XXIX

[5] M. Melsens. *Sur les plaies produitspar les arrnes a feu.* 1872. 95

[6] E. Mach P. Salcher. Brief vom 10. dez. 1886, ernst-mach-archiv, freiburg i. br. 1886. 96

[7] George P Sutton and Oscar Biblarz. *Rocket propulsion elements.* John Wiley & Sons, 2017. 96

[8] Robert Emden. Ueber die ausströmungserscheinungen permanenter gase. *Annalen der Physik*, 305(9):264–289, 1899. 96

[9] L. Prandtl. *Neue Untersuchungen über die strömende Bewegung der Gase und Dämpfe, vol. 8, p. 23-30.* 1907. 96

[10] M. L. Norman, K.-H. A. Winkler, L. Smarr, and M. D. Smith. Structure and dynamics of supersonic jets. *aap*, 113:285–302, September 1982. 96, 99, 102, 106

[11] D. E. Carlucci and S. S. Jacobson. *Ballistics: Theory and design of guns and ammunition*. Boca Raton, FL: CRC Press, Taylor and Francis Group, 2014. 97

[12] M. S. Brotherton. Astrophysics: Quasar complexity simplified. *Nature*, 513:181–182, September 2014. 98, XXIX

[13] R. Mundt. Highly collimated mass outflows from young stars. In D. C. Black and M. S. Matthews, editors, *Protostars and Planets II*, pages 414–433, 1985. 97

[14] R. D. Blandford and M. J. Rees. A 'twin-exhaust' model for double radio sources. *mnras*, 169:395–415, December 1974. 97

[15] A. C. Raga and L. Kofman. Knots in stellar jets from time-dependent sources. *ApJ*, 386:222–228, February 1992. 99

[16] Frederick S. Simmons. *Rocket Exhaust Plume Phenomenology*. 99

[17] Martin Brouillette. The richtmyer-meshkov instability. *Annual Review of Fluid Mechanics*, 34(1):445–468, 2002. 100

[18] Michael P Paidoussis. *Fluid-structure interactions: slender structures and axial flow*, volume 1. Academic press, 1998. 100

[19] Ron Ekers, Carla Fanti, and Lucia Padrielli. *Extragalactic Radio Sources: Proceedings of the 175th Symposium of the International Astronomical Union, Held in Bologna, Italy 10–14 October 1995*, volume 175. Springer Science & Business Media, 2012. 102

[20] A. Ferrari, E. Trussoni, and L. Zaninetti. Magnetohydrodynamic Kelvin-Helmholtz instabilities in astrophysics. II Cylindrical boundary layer in vortex sheet approximation. *mnras*, 196:1051–1066, September 1981. 103

[21] DD Ryutov, RP Drake, and BA Remington. Criteria for scaled laboratory simulations of astrophysical mhd phenomena. *The Astrophysical Journal Supplement Series*, 127(2):465, 2000. 103, 106

[22] F. Shu, J. Najita, E. Ostriker, F. Wilkin, S. Ruden, and S. Lizano. Magnetocentrifugally driven flows from young stars and disks. 1: A generalized model. *ApJ*, 429:781–796, July 1994. 111

Chapter 5

Generation of astrophysically-relevant jets in the laboratory

Sommaire

5.1 Introduction **120**

5.2 Experimental production of magnetically collimated jets **120**

5.3 Initial numerical setup and laser parameters **123**

5.4 General plasma dynamics **124**

5.4.1 Velocity profiles 126

5.4.2 Density profiles 127

5.5 Cavity formation and evolution **129**

5.6 Jet structure and dynamics **133**

5.7 Jet 3D instabilities **134**

5.8 Jet structure dependence with different parameters **138**

5.9 Influence of a gas background and mitigation of the Rayleigh-Taylor instability **142**

5.10 Frequency resolved radiations imaging **144**

5.11 Influence of the spatial resolution on the jet 3D structure **145**

5.12 Bibliography **147**

5.1 Introduction

In the previous chapter 4 we have studied some of the general features of idealized supersonic jets propagating in a magnetized or unmagnetized medium. We characterized the structures that develop in the jet, such as internal shocks, cocoon, working surface, etc (4.3), as a function of the main jet parameters, namely, the internal Mach number of the jet M_{jet}, its density ratio relative to external medium η and the pressure ratio K between the jet internal thermal pressure and the background thermal pressure. In particular, at the end of this previous chapter, we showed that stable supersonic jets can be generated by removing completely the external material and imposing instead a magnetic field aligned with the direction of the jet propagation. In this case, the external magnetic pressure was initialized to match exactly the thermal pressure of the jet. The improved stability of this configuration was found to come from the complete suppression of the Kelvin-Helmholtz instability. In all these idealized simulations we choose to use plasma parameters (see 4.5) close to those expected from a plasma produced by "high intensity" lasers ($\gtrsim 10^{12}$ W.cm^{-2}). In fact, the "deactivation" of all dissipative processes when performing these simulations implied that the results obtained are general and should apply for any scale of supersonic jets that is both for laboratory jets and astrophysical jets.

In the present chapter we are going to investigate the case where the supersonic jet is produced through the interaction of a laser-produced plasma with a strong stationary and homogeneous magnetic field. Of course, contrary to the previous chapter, we will use here the complete set of physics modules implemented in our GORGON code (described in 2.4).

As explained in the introductory chapter (1), a laser generated plume can be effectively collimated by a magnetic field under certain conditions. This was shown by our collaboration, numerically in 2013 and experimentally in 2014 [1; 2]. Further experimental work has been performed since then [3; 4], and the present thesis largely expands on our previous numerical work [1]. The present chapter is dedicated to a in-depth study of these laser generated plasma jets.

First, as a general presentation of our laboratory jets, we recall very briefly the experimental setup as well as some general results obtained on the EFLIE installation at the LULI laboratory [5]. Then we use our numerical simulations to describe in details the general dynamics which leads to the generation of the jets paying a particular attention on the density and velocity profiles for such magnetically collimated flows (5.4). In the following sections we go through the details of the main features observed among which the presence of collimation shocks is analyzed carefully (5.5). We also characterize the jet structure as well as its stability 5.7. Finally, we investigate the effects of varying the direction of the applied magnetic field (5.8) as well as of adding a gas background in addition to the field (5.9).

5.2 Experimental production of magnetically collimated jets

The results presented here are taken from our paper [3] where the read can find much more informations on the experimental results. Here we briefly present the experimental setup as well as some general results that will be more deeply detailed in our numerical work in the following sections. The experiment has been performed using a platform [6; 7] developed in collaboration between the LNCMI [8] and LULI laboratories (France) and on which, as mentioned in the introduction, our collaboration has already demon-

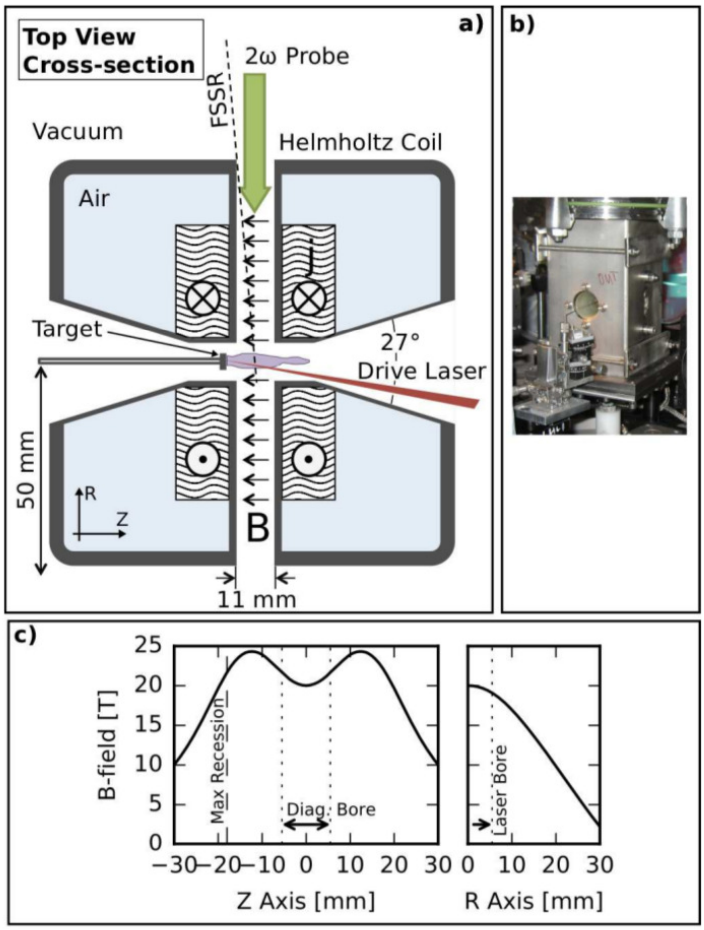

Figure 5.1: a) Top view schematic of the Helmholtz coil system. The "laser bore" (left-right axis) of the coil would allow a maximum of 27° full-angle beam for a laser beam at normal incidence. The "diagnostic bore" (up-down axis) is of constant 11 mm diameter. b) Photograph of the Helmholtz coil in the chamber looking into the "laser-bore". Motorized stages are not shown. c) Magnetic field profiles along the coil central axes. The target is recessed along the longitudinal (laser bore) axis which is parallel to the field lines. Dotted and dashed lines show the extent of the coil bore and the maximum distance over which the target was recessed.

strated the possibility to produce astrophysically relevant magnetically collimated flows [2]. The experiment was performed at the ELFIE laser facility[45] at the Laboratoire pour l'Utilisation des Lasers Intenses (LULI) in France [9]. The setup for this experiment is shown schematically if fig.5.1(a).

The 40 J, 0.6 ns Ti:Sa laser pulse is used to ablate a 2 mm diameter CF_2 (Teflon) target with an on-target intensity of $2\,10^{13}\,\mathrm{W}.cm^{-2}$ (and a $700\,\mu m$ diameter focal spot). The solid target is embedded in a relatively homogeneous magnetic field of 20 T. The spatial profile of the magnetic field magnitude is represented in fig.5.1(c). The field can be considered uniform at ±10% in a volume of $\approx 1\,cm^3$. The rise time of the coil is $190\,\mu s$, meaning that the field can be considered also as constant in time on the experiment time scale ($\sim 100\,ns$). Interferometry is accomplished via the Mach-Zehnder technique with a frequency doubled probe laser with a pulse length of 5 ps and ~100 mJ of energy. The interferograms recorded on CCD cameras are analyzed using the Neutrino code [10]. Then a wavelet model enables to fit the fringes arrangement, from which a phase map is then unwrapped. Using an Abel transform [11], the plasma electron density n_e is retrieved from the phase map assuming an axisymmetric distribution of the plasma.

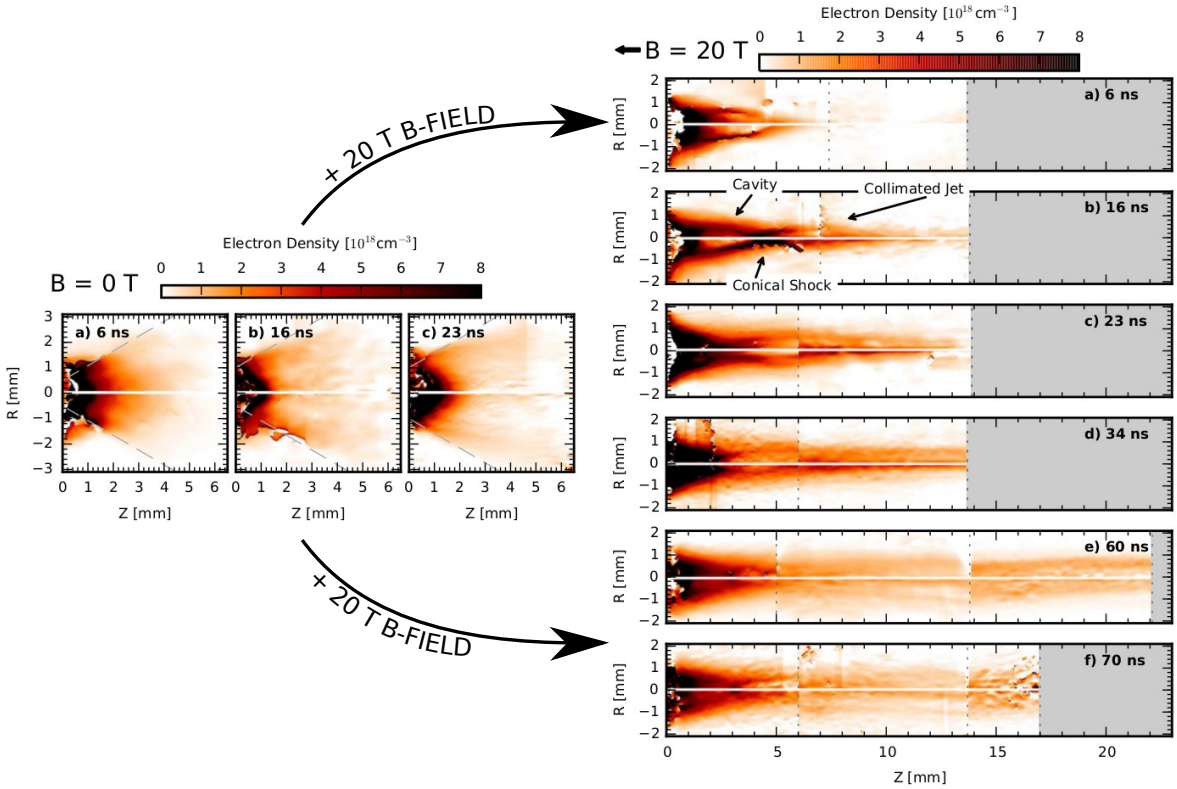

Figure 5.2: Pseudo-color images of electron density taken via interferometry showing jet propagation from 6 to 70 ns as indicated in the plots. The jet was created by a $2\,10^{13}$ W.cm^{-2} laser irradiating a CF_2 target in a 20 T ambient magnetic field. The dotted vertical lines indicate the edges of the individual images. The gray background indicates a region where no data was taken or the fringes were not of sufficient quality to be unwrapped properly. The central ±5 pixels (±55 µm) have been removed due to the uncertainty of the Abel inversion on axis. Note that many of the fine structured features are due to noise in the fringes of the interferometer and thus are non-physical. From [3].

In fig.5.2 we show the electron density maps obtained during this experiment. They highlight the critical effect of adding a strong magnetic field on a laser-produced expanding plasma. Indeed, in the left panel are shown maps observed in the case where the magnetic field is absent. In this case, we clearly see that the plasma expands with a wide semi-angle of ≈ 30°. This non perfectly hemispherical expansion is due to the fact that the pressure gradients generated by the laser deposition are much stronger in the Z-direction than in in the X-Y directions. Even if some previous work have referred to this type of free expanding flows as "jets" due to this anisotropy, it is admitted now that their aspect ratios (length/diameter) are much to small to be qualified as jets [12–14]. In the right panel of fig.5.2 we see the dramatic increase of the aspect ratio with values which can reach at least 11 in the fifth maps of the right panel, taken 60 ns after the laser pulse. This last point is also a very important parameter of our setup since it allows the production of jets, with relatively uniform densities ($n_e \approx 10^{18}\, cm^{-3}$), on a time scale that is ~ 200 times the laser pulse duration. As we shall see in a next chapter, this almost "steady-state" feature is the starting point of our work on laboratory magnetized accretion (9). In the right panel of fig.5.2 are also labeled some important features involved in the magnetic collimation of the laser-produced plasma (e.g. "cavity", "conical shocks"). The detailed description of all the collimation process is essentially the subject of this chapter and thus the reader is invited to see the details of these features in the following sections but keeping in mind that shocks are basically the indirect mechanism by which the magnetic field acts on the expanding plasma in order to collimate it.

5.3 Initial numerical setup and laser parameters

The standard configuration studied, shown schematically in Fig. 5.3, consists of a solid planar target immersed in an externally applied, homogeneous magnetic field B_0 parallel to the z-axis and perpendicular to the target.

In this chapter we focus on a single laser pulse impacting a carbon target (the effects of changing the target material are discussed in 5.8) and the resulting plasma plume evolution. In chapter 6 we will study the impact of adding a pre-pulse to this configuration. The computational domain in GORGON is defined by a uniform Cartesian grid of dimension $6\,mm \times 6\,mm \times 14.4\,mm$ and a number of cells equals to $300 \times 300 \times 720 = 6.48\,10^7$. The spatial resolution is homogeneous and its value is $dx = dy = dz = 20\,\mu m$. The laser parameters are:

- Energy: 17 J
- Pulse duration (FWHM): 0.5 ns
- Focal spot diameter: 750 μm
- Intensity: 7.7×10^{12} W cm^{-2}
- wavelength: 1.057 μm

The initial laser interaction with the solid target is performed in the present case using the DUED code [15]. This two-dimensional Lagrangian fluid code solves the single fluid, 3-Temperature equations in 2D cylindrical geometry in Lagrangian form. The code uses the material properties of a two-temperature equation of state model (EOS) including

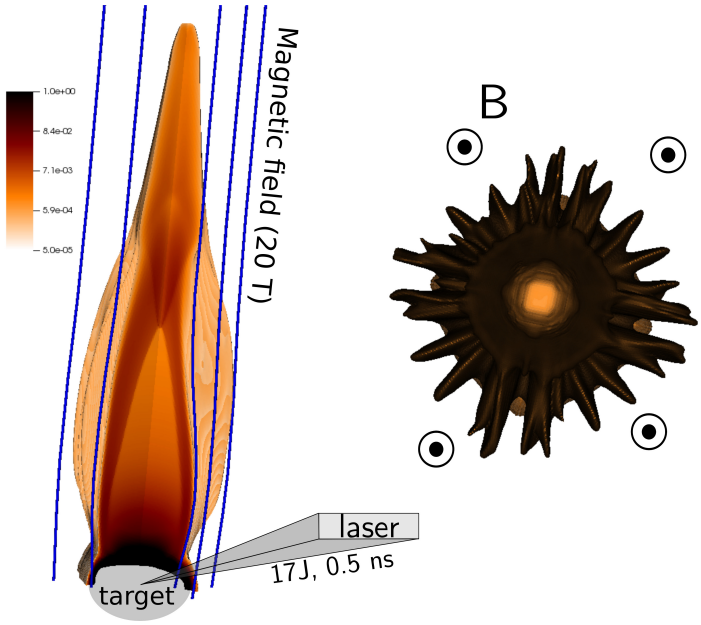

Figure 5.3: Simulated configuration with the GORGON code. The solid target is composed of carbon, the laser pulse impacts this target with an intensity of $\approx 7.7\,10^{12}\,\mathrm{W}.cm^{-2}$ (the laser-solid-plasma interaction is performed using the DUED code [15]). The magnetic field is initialized as been perpendicular to the surface target (it corresponds to the z-direction) and its magnitude is 20 T. The left image shows, at $t = 8\,ns$, an isovolume rendering of the mass density of the jet resulting from the dynamic described in the main text. The right image shows the same jet but seen from above.

solid state effects, and a multi-group flux-limited radiation transport module with tabulated opacities. The laser-plasma interaction is performed in the geometric optics approximation including inverse-bremsstrahlung absorption. At the end of the laser pulse (1 ns), the plasma profiles of density, momentum and temperature (electronic and ionic) from the DUED simulations are remapped onto the 3D Cartesian grid of GORGON with a superimposed uniform magnetic field of 20 T (in the z-direction) and used as initial conditions. To remove the symmetry imposed by the initial conditions and to account for the effect of inhomogeneities in the laser intensity over the focal spot, we introduce uniformly distributed random perturbation on the plasma velocity components, with a maximum amplitude of ±5% the initial value. The choice to use the DUED code for the initial plasma formation is guided by the fact that this code captures more finely the laser-solid interaction physics than the model implemented in GORGON (thanks mainly to better adapted EOS's). Furthermore, results obtained with DUED data as inputs have already been published in peer-reviewed papers [15]. We remind that the physics included in the GORGON code is described in 2.4.

5.4 General plasma dynamics

In Fig.5.4 we plot 2D slices in the xz-plane, of the electronic density at three different times (2, 10 and 30 ns) after the laser pulse arrival. The overall dynamic consists of basically three phases: the initial almost free expansion of the the highly conductive laser-produced plasma (Fig.5.4(a)), the collimation of the plasma flow by the magnetic field which results in the formation of a diamagnetic cavity with a conical shock at its tip

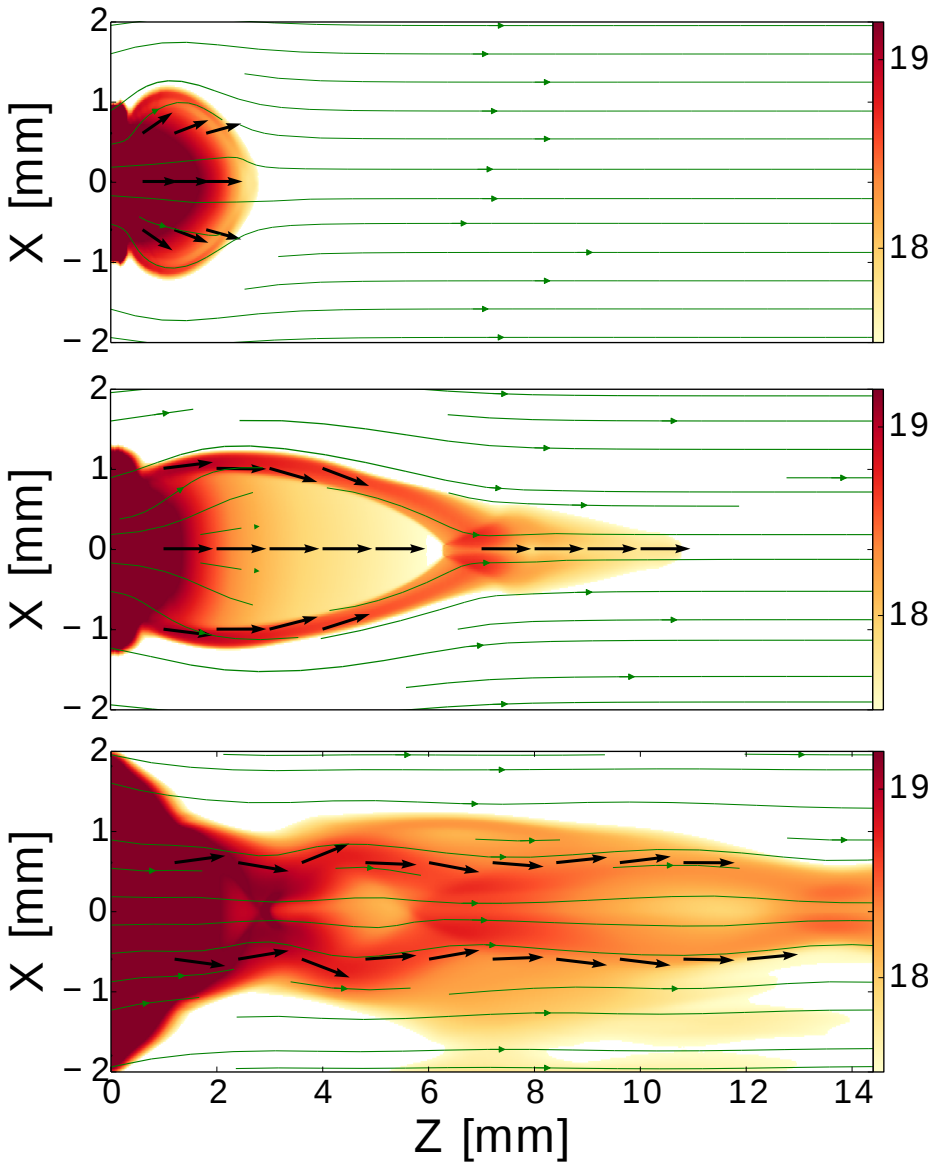

Figure 5.4: 2D slices of the decimal logaristm of the electron density at t=2,10 and 30 ns. The carbon target is located on the left of each images (between $x = \pm 1\,mm$) and the laser pulse is coming from the left. The magnetic field lines are represented in green.

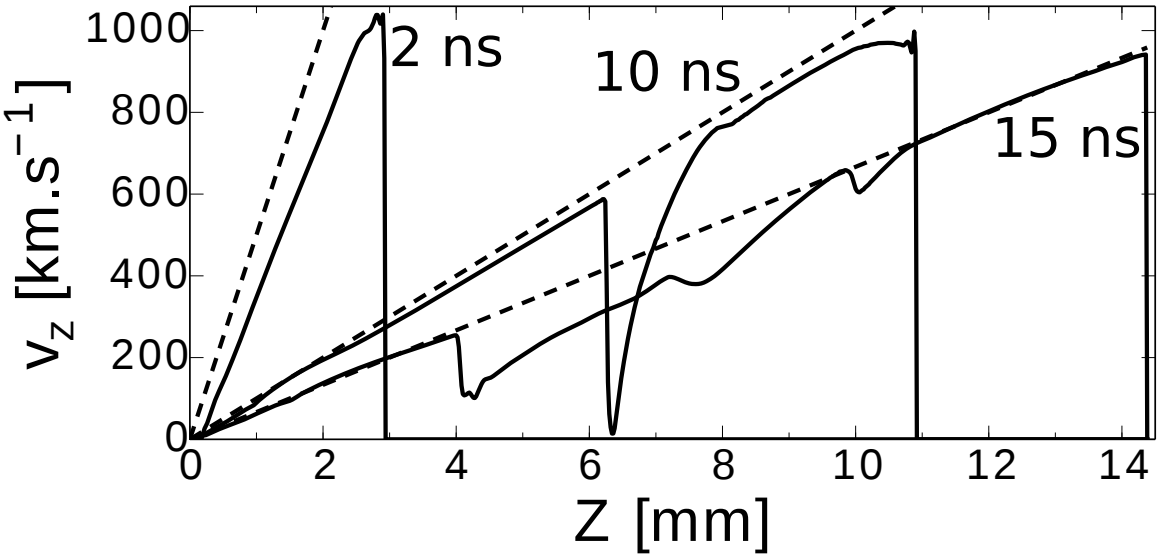

Figure 5.5: 1D profiles from GORGON simulations of the velocity (v_z) on the z-axis at t=2,10 and 15 ns. Dotted lines represent the solution of Eq.5.2, $v_z = z/t$.

(Fig.5.4(b)). And finally, the formation of a super-Alfvenic jet (Fig.5.4(c)). The entire plasma flow structure is sustained for over 100 ns, until the plasma flux coming from the ablated target becomes negligible.

Before delving into the details of these different phases, it is interesting to review the general features (velocity profile, density profile, etc.) of the expanding plasma plume in the presence of a magnetic field.

5.4.1 Velocity profiles

In Fig.5.5 we plot the simulated profiles of the axial velocity (v_z) as a function of distance from the target (z), for three different times. The profile is taken on the axis of the flow, and it is shown together with the analytical profiles given by:

$$v_z = \frac{z}{t} \tag{5.1}$$

where $z = 0$ corresponds to the position of the initial target surface and $t = 0$ corresponds to the arrival time of the laser pulse. The analytical profiles given by 5.1 are actually equivalent to the self-similar velocity solution developed in the chapter dealing about laser-produced plasma expansions (3.3). In addition, we will show later that the density profiles given by this model match relatively well the simulation profiles.

An other way to see the origin of this solution, is to realize that along the magnetic field (z-direction), the plasma flow is roughly governed by the simplified 1D momentum equation (see 2.3.1), which is valid for supersonic/hypersonic Mach numbers flows:

$$\frac{\mathrm{D}v_z(z,t)}{\mathrm{D}t} = \frac{\partial v_z(z,t)}{\partial t} + v_z(z,t)\partial_z v_z(z,t) = 0 \tag{5.2}$$

Indeed, it can be verified that $v_z(z,t) = z/t$ is solution of this equation (also called the inviscid Burgers' equation). Physically, equation 5.2 describes the ballistic trajectory for Lagrangian fluid particles or in other words, fluid particles propagate at a roughly constant velocity. This reflects the fact that very quickly the local Mach number of the flow

becomes sufficiently large, so that the pressure gradient term in the momentum equation becomes negligible with respect to the advection term. In the section dedicated to the derivation of the adiabatic expansion (3.3.2), we did not suppose that the pressure term vanish. However it can be easily shown that a large part of the expanding plasma in this model is actually in a regime such that equation 5.2 is valid, and that both descriptions are equivalent in these regions. Indeed, in the adiabatic expansion model, the local Mach number is given by (from 3.3.2):

$$\mathrm{M} = \frac{|u|}{c} = \frac{|u|}{c_0 - \frac{\gamma-1}{2}|u|} \tag{5.3}$$

The point from where the pressure forces ($-\nabla p$) will start to loose significantly their importance compared to the advective term ($\rho(\mathbf{u}\nabla)\mathbf{u}$) is basically the sonic point, that is where the fluid velocity is equal to the local sound speed (M = 1, see 3.3.4 for details). Solving 5.3 for this case, we find that the fluid particles having a sonic velocity $|u| = |u_s| = c$ must have a fluid velocity $|u_s| = 2c_0/(\gamma+1)$. In the free-reservoir adiabatic model, the only point where the fluid has this velocity is the point $z = 0$! (It can be seen solving 3.45 with $|u| = |u_s|$). Thus, in this model, basically all the expanding plasma is supersonic and thus equation 5.2 become almost instantly valid. The validity of the free-reservoir adiabatic expansion can be "naively" justified by saying that the initial plasma ablated from the solid target can be considered as a reservoir of ionized gas at density ρ_0, pressure p_0 and temperature T (with the corresponding sound speed $c_0 = \sqrt{\gamma p_0/\rho_0}$ (variables defined in 3.3.2).

In the case where the expansion is isothermal (see 3.3.3), the sonic point is also generally close to the target surface (see 3.2) and thus this solution tends also toward the Burger' equation. The relative good agreement seen in fig.5.5 is also the starting point of the small model we tentatively developed in section 3.3.4. We note also the fact that the Burgers equation become rapidly valid partially because of the M^2 dependence of the ratio of the ram pressure on the thermal pressure (see 3.55). The simple relation 5.1 presents a great interest for laboratory experiments similar to ours (almost 1D expansion), as a means to obtain a fairly accurate estimate of the bulk velocity of the plasma, which is in general a very difficult quantity to measure experimentally.

5.4.2 Density profiles

The next step is naturally to look at obtaining analytical expressions for the density profiles also along the magnetic field (z-axis), where $\mathbf{j} \times \mathbf{B} = \mathbf{0}$. The problem here is to find the solution to the mass conservation equation 2.3.5 associated to the momentum equation 5.2 (valid for the supersonic expansion). If we use the adapted Raga model 3.3.4 to solve this problem we have seen that a major problem concerning the nature of this solution is that it depends strongly on the initial conditions. Several models for three dimensional laser-produced unmagnetized plasma expansions exist [16] and recent experiments with laser-produced carbon plasmas have shown it to be in good agreements with these models [17]. In our case, the strong collimation by the magnetic field allows us to use as a first approximation a one dimensional description of the flow in the z direction (see Fig.5.4(c)). As seen in the previous section, a very simple but useful solution should be obtained within the free-reservoir adiabatic model 3.3.2. In this case, the expanding plasma has a density profile given by 3.41:

$$\rho(z) = \rho_0 \left(1 - \frac{(\gamma - 1)\, v_z(z)}{2c_0}\right)^{2/(\gamma-1)} \tag{5.4}$$

In Fig.5.6, we plot mass density profiles (full lines) at three different times (t=8, 15 and 25 ns) for a carbon plasma produced by a laser pulse with the same parameters introduced above except for the laser energy, which is here of 6J. We choose this lower laser energy only because the density profiles are closer to a 1D expansion in this case and results are more directly comparable with the theory. We will justify this point and explain the deviation when increasing the laser energy in the section detailing the jet structure. However, it should be noted that the velocity profiles, being taken on the z-axis, are less sensitive to the initial conditions.

Profiles computed from 5.4 are represented in dashed lines. These curves are obtained for an adiabatic index $\gamma = 5/3$ (as in the GORGON code) and an initial temperature $T_0 = 375\,eV$. This value is clearly too high for the laser energy used and and in fact, it is not coherent with our simulations which gives $T_0 \sim 60\,eV$. In fact, it has been experimentally observed that for laser-produced plasmas [18], the maximum speed reached by the expanding flow is generally 2-3 times greater than the theoretical maximum speed given by the free-reservoir model ($3c_0$). So in our case, if we take the temperature from the simulation ($\sim 60\,eV$) as the initial temperature T_0), we would need to multiply our sound speed by a factor 2.5, which would be coherent with the estimates found experimentally. We note that several explanations have been put forward to resolve this discrepancy, such as a different adiabatic index, see [18]). However an obvious possibility is that for laser-produced plasmas the pressure of the "reservoir" is not homogeneous. Strong pressure gradients generated by the laser pulse, can then increase the conversion of thermal energy into kinetic energy. We have also seen in the section detailing free-expansions, that the energy associated with ionization can increase the maximum velocity reached by the plume 3.3.2. We must also point out that in Fig.5.6, the simulated profiles are averaged around the z-axis over a radius of $700\,\mu m$, which is approximately the laser beam radius. Their relatively good agreement with 1-D theoretical profiles further support the assumption of a magnetically-collimated nearly 1-D expansion.

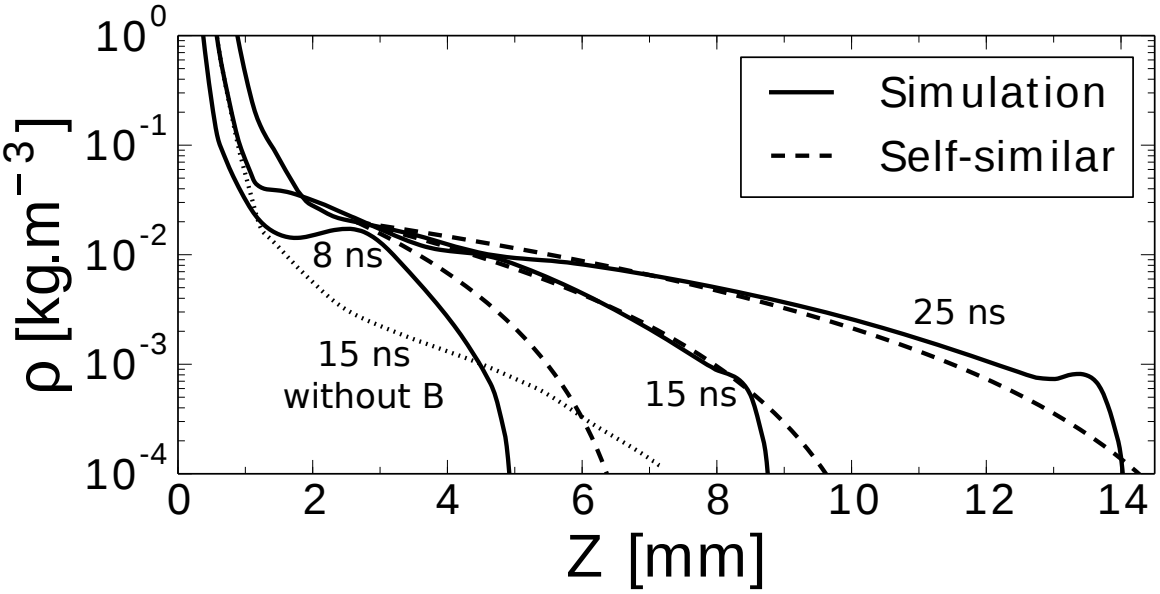

Figure 5.6: Full lines: simulation profiles of mass density (as a function of z) averaged around the z-axis over a radius of 700 μm. Dotted lines: solution computed from the adiabatic expression 5.4

5.5 Cavity formation and evolution

We focus now on the main dynamics of the laser produced plasma and its collimation by the magnetic field.

The plasma expansion will differ from the free 3D expansion case only if there is a force strong enough compared to the ram pressure ρv^2 where ρ is plasma density and v the fluid velocity. The initial plasma expansion is largely dominated by the ram pressure of the flow, $\rho v^2 \sim 25\,\mathrm{GP}a$, which is approximately 150 times greater than the magnetic pressure of $\approx 160\,\mathrm{MP}a$. However, this three-dimensional, free expansion is halted very quickly by the distortion of the magnetic field lines and the rapid increase of the magnetic field. Perpendicular to the target, the flow velocity and the field lines are almost parallel (there is no Lorentz force on the plasma) and the plasma propagates essentially unimpeded. However, parallel to the target surface, the flow velocity and the field lines are perpendicular. Shear then distorts the magnetic field lines generating a magnetic tension that decelerates the flow. Initially this deceleration is small, but it is rapidly amplified by the accumulation of magnetic field on the edge of the oval cavity, as shown in Fig.5.4(b). This magnetic compression is possible because the laser-produced plasma has speeds (relative to the decelerated plasma near the interface) greater than the fast magneto-acoustic speed and thus shocks are produced. The shock envelope can be clearly seen in Fig.5.7(a), on the top of the image where we plotted the thermal beta. One can see two different kind of high beta regions: inside the cavity, where the plasma is relatively cold $\sim 50\,e\mathrm{V}$ but the magnetic field is low ($< 5\,\mathrm{T}$) and on the cavity walls, where the ion temperatures are large $\sim 500\,e\mathrm{V}$ and the field is relatively strong $> 20\,\mathrm{T}$. In these regions with significant magnetic fields gradients there is generation of strong electrical currents ($\mathbf{j} = (\nabla \times \mathbf{B})/\mu_0$) and strong magnetic forces ($\mathbf{j} \times \mathbf{B}$). The resulting structure is often called in the literature a diamagnetic cavity.

The magnetic confinement of the plasma just described largely depends on the relative importance the advection of magnetic field by the flow with respect to resistive diffusion. If the latter dominates, the field cannot be easily distorted or compressed. For

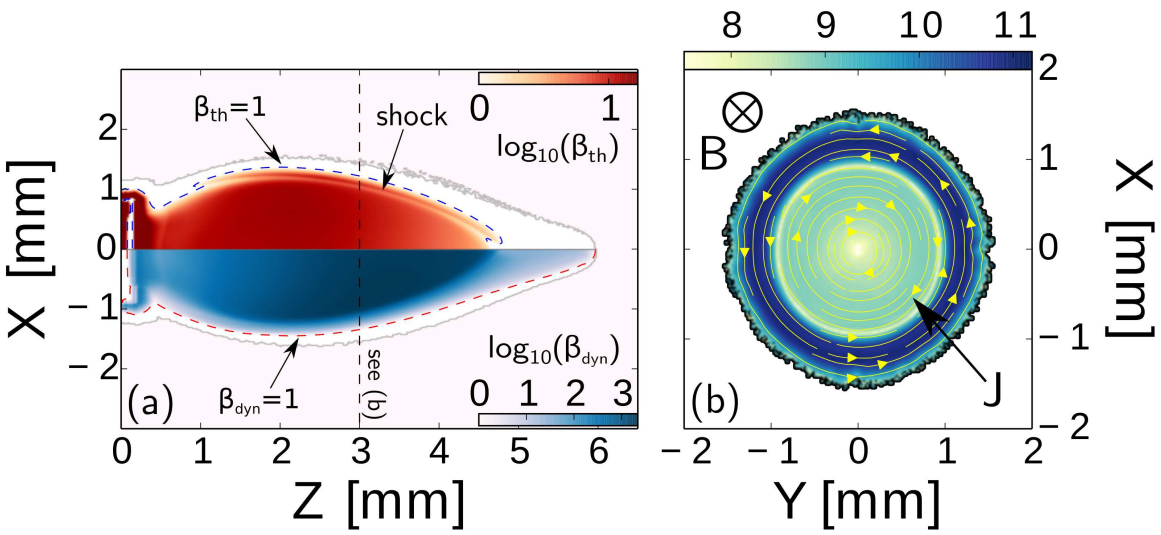

Figure 5.7: (a): 2D maps of the plasma betas: the thermal beta (thermal pressure over magnetic pressure) is shown with the red colormap while the dynamic beta (ram pressure over magnetic pressure) is represented using the blue colormap. (b):2D map of the decimal logarithm of the electrical current density taken in a x/y slice at $z = 3\,mm$ (see the vertical line in (b)). Both images are taken at $t = 8\,ns$.

the regime investigated here, the initial electron temperature is high and because the plasma resistivity $\eta \propto T_e^{-\frac{3}{2}}$, we have that the plasma conductivity is high. This "ideal MHD" regime, where the flux is "frozen" in the plasma, corresponds to a relatively high magnetic Reynolds number $R_m = UL/D_m \sim 100$ where $U \sim 10^5\,m.s^{-1}$, $L \sim 10^{-3}\,m$ and $D_m = \eta/\mu_0 \sim 1\,m^2.s^{-1}$ are the characteristic velocity, length-scale and magnetic diffusivity respectively (and μ_0 is the vacuum permeability).

We can estimate the intensity of current density on the cavity walls by comparing the magnetic force with the force associated to the ram pressure $(\rho(\mathbf{v}.\nabla)\mathbf{v})$. Shocks occur when the ratio of the two forces approaches unity, giving an estimated current density intensity $j \approx \rho v_\perp^2/Be_{shock} = 10^{11}\,A.m^{-2}$, where $e_{shock} = 100\,\mu m$ is the shock thickness, $\rho = 0.02\,kg.m^{-3}$ is the characteristic plasma flow density, $B = 20\,T$ is the characteristic magnetic field magnitude and $v_\perp = 100\,km.s^{-1}$ is the plasma velocity perpendicular to the magnetic field lines. The structure of electrical currents is shown in Fig.5.7(b). In the cavity region, the induced magnetic forces are directed inward, acting against the plasma expansion. These magnetic forces can be separated into two parts (Eq.5.5): a force resulting from a gradient of magnetic pressure (the first term in the right side of the equation) and an other one associated to the curvature of the magnetic field lines, the magnetic tension.

$$\mathbf{F_{magnetic}} = -\mathbf{n}(\mathbf{n}.\nabla)\frac{B^2}{2\mu_0} + \frac{B^2}{\mu_0}\frac{\mathbf{n}}{R_c} \tag{5.5}$$

where $\mathbf{n}$ is the unit vector perpendicular to the magnetic field vector pointing towards the center of the osculating circle of radius of curvature R_c. We can estimate the relative importance of these two components in evaluating their ratio:

$$r = \frac{Pressure}{Tension} \approx \frac{R_c}{e_{shock}} > 10$$

where e_{shock} is the shock thickness and we evaluated the gradient near the shock: $(\mathbf{n}.\nabla) \approx 1/e_{shock}$. We took typical values $R_c = 1\,mm$ and $e_{shock} = 100\,\mu m$. Whereas the shocks thickness doesn't change very much along the cavity walls, the curvature radius can be very large in some regions leading to a ratio r usually much greater than unity. The magnetic pressure is therefore the dominant component acting against the plasma flow. We highlight here the fact that magnetic forces appears because of a modification of the topology of the field (eq. gradients) but we notice that magnetic pressure values reached because of compression by the plasma flow are not very large. Indeed it appears that the magnetic pressure is at most ~ 1.56 greater than the nominal one ($P_{mag,0} \approx 160MPa$ and $P_{mag,max} \approx 250MPa$). It corresponds to a increase of the magnetic field magnitude of only ~ 25% ($B_{max} \approx 25T$). Here we don't take account of potential self-generated magnetic fields by the existence of regions with non-null electronic baroclinicity ($\nabla p_e \times \nabla n_e \neq 0$). For instance, because of the laser spatial energy profile, during the initial plasma expansion ($t < 1\,ns$) misaligned pressure and density electronic gradients can potentially generate significant magnetic fields (> 1T). We will discuss this mechanism in a dedicated section.

When the plasma crosses the shocks on the cavity edges, it is only the velocity component perpendicular to the shock front ? ($v_\perp$) that is reduced, while the parallel component is continuous across the shock front. The flow is then refracted at the shock and it is constrained to follow the cavity walls up to its tip where a conical shock occurs (Fig.5.4(b)). Then, if the pressure of the shocked plasma emerging from the conical shock is sufficiently high ($\beta_{th} >> 1$) another cavity is formed and the same process occurs again. This dynamics can be clearly seen in Fig.5.4(c) with three conical shocks resulting from the successive re-collimation events. The number of observable cavities is actually a function of the initial thermal beta (just after the laser pulse). Indeed, the greater the plasma beta the more cavities will be necessary to perfectly collimate the flow. This process is equivalent to the shock diamonds seen in supersonic exhaust plumes of aerospace propulsion systems but in our case this is the magnetic pressure which plays the role of the atmospheric pressure. We shall see in more details this process in the section describing the jet structure.

Now we address the heating processes that is responsible for the high temperatures seen in the shocks. This comes from two sources: ohmic heating which heats the electrons and is given by ηj^2, and of course, the conversion of kinetic energy into ion thermal energy in the shock. Inside the shock envelope, the characteristic plasma electrical resistivity is of the order of $\sim 10^{-6}\,\Omega.m$. We can also define an approximate volume of shocked plasma as $S_{cav}e_{shock}$, where the shock thickness is of the order of $e_{shock} \sim 100\,\mu m$ and S_{cav} is the surface of the cavity wall. We can then estimate the total energy transfered by the electromagnetic field to the electrons through ohmic heating, over the cavity lifetime δt, as:

$$E_{ohm} = \eta j^2 e_{shock} S_{cav} \delta t \tag{5.6}$$

Concerning the heating by the shock itself, the increase $\delta\epsilon_i$ in ion internal energy is related to the conversion of incoming kinetic energy, as [19]:

$$\delta\epsilon_i \approx \frac{12}{16(\gamma-1)} \rho v_\perp^2 \tag{5.7}$$

Given the relatively high Mach number, we can assume a strong shock and estimate the total energy transfered to ions during the cavity lifetime, as:

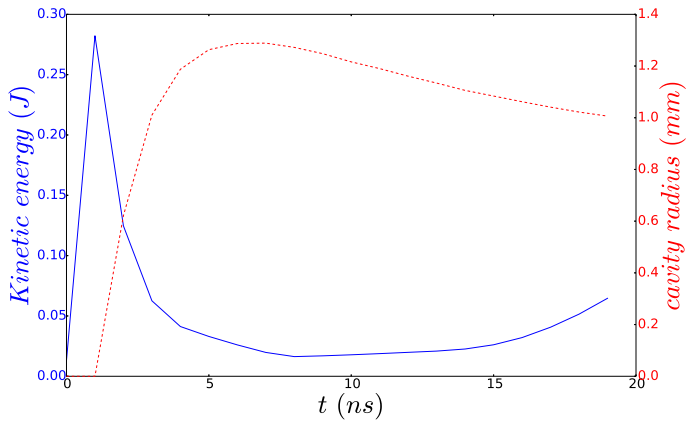

Figure 5.8: Plasma flow kinetic energy at z=0.6 mm and cavity radius time behavior

$$E_{shock} = \delta\epsilon_i v_\perp S_{cav} \delta t \tag{5.8}$$

Using these results, we can quantify the relative importances of these two sources of heating in the shock envelope: $E_{shock}/E_{ohm} = v_\perp \delta\epsilon_i / \eta j^2 e_{shock}$. Using the expression already found for the estimation of the current and the relation 5.7 for ϵ_i; we get:

$$\frac{E_{shock}}{E_{ohm}} \approx \frac{12}{16(\gamma-1)} \frac{e_{shock} B^2}{\rho v_\perp \eta} \tag{5.9}$$

Using typical values for the parameters present in this expression, and $\gamma = 5/3$, we estimate a ratio of $\frac{E_{shock}}{E_{ohm}} \sim 50$, indicating that the heating is dominated by the conversion of kinetic energy in the shocks. This is consistent with the idea that magnetic Reynolds number is high, and magnetic field diffusion is relatively unimportant. It has to be noted that if we evaluate the resistivity with the Spitzer expression [20], as the temperature of electrons in the shock envelope increases through equilibration with the hot ions, the ohmic heating becomes an even less important process.

Another interesting feature of the cavity dynamic is related to the fact that it is not stationary. Indeed, one can see that between Fig.5.4(b) and Fig.5.4(c) the (first) cavity has collapsed. This behavior is closely related to the time-dependent plasma outflow kinetic energy coming from the target.

In Fig.5.8 we plot the integrated kinetic energy ($\iint_{plane} 1/2\rho v_z^2 dS$) of the plasma crossing the intersecting plane at z=0.6 mm, very close to the initial target position, as a function of time. On this same figure, we also plot in red the radius of the cavity as a function of time. It can be seen that the radius of the cavity reaches its maximum value at $\approx 5\,ns$. The rise of the kinetic energy after 15 ns is due to the very dense, but slowly expanding plasma from target reaching the surface over which the integral is calculated. It is not due to an increase of the plasma velocity. Therefore, the shape of the kinetic energy in fig.5.8 described a pulsed ejection (in term of kinetic energy) from the target and implies that the cavity can not be sustained indefinitely. This is why the cavity collapses after reaching its maximum at $t \approx 5\,ns$.

In terms of characterization of the plasma inside the cavity, we have summarized some relevant plasma parameters at three different times in table 5.1. We note that because the magnetic field has been pushed out of the cavity, the plasma beta ($\beta = P_{th}/P_{mag}$) and the dynamic beta ($\beta_{dyn} = P_{ram}/P_{mag}$) are both greater than unity (the latter reaches values 1000). The magnetic Reynolds number R_m shows that the plasma is in a ideal

Table 5.1: Plasma parameters in the cavity at three different times. Values taken near the center of the cavity (z=1 mm at t=2 ns, z= 3 mm at t=10 ns and z=1.5 mm at t=15 ns).

Cavity	2 ns	10 ns	15 ns
β	13	11	2.8
β_{dyn}	490	1107	61
R_m	76	8	2.5
M	4.54	7.3	3
δ_e	$1.9.10^{-2}$	1.10^{-2}	$2.4.10^{-2}$
δ_i	5.10^{-2}	0.3	$8.6.10^{-2}$
$\omega_{ce}\tau_e$	0.24	0.11	0.08
$\omega_{ci}\tau_i$	4.10^{-4}	$1.6.10^{-4}$	$1.7.10^{-4}$
$\tau_{eq}\,(ns)$	0.24	1.5	0.32
$T_e(eV)$	73.9	18.1	12.6
$T_i(eV)$	72.8	14.9	12
$\rho\,(kg.m^{-3})$	0.15	0.005	0.025
$v\,(km.s^{-1})$	385	287	107

regime ($R_m >> 1$) for several nanoseconds after the laser energy deposition but that progressively, as time increases, magnetic diffusion can become an non negligible mechanism in the field transport ($R_m \rightarrow 1$ for t>15 ns). The fast magneto-acoustic Mach number, defined as $M_{ma} = v/c_{ma}$ where $c_{ma} = \sqrt{c_s^2 + c_a^2}$ is the fast magneto-acoustic speed (c_a is the Alfven speed $c_a = B/\sqrt{\mu_0\rho}$ and $c_s = \sqrt{Zk_bTe/m_i}$ is the ion acoustic speed) corresponds to supersonic and superalfvenic regimes ($M_{ma} \sim 1-5$). Values of $\delta_{e/i} = r_{gyro,e/i}/L$ ($r_{gyro,e/i}$ is the gyroradius of electrons/ions and L is the characteristic size of the cavity $L \sim 1\,mm$) are also shown in the table, and confirm the validity of the fluid description used here. Not shown in table.5.1, we note also that the mean free paths are $\sim 1\,\mu m$ for electrons and $\sim 10\,nm$ for ions justifying also the fluid description. Equilibration times are of the order of the plasma time scale dynamics ($\sim 1\,ns$) but in the cavity this is not really relevant since ion and electron temperatures are essentially the same. Finally, we see that $\omega_{ci}\tau_i \sim 10^{-4}$, indicating that ions are not magnetized inside the cavity. The electrons have also a parameter $\omega_{ce}\tau_e$ below unity and can be considered as relatively unmagnetized. Interestingly, we shall see later that in the jet formation we could have regions with strongly magnetized electrons. From this characterization, we can say somehow that the interior of the cavity is an "hydrodynamic" structure.

5.6 Jet structure and dynamics

We define the plasma jet as the relatively well collimated flow emerging from the tip of the cavity and propagating along the longitudinal direction (z-axis). For its description an interesting analogy can be made with the already studied supersonic jets propagating in external gas mediums (4.3). Two major families of these jets exist: one where the jet internal thermal pressure is approximately equal to the thermal pressure of the ambient medium, and one where the respective thermal pressures a very different. A useful dimensionless parameter to characterize supersonic jets is the ratio of pressures $K = p_{th}^{jet}/p_{th}^{amb}$ where p_{th}^{amb} is the ambient thermal pressure (see the chapter on idealized supersonic jets 4.3). In the case studied here, where the ambient gas medium is replaced by a background

magnetic field, the parameter K is replaced by the thermal plasma beta $\beta_{th} = p_{th}^{jet}/p_B^{ext}$ where $p_B^{ext} = B^2/2\mu_0$ is the external magnetic pressure. Based on the nomenclature used for hydrodynamic supersonic jets [21], we can classify our magnetically-collimated jets as: (a) , magnetically overexpanded jets, if $\beta_{th} << 1$; (b) magnetically pressure matched jets, if $\beta_{th} = 1$ and (c) magnetically underexpanded jets, if $\beta_{th} >> 1$. The parameters K and β_{th} give an indication on the internal structure inside the jets. Indeed, it is known that when the mismatch of jet and background pressure is strong (K,$\beta_{th} >> 1$ or K,$\beta_{th} << 1$), the flow develops the famous Mach diamonds (disks) pattern inside the jet [22]. In contrast, when $K \approx 1$, an internal network of conical shocks is observed. We observe the same behavior in our laser-produced magnetic jets. For example, in fig.5.4(b), the shock observed at cavity tip is in fact a small Mach disk. It appears in our regime because we have typically $\beta_{th} \sim 300$. A Mach disk is very effective (much more so than conical shocks) in converting bulk kinetic energy into thermal energy. Thus, in the case of magnetically over/under-expanded jets, we expect the laser-produced plasma flow to be strongly decelerated in the longitudinal direction and to become subsonic in the Mach disks post-shock regions. This is not necessarily the case in a conical shock. The location of the Mach disk corresponds in fig.5.5 to the large drop of velocity at $z \approx 6.2\,mm$ for the profile at t=10 ns. We can now further explore the validity of the solution $v_z = z/t$ for the velocity profile discussed earlier. This solution should be well verified for pressure-matched jets, but should break down when the pressure mismatch increases since in these cases, the flow velocity profile is strongly "parasitized" by the presence of decelerating Mach disks (as in fig.5.5 with the profile at $t = 10\,ns$).

An interesting aspect of the dependency of the internal shock pattern with the parameter β_{th} concerns the possibility to control a large number of plasma parameters of the jet, mainly through the temperature. Indeed, the decelerating effect of the Mach disks is of course associated with a strong heating of ions after the shock. Through equilibration with electrons, the temperature of both species is thus increased each time they cross the shock surface. One of the main repercussion of this effect is that, while one would expect the resistivity to increase as the plasma expands (because of the rarefaction and radiation losses), the jet in fact, keeps itself in a low resistivity regimes and thus large magnetic diffusivity times (and large magnetic Reynolds numbers). Now, as previously explained, the plasma containment/collimation by the magnetic field is possible because the field cannot diffuse inside the plasma. Thus, the internal shock structure of the jet appears as a self-regulated process which allows the flow to stay collimated over very large distances.

5.7 Jet 3D instabilities

First, the jet structure is a configuration potentially sensitive to the firehose/gardenhose instability, which may disrupt the flow through long (axial) wavelength, helical-like distortions (see [23]). The firehose instability, in our context, is due to the self-amplification of currents driven by transverse perturbations. This instability arises if the condition $P_{||} - P_{\perp} < B^2/2\mu_0$ is met in the jet (pressures are the sum of thermal and ram pressure). In the jet $P_{||} - P_{\perp} \sim \rho v_{||}^2$ because $v_{||}/c_s >> 1$ and $v_{\perp} \sim 0$. We have typically $\rho v_{||}^2 \sim 1330\,\mathrm{MP}a$ and the magnetic pressure is $\sim 160\,\mathrm{MP}a$ so the condition is not met. Thus it appears that the jet is expected to be relatively insensitive to the firehose instability generation but as we shall see hereinafter, the jet structure can still be affected by other instabilities.

We now focus on the plasma dynamics and the instabilities that develop in the flow in

the plane perpendicular to the initial magnetic field. In Fig. 5.9(b,c) we show the electron density in the $x-y$-plane, at the axial position z=4 mm and z=9 mm. The jet structure in the x-z plane is also shown at the same time (20 ns).

The observed structuring of the flow along the plasma/vacuum interface with the protruding "fingers" is characteristic of the Rayleigh-Taylor instability (RTI). The underlying physics of the RTI is given in A.4. This result shows that the structure of magnetically-collimated supersonic laboratory jets is intrinsically three dimensional. Indeed, the RTI is triggered if, in the frame of the interface, the effective acceleration g_{eff} has the opposite direction to the density gradient. Here, in our case, we have two phases that are favorable to the growth of the RTI. The first phase, $\lesssim 10\,ns$, corresponds to the deceleration of the laser-produced plasma by the action of the magnetic field on diamagnetic currents generated on the plasma/vacuum interface. In this situation, in the frame of the interface, the effective deceleration is pointing toward the vacuum (A.4) and thus this decelerating phase is Rayleigh-Taylor unstable. In our simulation, the maximum deceleration is $\sim 5\,10^{13}\,m.s^{-2}$ and corresponds to the end of the cavity expansion, a few nanoseconds before cavity stagnation.

We can interpret and formulate the deceleration process using simple energy considerations (see [24]). The initial kinetic energy of the laser-produced plasma plume is, as time increases, used to expel the magnetic energy from the diamagnetic cavity. As the cavity radius $r(t)$ increases up to its maximum value r_{max}, the magnetic pressure, $B_0^2/2\mu_0$, is applied over an increasing area, which is proportional to r^2. The resulting force, and thus the magnetic deceleration g_{eff}, is itself proportional to the radius squared and it is given by

$$g_{eff,dec,1}(t) = \frac{\pi B_0^2}{\mu_0 f M_{abl}} r^2(t) \tag{5.10}$$

where f is the fraction of the laser-ablated mass M_{abl} (typically we have, depending on the laser intensity, ablated mass of the order of $\sim 1\,\mu g$ [25]) effectively expelling the field. As the RTI growth rate is $\gamma = \sqrt{k g_{eff}}$ for flutelike modes, it is maximum near the diamagnetic cavity stagnation, where $r = r_{max} \approx 1.5\,mm$. The factor f is a rather ill-defined quantity but we estimate it from our simulations to be of the order of $\sim 10^{-4}$. Such a value gives a deceleration (using relation 5.10) of $2.25\,10^{13}\,m.s^{-2}$. This is consistent with the observed deceleration value mentioned above.

We will describe a simple way to obtain experimentally the factor f in the section concerning the jet variability with different parameters. Another way to estimate the deceleration is by using the expression we previously deduced for the diamagnetic currents, namely $j = \rho v_\perp / B e_{shock}$. The deceleration, which is due to the Lorentz force $\mathbf{j} \times \mathbf{B}$, thus corresponds to a deceleration $g_{eff,dec,2} \approx jB/\rho = v_\perp^2 / e_{shock}$. Taking characteristic values $e_{shock} = 100\,\mu m$ and $v_\perp = 100\,km.s^{-1}$ we find: $g_{eff,dec,2} = 10^{14}\,m.s^{-2}$. This expression is actually more useful since both the shock thickness and the lateral flow velocity can be inferred experimentally, for example from laser probing interferometry measurements. In addition to the initial deceleration undergone by plasma, a supplementary acceleration that may trigger the RTI occurs as plasma flowing along the cavity walls experiences a centrifugal force directed toward the exterior of the cavity.

This acceleration can be written as $g_{eff,c} = v_\parallel^2 / R_c$ where $v_\parallel$ is the velocity parallel to the field lines and R_c the curvature radius of this field. The relative importance of the two different possible accelerations is given by the ratio:

$$g_{eff,dec,2}/g_{eff,c} = \frac{\mathrm{R}}{e_{shock}}\left(\frac{v_{cdot}}{v_{\parallel}}\right)^2 \tag{5.11}$$

As a first approximation we can take the curvature radius to be equal to the cavity radius, $\frac{\mathrm{R}}{e_{shock}} \sim 6$, and from the simulation, the velocity ratio to be $\frac{v_{cdot}}{v_{\parallel}} \sim 3$. Then the ratio of the accelerations $g_{eff,dec,2}/g_{eff,c}$ turns out to be close to unity, indicating that both effects can play a role in the growth of the RTI. However in our case we see the flutes growing before the redirection of the flow, that is, before the centrifugal acceleration becomes important. Indeed the redirection of the flow along a well-formed, stationary cavity occurs only for a relatively short time and thus the centrifugal acceleration is negligible for the conditions investigated here. It is interesting to note that if one can establish a long-lived cavity, for example using repetitive laser pulses, the effect of centrifugal acceleration on the RTI growth should be much more important. This situation is indeed closer to astrophysical case, where one expects the lifetime of a cavity to be longer than the growth time of the instability [Ciardi et al, in preparation].

Taking into account the effect of a finite resistivity, which can damp the RTI through diffusion of magnetic field across the cavity walls, as well as the effect of ion viscosity which, through sheared velocities at fine scales, can mitigate the instability growth on these scales, the classical MHD RTI growth γ rate can be estimated by:

$$\gamma = \sqrt{k_\theta g_{eff}} - k_\theta^2(\nu + \mathrm{D_M}) \tag{5.12}$$

where $k_\theta = m/\mathrm{R}_c$ is the azimuthal wave number, m a positive integer and R_c the cavity radius. $\mathrm{D_M}$ is the magnetic diffusivity and ν is the ion kinematic viscosity (see [26]). Writing equation 5.12 we have only considered flutelike ($\mathbf{k}\cdot\mathbf{B} = 0$) modes because of the strong damping of the instability by magnetic tension (for non aligned modes, i.e. such that $\mathbf{k}\cdot\mathbf{B} \neq 0$, a third damping term should be added in eq.5.12:$-\sqrt{2(\mathbf{k}\cdot\mathbf{B})^2/(\mu_0\rho)}$).

Also the "quantification" introduced by the integer m in the wave number k_θ expresses the fact that the strongly unstable modes in the cavity of radius R_c are only those who are constructive, that is, such that $m\lambda = 2\pi\mathrm{R}_c$ where λ is the wavelength.

To study more quantitatively the observed instabilities, we performed a spatial Fourier analysis of the cavity/jet radius.

In a z-slice at a given z, we find the radius $r(\theta_n)$ as the distance between the central axis (r=0 mm) and the farthest point on the line defined by $\theta_n = cste$ with $\rho > \rho_{vac}$ (where in our simulations we fixed the vacuum for densities below $\rho_{vac} = 10^{-4}\, kg.m^{-3}$). We take N samples of the radius with $\theta_n = n2\pi/\mathrm{N}$ and we compute the Discrete Fourier transform (DFT) using the fast Fourier transform (FFT) algorithm:

$$\mathrm{A}_m = \sum_{n=0}^{\mathrm{N}-1} r(\theta_n)\exp(-2\pi i n m/\mathrm{N}) \tag{5.13}$$

A k-mode of complex amplitude A_m corresponds to a frequency $2\pi/m\,(rad)$ in the angle space and to a wavelength $\lambda_m(t) = 2\pi\bar{r}(t)/m$, where $\bar{r}(t) = \mathrm{A}_0(t)/\mathrm{N}$ is the mean radius obtained via the $k = 0$ mode amplitude. In the following discussion, we refer to a given mode as the "mode m", knowing that the number m corresponds to the number of observed spikes around the cavity at a given z. To take advantage of our 3D data, we used this method to obtain the cavity radius plotted in Fig. 5.8.

In fig.5.9(d,e) we plot the Fourier spectrum, $|\mathrm{A}_m|$, of the perturbations at the same axial position as the slices of fig.5.9(b,c). The first observation is that the modes that are excited depend strongly on the position along the jet's main axis (z). This aspect can

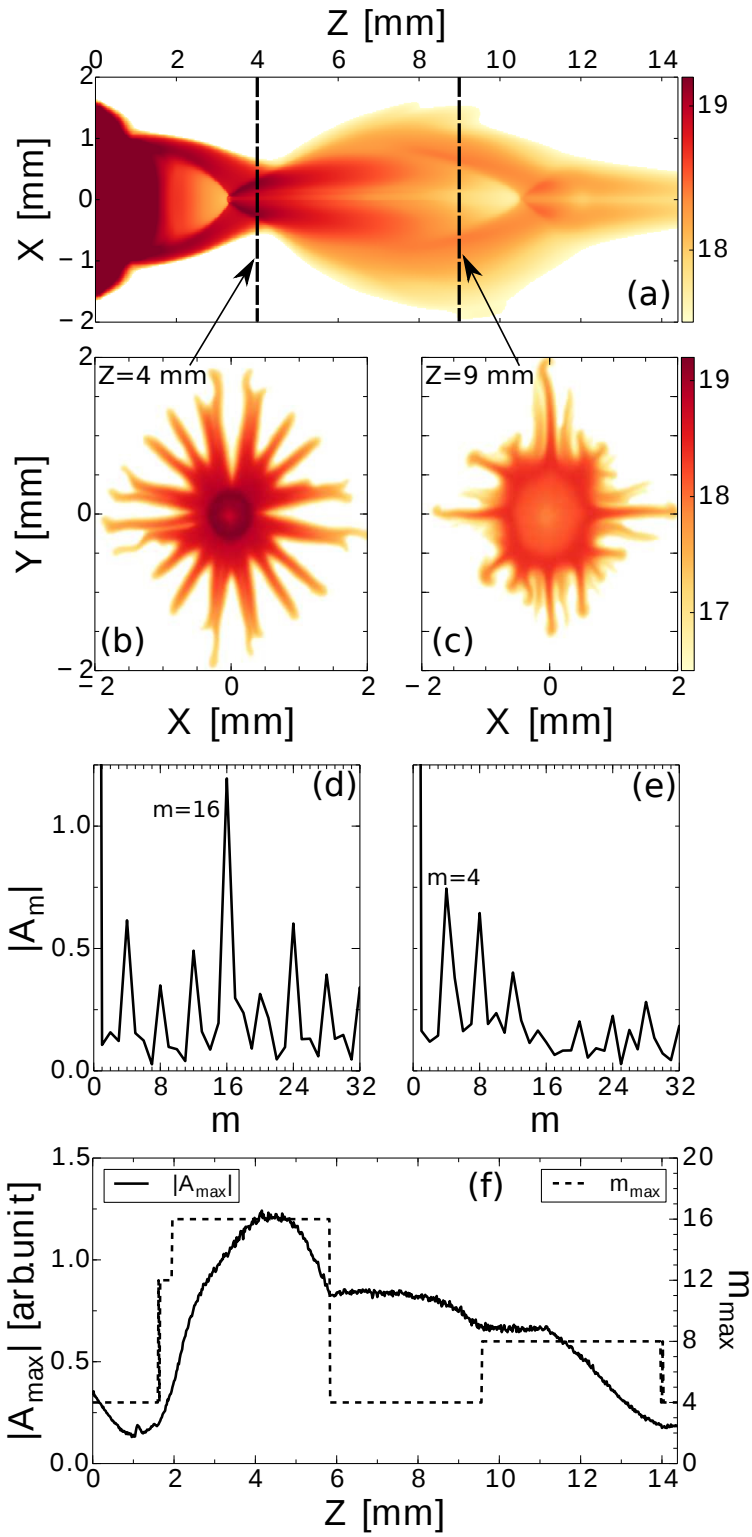

Figure 5.9: (a) 2D x/z maps of the decimal logarithm of electronic density at t=20 ns. (b/c) 2D x/y slices of (a) at z=4mm and z=9 mm showing the Rayleigh-Taylor filaments developing around the jet. (d/e) Mode amplitudes of the azimuthal perturbations (at z=4mm (d) and z=9 mm (e)) obtained from discrete Fourier transform (f) Full line:Amplitude of the most developed mode as a function of z. Dotted line: m value of the maximum mode. (5.13)

be clearly seen in fig.5.9(f) where, at a given time (18 ns), we plot the amplitude of the dominant mode as a function of z (full line) and the corresponding m number (dashed line). One can see that generally, high amplitude modes correspond to high number of spikes. It is consistent with the dependency of the RTI growth rate with $\sqrt{m}$. The maximum number of spike at this time is m=16 for z between 2 and 6 mm and it corresponds to the regions where the cavity had previously developed and collapsed (see fig.5.4). The maximum amplitude is observed at $z \sim 4\,mm$ and it reveals flutes of dimensions $\sim 1\,mm$, which is of the same order of the cavity radius. Thus in the case of a vacuum expansion, the scale of the developed instabilities cannot be considered as a marginal aspect of the plasma dynamics and backs the fact that such jets are 3D by nature. Farther, in the jet itself, we observe both strong $m = 4$ and $m = 8$ modes. As can be seen in the electron density slice in fig.5.9(c) the structure seems to be less "physical" with, for $m = 4$, very long flutes aligned on the computational Cartesian grid. This last point must be discussed because it is inherent to (magneto-)hydrodynamic 3D-simulations and should be taken into account when analyzing the occurrence of instabilities. Indeed, looking at both spectrum in fig.5.9(d,e), one can see the preferential excitation of modes such that $m = 4 \times k$ where k is a natural integer. Even more importantly, this preferential feeding is the larger when m is small. This effect can be somehow associated to a numerical damping (in addition to the resistive damping present in our simulation) and a frequency filter which selects the modes m which are multiples of 4. The reason of this behavior comes from the fact that the mass fluxes are computed at the center of each face of the cells and thus, it is always easier to fill adjacent face-to-face cells. Of course, the spatial resolution used in the simulations has also a strong effect but does not change this effect. For a discussion about the influence of the spatial resolution see the dedicated section 5.11. The presence of RTI flutes all around the cavity and jet present some interesting implications related to the applications of such magnetically-collimated jets. We already mentioned the possible study of magnetized accretion dynamics, but there could be also interests in the field of laser deposition, material ablation [27].

As a last point, supersonic jets are often associated with the Kelvin-Helmholtz instability (KHI) [22]. Of course, in a vacuum expansion, not such behavior is observed because of the absence of strong sheared flows. As we shall see later, when adding a gas background in our setup, the growth of the KHI is also absent because of the stabilizing effect of the magnetic field. In definitive, the described setup in this paper allows one to generate strongly stable jets in the longitudinal (z) direction but very unstable in the azimuthal direction (x-y). Contrary to the very disruptive current-driven instabilities, the Rayleigh-Taylor instability does not cause the rupture of the plasma jet. Once the feeding source of the RTI, namely the effective acceleration, is attenuated, the existing flutes are simply advected with the flow. The strongest accelerations occurs in the cavity, a few millimeters from the target surface, and at relatively early times ($\lesssim 20\,ns$).

5.8 Jet structure dependence with different parameters

It is interesting to evaluate the dependence of the cavity radius with laser energy and magnetic field magnitude. If we consider that the laser energy ϵ_L is absorbed in a hemispherical volume $V = 2/3\pi R^3$ the plasma ram pressure can be estimated by $p_{ram} = f\epsilon_L/V$ where f represents the fraction of laser energy converted into plasma kinetic energy. A rough estimate of the maximum cavity radius is obtained by equating the plasma ram pressure to the magnetic pressure: :

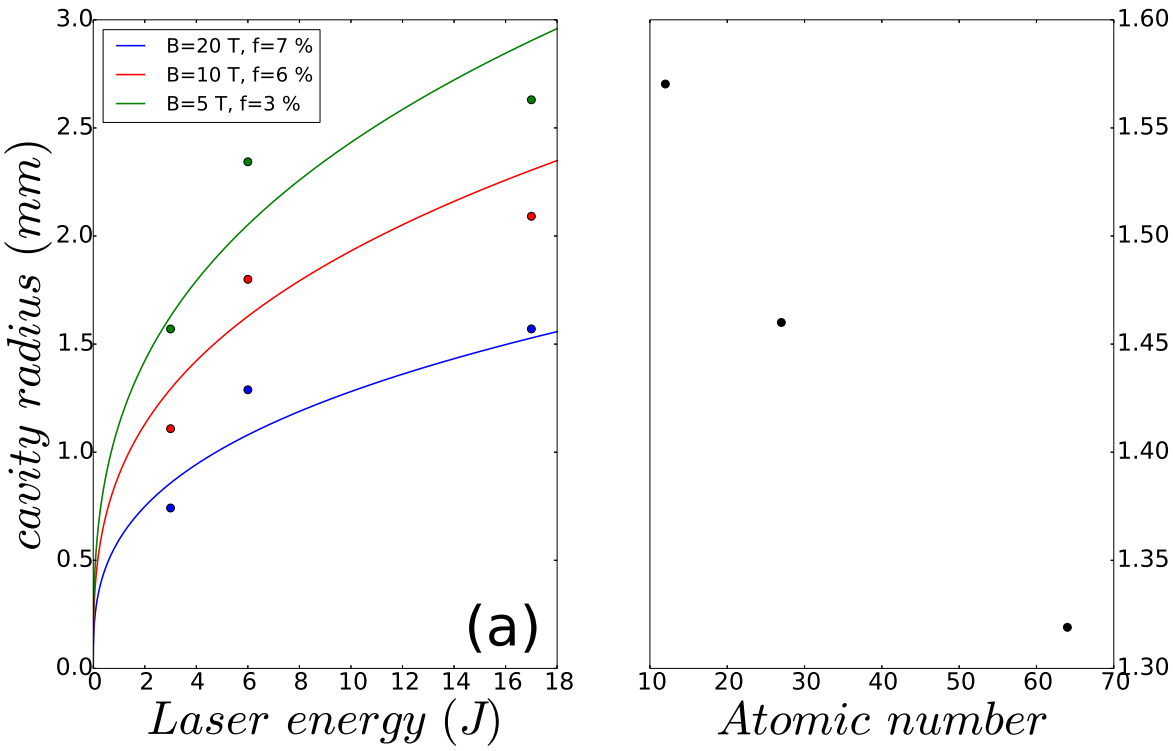

Figure 5.10: Left: Cavity maximum radius as a function of the laser energy (for 0.5 ns pulses) for three different magnetic fields (5, 10 and 20 T). Dots are taken from simulations whereas full lines are computed from 5.14. Right: Maximum cavity radius as a function of the target material atomic number for a 3 J pulse and a 5 T field.

$$R(\epsilon_L, B) \sim (\frac{3\mu_0 f' \epsilon_L}{\pi B^2})^{1/3} \tag{5.14}$$

In Fig.5.10(a) we plot both the dependence of the cavity radius with ϵ_L and the magnetic field B. We find good agreement with $f' = 3-7\%$. The new factor f' is actually closely related to the factor f introduced before in formula 5.10. Indeed, the ratio of laser energy used to expel the magnetic field from the cavity can be written as the kinetic energy of the ablated mass times the factor f, so that $1/2 f M_{abl} v^2 = f' \epsilon$. Thus, for experimental purposes, supposing that we know the energy laser and the magnetic field magnitude, we need to measure experimentally the maximum cavity radius, the (lateral) plasma velocity and the ablated mass in order to retrieve the value of both factors f and f'. The first two quantities can be quite easily estimated using interferometry images, for example, whereas the ablated mass, as discussed in the first section, may be measured after the experiment, with much less constraints on the diagnostic tools.

An other interesting discussion concerns the behavior of the plasma dynamics when changing the target material. From Fig.5.10(b), one can see the decrease of maximum reached radius with the atomic number Z.

Finally, we want to look at the influence of the initial magnetic field orientation on the plasma dynamic. In early studies of Classical T Tauri stars, it has been stated that the fact that bright and well collimated outflows (jets) from these systems are observed is strongly associated to large scale aligned magnetic fields [28]. More recently, with improved imaging techniques, weaker and/or shorter jets have been discovered and it appears that these jets are more often oriented far away form the direction of the magnetic field [29]. Thus, studying in the laboratory the impact of misaligned flows and fields present a strong interest to understand the mechanisms at work.

In the top three images of fig.5.11 we show 3D rendering of the mass density at the same time (15 ns) for three different angles (10, 30 and 45 degrees). The initial laser energy is exactly the same in all cases. Thanks to the ideal regime and the efficient magnetic collimation of the laser-produced plasmas, one can expect the flow to always tend to align itself with the magnetic field lines direction and this is indeed what we see for the three cases. However it must be noted that as the angle increases, the shape of the jet changes significantly. Whereas for relatively small angles ($\theta <\sim 30°$) the jet can be considered as almost axisymmetric, around the direction of the field, for larger angles the flow become much more spread. In order to quantify the efficiency of the collimation, we plot, in fig.5.11, the total plasma momentum parallel to the magnetic field orientation as a function of the angle of inclination. These results led us to define an approximate critical angle for which the interaction of the flow with the magnetic field leads to weakly collimated jet. From our simulation, this angle lies between 20 and 30°. This value is consistent with very recent experimental results in the same configuration studied here [Revet.G, Khiar.B et al., in prep.].

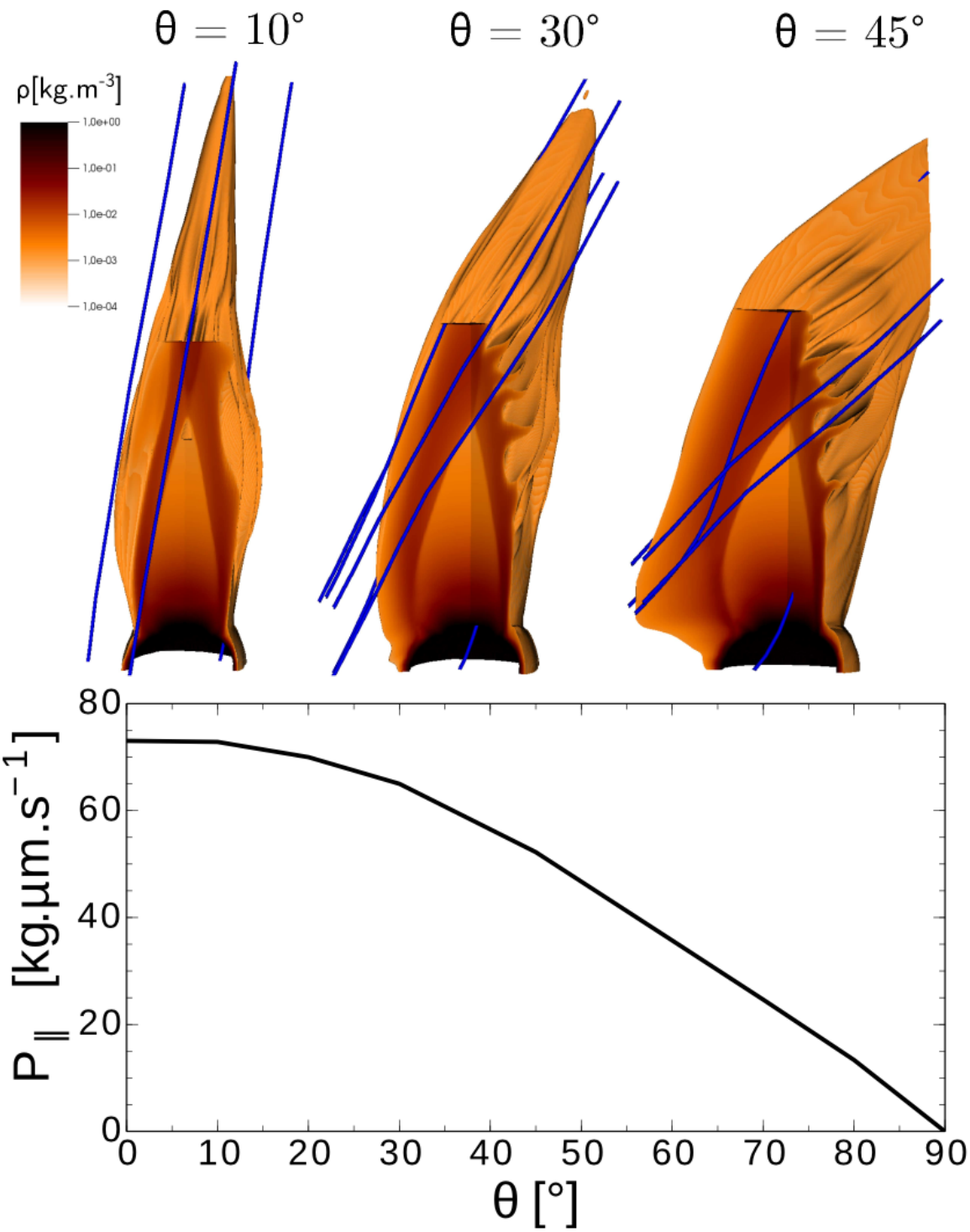

Figure 5.11: Above: 3D iso-volumes of mass density when changing the orientation of the magnetic field at θ = 10°, 30° and 45°. The three pictures correspond to a time t=14 ns. Curve: Mean total impulsion in the direction of the magnetic field as a function of tilt angle. The initial laser energy is the same in all cases: 17 J (for a 0.5 *ns* pulse).

5.9 Influence of a gas background and mitigation of the Rayleigh-Taylor instability

In this part we briefly explore a set up with a low pressure gas background in addition to the external magnetic field. The initial setup is exactly the same as in the previous discussion but the domain is filled with a carbon gas at the room temperature (290 K) at a density of $\rho_b = 5 \cdot 10^{-4}$. It corresponds to a thermal pressure $\sim 1\,kPa$, a value completely negligible regarding the magnetic pressure of $\sim 160\,MPa$. We are thus staying in a regime where the collimation process will be realized by the magnetic field and not the external medium, as it well known in the study of many radio astrophysical supersonic jets [30]. Although a carbon gas in not realistic, the set up serves nevertheless to explore the jet dynamics in the presence of an external medium. However, the anisotropy of the magnetic pressure implies that along the jet axis (z), the background pressure will play the dominant role. In fig.5.12(a) we show a 2D mass density slice of this configuration. As one can see, in the presence of a background the plasma jet presents several features not seen before in the "vacuum" expansion. First, a layer of background material denser than that of the unperturbed medium develops around the jet. The head of this layer is the front of the bow shock set off because the jet speed is highly supersonic relative to the sound speed of the background (corresponding to mach numbers > 1000). All the material inside this layer comes from the shocked background gas and is typically at ion temperatures $\sim 4\,keV$. Supersonic jets propagating in external medium are known to often develop what is called a "cocoon" which is a layer, between the jet core and the background gas, composed of jet material flowing backward after passing through the terminal shock at the jet head [31]. Here, we are in a situation where the cocoon cannot be observed because of the relatively large density ratio $\rho_{jet}/\rho_b > 2$ as well as the radiative losses (see [22]). Interestingly, there is no mixing of material from the jet with material from the background because the high supersonic regime as well as the presence of the strong axial magnetic field annihilate completely the Kelvin-Helmholtz instability typically arising from the velocity shear at the jet interface. Of course, another important aspect of adding a background gas to the initial setup concerns the influence on the Rayleigh-Taylor instability. Indeed, when studying previously the RTI in the vacuum expansion, we implicitly considered an Atwood number A equals to one, which is the "worst" case in terms of instability growth, but in the present case we have $A \lesssim 0.3$ and thus in terms of growth rate we should expect a reduction of a factor $\sqrt{0.3} \sim 0.5$. To verify this prediction, we plot in fig.5.12(b) the amplitude of the maximum mode as a function of z, averaged on the first 30 ns. We compare the case of the vacuum expansion with the case where a background has been added (with both densities $\rho_b = 5 \cdot 10^{-4}$ and $\rho_b = 1 \cdot 10^{-3}$. As one can see, we observe a reduction of the mean amplitude of the unstable mode of at least a factor ~ 0.5 when the background gas is present. We also see, in agreement with the definition of the Atwood number, that if the gas background is more dense, the instability is reduced even further. A slice of the mass density at z=9 mm is shown in fig.5.12(c), to be compared with the one already discussed in fig.5.9(c), and we clearly see the smaller Rayleigh-Taylor fingers constrained by the shell of background material. Another non-previously seen feature in this case is the development of the RTI at the jet head. The jet is decelerated by the material in front of it and thus we find ourselves again in a favorable situation for the development of the RTI. The conclusion on the influence of a non-vacuum medium in our setup goes quite in the opposite direction to the one given in the previous section on the instabilities. Indeed, when a background gas is added, the stability of the jet in the longitudinal direction (z) is weaker (only at the jet head actually) whereas in the azimuthal direction (x-y), it is en-

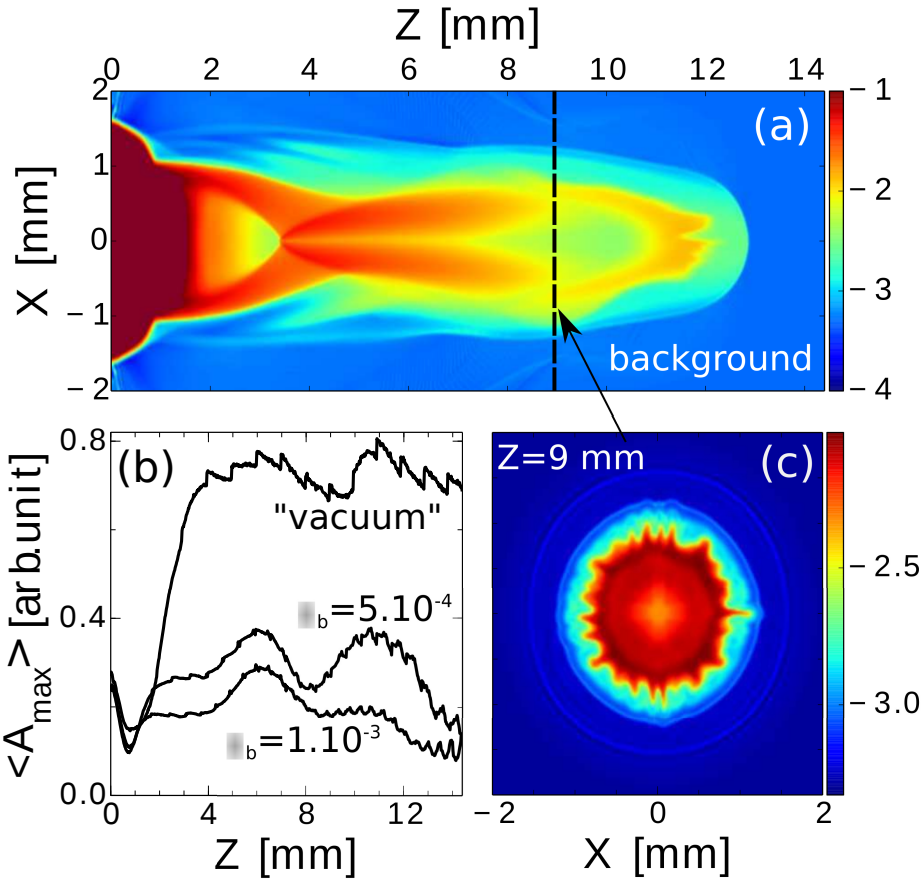

Figure 5.12: (a)2D maps of the decimal logarithm of the mass density for the case where a gas background, in addition to the magnetic field of 20 T, fills the simulation domain. It corresponds to $t = 20\,ns$(b) Time-averaged (on the first 30 ns) of the maximum mode amplitude as a function of z. (c) 2D x/y slice of the decimal logarithm of the mass density at z=9 mm.

hanced. This modified setup could thus be interesting for applications where one wants to obtain quasi two-dimensional magnetically-collimated plasma jets.

5.10 Frequency resolved radiations imaging

Here we investigate plasma self-emission in different frequency ranges. The radiation losses model in GORGON does not allow us to distinguish the interesting frequency domains where we could identify characteristics structures like shocks. Indeed, the optically thin model considers only free-bound, frequency integrated radiation. Therefore we conduct post-treatment of the 3D MHD simulation data via an in-house code which solves the population balance equations of different excited states and for each degree of ionization. We use here the Screened Hydrogenic Model (SHM) [32]. We seek to compute the integrated plasma emissivity ϵ on a limited frequency range $[\nu_1, \nu_2]$

$$\epsilon = \kappa_P \int_{\nu_1}^{\nu_2} B_\nu d\nu \tag{5.15}$$

where κ_P is the average Planck opacity between ν_1 and ν_2 and it is computed by the code. B_ν is the spectral radiance given by the Planck's law. The emissivity is thus given by

$$\epsilon = \frac{2\kappa_P (k_B T_e)^4}{c^2 h^3} \sum_{n=1}^{+\infty} \left[e^{-nx} \left(\frac{x^3}{n} + \frac{3x^2}{n^2} + \frac{6x}{n^3} + \frac{6}{n^4} \right) \right]_{x_2}^{x_1} \tag{5.16}$$

where $x_{1/2} = h\nu_{1/2}/k_B T_e$. Practically, convergence is obtained with n=500. 2D maps of emissivity integrated along the line of sight are shown in Fig. 5.13 for two energy ranges. One can see that for energies between 1 eV and 100 eV (including the visible range), the largest source of emission comes from the relatively cold dense plasma expanding slowly at the sound speed just in front of the target. At higher energies, radiations come mainly from the shocked plasma in the cavity walls and the dense plasma at the foot of the cavity is weakly emitting. More interestingly, in this energy range we can clearly see the effect of the RT type filaments on the emission maps. The three darkest fringes inside the cavity should be correlated with the electron density x/y maps in fig.5.9(b,c). Observing these instabilities experimentally through electron map density is not straightforward because the probing direction of the laser has to be in the same direction than the jet propagation. It results in an integrated laser path that is far too large to have a detectable signal. We show here that it could be possible to get clues about the presence of these instabilities via self-emission of the plasma, provided that a good choice of energy range is done. Furthermore, one has to take account that a time-integrated diagnostic would likely wash out the striation features associated with the instabilities.

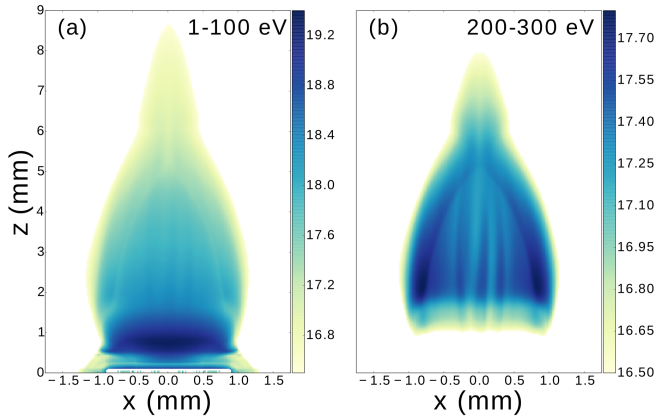

Figure 5.13: 2D maps of the decimal logarithm of the emissivity integrated along the line of sight at t=10 ns.

5.11 Influence of the spatial resolution on the jet 3D structure

As mentioned before, the spatial resolution has an important effect on the modeled structure of the jet. In fig.5.14(a,b,c,d) we show x/y slices of the decimal logarithm of the electron density at $t = 20\,ns$ for four different resolutions: $dx = 10, 30, 40, 50\,\mu m$ and at $z = 4\,mm$ (comparable to the slice for the $dx = 20\,\mu m$ case shown in fig.5.9(b)). It can be clearly seen that as the resolution decrease, the finest structures disappear and the unstable modes that subsist are mainly the $m = 4$ and $m = 8$ modes. In fig.5.14(e) we show the time-averaged (on the first 30 ns) amplitude of the maximum mode as a function of z. As one can see, a lower resolution (i.e a greater dx) triggers an important growth of the numerical-enhanced m=4 mode all along the jet whereas near the cavity ($z \lesssim 4\,mm$), where lateral deceleration is important, the resolution does not change that much the results since in these regions the growth of RT filaments is really "fed" by the same physical process.

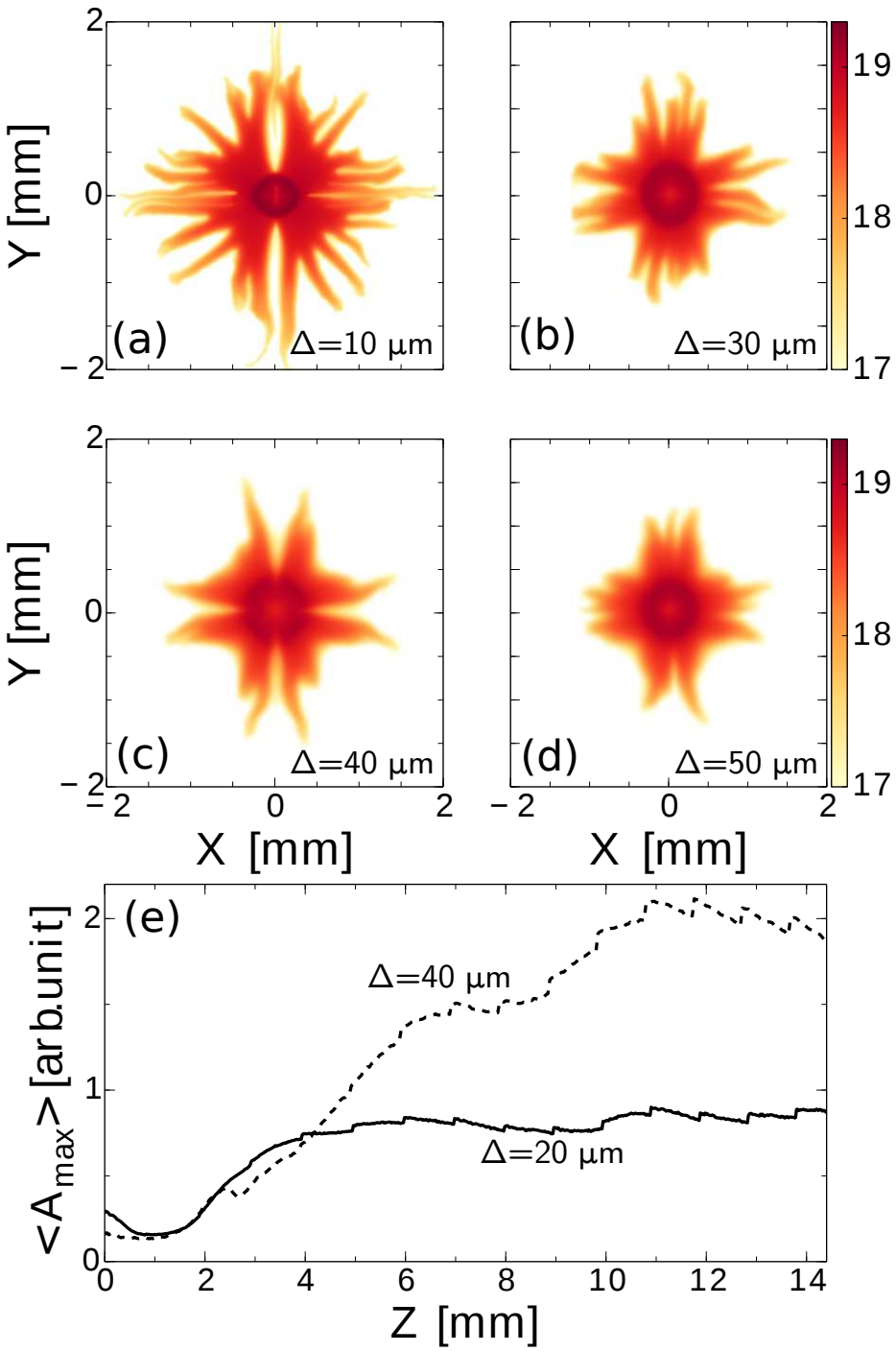

Figure 5.14: **(a,b,c,d)** X/Y slices of the decimal logarithm of the electron density at $t = 20\,ns$ for four different resolutions: $dx = 10\,\mu m$ (a), $dx = 30\,\mu m$ (2),$dx = 40\,\mu m$ (c),$dx = 50\,\mu m$ (d). **(e)** Time-averaged (on the first 30 ns) amplitude of the maximum mode as a function of z.

5.12 Bibliography

[1] A. Ciardi, T. Vinci, J. Fuchs, B. Albertazzi, C. Riconda, H. Pépin, and O. Portugall. *Phys. Rev. Lett.*, 110:025002, 2013. 120

[2] B. Albertazzi, A. Ciardi, M. Nakatsutsumi, T. Vinci, J. Béard, R. Bonito, J. Billette, M. Borghesi, Z. Burkley, S. N. Chen, T. E. Cowan, T. Herrmannsdörfer, D. P. Higginson, F. Kroll, S. A. Pikuz, K. Naughton, L. Romagnani, C. Riconda, G. Revet, R. Riquier, H.-P. Schlenvoigt, I. Yu. Skobelev, A.Ya. Faenov, A. Soloviev, M. Huarte-Espinosa, A. Frank, O. Portugall, H. Pépin, and J. Fuchs. Laboratory formation of a scaled protostellar jet by coaligned poloidal magnetic field. *Science*, 346(6207):325–328, 2014. 120, 121

[3] DP Higginson, G Revet, B Khiar, J Béard, M Blecher, M Borghesi, K Burdonov, SN Chen, E Filippov, D Khaghani, et al. Detailed characterization of laser-produced astrophysically-relevant jets formed via a poloidal magnetic nozzle. *High Energy Density Physics*, 23:48–59, 2017. 120, 122, XXX

[4] B. Khiar et al. D. Higginson. Enhancement of quasi-stationary shocks and heating via temporal-staging in a magnetized, laser-plasma jet. *PRL*, 2017 (submitted). 120

[5] Claire Baccou. *Initiation de réactions nucléaires par des protons accélérés par laser*. PhD thesis, 2016. Thèse de doctorat dirigée par Labaune, Christine Physique des plasmas Paris Saclay 2016. 120

[6] B Albertazzi, J Béard, A Ciardi, T Vinci, J Albrecht, J Billette, T Burris-Mog, SN Chen, D Da Silva, S Dittrich, et al. Production of large volume, strongly magnetized laser-produced plasmas by use of pulsed external magnetic fields. *Review of Scientific Instruments*, 84(4):043505, 2013. 120

[7] D. P. Higginson, P. Korneev, J. Béard, S. N. Chen, E. d'Humières, H. Pépin, S. Pikuz, B. Pollock, R. Riquier, V. Tikhonchuk, and J. Fuchs. A novel platform to study magnetized high-velocity collisionless shocks. *High Energy Density Physics*, 17:190–197, December 2015. 120

[8] J. Béard and F. Debray. The French High Magnetic Field Facility. *Journal of Low Temperature Physics*, 170:541–552, March 2013. 120

[9] J P Zou, C L Blanc, P Audebert, S Janicot, A M Sautivet, L Martin, C Sauteret, J L Paillard, S Jacquemot, and F Amiranoff. Recent progress on luli high power laser facilities. *Journal of Physics: Conference Series*, 112(3):032021, 2008. 121

[10] A. Flacco T. Vinci. Neutrino. 2014. 121

[11] T. Pisarczyk, R. Arendzikowski, Z. Patron, and P. Parys. Polari interferometer with automatic images processing for laser plasma diagnostic. *Laser and Particle Beams*, 12:549, 1994. 121

[12] D. D. Ryutov, N. L. Kugland, H.-S. Park, S. M. Pollaine, B. A. Remington, and J. S. Ross. Collisional current drive in two interpenetrating plasma jets. *Physics of Plasmas*, 18(10):104504, 2011. 123

[13] D. D. Ryutov, N. L. Kugland, H.-S. Park, C. Plechaty, B. A. Remington, and J. S. Ross. Intra-jet shocks in two counter-streaming, weakly collisional plasma jets. *Physics of Plasmas*, 19(7):074501, 2012.

[14] D. D. Ryutov, N. L. Kugland, M. C. Levy, C. Plechaty, J. S. Ross, and H. S. Park. Magnetic field advection in two interpenetrating plasma streams. *Physics of Plasmas*, 20(3):032703, 2013. 123

[15] S. Atzeni, A. Schiavi, F. Califano, F. Cattani, F. Cornolti, D. Del Sarto, T. V. Liseykina, A. Macchi, and F. Pegoraro. Fluid and kinetic simulation of inertial confinement fusion plasmas. *Computer Physics Communications*, 169:153–159, July 2005. 123, 124, XXXI

[16] Sergei I Anisimov and B S Luk'yanchuk. Selected problems of laser ablation theory. *Physics-Uspekhi*, 45(3):293, 2002. 127

[17] D. B. Schaeffer, A. S. Bondarenko, E. T. Everson, S. E. Clark, C. G. Constantin, and C. Niemann. Characterization of laser-produced carbon plasmas relevant to laboratory astrophysics. *Journal of Applied Physics*, 120(4):043301, 2016. 127

[18] K. R. Chen, T. C. King, J. H. Hes, J. N. Leboeuf, D. B. Geohegan, R. F. Wood, A. A. Puretzky, and J. M. Donato. Theory and numerical modeling of the accelerated expansion of laser-ablated materials near a solid surface. *prb*, 60:8373–8382, September 1999. 128

[19] Naval Research Laboratory. *NRL Plasma Formulary*, 2013. 131

[20] Lyman Spitzer Jr. Physics of fully ionized gases. *American Journal of Physics*, 31(11):890–891, 1963. 132

[21] Winkler Norman. Supersonic jets. *LOS ALAMOS SCIENCE*, 1985. 134

[22] M. L. Norman, K.-H. A. Winkler, L. Smarr, and M. D. Smith. Structure and dynamics of supersonic jets. *aap*, 113:285–302, September 1982. 134, 138, 142

[23] G. Benford. Stability of galactic radio jets. *ApJ*, 247:792–802, August 1981. 134

[24] J. D. Huba. Onset criteria for structure in magnetically confined plasma expansions. Technical report, July 1987. 135

[25] J. Grun, R. Decoste, B. H. Ripin, and J. Gardner. Characteristics of ablation plasma from planar, laserdriven targets. *Applied Physics Letters*, 39(7):545–547, 1981. 135

[26] T.S Green and G.B.F. Niblett. Rayleigh-taylor instabilities of a magnetically accelerated plasma. *Nuclear Fusion*, 1(1):42, 1960. 136

[27] Chao-Ching Ho, Guan-Ru Tseng, Yuan-Jen Chang, Jin-Chen Hsu, and Chia-Lung Kuo. Magnetic-field-assisted laser percussion drilling. *The International Journal of Advanced Manufacturing Technology*, 73(1):329–340, Jul 2014. 138

[28] K. M. Strom, S. E. Strom, S. C. Wolff, J. Morgan, and M. Wenz. Optical manifestations of mass outflows from young stars - At atlas of CCD images of Herbig-Haro objects. *ApJS*, 62:39–80, September 1986. 140

[29] Menard, F. and Duchene, G. On the alignment of classical ttauri stars with the magnetic field in the taurus-auriga molecular cloud. *A&A*, 425(3):973–980, 2004. 140

[30] George Miley. The structure of extended extragalactic radio sources. *Annual Review of Astronomy and Astrophysics*, 18(1):165–218, 1980. 142

[31] R. D. Blandford and M. J. Rees. A 'twin-exhaust' model for double radio sources. *mnras*, 169:395–415, December 1974. 142

[32] K Eidmann. Radiation transport and atomic physics modeling in high-energy-density laser-produced plasmas. *Laser and particle beams*, 12(2):223–244, 1994. 144

Chapter 6

Toward controlling the temporal properties of laser-produced plasma jets

Sommaire

6.1 Introduction 152
6.2 Experimental and numerical setup 152
6.3 Results 153
6.4 Bibliography 158

6.1 Introduction

In the chapter where we described the general laboratory supersonic jets (5), we mentioned the possibility of adding a laser precursor to study unsteady jets. This is the topic of this chapter, where we present the investigation, both experimental and numerical, of two laser pulses (delayed in time) interacting with a solid target in a magnetic field. This work has been submitted to Physical Review Letters and was done in collaboration with the experimental group lead by Julien Fuchs at LULI. So far, little attention has been paid on how variations at the base of the ejected plasma can play a role in the long-term dynamics of the system [1]. While few experimental studies, temporal variations of mass ejection are important in astrophysical jets are responsible for the internal shocks seen in the jet body, and provide a proxy to understand mass accretion. Typical temporal variations in YSOs jets are of the order of a few years to several decades (see [2] for a recent review on YSOs jets).

Experimentally, unsteady mass ejection is realized by irradiating a solid-target placed in a 20 T magnetic field with, first, a co-linear precursor laser pulse (10^{12} W/cm^2) and, then, a main pulse (10^{13} W/cm^2) arriving 9 to 19 ns later. Varying the time-delay between the two pulses is found to control the divergence of the expanding plasma cavity, which is shown to increase the strength and heating in the conical shock that is responsible for jet collimation. In this staged pulse configuration, measurements show that electron temperatures are a factor 2-4 higher than when using only the main pulse alone; also, plasma density is increased in the shock. Overall, the results show that plasma collimation due to shocks against a strong magnetic field can lead to stable, astrophysically-relevant jets, even in the case of strong variability at the source.

6.2 Experimental and numerical setup

The experiment was performed using the chirped Nd:glass laser (τ_L = 0.6 ns, λ_L = 1057 nm) of the ELFIE facility at the Laboratoire pour l'Utilisation des Lasers Intenses (LULI). The laser beam was split temporally into two beams, separated by either 9 or 19 ns, and subsequently recombined co-linearly using non-polarizing beam splitters and focused on target (diameter, $\phi_L = 0.7\,mm$) using the same lens and random phase plate [3]. In the temporally-staged configuration, the first beam, called the precursor, had an on-target energy (intensity) of 3 J (1×10^{12} W/cm^2) and the second pulse, called the main pulse, had 17 J (7×10^{12} W/cm^2). Additionally, we also present for comparison results with a main pulse only setup (i.e. identical but without the precursor). As shown in Fig.6.1, both beams irradiated a CF_2 (i.e. Teflon) target immersed in a 1-µs pulsed, 20 T external magnetic field aligned along the plasma expansion axis[4; 5]. The plasma electron density evolution was investigated via a Mach-Zehnder interferometer using a 5 ps (λ_L = 528 nm) probe beam. Optical emission along the same line-of-sight was studied through a one-dimensional slice taken along the jet propagation axis and streaked in time using a Hamamatsu C7700 streak camera with S20 photocathode. To diagnose the electron temperature, T_e, a time integrated X-ray focusing spectrometer with spatial resolution (FSSR) was used along the jet axis. The relative intensities of He-like Fluorine lines were analyzed to obtain the time-integrated T_e and electron density, n_e[6; 7].

Simulations are performed with the code GORGON, with the precursor laser pulse interaction modeled with the code DUED [8], as described in section 5.3. The main laser pulse is modeled using our own laser transport module implemented in GORGON (see

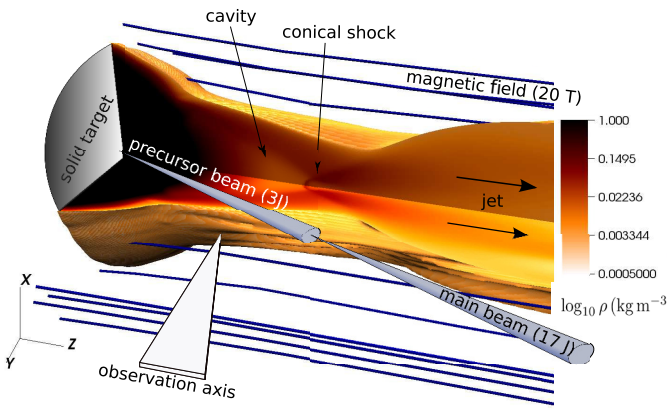

Figure 6.1: Schematic of the experimental setup and 3D MHD simulations of the overall plasma dynamics. The volume rendering shows the simulated mass density at 22 ns, for the case of a single 17 J pulse, with a 1/4 of the volume removed to show the internal structure of the flow. Two co-linear laser pulses (3/17 J), that are temporally-offset by either 9 or 19 ns, irradiate a CF_2 target embedded in a 20 T magnetic field. The diagnostic observation axis is also shown.

2.5.5). The pulses parameters in the simulation are identical to the experimental ones. The computational domains in GORGON is defined by a uniform Cartesian grid of dimension $6\,mm \times 6\,mm \times 14.4\,mm$ and a number of cells equals to $300 \times 300 \times 720 = 6.48\,10^7$. The spatial resolution is homogeneous and its value is $dx = dy = dz = 20\,\mu m$.

6.3 Results

The top row of Fig. 6.2 shows the plasma electron density at three times for the case of the main pulse alone. The plasma dynamics consist of three distinct phases (for an extensive discussion see section 5.5 and [4; 11]): (i) the creation of a low density cavity surrounded by a shock envelope (Fig. 6.2a); (ii) the formation of a conical shock (Fig. 6.2d) at the tip of the cavity, which then (iii) re-collimates the plasma plume into a jet (Fig. 6.2g). These phases are also captured in the MHD simulations shown in Fig. 6.5. The next two rows in Fig. 6.2 show electron density maps in the temporally-staged cases with either 9 or 19 ns delay between the precursor and main laser pulses.

Let's focus first on the formation of the cavity and the shock envelope bounding it (Fig. 6.2a-c, also Fig. 6.5b,c). Initially, the ram pressure of the plasma plume, $P_{dy} = \rho v^2$, is much larger than the magnetic pressure, $P_m = B^2/2\mu_0$, and the plasma expansion proceeds unimpeded (ρ is the mass density, v is the flow velocity, B is the magnetic field strength). Our simulations indicate that 2 ns after the main pulse arrival, the dynamic plasma-β, ($\beta_{dy} = P_{dy}/P_m$), is $\sim 10^3$. The expanding plasma plume has a relatively high magnetic Reynolds number ($Re_m = vL/\eta \sim 100$), and the magnetic field is "frozen" in the plasma as predicted by ideal MHD (i.e. low electrical resistivity). For Re_m we have used: $v = 100$ km/s, $L = 1$ mm and $\eta = 10^4$ cm^2/s, as the characteristic velocity, length-scale and magnetic diffusivity, respectively. From X-ray spectrometry measurements (Fig. 6.3) in the cavity at $z = 1$ mm, we infer $T_e \sim 40 - 60$ eV. The advection of the magnetic field by the plasma flow leads to a large increase of the magnetic pressure on the edges of the expanding plasma. The radial expansion of the plasma is halted when ram and magnetic pressures become comparable ($\beta_{dy} \sim 1$). The flow has typical expansion velocities of 100–500 km/s, and an internal magnetosonic Mach-number, $M_{ma} = v/c_{ma}$, of around 4, where c_{ma} is the fast magneto-acoustic speed. Therefore the slowing down of the plasma flow by

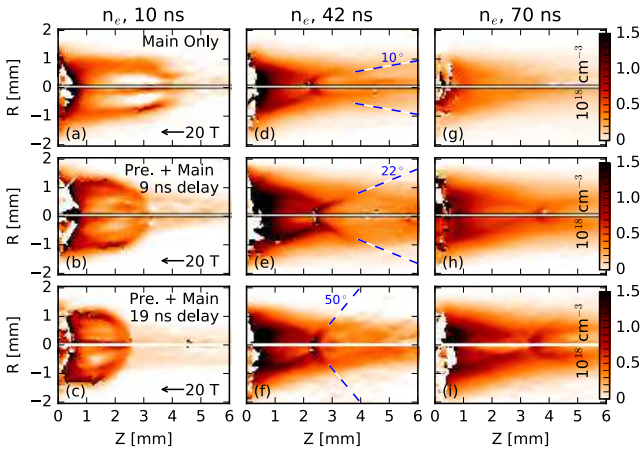

Figure 6.2: Plasma electron density measured via interferometry, and analyzed using Abel inversion[9; 10], in pseudo-color with identical colorscales as shown on the right. The central pixels are removed due to the uncertainty of the Abel inversion on-axis. Notice that the images appear very symmetric. The three columns show different times, measured from the beginning of the main pulse irradiation. The times highlight: cavity formation (10 ns), conical shock development (42 ns) and shocks and jet persistence over long times (70 ns).

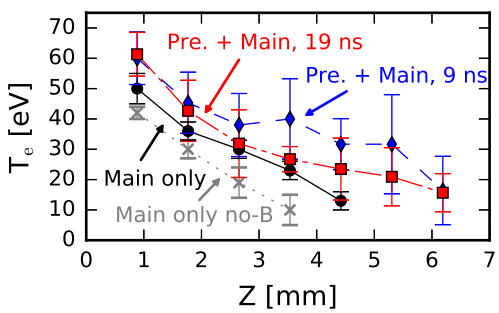

Figure 6.3: X-ray spectrometry measurements of T_e from the FSSR. Lines with circles (and X's) represent the main pulse alone with (and without) an applied 20 T B-field. Lines with diamonds and squares show cases with a precursor of 9 and 19 ns delay, respectively.

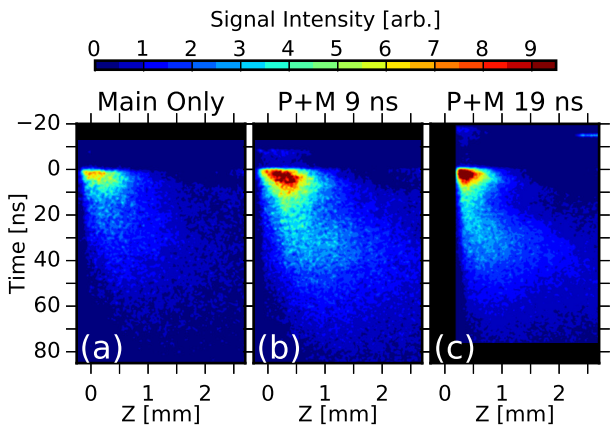

Figure 6.4: Streaked optical emission profiles along the center of the plasma expansion axis (smoothed with a 5-pixel Gaussian) plotted with the same linear color scale for (a) the main pulse alone and (b)/(c) the precursor and main pulses with a 9/19 ns delay between them. Time is measured from the beginning of the main pulse. Notice the small signal from the precursor interaction in (b), at -9 ns, and in (c), at -19 ns. The profiles in (a) and (b) were taken over successive shots and with the exact same detector settings. Profile (c) was taken at a later time and thus was slightly scaled and shifted for comparison with the previous profiles. Note that the thin streak in (c) at $t = -15$ ns, $z = -2.25$ mm is from the probe used for interferometry.

the magnetic field leads to the formation of a reverse shock, observed as a jump in density around the edges of the cavity (see Fig. 6.2), and to plasma heating (see Fig. 6.3).

While the general flow structure is similar with and without precursor irradiation, it is clear that adding a precursor laser pulse crucially modifies the dynamics and physical characteristics of the plasma in the cavity. Electron density maps taken 10 ns after the arrival of the main pulse (Fig. 6.2a-c) show the cavity becoming more spherical when the precursor laser pulse is used. The relatively small, 14%, increase in the the radial extent of the cavity is accompanied by a considerable reduction in its longitudinal extent: from 4 mm with main pulse only to around 2.5 mm with the addition of the precursor offset by 19 ns. We notice that in the temporally-staged configurations higher electron densities are measured (2×10^{19} cm^{-3}) along the shocks bounding the cavity (see in particular Fig.6.2d-f), a clear sign that shocks are stronger. This agrees with the T_e measurements shown in Fig. 6.3, which are larger with temporally-staging. Additionally, as shown in Fig. 6.4, optical emission inside the cavity ($z < 2$ mm) is clearly enhanced, both in intensity and duration, when using the precursor. Non-LTE calculations of photon absorption in the visible range (400 – 550 nm) corresponding to the S20 cathode response, for a CF_2 plasma show that above $T_e = 10$ eV and below $n_e = 10^{19}$ cm^{-3} the photon mean free path is greater than 30 mm, indicating an optically thin regime in this range. Given the higher electron temperatures and given that optical emission decreases with temperature in this regime, the brighter areas seen in Fig. 6.4 indicate the presence of denser plasma, consistent with the interferometric data.

Differences in the plasma properties and flow dynamics when introducing the precursor pulse can be understood by considering the location in the precursor plasma where the energy of the main laser pulse is absorbed. Fig. 6.5a shows the simulated density produced by the precursor pulse at the time of the arrival of the main pulse (considering a 19 ns separation). Due to the fast expansion of the plasma in the z-direction at speeds of 100–500 km/s the longitudinal density profiles change rapidly. These are shown in Fig. 6.5d at three different times for both the magnetized (solid lines) and an unmagne-

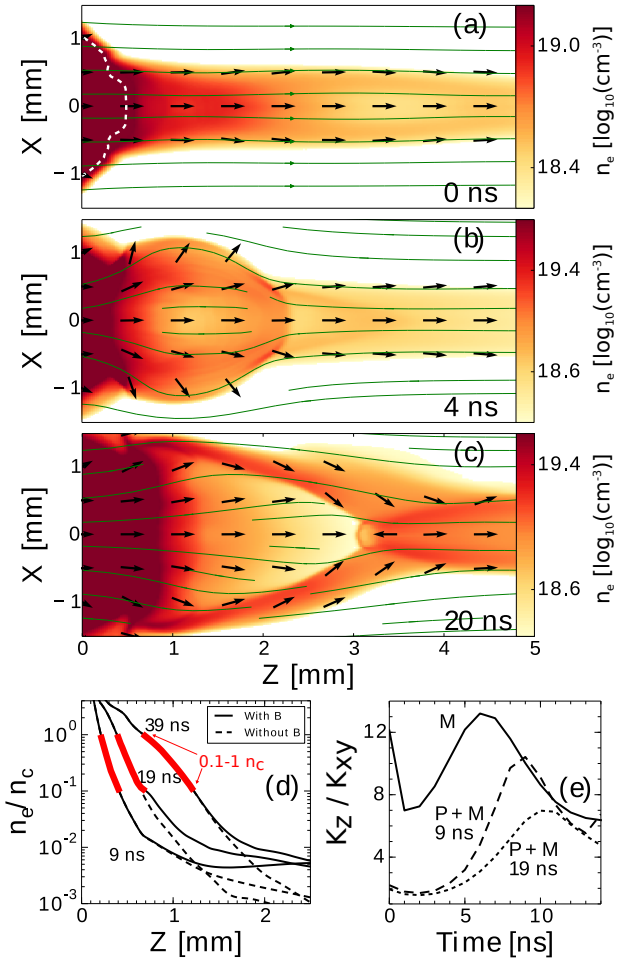

Figure 6.5: 3D MHD simulations results. (a,b,c) Pseudo-color maps of electron density in the temporally-staged configuration with a 19 ns delay. Times shown are measured from the main-pulse arrival. Arrows represent fluid velocity (not scaled in magnitude) and magnetic field lines are shown. Panel (a) shows the plasma created by the low energy precursor at a time just before the arrival of the main pulse. The white dashed line corresponds to the iso-contour at $0.1n_c$. (d) Profiles of n_e, averaged over the laser focal spot, for a case of precursor-only irradiation at 9, 19, and 39 ns after *precursor* irradiation. Cases with (solid) and without (dashed) magnetic field are shown. (e) Ratio of longitudinal ($K_z = 0.5\rho v_z^2$) to radial ($K_{xy} = 0.5\rho(v_x^2 + v_y^2)$) kinetic energy integrated over the entire plasma volume, for the main pulse only (M), and the temporally-staged cases (P+M).

tized (dashed lines) case of precursor irradiation. On the figure, regions where the electron densities are in the range from 0.1–1.0 n_c, where $n_c = 10^{21}$ cm^{-3} is the critical density of the laser, are highlighted with thicker lines; in this region over 90% of the laser energy from the main pulse is absorbed. From this plot it is clear that the n_e profiles for the unmagnetized and magnetized cases are essentially the same for times up to 50 ns with substantial differences arising only in the low density regions where laser absorption is insignificant. The applied 20 T magnetic field is thus unable to alter the absorption of the main laser pulse and only plays a role on the dynamics of the plasma that follows the laser absorption. Nevertheless, because of the expansion of the precursor plasma, the region over which most of the main laser is absorbed moves away from the initial target surface and increases in longitudinal extent, l_{abs}, as well as volume $\sim l_{abs} \times \phi_L^2$. That is, the absorbing plasma becomes more cylindrical and has lower thermal pressure, $\sim E_L/(l_{abs}\phi_L^2)$, when using two pulses, or for longer time-delays. The longitudinal stretching of l_{abs} causes more plasma to be accelerated radially and the overall expansion to be more divergent. This is indeed observed in the experiments, which show a more spherical expansion for the double pulse cases and for longer time-delays (Fig.6.2b,c). Further corroboration comes from Fig. 6.5e, which shows a reduction of the ratio of the longitudinal to radial kinetic energy when passing from a main pulse only (M) to the temporally-staged (P+M) configuration and when increasing the delay between pulses.

Collimation of the plasma plume into a jet takes place through a conical shock, which forms 2–4 mm from the initial target (Fig. 6.2d-f, Fig. 6.2g-i). The conical shock is the result of oblique shocks redirecting the plasma flow along the cavity walls and towards its tip [11]. In particular, we find that the opening angle of the conical shock and jet depends on the laser irradiation conditions, increasing from around 10° with only the main pulse to 50° in the temporally-staged configuration with 19 ns delay (see Fig. 6.2d-f). This variation is consistent with the cavity shape becoming more spherical: the flow converges at the tip of the cavity almost head-on. The more planar-like collision leads to an increased thermalization of the flow kinetic energy, leading to higher temperatures and thus more diverging flows. Remarkably, the experiments show that the re-collimating conical shock is quasi-steady-state and independent of the presence of an ambient plasma or of the laser irradiation delay, and that the collimation is very effective even for more isotropically expanding ejections. These results strengthen the claim [4; 11] that magnetic fields may be responsible for generating re-collimation shocks which are the source of the stationary x-ray emission observed in young stellar objects[12]. Past the conical shock, the jet properties are also modified. In addition to an increase in temperature, the simulations show that the second pulse produces a temporal increase in the jet's mass flux (ρv_z) and kinetic energy flux ($\rho v^2 v_z/2$) of almost a factor of 10, as well as velocity variations, $\Delta v_z \sim 100$ km/s (Mach 2-3), which drive shocks within the jet itself. Indeed, observations of astrophysical jets indicate that it is the unsteadiness of mass ejection drives shocks (so called "knots") inside the jet body (see [2] for a review). The experiments presented here, and further modifications of the experimental setup, thus help to assess how time-variability affects the formation and stability of the re-collimation shock and the jet itself.

In summary, we have presented a study of the interaction of two, temporally-staged, high-power laser pulses with a solid target in the presence of a 20 T magnetic field aligned along the main axis of the plasma expansion. The first low-energy (precursor) laser pulse generates a plasma that is collimated by the magnetic field into a jet. The ensuing plasma dynamics can then be controlled by delaying the arrival of the second (main) pulse, so that its absorption occurs further away from the initial target and over larger volumes. However, even at this relatively high field strength, we see no impact of the magnetic field on

the laser absorption itself; a finding that may be of particular interest to the (magnetized) ICF community. The time delay between the two laser pulses has clear effects on the plasma: a more divergent cavity expansion, higher electron temperatures and stronger shocks; yet, long-lived, stable jets are still formed. This demonstration of control over the flow dynamics and variability opens the door to a range of new laboratory studies related to accretion and ejection phenomena in astrophysics.

6.4 Bibliography

[1] Andrea Ciardi and Patrick Hennebelle. Outflows and mass accretion in collapsing dense cores with misaligned rotation axis and magnetic field. *Monthly Notices of the Royal Astronomical Society: Letters*, 409(1):L39–L43, 2010. 152

[2] A. Frank, T. P. Ray, S. Cabrit, P. Hartigan, H. G. Arce, F. Bacciotti, J. Bally, M. Benisty, J. Eislöffel, M. Güdel, S. Lebedev, B. Nisini, and A. Raga. Jets and Outflows from Star to Cloud: Observations Confront Theory. *Protostars and Planets VI*, pages 451–474, 2014. 152, 157

[3] Yoshiaki Kato, K Mima, N Miyanaga, S Arinaga, Y Kitagawa, M Nakatsuka, and C Yamanaka. Random phasing of high-power lasers for uniform target acceleration and plasma-instability suppression. *Phys. Rev. Lett.*, 53(11):1057, 1984. 152

[4] B. Albertazzi, A. Ciardi, M. Nakatsutsumi, T. Vinci, J. Béard, R. Bonito, J. Billette, M. Borghesi, Z. Burkley, S. N. Chen, T. E. Cowan, T. Herrmannsdörfer, D. P. Higginson, F. Kroll, S. A. Pikuz, K. Naughton, L. Romagnani, C. Riconda, G. Revet, R. Riquier, H.-P. Schlenvoigt, I. Yu. Skobelev, A.Ya. Faenov, A. Soloviev, M. Huarte-Espinosa, A. Frank, O. Portugall, H. Pépin, and J. Fuchs. Laboratory formation of a scaled protostellar jet by coaligned poloidal magnetic field. *Science*, 346(6207):325–328, 2014. 152, 153, 157

[5] DP Higginson, G Revet, B Khiar, J Béard, M Blecher, M Borghesi, K Burdonov, SN Chen, E Filippov, D Khaghani, et al. Detailed characterization of laser-produced astrophysically-relevant jets formed via a poloidal magnetic nozzle. *High Energy Density Physics*, 23:48–59, 2017. 152

[6] S. N. Ryazantsev et al. *JETP Letters*, 102:817, 2015. 152

[7] SN Ryazantsev, I Yu Skobelev, A Ya Faenov, TA Pikuz, DP Higginson, SN Chen, G Revet, J Béard, O Portugall, AA Soloviev, et al. Diagnostics of laser-produced plasmas based on the analysis of intensity ratios of he-like ions x-ray emission. *Phys. Plasmas*, 23(12):123301, 2016. 152

[8] S. Atzeni, A. Schiavi, F. Califano, F. Cattani, F. Cornolti, D. Del Sarto, T. V. Liseykina, A. Macchi, and F. Pegoraro. Fluid and kinetic simulation of inertial confinement fusion plasmas. *Computer Physics Communications*, 169:153–159, July 2005. 152

[9] Kjell Bockasten. Transformation of observed radiances into radial distribution of the emission of a plasma*. *J. Opt. Soc. Am.*, 51(9):943, 1961. 154, XXXII

[10] T. Vinci and A. Flacco. Neutrino, 2015. 154, XXXII

[11] A. Ciardi, T. Vinci, J. Fuchs, B. Albertazzi, C. Riconda, H. Pépin, and O. Portugall. *Phys. Rev. Lett.*, 110:025002, 2013. 153, 157

[12] S Ustamujic, S Orlando, R Bonito, M Miceli, AI Gómez de Castro, and J López-Santiago. Formation of x-ray emitting stationary shocks in magnetized protostellar jets. *Astron. Astrophys.*, 596:A99, 2016. 157

Chapter 7

Generation of unstable supersonic plasma pancakes in strong transverse magnetic fields

Sommaire

7.1 Introduction **162**

7.2 Initial setup and lasers parameters **162**

7.3 General 3D dynamic **163**

7.4 Three-dimensional stability of the produced plasma pancake **165**

7.4.1 Rayleigh-Taylor instability in the MHD regime 168

7.5 The effects of the plasma beta on the instability **169**

7.6 Experimental results **171**

7.7 Bibliography **173**

7.1 Introduction

In the chapter dedicated to the generation of supersonic jets in the laboratory we investigated plasma dynamics with a "longitudinal" magnetic field, that is, perpendicular to the laser target surface. In this chapter we investigate the case where the magnetic field is parallel to the target surface. To our knowledge this represent the first complete three dimensional description of the dynamics of a hot and dense laser-produced plasma embedded in a strong transverse magnetic field. We show that using a nanosecond, Joule-class laser and 20 T magnetic field, it should be possible to generate astrophysically-relevant slender slabs that are structured by instabilities. We identify the magnetized Rayleigh-Taylor instability to be main responsible for the first of these instabilities. We also understand that in the past, laser experiments with an externally imposed magnetic field were such that the ion Larmor radius was too large to observe the MHD Rayleigh-Taylor instability. Instead the lower hybrid drift instability or other non-fluid instabilities were responsible for the striations and flutes observed in the experiments. The numerical results presented here have been experimentally verified with a remarkably good agreement by our experimental collaborator and we will present some of the results at the end of this chapter.

In 1989, Mostovych et al. [1] demonstrated the collimating effect of a transverse 1 T magnetic field on a barium laser-produced plasma. Notably they reported observation of flutelike striations using their resonant absorption diagnostic redwhat's that diagnostic? May be put a footnote to briefly explain. They attributed these instabilities to the lower hybrid drift instability (LHDI) because of the large ion larmor radius ($> 2\,cm$) and the relatively low collisionality associated with the low plasma densities produced ($< 10^{14}\,cm^{-3}$). More recently (in 2013) Plechaty et al. [2] presented similar results in a regime of laser parameters very close to what we study here. However their experiment was performed with a strongly non-homogeneous magnetic field, varying from 7 T to 13 T on a distance of ~ 10 mm, which is of the order of the plasma size. Their experimental results show the same general plasma dynamics than what we will present here, however they did not observe any instabilities. In addition, their 2D numerical simulations were done, contrary to our study, within the ideal MHD framework and they pointed out the necessity to perform resistive MHD simulations. Indeed from their work it remains unclear what the full three dimensional plasma dynamics is, and we propose to present in this chapter such analysis.

7.2 Initial setup and lasers parameters

The initial setup used for these simulations is very similar to the one described in section 5.3 with laser parameters given by:

- Energy: 17 J
- Pulse duration (FWHM): $0.5\,ns$
- Focal spot diameter: $750\,\mu m$
- Intensity: $7.7\,10^{12}\,\mathrm{W}.cm^{-2}$

and a carbon target. The initial laser-solid interaction is done using the DUED code [3]. The computational domains in GORGON is defined by a uniform Cartesian grid of dimension $8\,mm \times 6\,mm \times 20\,mm$ and a number of cells equals to $400 \times 300 \times 1000 = 1.2\,10^8$.

The spatial resolution is homogeneous and its value is $dx = dy = dz = 20\,\mu m$. The magnetic field is initialized in the x-direction with a magnitude $B_0 = 20\,T$

7.3 General 3D dynamic

In Fig.7.1(a,b,c) we show 3D rendering of the mass density at 8, 20 and 48 ns after the laser pulse. The next three images (d,e,f) show the corresponding integrated electron density along the y direction (perpendicular to the B-field). These images should be directly comparable with experimental results obtained using interferometry probes [4; 5]. The very initial plasma expansion following the laser deposition (up to $\sim 2-3\,ns$) is relatively similar to a free-expansion since the dynamic plasma beta (β_{dyn}=ram pressure/magnetic pressure) at this time is much larger than unity ($\sim 10^4$). We point out that because of that, this initial expansion phase is very similar to the case where the field is longitudinal (i.e. along the z-axis). The large electron temperatures ($\sim 100\,eV$) resulting from the laser heating result in magnetic diffusivity η low enough for the magnetic Reynolds number to be large ($R_m = L_c V_c/\eta \sim 100$, where $L_c \sim 1\,mm$ and $V_c \sim 1000\,km.s^{-1}$ are characteristic length and velocity in our experiment), at least during the initial expansion. Thus the resulting ideal MHD regime allows an effective and rapid advection of magnetic field lines by the flow. Furthermore, the fact that the plasma is expanding at speeds sim greater than the fast magnetoacoustic speed $c_{ma} = \sqrt{c_s^2 + v_A^2}$ (where c_s is the sound speed and v_A the Alfven speed) results in the generation of a shock and the compression of the magnetic field. The initial deceleration of the plasma/vacuum interface by the magnetic tension arising from magnetic lines bending gives rise to a finite diamagnetic cavity seen in Fig.7.1(a,d). Indeed, as the initial magnetic flux is compressed in a narrow shell of $\sim 100\,\mu m$ around the cavity, the resulting Lorentz forces $\mathbf{j} \times \mathbf{B}$ are responsible for stopping the lateral plasma expansion. In Fig.7.2(a) we show a detailed zoom of the white dashed frame seen in Fig.7.1(a). The diamagnetic nature of the cavity can be observed through the presence of the strong electrical currents (green lines) in the shell. At stagnation, the current present in the cavity shell can be estimated by equalizing this force with the force associated to the ram pressure ($\rho(\mathbf{v}.\nabla)\mathbf{v}$) leading to: $j \approx \rho v_\perp^2/Be_{shock} = 10^{11}\,A.m^{-2}$ where $e_{shock} = 100\,\mu m$ is the shock thickness, $\rho = 0.02\,kg.m^{-3}$ is the characteristic plasma flow density, $B = 20\,T$ is the magnetic field magnitude and $v_\perp = 100\,km.s^{-1}$ is the plasma velocity perpendicular to the magnetic field lines. Inside this cavity the magnetic field is relatively low $< 5\,T$. The image shown in fig.7.1(a) represents the final stage of this initial expansion phase (near stagnation) and one can clearly observe the already remarkable asymmetry between the x-direction (that of the magnetic field) and the y direction. The ratio of expansion length in both direction $r = r_{exp,x}/r_{exp,y} \sim 1.5$ highlight the fact that, along the x-direction of the external magnetic field the plasma expansion is almost free. As in the case of a longitudinal magnetic field [6], the plasma flow in the y direction is redirected by a curved shock towards the z-axis, where it forms a conical shock at the tip of the cavity. Also, we want to emphasize the appearance, near the stagnation time, of flute-like ($\mathbf{k}\cdot\mathbf{B} \approx \mathbf{0}$) perturbations on the cavity walls. An extensive discussion about the instabilities present in this configuration is given after the general description of the plasma dynamics. In fig.7.1(b), showing the plasma structure 20 ns after the laser pulse, one can see that the plasma flow results in a thin $\sim 800\,mm$ plasma layer in the y-direction whereas in the x-direction the flow is basically spreading unconstrained. The resulting general shape is that of a "slender" slab. The cavity seen previously in 7.1(a) has collapsed very quickly due to the pulsed nature of the plasma energy source (the laser), but the conical shock can still be seen much closer

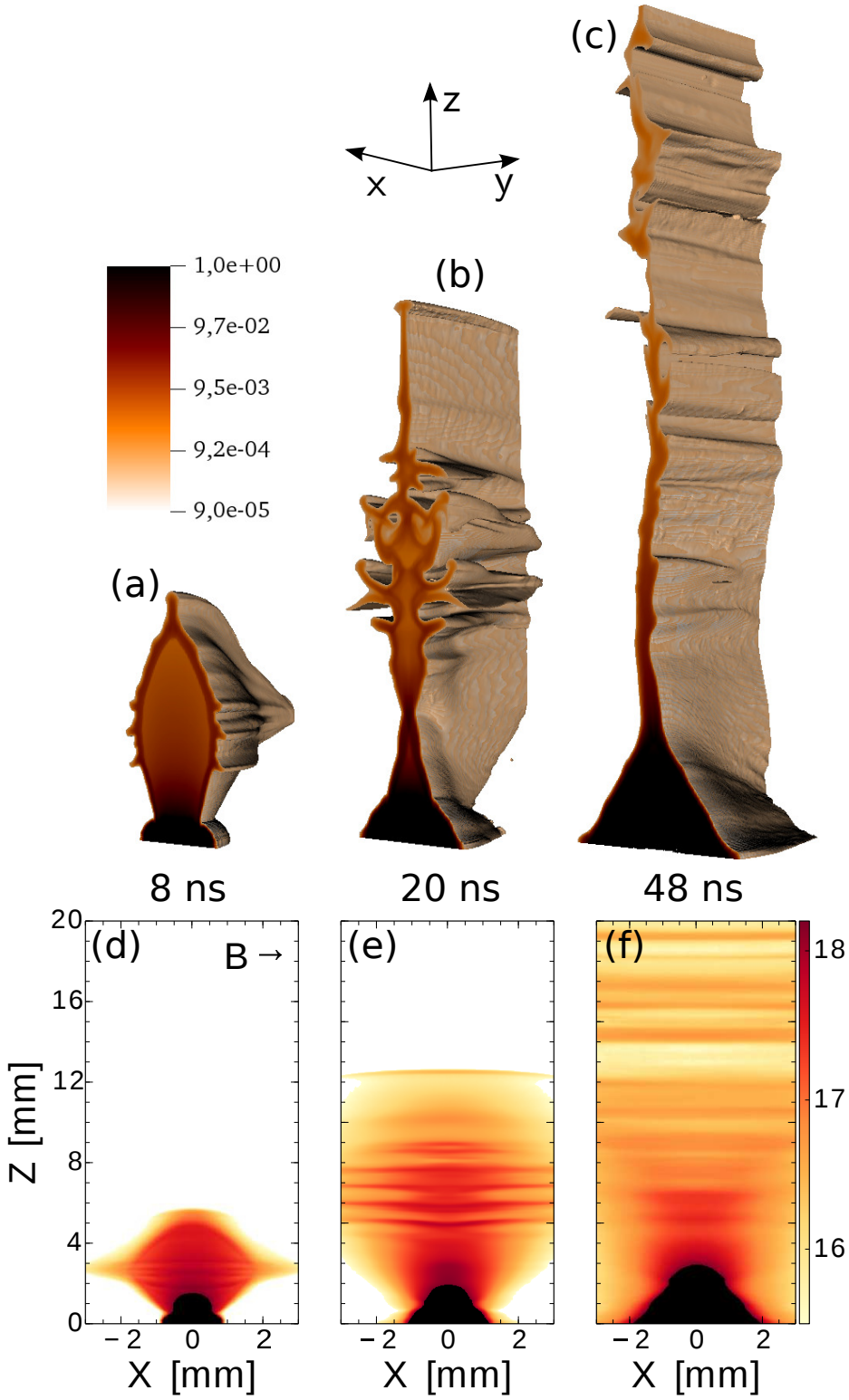

Figure 7.1: (a-b-c) 3D isovolumes of the decimal logarithm mass density at t=8, 0 and 48 ns after the laser pulse. The external magnetic field of 20 T is oriented along the x-axis. (d-e-f) Decimal logarithm of the integrated electron density along the y-direction (perpendicular to the external magnetic field) at the same times.

to the target ($\sim 2\,mm$). If one would experimentally measure the integrated electron density of the plasma in the xz-plane (see fig.7.1(e)), one would see a very elongated ($> 6\,mm$) plasma "pancake" with no evidence of a collimating effect of the magnetic field. This result is in agreement with previous experimental work [1; 2; 7].
Alongside these general features, it is obvious that large structures coming from instabilities are present in this configuration. In the yz-plane (see fig.7.1(b)), we see the generation of large filaments with dimensions ($\sim 1\,mm$) comparable with the thickness of the plasma layer. Clues of the presence of these filaments can be seen at earlier times, near the stagnation time (see fig.7.1(a)). The striations seen in the xz-plane in fig.7.1(e) also indicate the presence of these filaments and thus experimental interferometry diagnostics should observe this effect. The filaments are also elongated along the plasma slab, aligned with magnetic field lines. Actually, these kind of striations have already been seen experimentally in laser-produced plasmas by Mostovych et al.[1] but we will show later that the instability producing the filaments is not the same. Finally, at later times, here shown in fig.7.1(c) at 48 ns after the laser pulse, one can see the fully-developed plasma slab with longitudinal extent (in the z-direction) greater than $20\,mm$. The corresponding integrated electron density is shown in fig.7.1(f). The slab is, at these late times, even thiner ($\sim 400\,\mu m$) than earlier, at 20 ns. A kind of striations can also be seen on the integrated electron density (fig.7.1(f)) but here, contrary to the situation at 20 ns, they are not generated by filaments growing at the plasma/vacuum interface but are instead produced by "kinks" of the elongated slab. These behavior comes from the destabilization of magnetoacoustic modes allowed to propagate in a magnetic slab (see [8–10]). In this regard, as an example of application of the setup studied in this paper, we suggest the possibility to study in the laboratory (adding a gas background for example), the physics of the propagation of waves in strongly magnetically-structured inhomogeneous mediums, such as those encountered in the solar atmosphere. For example, it has been stated that magnetoacoustic surface waves arising because of the magnetic structuring of the plasma could play a role in the heating of the solar corona (see [11; 12]). We notice here the important fact that the ideal MHD regime of the plasma is the basic requirement in order to apply a possible scaling from the laboratory to the space plasmas ([13]).

7.4 Three-dimensional stability of the produced plasma pancake

We focus not on a detailed discussion on the strong plasma structuring driven by unstable filaments, as seen fully developed in fig.7.1(b) and at an earlier stage in fig.7.1(a). From our 3D MHD simulations, we see these flutelike ($\mathbf{k}\cdot\mathbf{B} = 0$) filaments starting to grow $\sim 2\,ns$ before the maximum cavity expansion. During this period the deceleration of the interface is close to $\sim 5.5\cdot 10^{13}\,m.s^{-2}$. At the stagnation point (see fig.7.2(a)), when the cavity has reached its maximum radius of $\sim 1.2\,mm$, we can see on each edge of the cavity three main spikes spaced of $\sim 0.6\,mm$ apart. After the stagnation, the cavity collapse because of the changing pressure equilibrium at the interface and thus the plasma/vacuum interface is this time accelerated toward the central axis (z). We also observe during this phase the growth of the spikes. Then the plasma flow undergoes a succession of lateral expansion and contractions, during which further flutes are generated. The resulting structure corresponds the one seen in fig.7.1(b). To make contact with potential experimental results, in addition to the integrated electron density maps (fig.7.1(a,b,c)), we show here that the presence of these unstable flutes can also be revealed through a synthetic Faraday rota-

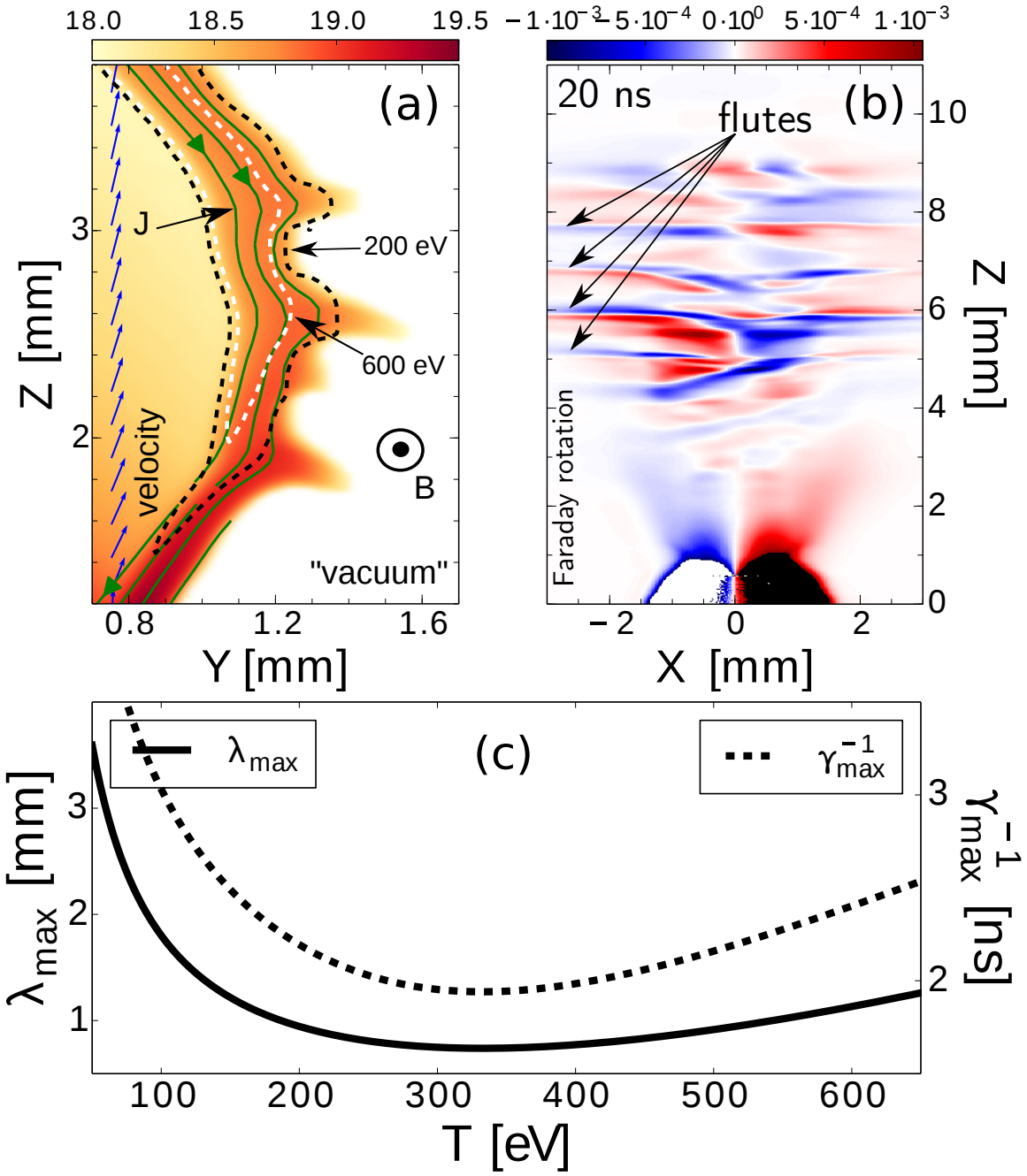

Figure 7.2: (a) Zoom of the plasma/vacuum interface at t=8 ns. The colormap corresponds to the decimal logarithm of the electron density. (b) Faraday rotation numerical diagnostic when looking in the y-direction (c) Temperature dependence of the wavelength (in millimeters) and the corresponding growth time (in nanoseconds) of the fastest growing mode for the MHD Rayleigh-Taylor instability in presence of resistivity and viscosity. At low temperatures the resistive damping dominates whereas at high temperatures the viscous dissipation predominant.

tion diagnostic. The probing laser is in this case supposed to propagate along the y direction, perpendicular to the magnetic field lines. Since this diagnostic measure roughly the quantity $\int n_e \mathrm{B}_y dy$, the computed rotation angle is an indication of the asymmetry of the plasma slab and the primary responsible for this asymmetry should be the flutes. Interestingly, a strong Hall effect, not taken into account in our code, would increase even more the rotation angle predicted here since the two side interfaces of the slab have electrical currents $\mathbf{j}$ flowing in opposite directions and thus opposite Hall fields $\mathbf{j} \times \mathbf{B}/en_e$ (the B-field has the same direction on both sides). Of course, the instabilities seen in our simulations are necessarily of fluid type because of our model but we want to give here a more general discussion, for experimental purpose, of the possible instabilities that one may expect in this setup.

We consider here three candidates: the classical magnetized Rayleigh-Taylor instability (RTI) [14], the lower hybrid drift instability (LHDI) [15] through one of its "versions" (the unmagnetized ion Rayleigh-Taylor instability) and a Kelvin-Helmhotz like instability. First, the LHDI has been thought to be responsible for a large number of striations and flutes observed both in laboratory and space plasma experiments. This instability arises in configurations where electrons are magnetized and ions are not (Larmor radius large compared to the density scale length). Typically, the free energy feeding the growth of the LHDI comes from the electron-ion drift caused by the density gradient at the plasma-vacuum interface [15]. Nevertheless, it has been shown [16] that this instability can also be triggered by a decelerating interface, where the escaping out of unmagnetized ions is partially hindered by the polarizing electric field $\mathbf{E_p}$ generated because of the magnetized electrons. The electrical currents generated on the interface by the resulting $\mathbf{E_p} \times \mathbf{B}$ drift is the feeding source of the instability. This variant of the original LHDI has been called the unmagnetized ion Rayleigh-Taylor instability because of the importance of the effective (de-)acceleration and its linear dispersion equation has been deduced from a modified set of MHD equations ([17–19]), incorporing large Larmor radius effects. It has been invoked to explain striations and flutes observed on the surface of the Active Magnetospheric Particle Tracer Explorers (AMPTE) barium cloud [20], in θ-pinches experiments [21] and even in laser-produced plasmas that are magnetically constrained [22] but at much lower field strength (< 1 T) than in our case. The flutelike behavior of the LHDI comes from the fact that in parallel propagation modes are mitigated by electron Landau damping. To assess the relevance of the LHDI in our setup we first evaluate the ion Larmor radius (the thermal Larmor radius $r_{\mathrm{LT}} = v_{\mathrm{T}i}/\omega_{ci}$) and the directed Larmor radius, given by $r_{\mathrm{LD}} = \mathrm{V}_c/\omega_{ci}$, where $v_{\mathrm{T}i}$ is the ion thermal velocity. Assuming almost completely ionized ions (Z=6), an ion temperature of 50 eV (temperature before shocks), a velocity of 500 $km.s^{-1}$ and a magnetic field of 20 T, we obtain $r_{\mathrm{LT}} \sim 20\,\mu m$ and $r_{\mathrm{LD}} \sim 450\,\mu m$. Considering the density scale length near the interface to be of few hundreds of microns it thus seems unlikely that the LHDI could play a major role here, even if the plasma would be non collisional, which is not the case. Actually it turns out that in all our simulation domain, corresponding to fig.7.2(a), we have the Hall parameter (ratio of the ion gyro frequency to the ion collision frequency) always less than ~ 0.1, meaning that collisions dominate and prevent the growth of the LHDI (see [23]).

Another candidate for the observed spikes is the Kelvin-Helmholtz instability (KHI). We reject directly the unmagnetized versions of this instability in the lower-hybrid range because of the small ion Larmor radius and the high collisionality, as showed previously. The classical Kelvin-Helmholtz instability is fed by shear flows and momentum transfer between two adjacent drifting layers. This instability is generally invoked to explain the

generation of vortex or eddy structures in the plasma flow. As one can see in fig.7.2(a) at 8 ns, such structures are clearly not seen but later, at 20 ns (fig.7.1(b)), it seems that plasma spikes are slightly twisted. A good way to conclude on the possible presence of the KHI is to estimate its growth rate/time. The dispersion equation leads to $\gamma_{\mathrm{KHI}} \sim k\mathrm{V}_{drift}/2$ for flutelike modes ($\mathbf{k}\cdot\mathbf{B} = 0$) [24]. To obtain this expression we assumed homogeneous density of the adjacent layers. Here the velocity V_{drift} has to be understood as the characteristic drift velocity (perpendicular to the magnetic field lines) between two layer of plasma within the shell itself. In our simulation this velocity is relatively small leading to growth times of several tens of nanoseconds but our single fluid model does not account for the effect of the electron drift (i.e. Hall "velocity") on the Kelvin-Helmholtz instability (even if estimated to be relatively negligible since we are not in a current-driven plasma). Thus, in any case, we can not exclude the presence of this instability but it is clear that it is not the instability responsible for the spikes see near the stagnation point.

7.4.1 Rayleigh-Taylor instability in the MHD regime

In this section focus on the MHD RTI and we argue why this setup should allow its first observation within a laser based experiments.

The MHD Rayleigh-Taylor instability growth rate (for a mode $\mathbf{k}$) is given by the relation $\gamma^2_{\mathrm{RTI}} = kg_{eff} - 2(\mathbf{k}\cdot\mathbf{B})^2/(\mu_0\rho)$ where g_{eff} is the effective (de-)acceleration of the plasma in the frame of the plasma-vacuum interface (corresponding to an Artwood number equal to one). A finite value of $\mathbf{k}\cdot\mathbf{B}$ opposes the effect of the destabilizing deceleration thus this is of course the reason why we observe flutelike modes $\mathbf{k}\cdot\mathbf{B} = 0$, clearly seen through the magnetically-aligned elongated striations in the integrated electron density maps (fig.7.1(e)).

Focusing our discussion on early times (up to $\sim 8\,ns$, see 7.2(a)), there are two effective accelerations that are at play: the deceleration $g_{eff,dec}$ of the interface by the Lorentz forces $\mathbf{j}\times\mathbf{B}$ and the centrifugal force that experiences, in its rest frame, the plasma flow redirected near the interface. For the latter, the corresponding effective acceleration can be approximated by $g_{eff,c} = v_\parallel^2/\mathrm{R}_c$ where $v_\parallel$ is the velocity parallel to the field lines and R_c the curvature radius of this field lines taken, as a first approximation, to be equal to the cavity radius ($\sim 1.2\,mm$). The deceleration $g_{eff,dec} = j\mathrm{B}/\rho$ can be roughly approximated using the expression we already derived for the electrical current and we get $g_{eff,dec} = v_\perp^2/e_{shock}$, In both cases, the configuration is favorable to the growth of the Rayleigh-Taylor instability (RTI) since in the frame of the interface, the effective acceleration has the opposite direction to the density gradient. The ratio of both acceleration $g_{eff,dec}/g_{eff,c} = \mathrm{R}v_\perp^2/(e_{shock}v_\parallel^2)$ is, using our characteristic values, close to unity. Thus, both effect can play a role in the growth of the RTI. However, we see the flutes growing before the redirection of the flow, so we consider here only the effect due to the deceleration of the cavity. However, it is worthwhile to note that in the case where one can establish a stationary or long-lived cavity (for example using repeated laser pulses), the configuration can still be unstable because of the centrifugal force. With $v_\perp = 100\,km.s^{-1}$ and $e_{shock} = 200\,\mu m$ we have $g_{eff} \sim 5\cdot 10^{13}\,m.s^{-2}$, in agreement with our previous numerical estimations. Now the fact that a particular mode is excited should be related to the existence of a damping mechanisms which tends to stabilize short wavelength modes. Indeed, it is well known that a large amount of different effects can mitigate the growth of the Rayleigh-Taylor instability (see [25]). For example it has been shown that a finite ion Larmor radius (FLR) tends to slow down the instability [26] but in our case, during initial

expansion, ions are probably too collisional for FLR to be important. Here we consider the effect of finite resistivity which can damp the RTI through diffusion of magnetic field inside the cavity as well as the effect of viscosity which, through sheared velocities at fine scales, can mitigate the instability growth on those scales. Even though in our code we only use a non-physical numerical viscosity, which is only important at shocks, we want to keep the discussion generally applicable to experiments and thus consider this effect for the following analytical considerations. The electrical resistive contribution to the RTI dispersion relation can be written $D_M k^2$ (where D_M is the magnetic diffusivity) whereas the viscous term is given by νk^2, where ν is the ion kinematic viscosity (see [27]). The relative importance of viscosity and resistivity as damping processes can be estimated with the ratio of the two terms which is also equal to the ratio of magnetic to hydrodynamic Reynolds number: $P = R_m/R_e = \nu/D_M$. Using the Spitzer conductivity [28] and the ion dynamic viscosity expression in the magnetized case given in [29], we obtain (considering $T_e = T_i = T$): $P = 2.2\cdot 10^{-9}\sqrt{A}T^4/(\Lambda Z^5\rho)$ with ρ in $kg.m^{-3}$ and T in electronvolts and Λ is the coulomb logarithm. Then we use our simulations to infer a reasonable range for the temperature at the decelerating interface during the first ten nanoseconds. While initially the temperature is $\sim 50\,eV$ (corresponding to $P \sim 3\cdot 10^{-4}$), because of the strong compression of the magnetic field, in the cavity shell we observe temperatures very quickly exceeding few hundreds of eV, and thus leading to values of P greater than unity ($P = 1$ at $T \approx 380\,eV$). The ion temperature structure is shown in fig.7.2(a) as two isocontour representing ion temperatures of 200 eV (black dashed line) and 600 eV (white dashed line). As the cavity increases its radius towards its stagnation point, viscous dissipation also increase and becomes larger than resistive damping. To take into account this variation we keep both processes in our estimates. To determine the wavelength λ_{max} of the fastest growing mode we localize the extrema of the growth rate function $\gamma(k) = \sqrt{g_{eff}k - k^2(\nu + D_M)}$ to obtain:

$$\lambda_{max}[mm] \approx 1.1\pi g_{eff}^{-1/3}[\frac{\sqrt{A}T^{5/2}}{\Lambda Z^4\rho} + 4.5\cdot 10^8\frac{Z}{T^{3/2}}]^{2/3} \tag{7.1}$$

where g_{eff} and ρ are in SI units and T is in electronvolts. Using our previous estimate of g_{eff} we can thus determine the behavior of the RTI in the presence of resistivity and viscosity. In fig.7.2(c) we plot $\lambda_{max}(T)$ and the corresponding growth rate $\gamma_{max}(T)$, as a function of ion temperature. One can see that, as the temperature increases, the fastest growing mode wavelength decreases until it reaches a minimum at $\sim 0.7\,mm$ for a temperature of $\sim 300\,eV$. The corresponding characteristic growth time is $\sim 1.9\,ns$,. These results are in very good agreement with with the values inferred from our simulations, thus strengthening the argument that it is indeed the MHD RTI that is observed in the simulations.

7.5 The effects of the plasma beta on the instability

As a last point, we investigate the behavior of the instability for different plasma thermal/dynamic beta. Keeping the same laser parameters, we increase or decrease the initial magnetic field. We show in the top three images in fig.7.3 the integrated electron density maps along the direction of the magnetic field, for B 5 T, 10 T and 100 T. The images show the plasma 20 ns after the laser pulse. In the three cases, the field is strong enough to confine the plasma within a cavity radius that varies approximately as $B^{-2/3}$ (see [6]). In all cases the RTI flutes are seen to develop, however we point out that for B = 5 T, the characteristic ion Larmor radius would be of the order of $\sim 2\,mm$, thus we may expect the

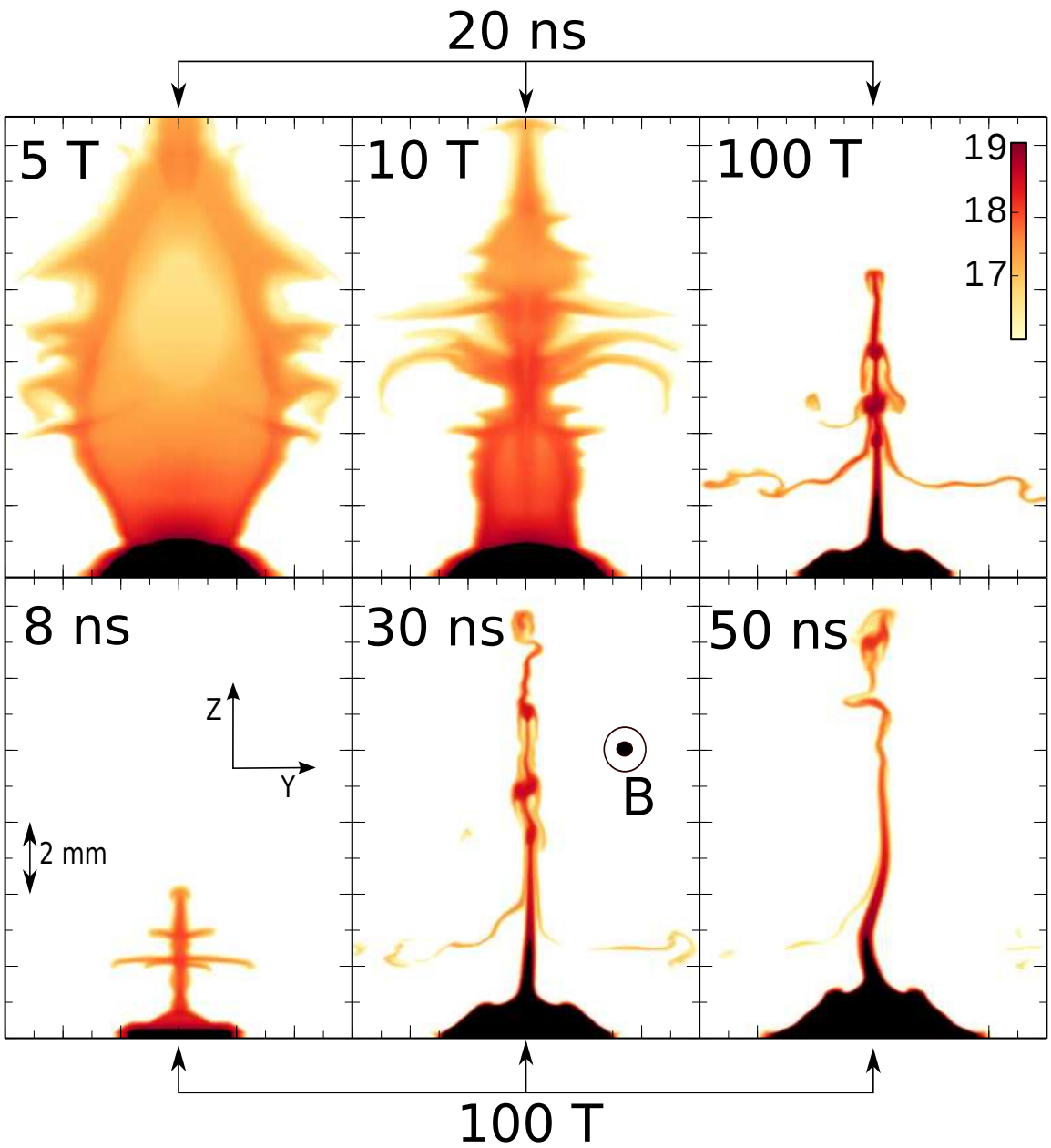

Figure 7.3: 2D slices of the decimal logarithm of the electron density. The top three images represent three different fields (5, 10 and 100 T) at the same time (20 ns). The three bottom images are for the same field (100 T) but at three different times (8, 30 ,50 ns).

LHI to become important near plasma-vacuum interfaces in this case. For much larger magnetic fields, B = 100 T, the structure consists of a very thin plasma slab (~ 100 µm) with filaments anchored on knots corresponding to very small cavities. Another important difference between the case at low fields (5, 10 T) and the case at 100 T, concerns the much smaller spatial extension of the plasma in the z-direction. For the latter case $z \sim 8.5\,mm$ instead of $> 12.5\,mm$, indicating a strong decelerating effect in this direction. This enhanced deceleration is due to the larger magnetic tension caused by increasingly bent field lines. In the top bottom images in fig.7.3 we show three different times (8, 20 and 50ns) for the B = 100 T case. As previously mentioned, we observe kink-like deformations of the slab at later times. This acts as a limiting factor on the dimensions of the slab that one may obtain when increasing the B-field: as the slab become thinner, it also become more prone to kink-unstable modes and actually breaks up for very low plasma betas, like in this case.
We elucidated the overall 3D dynamics of a laser-produced plasma in a 20 T magnetic field, the resulting plasma shows structuring by instabilities in the MHD regime. These numerical results are of interest for understanding forthcoming magnetized laser experiments, with, in the not-so-distant future, magnetic fields reaching magnitudes as high as 100 T. We also demonstrated the possibility to generate with this setup the well-studied (in solar physics research) plasma configuration of a magnetized "slender" slab.

7.6 Experimental results

In this section we present very recent experiments done with a setup similar to that studied numerically in this chapter. The experiments were performed on two different facilities, the Elfie facility (LULI, Ecole Polytechnique) and the TITAN facility (Livermore). On the Elfie facility, a chirped laser beam 0.6 ns/30 J, at the wavelength of 1057 nm and focused in a~ 700 µm diameter spot on a Teflon (CF2) target placed in a vacuum chamber, was used. This gives access to a maximum intensity on target of $I_{max} = 1.3\,10^{13}\,W.cm^{-2}$ allowing the ablation and ionization of the target material, into an expanding, relatively hot (100 eV) thermal plasma. The strength of the magnetic field was set to 20 T, via the coupling with a 32 kJ/16 kV capacitor bank delivering 20 kA to a Helmholtz coil, specifically designed to work in a laser chamber environment [5]. This coil allows a configuration where the plasma electron density is probed by interferometry collinear to the magnetic field lines. The TITAN facility provided a long pulse of 1.2 ns/20 J, at the wavelength of 527 nm and focalized in a~ 300 µm diameter spot on a Teflon (CF2) target placed in a vacuum chamber. This allowed to access similar intensity into the target surface,i.e. $I_{max} = 1.2\,10^{13}\,W.cm^{-2}$. For TITAN campaign, a different coil was used, The coil provided a similar 20 T pulsed magnetic field, but the design allowed the probing of the plasma electron density along the line of sight perpendicular to the magnetic field. On both facilities, interferometry was accomplished using a Mach-Zehnder with a 2ω laser pulse of energy at Elfie Facility, while a 1ω laser pulse was used at the Titan facility. Both probe beams where ~ 1 ps duration and ~ 100 mJ energy (negligible effect on the plasma dynamics).

In fig.7.4 are shown 2D maps of the of the integrated electron density obtained form these experiments. The three top images represents side views of the generated slab whereas the two bottom images are front views. At early times (fig.7.4(a,d)) one can see the initial development of the cavity with no real observation of magnetic effects (as explained before, because at these times the thermal/dynamic betas are much larger than one). A little while later (fig.7.4(b,e)), the formation of the cavity is clearly observed with the collimation of the flow being really important. These times correspond roughly to the

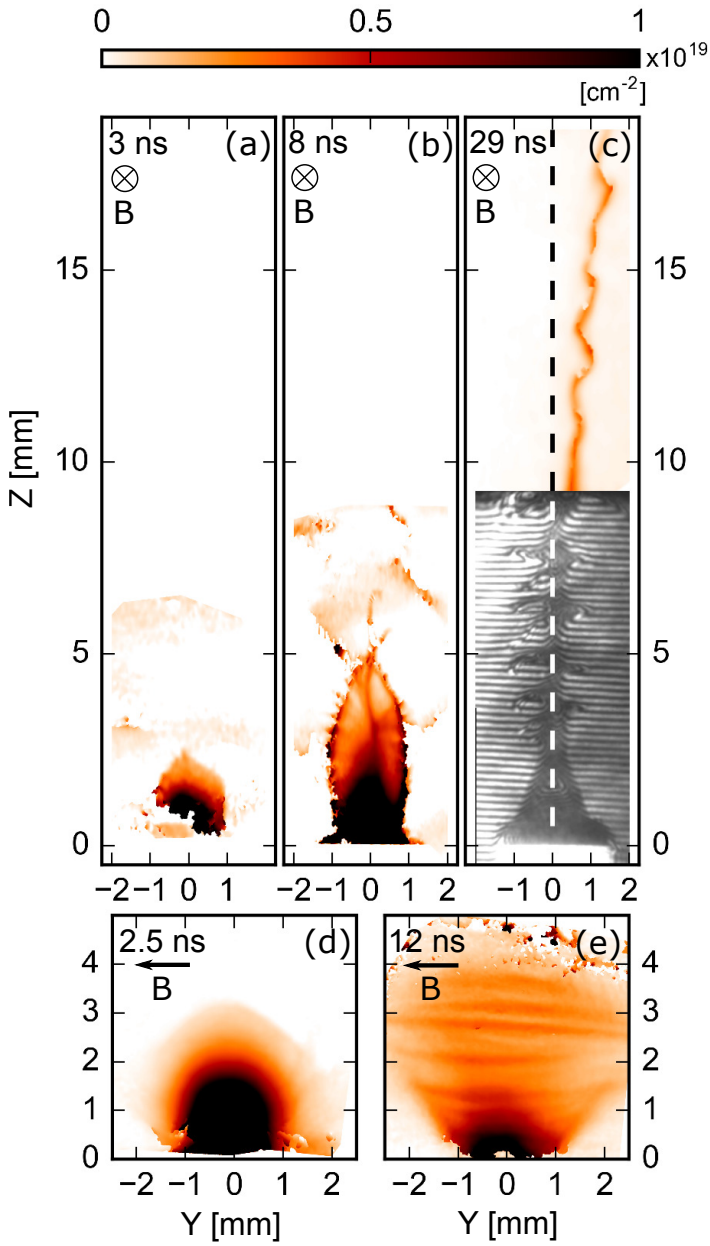

Figure 7.4: 2D maps of the of the integrated electron density, showing the plasma dynamic at different times and for two perpendicular probing lines of sight. (a)-(c) Three different times, 3 ns, 8ns and 29 ns respectively, coming from the Elfie campaign, i.e. the 20 T magnetic field being perpendicular to the figure plane. (d) and (e) two different times, 2.5 ns and 12 ns respectively, coming from the TITAN campaign, i.e. the 20 T magnetic field being in the figure plane.

stagnation points where the plasma/vacuum interface deceleration has been the greatest and thus, we observe very nicely the generation of the predicted flutelike RT filaments (clearly seen in fig.7.4(e)). The measured wavelength is $\approx 0.6\,mm$, very close to what we observe numerically. At latter times (fig.7.4(c)), the fully-developed magnetic slab extend on almost $2\,cm$ with the first $\sim 10\,mm$ been structured by the remaining of the RT filaments whereas the upper part of the slab is strongly deformed by kinks. In this region the slab is very thin ($dy < 0.5\,mm$) relative to its length leading to an aspect ratio > 20. Furthermore we observe the shift of the slab (as it has been observed by Mostovych et al. [1]) towards the right. The attributed this effect to the presence of a $\mathbf{E} \times \mathbf{B}$ drift coming from the generation of a polarizing electric field forming at the front of the jet as unmagnetized ions shoot ahead of magnetized electrons. As a result, this effect, can be observed in our MHD simulations (no polarizing fields). In any case, the experimental results presented here are a terrific confirmation that the overall AND the unstable behaviors are well captured by our 3D GORGON simulations. These results should be soon submitted.

7.7 Bibliography

[1] A. N. Mostovych, B. H. Ripin, and J. A. Stamper. Laser produced plasma jets: Collimation and instability in strong transverse magnetic fields. *Phys. Rev. Lett.*, 62:2837–2840, Jun 1989. 162, 165, 173

[2] C. Plechaty, R. Presura, and A. A. Esaulov. Focusing of an Explosive Plasma Expansion in a Transverse Magnetic Field. *Physical Review Letters*, 111(18):185002, November 2013. 162, 165

[3] S. Atzeni, A. Schiavi, F. Califano, F. Cattani, F. Cornolti, D. Del Sarto, T. V. Liseykina, A. Macchi, and F. Pegoraro. Fluid and kinetic simulation of inertial confinement fusion plasmas. *Computer Physics Communications*, 169:153–159, July 2005. 162

[4] DP Higginson, G Revet, B Khiar, J Béard, M Blecher, M Borghesi, K Burdonov, SN Chen, E Filippov, D Khaghani, et al. Detailed characterization of laser-produced astrophysically-relevant jets formed via a poloidal magnetic nozzle. *High Energy Density Physics*, 23:48–59, 2017. 163

[5] B. Albertazzi, A. Ciardi, M. Nakatsutsumi, T. Vinci, J. Béard, R. Bonito, J. Billette, M. Borghesi, Z. Burkley, S. N. Chen, T. E. Cowan, T. Herrmannsdörfer, D. P. Higginson, F. Kroll, S. A. Pikuz, K. Naughton, L. Romagnani, C. Riconda, G. Revet, R. Riquier, H.-P. Schlenvoigt, I. Yu. Skobelev, A.Ya. Faenov, A. Soloviev, M. Huarte-Espinosa, A. Frank, O. Portugall, H. Pépin, and J. Fuchs. Laboratory formation of a scaled protostellar jet by coaligned poloidal magnetic field. *Science*, 346(6207):325–328, 2014. 163, 171

[6] A. Ciardi, T. Vinci, J. Fuchs, B. Albertazzi, C. Riconda, H. Pépin, and O. Portugall. *Phys. Rev. Lett.*, 110:025002, 2013. 163, 169

[7] Hu Guangyue, Liang Yihan, Song Falun, Yuan Peng, Wang Yulin, Zhao Bin, and Zheng Jian. A 7 t pulsed magnetic field generator for magnetized laser plasma experiments. *Plasma Science and Technology*, 17(2):134, 2015. 165

[8] B. Roberts. Wave Propagation in a Magnetically Structured Atmosphere - Part Two - Waves in a Magnetic Slab. *Sol. Phys*, 69:39–56, January 1981. 165

[9] P. M. Edwin and B. Roberts. Wave propagation in a magnetically structured atmosphere. III - The slab in a magnetic environment. *Sol. Phys*, 76:239–259, March 1982.

[10] A. P. Singh and S. P. Talwar. Hydromagnetic stability of a plasma jet. *Sol. Phys*, 149:331–345, February 1994. 165

[11] J. A. Ionson. Resonant absorption of Alfvenic surface waves and the heating of solar coronal loops. *ApJ*, 226:650–673, December 1978. 165

[12] D. G. Wentzel. Hydromagnetic surface waves. *ApJ*, 227:319–322, January 1979. 165

[13] DD Ryutov, RP Drake, and BA Remington. Criteria for scaled laboratory simulations of astrophysical mhd phenomena. *The Astrophysical Journal Supplement Series*, 127(2):465, 2000. 165

[14] M. Kruskal and M. Schwarzschild. Some Instabilities of a Completely Ionized Plasma. *Proceedings of the Royal Society of London Series A*, 223:348–360, May 1954. 167

[15] Nicholas A. Krall and Paulett C. Liewer. Low-frequency instabilities in magnetic pulses. *Phys. Rev. A*, 4:2094–2103, Nov 1971. 167

[16] D. Winske. Short-wavelength modes on expanding plasma clouds. *Journal of Geophysical Research: Space Physics*, 93(A4):2539–2552, 1988. 167

[17] A. B. Hassam and J. D. Huba. Structuring of the ampte magnetotail barium releases. *Geophysical Research Letters*, 14(1):60–63, 1987. 167

[18] B. H. Ripin, E. A. McLean, C. K. Manka, C. Pawley, J. A. Stamper, T. A. Peyser, A. N. Mostovych, J. Grun, A. B. Hassam, and J. Huba. Large-larmor-radius interchange instability. *Phys. Rev. Lett.*, 59:2299–2302, Nov 1987.

[19] J. D. Huba, J. G. Lyon, and A. B. Hassam. Theory and simulation of the rayleigh-taylor instability in the limit of large larmor radius. *Phys. Rev. Lett.*, 59:2971–2974, Dec 1987. 167

[20] P. A. Bernhardt, R. A. Roussel-Dupre, M. B. Pongratz, G. Haerendel, A. Valenzuela, D. A. Gurnett, and R. R. Anderson. Observations and theory of the ampte magnetotail barium releases. *Journal of Geophysical Research: Space Physics*, 92(A6):5777–5794, 1987. 167

[21] D. B. Batchelor and R. C. Davidson. Nonlocal analysis of the lowerhybriddrift instability in thetapinch plasmas. *The Physics of Fluids*, 19(6):882–888, 1976. 167

[22] Shigefumi Okada, Kohnosuke Sato, and Tadashi Sekiguchi. Behaviour of laser-produced plasma in a uniform magnetic field–plasma instabilities. *Japanese Journal of Applied Physics*, 20(1):157, 1981. 167

[23] J. D. Huba and S. L. Ossakow. Physical mechanism of the lower-hybrid-drift instability in a collisional plasma. *Journal of Atmospheric and Terrestrial Physics*, 43:775–778, August 1981. 167

[24] J. P. Goedbloed, Rony Keppens, and Stefaan Poedts. *Advanced magnetohydrodynamics : with applications to laboratory and astrophysical plasmas*. Cambridge University Press, Cambridge; New York, 2010. 168

[25] M G Haines. A review of the dense z -pinch. *Plasma Physics and Controlled Fusion*, 53(9):093001, 2011. 168

[26] N. A. Krall Rosenbluth, M. N. and N. Rostoker. Finite larmor radius stabilization of 'weakly" unstable confined plasmas. *Nuclear Fusion Suppl.*, 143, 1962. 168

[27] T.S Green and G.B.F. Niblett. Rayleigh-taylor instabilities of a magnetically accelerated plasma. *Nuclear Fusion*, 1(1):42, 1960. 169

[28] Lyman Spitzer Jr. Physics of fully ionized gases. *American Journal of Physics*, 31(11):890–891, 1963. 169

[29] D. Ryutov, R. P. Drake, J. Kane, E. Liang, B. A. Remington, and W. M. Wood-Vasey. Similarity criteria for the laboratory simulation of supernova hydrodynamics. *The Astrophysical Journal*, 518(2):821, 1999. 169

Chapter 8

Accretion physics

Sommaire

8.1 Current picture of magnetospheric accretion onto young stars (T Tauri stars) 178

8.2 The accretion shock 182

8.3 State of the art of numerical simulations of accretion shocks. 186

8.4 Bibliography 191

8.1 Current picture of magnetospheric accretion onto young stars (T Tauri stars)

One of the main goals of this thesis was to perform a study of the dynamic, in the laboratory, of the accretion of matter in a strongly magnetized environment. Here, by "magnetized", we mean configurations where the thermal plasma-beta (the ration of thermal pressure to magnetic pressure) is relatively close to unity. Before presenting our main results in the next chapter 9, we give a small introduction to the topic with an overview of the basic physics of accretion in the class of young stars known as Classical T Tauri stars (CTTS). This introduction is largely based on a recent review by L.Hartmann [1] and we refer the reader to this work for an in-depth discussion about many aspects we will not present in this short introduction. These objects are young pre-main-sequence stars where several specific features, all associated with accretion process, are often observed in particular jets, winds and circumstellar disks [2]. Earlier in the manuscript we have presented work related to jets and we now focus on accretion from a disk, and more specifically on the interaction between the young star's magnetosphere and the accretion disk. There exist of course different phase in the evolution of young stars with the initial gas cloud collapsing to form the protostar accompanied of its accretion disk which is then "cleaned up" by both star and planetary accretion processes over the course of typically tens of millions of years [3]. Here we are interested in the accretion of matter from the disk toward the star surface through the existence of a sufficiently strong magnetic field linking both objects. For CTTS, the total accreted mass during the lifetime of the disk ($\sim 3\,\mathrm{M}yr$) represents only a small fraction of the total mass, typically estimated from millimiter-wave emission to $\sim 10^{-2}\mathrm{M}_{\odot}$ [4; 5]. However, this mass is comparable with the total mass present in the disk reservoir and thus this phase of mass accretion plays an important role in the evolution of circumstellar disks, where protoplanets are being formed. Indeed, within $\sim 10\,\mathrm{M}yr$ for low mass TTS, the disk is dispersed by planets formations (among others) and thus the accretion process stops. In our current picture of the evolution of young stars, the earlier, more intense, phases of mass accretion onto the protostar ($\lesssim 1\,\mathrm{M}yr$) are less understood, largely because the embryonic star is still embedded in a dense and opaque (at optical and near-IR wavelengths) infalling envelope that feed the mass onto the central objects (protostar+disk) [6].

In Fig.8.1, we present a schematic view, taken from [1], of a classical T Tauri star with its circumstellar disk. Observations have confirmed that the disk experiences a Keplerian rotation around the star [7] and its inner part couple to the stellar magnetic field at a radius (the truncation radius $\mathrm{R_T}$, see 8.2 for the definition) corresponding to the point of the disk where the ram pressure is approximately equals to magnetic pressure ($\mathrm{B}^2/2\mu_0 \approx \rho v^2$). The coupling between the disk gas and the magnetic field is possible because the stellar radiation field heats up the gas and establish a sufficiently high degree of ionization to allow the gas (a plasma) to be not far from an ideal MHD regime [8].

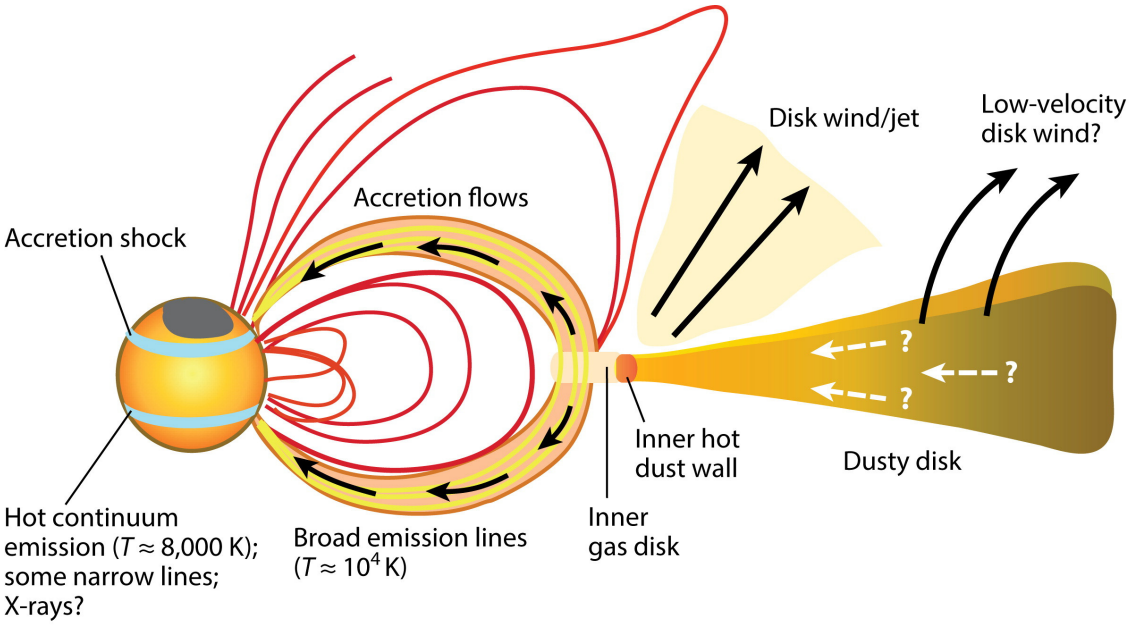

Figure 8.1: Schematic view a classical T Tauri star (from Hartmann L, et al., 2016. [1]). The disk rotating around its pre-main sequence star exchanges both matter and angular momentum through the existence of the stellar magnetic field (here represented as been dipolar). The coupling is done in the inner part of the disk where the gas is heated and ionized by the stellar radiations. The funneling of the disk material by the magnetic field to form the accretion flows leads to the generation of the polar accretions shocks which radiate in X-ray, UV and optical domains.

The truncation radius R_T

Here we derive an expression for the truncation radius.
In order to estimate this radius we suppose that at this point, R_T the ram pressure is equal to the magnetic pressure: $\rho v^2 \approx B^2/2\mu_0$. The magnetic field is taken to be dipolar and thus, $B_\star$ being the magnetic field on the star surface and $R_\star$ its radius, we can write $B(R) = B_\star(R_\star/R)^3$. The velocity v in the expression of the ram pressure ρv^2 is the characteristic speed of the material near the edge of the disk that is falling inward towards the star. The mass flux ρv can be related the accretion rate $\dot{M}$ by:

$$\dot{M} = \alpha R^2 \rho v \tag{8.1}$$

where $\alpha < 4\pi$ is a correction coming from the fact that accretion is not spherical (for a completely spherical accretion we would have $\alpha = 4\pi$). Thus we have $\rho v = \dot{M}/\alpha R^2$. Now if we make the rough approximation that the velocity at the truncation radius is equal to the free-fall velocity (which can not be the case), we can write: $v \approx \sqrt{2GM_\star/R}$, where $M_\star$ is the star mass. By gathering all these terms and squaring the pressure equality expression, we get:

$$\frac{R_T}{R_\star} \approx \epsilon \frac{B_\star^{4/7} R_\star^{5/7}}{\dot{M}^{2/7}(2GM_\star)^{2/7}} \tag{8.2}$$

using characteristics values of classical T Tauri stars $B_\star = 1\,kG$, $M_\star = 0.5M_\odot$, $R_\star = 2R_\odot$ and $\dot{M} = 10^{-8}M_\odot yr^{-1}$ we get $R_T \approx 7\epsilon R_\star$. Adopting typical value $\epsilon \approx 0.7$, we find that the truncation radius in TTS is roughly around five times the star radius.

This results in the funneling of material lifted from the disk into channels (accretion columns) that connect to the star surface (generally near the poles). This matter falls onto the star at velocities near the free-fall velocity ($\sim 300-500\,km.s^{-1}$ for typical stellar parameters, see 8.5) and then shocks on the surface chromosphere, producing temperatures of the order of 10^6 K $\sim 100\,eV$ [9]. This hot plasma radiates X-rays that are strongly absorbed and re-irradiated at lower wavelengths, producing strong ultraviolet-optical continuum in excess relative to the flux coming from the photosphere. The presence of these strong shocks is invoked to explain the observed excess, especially at ultraviolet wavelengths, which can be orders of magnitude higher than the flux of the "unperturbed" photosphere [10–12].

In the range of optical and near-IR wavelength, the excess makes the absorption lines of the photospheric flux appear less deep than in non-accreting stars. This is the so-called "veiling". From measured broad emission lines, temperatures of the order 10^4 K are estimated for the gas in the funnels; these are higher than the temperature of the inner part of the disk, which is heated by the stellar radiations to $\sim 10^3$ K. The origin of this heating is still unknown but presumably, the magnetic field is involved.

The free fall velocity V_{ff}

To find the free fall velocity of an object subject to the gravity of a star of mass $M_\star$ we must integrate the Newton's law for motion:

$$\frac{dv(t)}{dt} = -G\frac{M_\star}{r^2} \tag{8.3}$$

using the fact that dt=dr/v, we can write $dv(t)/dt = 1/2(dv^2/dt)$ and thus eq.8.3 can be written:

$$dv^2 = 2GM_\star d(\frac{1}{r}) \tag{8.4}$$

integrating and using the initial condition $v(r = R_T) = 0$, we get:

$$V_{ff} = \sqrt{\frac{2GM_\star}{R_\star}}\sqrt{1-\frac{R_\star}{R_T}} \tag{8.5}$$

where we used the notation $V_{ff} = v(r = R_\star)$. With typical TTS mass and radius, and assuming $R_T = 5.5R_\star$, we find $V_{ff} \approx 280\,km.s^{-1}$.

Another important question concerns the mechanism by which material from the outer parts of the disk is brought toward the inner parts. There is still no definitive answer about this point but the magnetorotational instability (MRI) [13] is strongly suspected to be involved through the generation of turbulence. It seems however that ambipolar diffusion effects as well as the effect of resistivity on the nonlinear stage of the MRI growth introduce difficulties in the original picture involving the MRI [14]. As a last important point of this introduction, one can understand that the transport of angular momentum must necessarily occur in this system, at least near the previously described truncation radius. Indeed, for matter to fall onto the star, it must lose the angular momentum that is associated with its Keplerian rotation. Several mechanisms are thought play a role to explain this loss. First, if the star magnetic field lines are sufficiently coupled to the disk material (high magnetic Reynolds numbers) then a differential rotation between the star

and the disk can transfer angular momentum through the magnetic field [15]. For this is the disk that transfer its momentum to the star, the magnetically-coupled parts of the disk have to be located below the corotation radius R_{co} of the star (the radius for which the matter has the same Keplerian velocity than the star angular velocity). For accretion onto the star to proceed, it is almost always assumed that we must have $R_T < R_{co}$ because if it is the opposite, the star actually tends to "push" away the disk matter through the increase of its angular velocity (if the material is sufficiently coupled to the field of course). This last situation is called the "propeller" regime [16]. Within this model, the accretion phenomenon is thus, not only a transfer of mass but also a transfer of angular momentum, the star increasing in the process both its total mass and its total angular momentum. In fact, many T Tauri stars are observed to be slow rotators [17], indicating that a large amount of angular momentum is transfered somewhere else, by an other mechanism. As shown in fig.8.1, near the truncation radius, the magnetic field can be at the origin of winds and/or jets (also discussed in this thesis) carrying angular momentum away from the star-disk system. The ejection process of this wind/jet comes from the deformation of field lines by differential rotation, thereby generating a Lorentz force directed perpendicular to the plane of the disk [18; 19].

Another important incertitude is related to the structure of the magnetic field itself. Indeed, it is well known that whereas far from the star surface the magnetic field is effectively well described as being dipolar, closer to the star, much of the field is distributed in quadrupolar or higher-order moments [20]. The consequence is that the measured surface-averaged fields on typical solar-mass T-Tauri stars (1-2 kG [21]) could be associated to high-order moments and so the dipolar field used in the current accretion models could be weaker than we think. In addition to the strength and order, it has been observed (for example on V2129 Oph [22]), that the dipolar moment of TTS can be tilted relative to the rotation axis of the star (and the disk). Two and three dimensional MHD simulations have shown that generally, for high tilt angle ($\gtrsim 20°$) the matter flows from the disk toward the star in two funnels whereas for small tilt angle, the accretion process is realized in multiple funnels [22].

The cororation radius R_{co}

The corotation radius of a star can be derived assuming Keplerian orbits rotations. The Keplerian velocity V_{Kep} of a body of mass m around a star is basically obtained by equalizing the centrifugal force with the gravitation force:

$$\frac{mV_{Kep}}{R} = \frac{mGM_\star}{R^2} \tag{8.6}$$

thus we get:

$$V_{Kep} = \sqrt{\frac{GM_\star}{R}} \tag{8.7}$$

The period of rotation of an object with this velocity is $2\pi R/V_{Kep}$ thus, in order the find the corotation radius, we just need to equalize this expression with $T_\star$, the rotational period of the star. After simplification we get:

$$R_{co} = \left(\frac{GM_\star T_\star^2}{4\pi^2}\right)^{1/3} \tag{8.8}$$

The corotation radius is important when a disk is present because stellar field lines which couple to the disk outside of R_{co} will act to slow the rotation of the star down, while field lines which couple to the disk inside R_{co} will act to spin the star up. Using the previously mentioned star mass and the typical rotation period $T_\star = 6\,days$ we find a typical corotation radius of $R_{co} \approx 11R_\odot \approx 5.5R_\star$.

8.2 The accretion shock

We now describe in details the physics of the accretion shock itself, focusing our discussion only on a small part of the global astrophysical object described in the previous subsection. In terms of laboratory astrophysics, shocks have always been one of most studied phenomenon in the laboratory because of the relative ease with which they can be produced, which is especially true since the advent of high-power lasers (see the thesis introduction). The accretion shocks occurring on the surface of TTS are complex and not fully understood. In fig.8.2 we show the currently accepted picture of the structure of these shocks (from [1]). As previously explained, the matter coming from the disk is accreted onto the stellar chromosphere at a velocity roughly equals to the free fall velocity v_{ff} (8.5).

In order to be shocked, this infalling gas must be sufficiently decelerated, which occurs where the thermal pressure is comparable to its ram pressure. Generally it is assumed that this occurs near the frontier between the chromosphere and the photosphere [10]. The object "accretion shock" is composed of four parts: the precursor, the shock, the post-shock region and the heated photosphere [10; 23; 24]. The precursor is located upstream of the shock itself, inside the accretion column and consists of gas preheated by x-ray radiation escaping the shock. These X-rays are produced because of the high typical temperatures reached by the infalling matter after the shock. This temperatures can be estimated from the Hankine-Hugoniot jump relations (see 8.10). We have: $k_B \Delta T = 3/16 m_H V_{ff}^2$ and using $V_{ff} = 280\,km.s^{-1}$ we find $\Delta T \approx 1.8\,10^6\,K \approx 150\,eV$, justifying the production of X-rays.

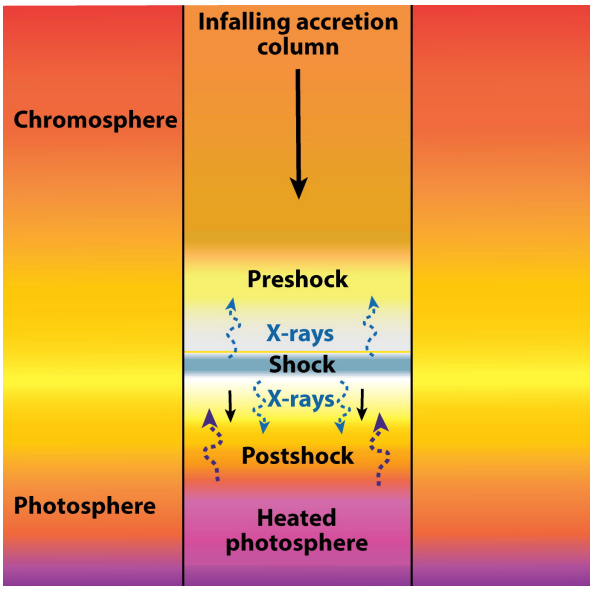

Figure 8.2: Schematic view of an accretion shock on the stellar surface (from Hartmann L, et al., 2016.). The infalling accreting material impact the star chromosphere and forms, where its ram pressure is comparable to the local thermal pressure, a shock. Temperature produced by this shock are of the order of few millions of kelvins and thus a large amount of X-rays are emitted. These radiations are then reprocessed by the preshock, the postshock and the ambient environment into larger wavelengths which creates the features observed on the TTS spectra.

Postshock temperature derived from Rankine-Hugoniot relations

In order to derive the postshock temperature, we make the assumption of a stationary shock, with the incoming flow indexed with the subscript "i" and the postshock flow with the subscript "f". The easiest way here is to use the conservation, along streamlines, of the sum of the specific kinetic energy $1/2v^2$ and the specific enthalpy $h_{spe} = \epsilon_{spe} + p/\rho$ where ϵ_{spe} is the specific internal energy and can be expressed as $\epsilon_{spe} = p/(\gamma - 1)\rho$. Thus across the shock we have

$$\frac{v_i^2}{2} + \frac{p_i}{\rho_i}\left(\frac{\gamma}{\gamma - 1}\right) = \frac{v_f^2}{2} + \frac{p_f}{\rho_f}\left(\frac{\gamma}{\gamma - 1}\right) \tag{8.9}$$

Now, if we suppose a strong shock, as it is the case for the accretion shock because of the high Mach number (VALUE), we have $\rho_f = 4\rho_i$ and $v_f = v_i/4$. With these values, expression 8.9 can be written as:

$$k_B \Delta T = m_H \frac{15}{32}\frac{\gamma - 1}{\gamma} v_i^2 \tag{8.10}$$

with $\Delta T = T_f - T_i$. In the case where $\gamma = 5/3$ we find the well known relation $k_B \Delta T = 3/16 m_H V_{ff}^2$. Estimates of the postshock temperature for a TTS accretion shock is given in the main text.

The postshock region is composed of plasma having passed trough the shock and being in the process of cooling, mainly trough radiation. A very important physical parameter which determine the scale and the strength of each part is the opacity. Typically the precursor can exist only if the incoming funneled flow can absorb a sufficient amount

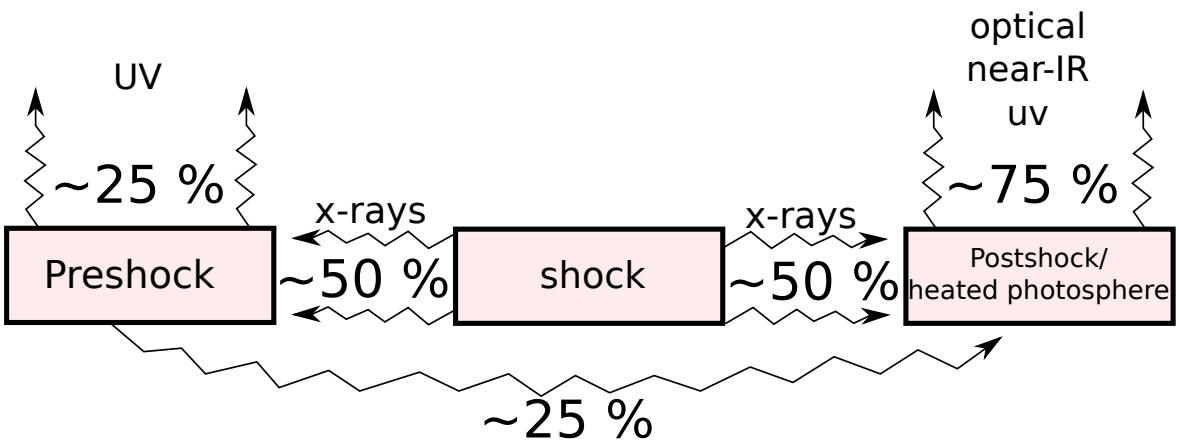

Figure 8.3: Schematization of the distribution of the total radiated energy by the accretion shock. All percentages indicates the portion of this total energy. The flux is first absorbed roughly equally by the preshock and the postshock/heated atmosphere whereas then the preshock radiates ~ 50 % of it outside the accretion region (mainly in UV band) and the other ~ 50% are reabsorbed and then re-radiated (in otpical, near-Ir and UV bands) by the postshock/heated atmosphere which is then finally responsible for emitting ~ 75 % of the initial shock radiation flux.

of radiations. This is why shocks where a precursor is present are often called "radiative shocks" [25]. A strong indication of the presence of opaque material in the accretion process comes from the fact that the excess of radiation flux inferred from star possessing a disk is observed mainly in non-X-ray ranges, mainly optical, UV and near-IR wavelengths [26].

The energy balance in the accretion process is schematically represented in fig.8.3. This is of course a very rough estimate of how the kinetic energy of the infalling flow is distributed and radiated. In the figure the percentages indicate the portion of the total emitted radiation flux from the shock region (which emits mainly in the soft x-ray band). About 50% of this emitted flux is radiated upwards and reabsorbed in the preshock region which reprocess this radiation, sending back toward the postshock/heated photosphere roughly half of it and the other half in the outer space, mainly in the far-ultraviolet domain. Thus, the postshock/heated photosphere receives ~ 75% of the radiated shock energy. This energy is reprocessed into UV, optical and near-IR radiations and then re-radiated.

In the UV domain, the radiation excess is very conspicuous since the relatively cold stellar photosphere produces weak UV fluxes whereas the preshock and the postshock/heated photosphere emit strongly in this domain [27]. In optical and IR ranges almost all the radiations comes from the postshock/heated photosphere region but the strong unperturbed part of the stellar photosphere has comparable flux in this domain, so the excess manifests as an increase of the continuum component of the spectrum (the so-called "veiling" [28]). Of course, in addition to the UV, IR and optical fluxes, there is still a small amount of x-rays escaping the shock region, but this generally represents less than ~ 5 % of the total radiated accretion energy [1].

Nevertheless, the x-ray spectrum typically has an important number of emission lines which are very useful since recently, high-resolution spectra of some CTTS have enabled measurement of individual emission lines sensitive to plasma density (i.e. He-like triplets). This important point allows one to distinguish the X-ray flux coming from the stellar coronae to the flux coming from the accretion process [29].

From the different spectra in the different bands (optical/IR, Uv, X-rays) we can re-

trieve two crucial informations (using either the continuum, for optical/IR domain or the lines for X-rays): the accretion rate $\dot{M}$, as well as the structure of accretion shocks. The accretion rate is the fundamental quantity that one wants to retrieve from observations, since it plays a key role in disk, as well, as star evolution models [30]. To estimate the accretion rate, one needs a measurement of the "magnitude" of the radiation flux in excess to the "unperturbed" stellar flux. Indeed, if we consider a complete conversion of the kinetic energy of the falling matter into radiations, we can estimate the accretion shock luminosity L_{acc} as:

$$L_{acc} = \frac{1}{2}\dot{M}v_{ff}^2 = \frac{GM_\star\dot{M}}{R_\star}\left(1 - \frac{R_\star}{R_T}\right) \tag{8.11}$$

where we used equation 8.5 for the free fall velocity. Thus, if we know the mass of the star, its radius and the truncation radius, measuring the total accretion (excess) luminosity can provide a reasonable estimate of the accretion rate. Of course, a relatively high uncertainty exists because of the presence of R_T, but this estimate can be considered valid as long as the truncation radius is at several stellar radii. Here, if we consider that the truncation radius is equal to the corotation radius, we have $R_T = 5.5R_\star$ (see the discussion about the truncation and corotation radii) and so $L_{acc} \approx 0.8GM_\star\dot{M}/R_\star$.

Concerning the shock structure, the one shown schematically in fig.8.2 has been extensively used as the basis to build synthetic spectra for a direct comparisons to observed spectra, and to derive accretion rates. The method is quite simple: the shocks are simulated, generally using (magneto-)hydrodynamic codes, with a given amount of "physics" included. For example, the models can include thermal conduction (sometimes with anisotropic coefficient), radiation transport, resistivity, viscosity... The resulting shock structure and plasma conditions are then used to compute synthetic spectra to compare to observations. Thus, to determine the exact the structure of accretion shocks, it is not only the "strength" of the excess luminosity that is important but also its "shape", that is the width and the ratios of lines. This is especially true in domains where strong emission lines are observed (e.g. optical and x-ray ranges). Today, relatively simple one-fluid, one-dimensional models coupled with an assumed uniform accretion around the star are able to reproduce reasonably well many of the features observed on the spectra [10], notably in the blue and the ultraviolet domains. However, with these uniform models, the predicted fluxes in red-optical wavelengths are lower than those measured through veiling [31]. This discrepancy can be eliminated by assuming accretion funnels of different densities, with high density funnels ($10^{11} - 10^{12}\,cm^{-3}$) representing spots covering at most $\sim 1\,\%$ of the star surface and lower density ($< 10^{11}\,cm^{-3}$) funnel spots covering up to $40\,\%$ of the star surface [1; 32]. However, it must be noted that no clear evidence of such variability in funnel densities have been observed and thus this problem is still largely model dependent.

Another important discrepancy that has been extensively discussed in previous works [24; 33] concerns the different mass accretion rates derived from UV/optical with the ones derived from the X-rays. The photoelectric absorption of these X-rays, emitted mainly by the postshock region, has been invoked to solve this discrepancy. Indeed, it has been shown that high column densities tends to penetrate deep into the stellar photosphere, leading to a much more favorable configuration for photon absorption [34; 35]. With this effect taken into account, the discrepancy can be eliminated [36; 37].

8.3 State of the art of numerical simulations of accretion shocks.

In this section we present a brief overview of the state of the art of numerical modeling carried out to unveil the physical processes at work in the accretion of matter onto TTS. First, the vast majority of the work being done on the accretion shocks simulations use 1D or 2D models. Generally, one may approximate the accretion column to a one-dimensional flow when its plasma (thermal) beta is very small, $\beta << 1$. To evaluate the column plasma beta, we first need to express the column density which can be done using simple arguments. If A is the area of the star covered by accretion columns, the mass density of the incoming material can be expressed as $\rho = \dot{M}/Av_{ff}$. Furthermore, introducing the well known "filling factor" f, the area A can be defined as $A = f4\pi R_\star^2$. The filling factor is actually estimated from observations to be close to $\sim 1\,\%$ (J.F-Donati et al. 2007). We can thus estimate the accretion column number density n (considering an hydrogen plasma) as:

$$n[cm^{-3}] = 6.9 \cdot 10^{-3} \frac{f^{-1}\dot{M}M_\star^{-1/2}R_\star^{-3/2}}{m_H}\left(1 - \frac{R_\star}{R_T}\right)^{-1/2} \tag{8.12}$$

Using the parameters we already used for TTS ($M_\star = 0.5M_\odot$, $R_\star = 2R_\odot$) with a filling factor $f = 0.01$ and $R_T = 5.5M_\star$ we find $n \approx 5.5 \cdot 10^{12}\,cm^{-3}$ ([10]). We also take a characteristic magnetic field strength at the star surface $B_\star = 1\,kG$, bearing in mind that the beta we will obtain will be certainly underestimated. We also take a column temperature $T_{col} = 10^4$ K, coherent with some observations [38] From $\beta_{col} = nk_BT_{col}/(B_\star^2/2\mu_0)$, we find $\beta_{col} \approx 2.10^{-4}$, indicating that the magnetic field should dominate the dynamic and the column should be relatively well described by 1D models. We must point out however that far from the star surface, we expect the B-field to be much weaker and the beta to be much higher. For example, taking the simple dipolar dependency of the magnetic field ($\propto R^{-3}$), the beta would be close to unity for a distance roughly equals to $4R_\star$. One can thus expect different behaviors in the "launching" region of the column, where material from the disk is loaded onto the accretion columns.

From here we must note that both the incertitude and the variability on the surface stellar magnetic field magnitudes can leads to accretion processes occurring within a large range of beta's. We show in figure 8.4 a table taken from [39] listing the predicted dipolar fields strengths for several low-mass ($< 2M_\odot$) TTS. As one can see, the expected fields range from 190 G to 10.6 kG and thus it represents a possible factor ~ 3000 in terms of magnetic pressure between the minimum and the maximum value.

The relevant parameter to estimate the plasma beta in the post-shock region is the dynamic beta of the column. Indeed, if we suppose a total conversion of incoming flow kinetic energy into thermal energy, we can estimate the postshock pressure as $P_{ps} \sim 1/2(\gamma - 1)m_H n V_{ff}^2$ where γ is the adiabatic index, taken here equals to 5/3 (mono-atomic gas). The thermal beta in the postshock region is thus given by $\beta_{ps} = 1/2(\gamma - 1)\beta_{col}^{dyn}$ where $\beta_{col}^{dyn} = \rho V_{ff}^2/(B_\star^2/2\mu_0)$ is the column dynamical beta. We can thus evaluate all the dependencies of the postshock thermal beta using the approximate expressions already given for the free-fall velocity (8.5), the column density (8.12) as well as the dependencies for the stellar magnetic field, taken from [39]:

Star	M_* ($M_\odot$)	R_* ($R_\odot$)	$\dot{M}$ ($M_\odot$ yr^{-1})	P_{rot} (days)	B_* [a] (G)	B_* [b] (G)	B_* [c] (G)
AA Tau	0.38	1.8	1.25×10^{-7}	8.2	3400	1400	4000
BP Tau	0.45	1.9	1.58×10^{-7}	7.6	3400	1400	4100
CY Tau	0.58	1.4	6.30×10^{-9}	7.5	2100	650	2500
DE Tau	0.24	2.7	3.16×10^{-7}	7.6	1000	480	1200
DF Tau	0.17	3.9	1.25×10^{-6}	8.5	570	320	670
DG Tau	0.67	2.3	1.99×10^{-6}	6.3	7700	3600	9100
DI Tau	0.31	2.2	1.58×10^{-8}	7.5	510	190	600
DK Tau	0.38	2.7	3.98×10^{-7}	8.4	1900	850	2200
DN Tau	0.42	2.2	3.16×10^{-8}	6.0	710	260	840
DR Tau	0.38	2.7	7.94×10^{-6}	9.0	9000	5100	10600
GG Tau	0.29	2.8	1.99×10^{-7}	10.3	1200	540	1400
GI Tau	0.30	2.5	1.25×10^{-7}	7.2	900	390	1100
GK Tau	0.41	2.2	6.30×10^{-8}	4.7	740	280	870
GM Aur.....	0.52	1.6	2.51×10^{-8}	12.0	4400	1600	5200
T Tau.....	2.00	3.4	1.10×10^{-7}	2.8	540	160	640
DH Tau	0.65	1.9	2.83×10^{-8}	7.2	1900	630	2200

NOTE.—Magnetic field values are the equatorial field strengths assuming a dipole magnetic field.

[a] Magnetic field values from the theory of Königl 1991.

[b] Magnetic field values from the theory of Cameron & Campbell 1993.

[c] Magnetic field values from the theory of Shu et al. 1994.

Figure 8.4: Table presenting stelar parameters for sixteen TTS (from C.M. Johns-Krull, 1999 ([39]). The main point regarding our discussion in the main text concerns the fact that surface magnetic field strengths spread over three order of magnitude (from 190 G TO 10,4 Kg) and thus one can expect a large range of plasma betas for the accretion process. The assumption of a 1D, 2D or 3D accretion dynamic relies heavily on the assumed value for this plasma beta.

$$B^{\star} \propto \frac{M_{\star}^{5/6}\dot{M}^{1/2}P_{\star}^{7/6}}{R_{\star}^{3}} \tag{8.13}$$

where $P_{\star}$ is the stellar rotational period.

We finally get all the postshock beta dependencies:

$$\beta_{ps} \propto M_{\star}^{-7/6}R_{\star}^{7/2}P_{\star}^{-7/3} \tag{8.14}$$

One can see that the thermal beta, in this model, does not depend on the accretion rate but instead of the intrinsic parameters of the star $M_{\star}$, $R_{\star}$ and $P_{\star}$. Therefore we see that stars with low mass, large radii and small rotation periods are more conducive to the establishment of high-beta accretion processes.

When the postshock thermal pressure is not small compared to the local magnetic field, the post-shock plasma is able to push aside the magnetic field and is then relatively free to spread over a much more larger area than the column cross section (see below) thus "breaking" the 1D behavior. If we take the previously used parameters, that is, a free fall velocity, calculated using formula 8.5, of $V_{ff} \approx 280\,km.s^{-1}$, a surface magnetic field of $B_{\star} = 1\,k$G and the density already derived for the accretion column, we find in this case $\beta_{col}^{dyn} \approx 6.10^{-2}$. Thus, with the TTS parameters used previously we thus find that both the beta of the accretion column and the postshock region are much lower than unity. The assumption of a 1D accretion shock appears then as reasonable in this case but, as we shall see later, even in low beta situations, the presence of MHD instabilities make the accreting flow intrinsically three dimensional. Furthermore, to obtain this postshock beta, we have taken a field of $1\,k$G but as we have seen (8.4), the variability in TTS magnetic fields strengths leaves room for high-beta accretion dynamics and we show in this manuscript for the very first time that 3D effects are important.

We shall now present a rapid overview of some of the work carried out on the topic of accretion shocks. This is not an exhaustive list but it presents at least the main numerical results already obtained in 2D and 3D.

- Sacco et al. (2008, [35]) used a 1D hydrodynamic model to describe the shock dynamic and stability, assuming an optically thin gas. The code included thermal conduction as well as tabulated cooling functions. The stellar atmosphere was setup using a heating function with the goal to retrieve the Sun chromosphere conditions. As the output of their simulations, they simulated x-ray spectra and compared them, with relatively good agreement, to observed spectra from the XMM-Newton satellite. They also observed in the simulation "Quasi-Periodic Oscillations" or "QPO" of the shock front. These oscillations are due to the cooling instability: as the accreting flow stacks progressively to form a slab of shocked material, the cooling by optically thin radiations reaches such a level that the slab collapses on itself. Then the process repeats itself with a typical period $\sim 400\,s$. At present these oscillations have not been observed [40] but if the accretion stream is strongly inhomogeneous, as suggested by 3D simulations [41], these oscillations would be difficult to observe.

- More recently (de Sa et al. 2014) our group developed a 1D model that includes radiative transfer as well as a self-consistent model for the stellar atmosphere structure. It was found that in this case the QPO's can be annihilated by the absorption of radiations in the slab which prevents the triggering of the cooling instability.

- Koldoba et al. (2008, [42]) have used a 1D MHD model where the magnetic field is tilted relatively to the star surface. They showed that in this case, and still in the optically thin regime, the shocked slab is unstable but with a very small period $< 1\,s$.

- Orlando et al. (2010, [43]) have used the PLUTO 2D MHD code ([44]) to study the case of accretion shocks where the beta is closer to unity, or even greater. They found that in these regimes, the shocked plasma is actually free to escape on the sides and large streams of both accreting material and chromosphere material are propelled by the high pressure core. These streams are found to be responsible of the suppression of QPO. In fig.8.5 we show results from these simulations, both for the case with gravity and the case without gravity (in order to quantify the importance of gravity in the dynamics, an important point for us since, in our experiments, gravity will have no effects). For each image, the left side represents the logarithm of the number density whereas the right side represents the logarithm of the temperature. In the first case, the shocked plasma of the slab (red bottom) can escape the sides forming what we will call the surrounding "shell". These process is responsible for mitigation of the QPO's. Very quickly, the ejected plasma is redirected toward the central accretion column and disturbs it. At later times, the shell collapses, because of the gravity, and the process repeats itself. In fact, a new oscillating behavior of the accretion dynamic appears but the main responsible here is not the cooling instability but rather the complex 2D geometry and the interaction of the shocked plasma with the magnetic field. In the case where the gravity is numerically removed (second column in fig.8.5), one can that the shell is still observed but, contrary to the previous case, it does not collapses but is instead "funneled" and stuck to the accretion column with a less disrupting effect. These simulations seems to show that the shell existence is not really linked to the presence of gravity but instead to the hot pressure slab at the base of the column which acts like a "propeller", the role of gravity being to trigger the shell collapsing.

- Sutherland et al. (2003a, [45]) and more recently Matsakos et al. (2013, [46]) have studied the effect of inhomogeneities on the accretion process. The first study, carried out with a 2D hydrodynamic code (no magnetic field), showed that the turbulent motion arising thanks to the additional dimension increase the cooling efficiency. In the second author studied the effect of disturbances of the infalling flow and showed that with a sufficiently strong magnetic field this flow is divided into independent fibrils (filamentary accretion column). When taken separately, each fibril behaves similarly to a 1D accretion column and shock, indeed showing QPO. However, taken together, the random QPO of each fibril washes out the resultant total radiation flux of the oscillations.

A central point emerging from this brief review concerns the impact of "dimensional" effects on the accretion dynamic. Indeed, as seen previously with the 2D simulations (fig.8.5), the material leaking on the sides of the accretion column changes strongly the structure of the shock itself and even annihilate features predicted by 1D simulation (QPO's). Then, naturally, arise the question about what 3D effects can change in the accretion dynamic, compared to the 2D case. We will address this important question. In all case, a better understanding of the complex 3D physics of accretion shocks would lead to better models to interpret the observed emissions from TTS.

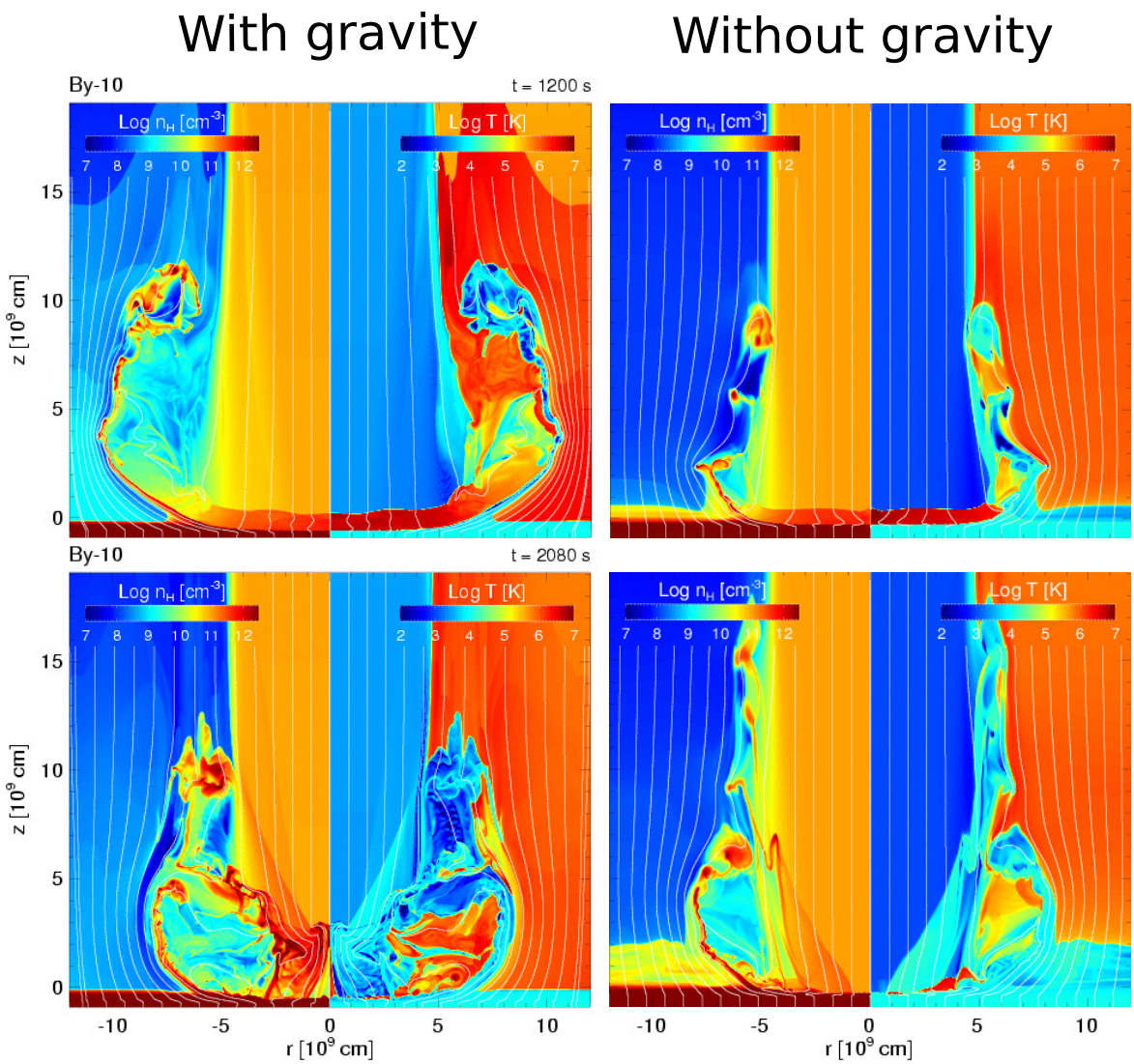

Figure 8.5: Density and temperatures maps of 2D MHD simulations of accretion shocks using the PLUTO code ([44]). On the left is shown the case where the gravity is included in the simulation whereas the right panel shows the case were it is artificially removed. The accreting column is coming from the top of the images, on each images, the left part represents the decimal logarithm of the number density whereas the right part shows the decimal logarithm of the temperature. It can be seen that in both cases, the dynamic reveals the development of a "shell" surrounding the accreting flow. It is important to remark that this shell develops with or without gravity included, indicating that the expulsion of material on the column sides is mainly pressure-driven. Courtesy of S. Orlando

8.4 Bibliography

[1] Lee Hartmann, Gregory Herczeg, and Nuria Calvet. Accretion onto pre-main-sequence stars. *Annual Review of Astronomy and Astrophysics*, 54(1):135–180, 2016. 178, 179, 182, 184, 185, XXXIII

[2] A. Frank, T. P. Ray, S. Cabrit, P. Hartigan, H. G. Arce, F. Bacciotti, J. Bally, M. Benisty, J. Eislöffel, M. Güdel, S. Lebedev, B. Nisini, and A. Raga. Jets and Outflows from Star to Cloud: Observations Confront Theory. *Protostars and Planets VI*, pages 451–474, 2014. 178

[3] Eric D. Feigelson and Thierry Montmerle. High-energy processes in young stellar objects. *Annual Review of Astronomy and Astrophysics*, 37(1):363–408, 1999. 178

[4] G. Basri and C. Bertout. Accretion disks around T Tauri stars. II - Balmer emission. *ApJ*, 341:340–358, June 1989. 178

[5] L. W. Hartmann and S. J. Kenyon. Optical veiling, disk accretion, and the evolution of T Tauri stars. *ApJ*, 349:190–196, January 1990. 178

[6] I. Appenzeller. Protostars. *Mitteilungen der Astronomischen Gesellschaft Hamburg*, 31:39, 1972. 178

[7] V. Mannings and A. I. Sargent. High-Resolution Studies of Gas and Dust around Young Intermediate-Mass Stars. II. Observations of an Additional Sample of Herbig AE Systems. *ApJ*, 529:391–401, January 2000. 178

[8] P. Godon. Accretion Disk Boundary Layers in Classical T Tauri Stars. *ApJ*, 463:674, June 1996. 178

[9] J. Bouvier, S. H. P. Alencar, T. J. Harries, C. M. Johns-Krull, and M. M. Romanova. Magnetospheric Accretion in Classical T Tauri Stars. *Protostars and Planets V*, pages 479–494, 2007. 180

[10] N. Calvet and E. Gullbring. The Structure and Emission of the Accretion Shock in T Tauri Stars. *ApJ*, 509:802–818, December 1998. 180, 182, 185, 186

[11] J. Muzerolle, P. D'Alessio, N. Calvet, and L. Hartmann. Magnetospheres and Disk Accretion in Herbig Ae/Be Stars. *ApJ*, 617:406–417, December 2004.

[12] I. Mendigutía, N. Calvet, B. Montesinos, A. Mora, J. Muzerolle, C. Eiroa, R. D. Oudmaijer, and B. Merín. Accretion rates and accretion tracers of Herbig Ae/Be stars. *aap*, 535:A99, November 2011. 180

[13] C. F. Gammie. Layered Accretion in T Tauri Disks. *ApJ*, 457:355, January 1996. 180

[14] Timothy P. Fleming, James M. Stone, and John F. Hawley. The effect of resistivity on the nonlinear stage of the magnetorotational instability in accretion disks. *The Astrophysical Journal*, 530(1):464, 2000. 180

[15] J. Li. Magnetic Interaction between Classic T Tauri Stars and Their Associated Disks. *ApJ*, 456:696, January 1996. 181

[16] G. V. Ustyugova, A. V. Koldoba, M. M. Romanova, and R. V. E. Lovelace. "Propeller" Regime of Disk Accretion to Rapidly Rotating Stars. *ApJ*, 646:304–318, July 2006. 181

[17] L. J. R. Machado, M. T. V. T. Lago, and J. J. G. Lima. *Rotation of T Tauri Stars Revisited*, pages 69–70. Springer Netherlands, Dordrecht, 1999. 181

[18] H. Shang, Z.-Y. Li, and N. Hirano. Jets and Bipolar Outflows from Young Stars: Theory and Observational Tests. *Protostars and Planets V*, pages 261–276, 2007. 181

[19] R. E. Pudritz, R. Ouyed, C. Fendt, and A. Brandenburg. Disk Winds, Jets, and Outflows: Theoretical and Computational Foundations. *Protostars and Planets V*, pages 277–294, 2007. 181

[20] S. G. Gregory, S. P. Matt, J.-F. Donati, and M. Jardine. The non-dipolar magnetic fields of accreting t tauri stars. *Monthly Notices of the Royal Astronomical Society*, 389(4):1839, 2008. 181

[21] C. M. Johns-Krull. The Magnetic Fields of Classical T Tauri Stars. *ApJ*, 664:975–985, August 2007. 181

[22] M. M. Romanova, M. Long, F. K. Lamb, A. K. Kulkarni, and J.-F. Donati. Global 3D simulations of disc accretion on to the classical T Tauri star V2129 Oph. *mnras*, 411:915–928, February 2011. 181

[23] E. Gullbring, N. Calvet, J. Muzerolle, and L. Hartmann. The Structure and Emission of the Accretion Shock in T Tauri Stars. II. The Ultraviolet-Continuum Emission. *ApJ*, 544:927–932, December 2000. 182

[24] H. M. Günther, J. H. M. M. Schmitt, J. Robrade, and C. Liefke. X-ray emission from classical T Tauri stars: accretion shocks and coronae? *aap*, 466:1111–1121, May 2007. 182, 185

[25] I. N. Kiselev, I. V. Nemchinov, and V. V. Shuvalov. Mathematical modeling of the propagation of intensely radiating shock waves. *Zhurnal Vychislitelnoi Matematiki i Matematicheskoi Fiziki*, 31:901–921, June 1991. 184

[26] E. Furlan, L. Hartmann, N. Calvet, P. D'Alessio, R. Franco-Hernández, W. J. Forrest, D. M. Watson, K. I. Uchida, B. Sargent, J. D. Green, L. D. Keller, and T. L. Herter. A Survey and Analysis of Spitzer Infrared Spectrograph Spectra of T Tauri Stars in Taurus. *ApJs*, 165:568–605, August 2006. 184

[27] L. Ingleby, N. Calvet, E. Bergin, G. Herczeg, A. Brown, R. Alexander, S. Edwards, C. Espaillat, K. France, S. G. Gregory, L. Hillenbrand, E. Roueff, J. Valenti, F. Walter, C. Johns-Krull, J. Brown, J. Linsky, M. McClure, D. Ardila, H. Abgrall, T. Bethell, G. Hussain, and H. Yang. Near-ultraviolet Excess in Slowly Accreting T Tauri Stars: Limits Imposed by Chromospheric Emission. *ApJ*, 743:105, December 2011. 184

[28] A. V. Dodin and S. A. Lamzin. Interpretation of the veiling of the photospheric spectrum for T Tauri stars in terms of an accretion model. *Astronomy Letters*, 38:649–666, October 2012. 184

[29] C. Argiroffi, A. Maggio, G. Peres, J. J. Drake, J. López-Santiago, S. Sciortino, and B. Stelzer. X-ray optical depth diagnostics of T Tauri accretion shocks. *aap*, 507:939–948, November 2009. 184

[30] L. Hartmann, N. Calvet, E. Gullbring, and P. D'Alessio. Accretion and the Evolution of T Tauri Disks. *ApJ*, 495:385–400, March 1998. 185

[31] W. Fischer, S. Edwards, L. Hillenbrand, and J. Kwan. Characterizing the IYJ Excess Continuum Emission in T Tauri Stars. *ApJ*, 730:73, April 2011. 185

[32] J.-F. Donati, S. G. Gregory, S. H. P. Alencar, J. Bouvier, G. Hussain, M. Skelly, C. Dougados, M. M. Jardine, F. Ménard, M. M. Romanova, and Y. C. Unruh. The large-scale magnetic field and poleward mass accretion of the classical T Tauri star TW Hya. *mnras*, 417:472–487, October 2011. 185

[33] B. Stelzer and J. H. M. M. Schmitt. X-ray emission from a metal depleted accretion shock onto the classical T Tauri star TW Hya. *aap*, 418:687–697, May 2004. 185

[34] Jeremy J. Drake, Paola Testa, and Lee Hartmann. X-ray diagnostics of grain depletion in matter accreting onto t tauri stars. *The Astrophysical Journal Letters*, 627(2):L149, 2005. 185

[35] G. G. Sacco, C. Argiroffi, S. Orlando, A. Maggio, G. Peres, and F. Reale. X-ray emission from dense plasma in classical T Tauri stars: hydrodynamic modeling of the accretion shock. *aap*, 491:L17–L20, November 2008. 185, 188

[36] N. S. Brickhouse, S. R. Cranmer, A. K. Dupree, G. J. M. Luna, and S. Wolk. A Deep Chandra X-Ray Spectrum of the Accreting Young Star TW Hydrae. *ApJ*, 710:1835–1847, February 2010. 185

[37] G. G. Sacco, S. Orlando, C. Argiroffi, A. Maggio, G. Peres, F. Reale, and R. L. Curran. On the observability of T Tauri accretion shocks in the X-ray band. *aap*, 522:A55, November 2010. 185

[38] C. F. Esau, T. J. Harries, and J. Bouvier. Line and continuum radiative transfer modelling of AA Tau. *mnras*, 443:1022–1043, September 2014. 186

[39] C. M. Johns-Krull, J. A. Valenti, and C. Koresko. Measuring the Magnetic Field on the Classical T Tauri Star BP Tauri. *ApJ*, 516:900–915, May 1999. 186, 187, XXXIV

[40] H. M. Günther, N. Lewandowska, M. P. G. Hundertmark, H. Steinle, J. H. M. M. Schmitt, D. Buckley, S. Crawford, D. O'Donoghue, and P. Vaisanen. The absence of sub-minute periodicity in classical T Tauri stars. *aap*, 518:A54, July 2010. 188

[41] M. M. Romanova, G. V. Ustyugova, A. V. Koldoba, and R. V. E. Lovelace. Three-dimensional Simulations of Disk Accretion to an Inclined Dipole. II. Hot Spots and Variability. *ApJ*, 610:920–932, August 2004. 188

[42] A. V. Koldoba, G. V. Ustyugova, M. M. Romanova, and R. V. E. Lovelace. Oscillations of magnetohydrodynamic shock waves on the surfaces of T Tauri stars. *mnras*, 388:357–366, July 2008. 189

[43] S. Orlando, G. G. Sacco, C. Argiroffi, F. Reale, G. Peres, and A. Maggio. X-ray emitting MHD accretion shocks in classical T Tauri stars. Case for moderate to high plasma-β values. *aap*, 510:A71, February 2010. 189

[44] A. Mignone, G. Bodo, S. Massaglia, T. Matsakos, O. Tesileanu, C. Zanni, and A. Ferrari. PLUTO: A Numerical Code for Computational Astrophysics. *ApJS*, 170:228–242, May 2007. 189, 190, XXXIV

[45] R. S. Sutherland, D. K. Bisset, and G. V. Bicknell. The Numerical Simulation of Radiative Shocks. I. The Elimination of Numerical Shock Instabilities Using a Local Oscillation Filter. *ApJS*, 147:187–195, July 2003. 189

[46] T. Matsakos, J.-P. Chièze, C. Stehlé, M. González, L. Ibgui, L. de Sá, T. Lanz, S. Orlando, R. Bonito, C. Argiroffi, F. Reale, and G. Peres. YSO accretion shocks: magnetic, chromospheric or stochastic flow effects can suppress fluctuations of X-ray emission. *aap*, 557:A69, September 2013. 189

Chapter 9

Magnetized accretion in the laboratory

Sommaire

9.1 Introduction 196
9.2 Experimental results 196
9.3 Numerical setup 199
9.4 Generation and characterization of the accretion column 201
9.5 Accretion shock 3D structure 203
9.6 Temperatures and emission in the laboratory accretion process 206
9.7 On the importance of the obstacle ablation 210
9.8 Influence of the orientation 212
9.9 Bibliography 214

9.1 Introduction

In the previous chapter 8 we have presented the general physics of accretion shocks in the context of variable stars called T Tauri stars (TTS), a particular case of young stellar object (YSO). The general picture used in the vast majority of accretion models is that of a one-dimensional (1D) shock structure, a model valid only if the thermal beta (thermal pressure/magnetic pressure) of the postshock plasma is much smaller than unity. It is known that these pre-main-sequence stars exhibits a large range of different surface magnetic field strengths [1] and thus a large panel of plasma betas. We have briefly described recent numerical works carried out to study the two-dimensional (2D) magnetohydrodynamic (MHD) accretion dynamics in situations where the beta is close to unity or even greater [2]. As explained it has been found that the supplementary dimension introduces the possibility for the shocked plasma to escape on the sides of the accretion column, forming a pressure-driven plasma "shell" composed of mixed materials from both the column and the star photosphere/chromosphere. We highlighted the fact that some 1D results were undermined by the presence of this shell in 2D simulations among which the mitigation of the never observed "Quasi-Periodic Oscillations" ("QPO's") citeSacco2008. Relying on these previous works, we propose in this chapter to investigate, in the laboratory, the possibility to produce accretion shocks using magnetically-collimated supersonic/superalfvenic jets impacting onto solid targets. We present, for the first time, a numerical, fully three-dimensional (3D) MHD characterization of a laboratory astrophysics experiment that allow, using existing facilities, to realize high-beta accretion shocks. As in the chapter about laboratory supersonic jets, we first give in 9.2 some of the recent experimental results that have been obtained by our collaboration on the ELFIE installation at the LULI laboratory. These experimental results are presented in [3] where the reader can find more details. We then briefly describe the numerical setup (9.3) which is very similar to the one used of the generation of supersonic jets (see 5.3). We also characterize in details our laboratory accretion column by introducing two important quantities: the accretion rate as well as accretion kinetic energy flux (9.4). Then the 3D structure of the shock region is analyzed (9.5) as well as the keV-temperatures et radiations generated (9.6). We insist on the important role of the material coming from the target on which the accreting flow is impacting (9.7). Finally, we investigate the influence, as suggested by observations [4], of varying the orientation of the magnetic field in our initial setup (9.8).

9.2 Experimental results

The results presented here are taken from our paper [3], where the reader can find much more details than presented in this section. The experiment was performed at the ELFIE Nd:glass laser facility of the LULI laboratory, at Ecole Polytechnique (France) [6]. The experimental setup used to study the accretion dynamic in the laboratory is shown in fig.9.1. An Helmholtz coil delivering a relatively homogeneous magnetic field of 20 T is used to embed two flat solid targets near its central region, the whole being disposed in vacuum chamber at a pressure $\approx 1\,\mathrm{P}a \approx 10^{-5}\,atm$. The 40 J, 0.6 ns (FWHM), 700 μm (laser spot diameter) ELFIE pulse is used to generate a laser-produced expanding plasma from a first target composed of PolyVinyl Chloride (PVC, $(C_2H_3Cl)_n$) whereas the second target, composed of Teflon (CF_2), is placed at 18 mm away from the first target and serve as the surface on which accretion is happening. As we have seen in section 5.6 (and recalled in this chapter in 9.4), the interaction of the expanding plasma with the magnetic

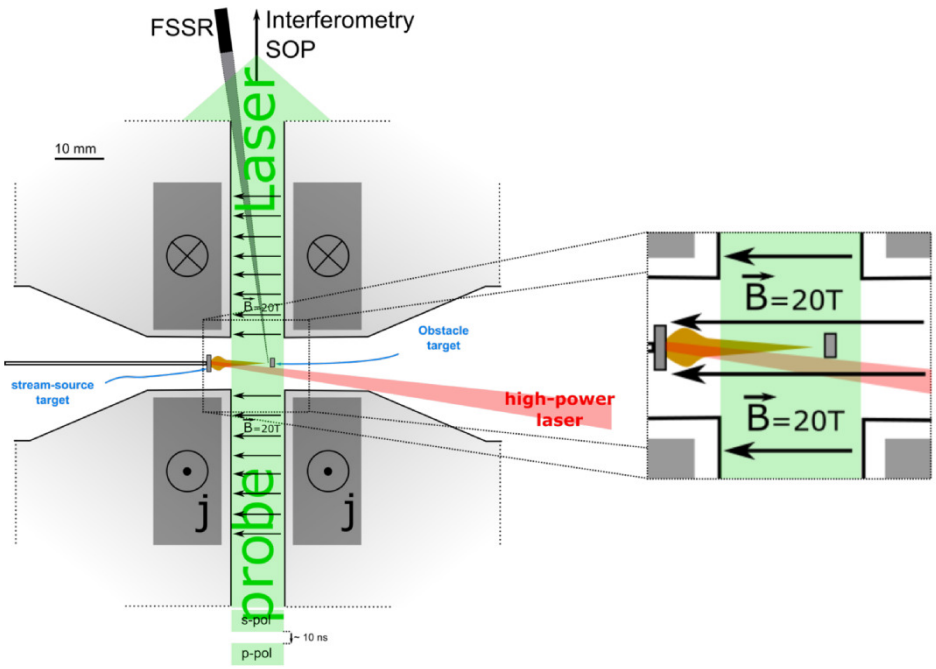

Figure 9.1: Cartoon showing the top view of the central coil-region of the experimental set-up and the diagnostics paths. The grey rectangle represents the Helmholtz coil, inside the airtight structure, delivering a magnetic field in the central region up to 20 T [5]. The conical apertures allow the insertion of the stream-source target as well as the main laser beam to reach the stream-source target without clipping the obstacle target. The obstacle target is inserted from the bottom of the coil through a vertical aperture. The probe beam travels along the coil following the perpendicular aperture, going through the interaction region.

field results in its collimation in a $\sim 1.4\,mm$ cylinder, representing the accretion column impacting the Teflon obstacle. The optical probing uses an interferometric technique to retrieve the plasma electron density in the low-density regions (density below $10^{20}\,cm^{-3}$) of the plasma. It consists in a standard Mach-Zehnder interferometer and uses a compressed probe laser pulse delivering $100\,m$J in $350\,fs$, at the wavelength of $\lambda = 528.5\,nm$, to probe the plasma. The interferograms recorded on CCD cameras are analyzed using the Neutrino code [7]. The very small energy of the probing pulse compared to the ablative pulse provides the guarantee that the probing does not affect significantly the dynamics. Then a wavelet model enables to fit the fringes arrangement, from which a phase map is then unwrapped. Using an Abel transform [8], the plasma electron density n_e is retrieved from the phase map assuming an axisymmetric distribution of the plasma (a point, as we shall see in our numerical analysis, that can be disputed).

In fig.9.2 are shown four different maps of the decimal logarithm of the electron density. Indicated times refer to the start of the accretion process, when the column head reaches the Teflon obstacle. These images reveal the presence of three different structure clearly identifiable. First, the accreting flow is seen, on all images, as the relatively low dense $n_e \sim 10^{18}\,cm^{-3}$ column at the center of the images, coming from the top. Then, a dense $n_e \sim 10^{19}\,cm^{-3}$ region is observed at the base of the obstacle and seems, as time increases, climb along the column. As we will see in our numerical work, we identify this region to the accretion shock itself as well as the resulting postshock plasma. We call this region the "core". Finally we clearly see the generation of relatively symmetric, at least at early times (i.e. $18\,ns$), structures on the sides of both the column and the core. The

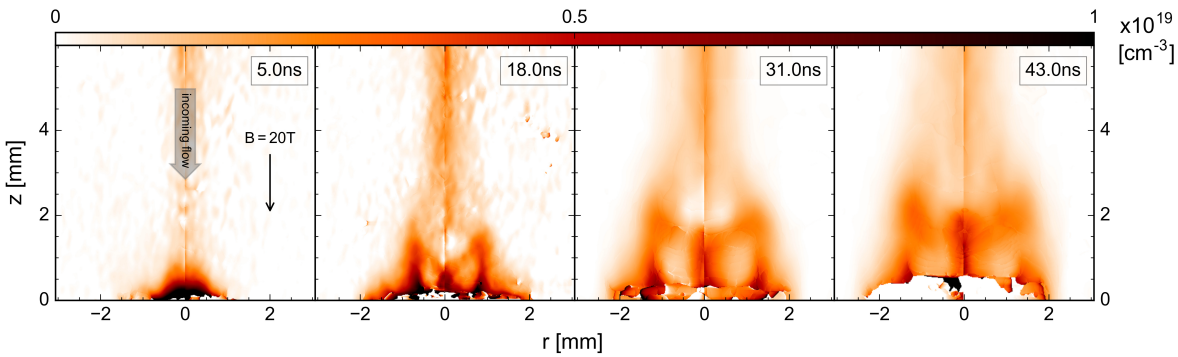

Figure 9.2: 2D maps of the decimal logarithm of electron density inferred from interferograms which have been Abel inverted (assuming axisymmetric distribution of the plasma). Times refer to the start of the accretion process when the head of the column hit the obstacle. (see G.Revet, PhD thesis, 2017)

plasma forming this structure is included in what we call the "shell". This last feature, as we have already mentioned in the introduction and as we shall see later (9.5), is a fundamental consequence of the multidimensional aspect of our accretion experiments and can be identified to structures observed in 2D MHD astrophysical simulations of accretion shocks[2]. These experiments, which are a first, serve as a basis for the numerical work we are going to present in the next sections.

On the obstacle pre-shock density profile

As we shall see later (9.7), the material from the obstacle plays a important role in the laboratory accretion process. Thus, in order to perform consistent numerical simulations, we have studied the structure of the obstacle itself when a laser pulse impact the first laser target. Without magnetic field, the ablated plasma expands largely in all directions an no measurable accreting flow is detected where the obstacle is located ($\sim 10\,mm$ away from the laser target). We have observed that the creation of the plasma on the first target was responsible for the generation of x-rays which ablate the obstacle surface. As a result, an other expanding plasma is created in front of the obstacle and a typical profile obtained with interferograms is shown in fig.9.3. As one can see, the resulting profile (green line) is best fitted with a $1/z$ function (blue line). Since no radiative transfer is performed in our code, we can not simulate this ablative process and thus we have used this experimental profile as an "input" for our simulations presented in the next sections.

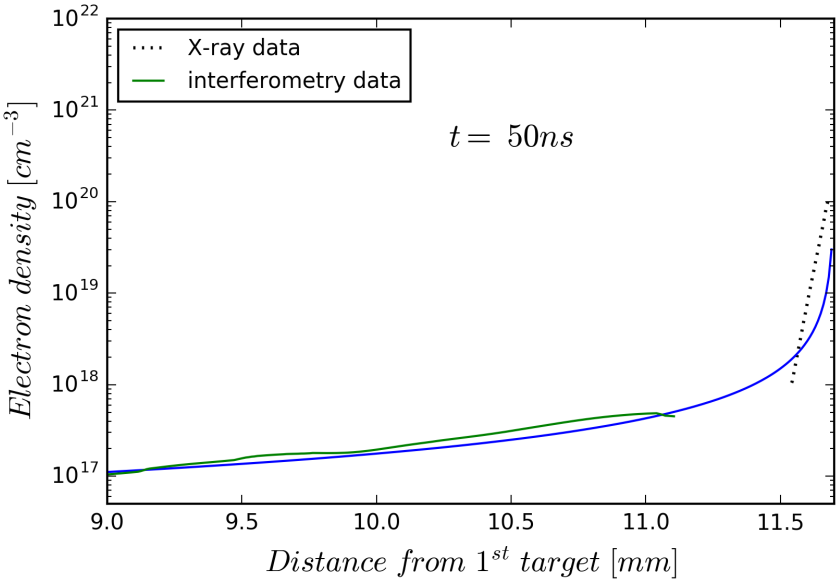

Figure 9.3: Profile of the decimal logarithm of electron density inferred from interferograms (green) which have been Abel inverted (assuming axisymmetric distribution of the plasma). Also shown is the density very close to the target (black dotted line) measured from x-rays absorption. The blue curve is the best interpolation obtained and corresponds to a decrease of the density in front of the obstacle inversely proportional to the distance. Here times refer to the start of the laser pulse. (see G.Revet, PhD thesis, 2017)

9.3 Numerical setup

The simulation setup aiming to study the experiment is shown in fig.9.4. It consists of two solid carbon targets separated by a distance 12.4 mm. These will be referred to as the "laser target" and the "obstacle". A homogeneous magnetic field is initialized, along the z direction, perpendicular to both targets, with a strength $B_0 = 20\,T$. The interaction of the laser pulse with the laser target is again modeled in axisymmetric, cylindrical geometry with the two-dimensional, three-temperatures, Lagrangian, radiation hydrodynamic code DUED ([9]). At the end of the laser pulse, the profiles of density, momentum and electronic/ionic temperatures are linearly mapped onto the 3D grid of the Eulerian, resistive MHD code GORGON (2.4). The simulation 3D domain is composed of $300 \times 300 \times 640 = 5.76 \cdot 10^7$ cells using a cartesian grid of dimension $6\,mm \times 6\,mm \times 12.8\,mm$ thus corresponding to a uniform resolution of $\Delta = 20\,\mu m$. The lasers parameters are presented in the table at the top right of fig.9.4. The laser energy is 17 J, the laser pulse duration (FWHM) $\tau_L = 0.5\,ns$, the focal spot diameter of $\phi = 750\,\mu m$ and thus the laser intensity at the focal point is $I \approx 7.7 \cdot 10^{12}\,W.cm^{-2}$. These values correspond to nominal parameters that are accessible on current high-power laser facilities, and are directly relevant to existing experiments and the one we presented in the previous section [5].

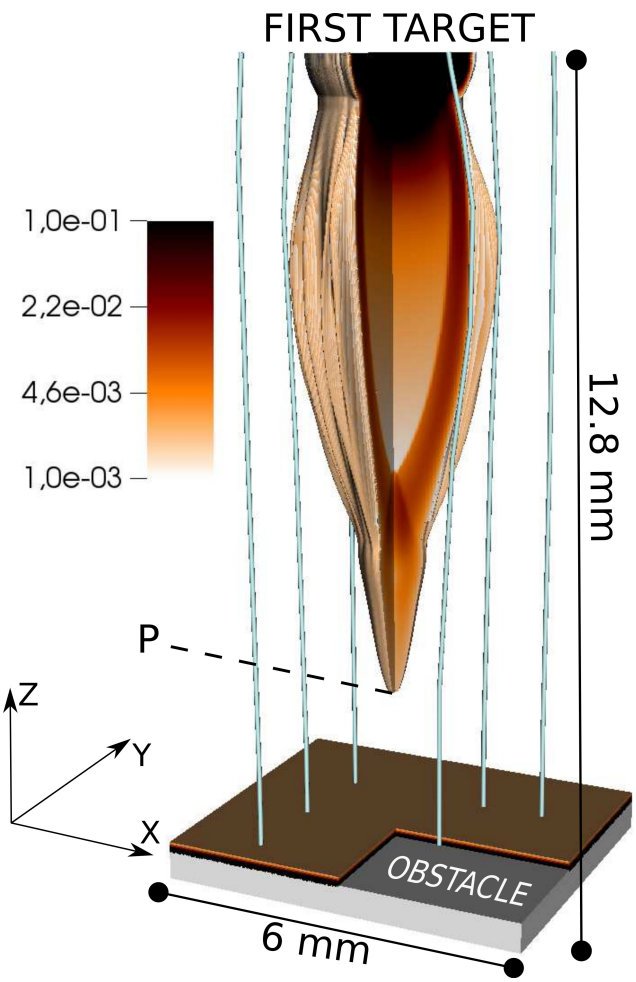

Laser parameters

Intensity [W.cm^{-2}]	$7.7\,10^{12}$
Energy [J]	17
Focal diameter [µm]	750
Pulse duration [ns]	0.5

	Lab	CTTS
Material	C	H
Magnetic field [T]	20	7.10^{-4}
density [g/cc]	$2\,10^{-6}$	10^{-13}
Flow velocity [km.s^{-1}]	870	500
T_e [eV]	95	0.22
T_i [eV]	91	0.22
Sound speed [km.s^{-1}]	93	7.4
Alfven speed [km.s^{-1}]	400	62
Mach number (sonic)	9.5	67
Mach number (FMA)	2.1	8
Reynolds number	$3.5\,10^{4}$	10^{11}
Magnetic Reynolds number	10^{3}	10^{9}
Peclet number	1.9	10^{9}
Thermal beta	$8\,10^{-2}$	10^{-2}
Dynamic Beta	10	128

Figure 9.4: Left: 3D iso-volume of the decimal logarithm of the mass density at $t = 8\,ns$. The laser target is located at the top whereas the collimated laser-produced plasma, forming our laboratory accretion column, is propagating towards the obstacle at the bottom of the image. The blue tubes represent the magnetic field lines. On the right, the top table gives the relevant laser parameters used to generate the expanding plasma whereas the second table gives a comparison of the important parameters for both the laboratory column and the TTS column.

9.4 Generation and characterization of the accretion column

We now focus our discussion on the laboratory "accretion column" alone. Using the initial setup described in the previous section, we have already demonstrated, both numerically [10] and experimentally [11; 12], the possibility to produce astrophysically-relevant magnetically collimated flows (jets) which are well described by ideal MHD (see the dedicated chapter 5). Indeed, one of the underlying mechanisms responsible for the generation of these jets is linked to "flux freezing" in the plasma, which is a consequence of the high plasma temperatures ($\gtrsim 100\,eV$) reached with high power lasers ($I \gtrsim 10^{12}\,W.cm^{-2}$). Within this condition, the laser-produced plasma is collimated by the magnetic field and essentially forms an expanding, cylindrical magnetized "accretion column" which is made to interact with the obstacle. The ideal MHD regime is in fact necessary for both the collimation and the scaling [13].

The astrophysical relevance of our laboratory column can be evaluated by comparing certain dimensionless parameters for both systems. In table 2 of fig.9.4 the relevant parameters of the collimated flow from the laser-target (the "accretion column") are presented. These parameters have been averaged over all the column head, on a distance of $\approx 3\,mm$. Alongside these laboratory parameters, we also indicate the corresponding values for the astrophysical system (TTS) taken from [3]. While the flow velocity is comparable between the two systems ($500-1000\,km.s^{-1}$), the laboratory accretion column is approximately ten million times denser and five hundred times warmer. In terms of dimensionless parameters, both systems are supersonic and have velocities greater than the fast magneto-acoustic speed ($\sqrt{cs^2+v_A^2}$, where cs is the sound speed and v_A the Alfven speed). Importantly, both the viscous and the magnetic Reynolds numbers are much larger than unity, meaning that dissipative processes are not dominant. The column Peclet number (for heat conduction) is in both cases greater than one but in the laboratory case it is low enough to not ignore thermal conduction effects. Finally, the plasma betas (the thermal beta been the ratio of the kinetic pressure on the magnetic pressure whereas the dynamic beta is the ratio of the ram pressure on the magnetic pressure) are comparable in the two systems, with similarly large dynamic beta > 10 and small thermal beta $< 10^{-1}$. The values presented in fig.9.4 highlight the possibility to perform, at least partially, the scaling between the laboratory and the astrophysical systems [13].

Two other parameters are useful in characterizing the accretion process, namely the mass accretion rate $\dot{M}_{acc}$, discussed earlier, as well as the accretion column flux of kinetic energy $1/2\dot{M}_{acc}v_z^2$, $v_z < 0$ being the velocity of the flow in the z direction. As we have seen in the previous chapter, the kinetic energy flux is crucial when studying accretion processes in astrophysics because it provides an upper limit on the accretion shock luminosity, and helps to deduce the accretion rates [14].

For the laboratory accretion flows, and very likely for astrophysical accretion flows ([15]), both quantities are time-dependent and are not homogeneous over the cross section of the column. Their temporal variation is shown in fig.9.5. Throughout this chapter, all times are given relative to the end of the laser pulse, when the input data from the DUED code are remapped in GORGON. The accretion rate and the kinetic energy flux are computed by integrating over the column cross section, the local mass flux $\Phi_{mass} = \rho|v_z|$ and the local kinetic energy flux $\Phi_{energy} = 1/2\rho|v_z^3|$, where ρ is the plasma mass density. All the integrated fluxes shown in fig.9.5 are calculated $2\,mm$ away from the obstacle surface (corresponding to the point P in fig.9.4).

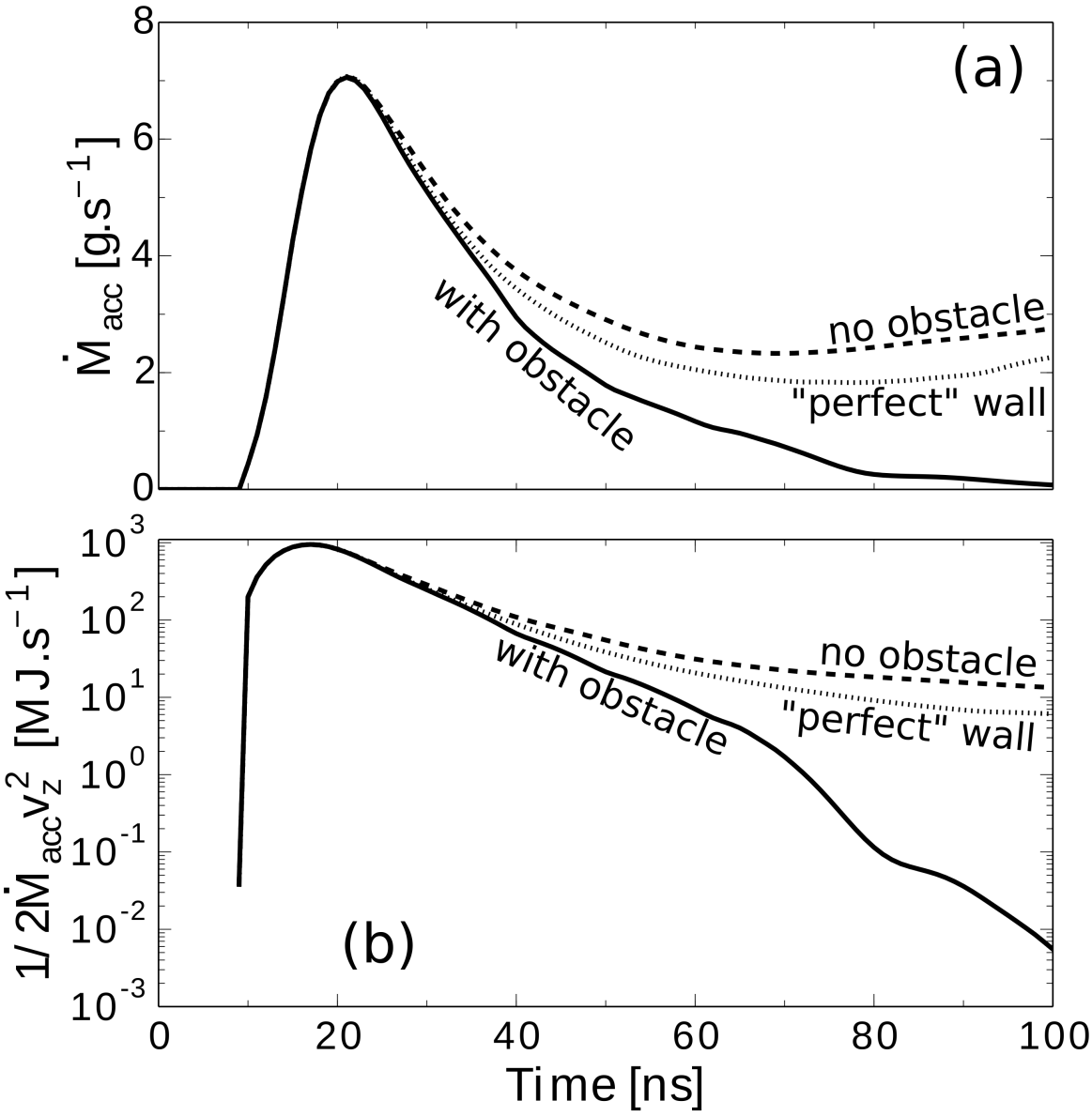

Figure 9.5: (a) Time-dependence of the mass accretion rate of the laboratory column computed at the altitude $z = 2\,mm$ (the point P in fig.9.4) and integrated over the column cross section: $\dot{M}_{acc} = \int \Phi_{mass} dS$ with $\Phi_{mass} = \rho|v_z|$. (b) Time-dependence of the accretion kinetic energy flux of the laboratory column computed at the altitude $z = 2\,mm$ (the point P in fig.9.4) and integrated over the column cross section: $1/2\dot{M}_{acc}v_z^2 = \int \Phi_{energy} dS$ with $\Phi_{energy} = 1/2\rho|v_z^3|$. For each quantity, we plot the case where the obstacle is removed, when it is present as well as when it is replaced by a "perfect wall" (i.e. reflecting boundary condition).

Three cases are shown in fig. 9.5. One where the obstacle was removed from the simulation and which provides the characterization of the accreting flow alone, without the effects the presence of an obstacle would induce. In addition to the standard obstacle case, the profiles for a simulation with a "perfect" wall (essentially a reflecting boundary condition) are also shown.

We focus first on the case without the obstacle. The curves for the accretion rate and kinetic energy flux then represent their nominal values for the case where the flow is unperturbed by back streaming plasma coming from the interaction with an obstacle. As we shall discuss later, the post-shock plasma largely modifies the dynamics of the accreting flow. It is clear from fig.9.5(a, b), that the accretion flow generated by the laser ablation of the primary target is not steady state. The accretion rate rapidly increases to a maximum of $\dot{M}_{acc} \approx 6.1\, g.s^{-1}$ at about $t = 22\, ns$, before slowly decreasing to reach an almost constant values of $\dot{M}_{acc} \approx 2.3\, g.s^{-1}$ at $t \sim 70\, ns$. Remarkably, the variation between the peak and the nearly steady state accretion rate is only a factor ~ 2.6 during a time of 100 nanoseconds, which is 200 times the laser pulse duration, and that we can produce accretion rates that are almost constant over ~ 60 ns. Opening the door to long term evolution studies of accretion flows using even longer laser pulses ($5-20$ ns).

The peak in the kinetic energy flux occurs slightly earlier than the mass accretion ($\sim$ 16 ns) and then decreases by almost two orders of magnitude over the next $\sim 80\, ns$. This very large variation is a consequence of the strong dependence of the flux with the velocity ($\propto v_z^3$) which itself depends on the time with t^{-3} (for a given z, see the velocity profile discussed in our chapter about laboratory jets 5.4.1).

Another interesting aspect of the curve of the kinetic energy flux is that it can be an important tool in order to deconvolve time-integrated spectra used to estimate plasma temperatures [16] since this curve should indicate the times at which the main contributions to the spectrum are realized by the emitting plasma. It is also interesting to note that the kinetic energy flux peak value arrives $\sim 8\, ns$ before the accretion rate reaches its maximum and thus, following the previous discussion about the accretion shock luminosity, an experimenter who would use a time-resolved diagnostic, for example an SOP [3], to measure the luminosity of the shock should not consider that its brightest point corresponds to the time of maximum mass inflow because of the $\sim 8\, ns$ delay between the two maximums.

This last point is also experimentally-relevant since it could have a strong effect on the times that are effectively "recorded" by the diagnostics using the radiations for their measure. Indeed, these instruments are often protected with filters in order to limit the flux of photons entering through their aperture and thus the radiations emitted late in the experiment ($\gtrsim 50\, ns$) could be largely attenuated, possibly below the detection threshold.

9.5 Accretion shock 3D structure

The general morphology of the shock region is presented in fig.9.6(a,b), which shows the iso-volumes of the mass density in one-half of the computational domain. Fig.9.6(a) corresponds to $t = 22\, ns$ whereas fig.9.6(b) corresponds to $t = 40\, ns$.

In both images, we identify three main structures: (1) the accretion column, (2) the accretion shock, forming what has been called the "core" (see section 9.2) and (3) the previously mentioned "shell" which is developing, in early times, on the sides of the core and, as time increases, starts to enfold the column itself.

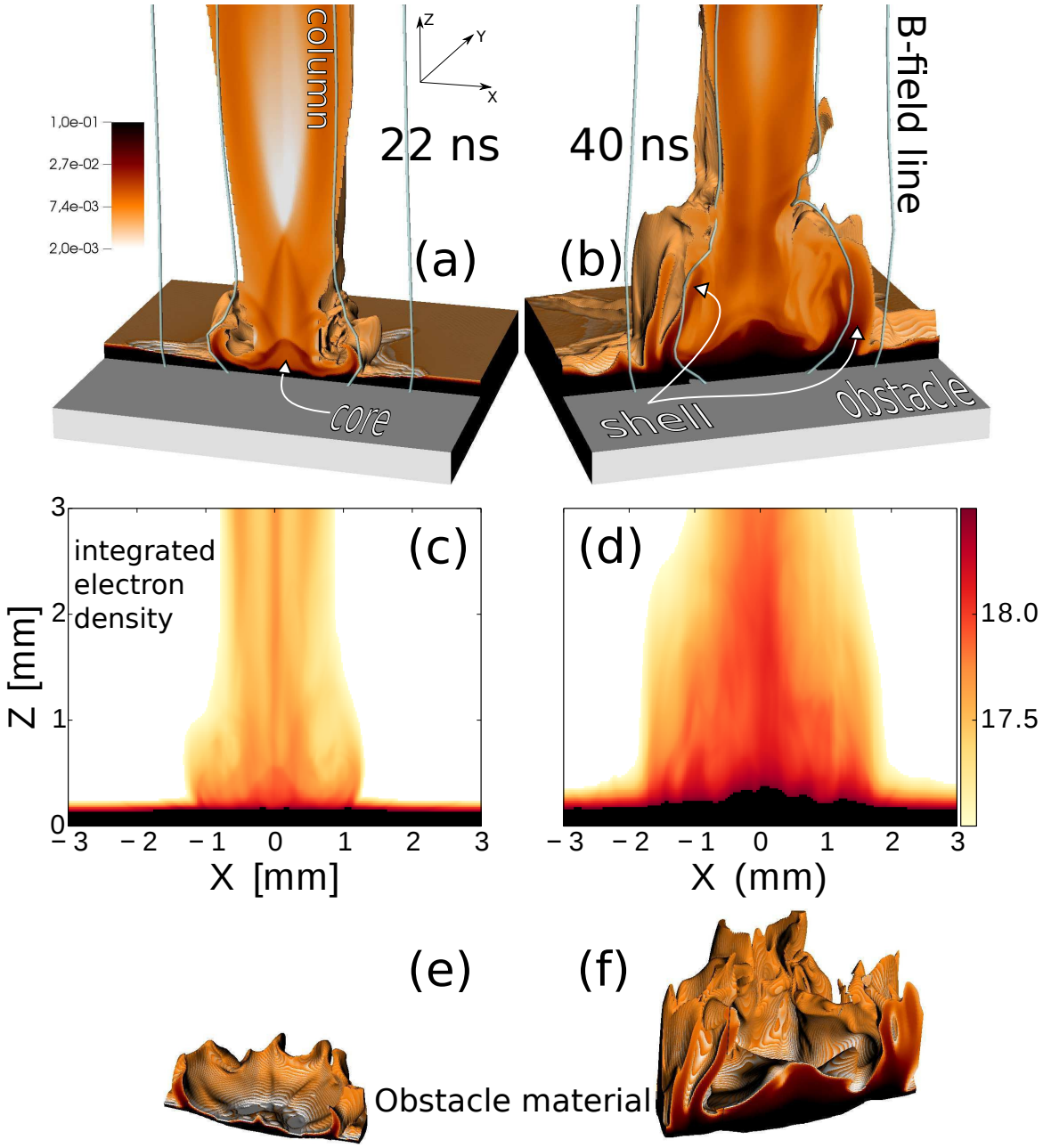

Figure 9.6: (a-b) Iso-volume of the decimal logarithm of the mass density near the obstacle (in a volume of 6mm x 6mm x 3mm). The gray slab is the solid obstacle material. The left image corresponds to $t = 22\,ns$ whereas the right to $t = 40\,ns$. (c-d) 2D maps of the decimal logarithm of the integrated (along y-direction) electron density. Both images correspond to the times indicated above (left:22 ns, right:40 ns). (e-f) Iso-volume of the decimal logarithm of the obstacle mass density for the same times indicated above. The material from the obstacle is followed in GORGON using a tracer.

All these components of the laboratory magnetized accretion shock have been observed experimentally and described in our recent paper [3], which strengthen the argument that the simulations capture correctly the dynamics of the accretion flow.

The shell dynamic is connected to the interaction of the shocked plasma with the magnetic field. The plasma beta of the core in our simulation is $\beta_{core} \approx 8$ at $t = 22\,ns$. Immediately after the shock, the magnetic field is unable to prevent the core plasma escaping laterally. We note that in all previous accretion experiments of which we are aware [see for example [17; 18]] this lateral expansion can't be observed because they were using solids tubes instead of the magnetic field, which effectively model the interior of the accretion column or the very low plasma beta case, but have unwanted side effects, for example shock reflexions on the walls of the tube or "pollution" of the accreting column by the material of the tube.

It is now conceivable that in the not so distant future it will be possible to perform laboratory accretion shocks in the small beta limit, without any tubes. For example, with our laser parameters (see table 1 in fig.9.4), a beta ≈ 1 would be obtained with a field of $\approx 50\,\mathrm{T}$, a field strength already within reach [5]. For much lower betas, e.g. $\beta < 0.1$, the required fields would be $\gtrsim 180\,\mathrm{T}$, a range also started to be explored but on a much more smaller scale [19]. Alongside the mass density presented in fig.9.6(a,b), magnetic field lines are also shown. When the core plasma is expelled on the sides, the high magnetic Reynolds numbers ($\mathrm{R}_e \sim l_{core} c_{core}/\mathrm{D}_m \approx 5000$ implies that the field lines are advected radially and that the core region is emptied progressively of its magnetic field to form a diamagnetic cavity [20]. In the expression of the magnetic Reynolds number $l_{core} \approx 1\,mm$ is the characteristic core size, $c_{core} \approx 400\,km.s^{-1}$ is core sound speed and $\mathrm{D}_m \approx 8\,10^{-2}\,m^2.s^{-1}$ the core magnetic diffusivity.

The lateral expansion of the plasma leads to the compression and bending of the magnetic field, and the resulting increase of magnetic force ($\mathbf{j} \times \mathbf{B}$, where $\mathbf{j}$ is the electrical current) on the edges of the cavity slows down the expansion. It is important to note that the bending of the field lines is possible because they are anchored into the solid target. For more details about the process by which a plasma is decelerated by a magnetic field at a plasma/vacuum interface, see [21]. The plasma being radially decelerated is then forced, by the pressure forces, to "climb up" the accretion column forming a shell of plasma around the shock and column. The image in fig.9.6(b) at $t = 40\,ns$ represents an advanced stage of the laboratory accretion process where the shell is fully formed and interacting with the incoming flow.
The origin of the plasma present in the shell is actually more complicated than just assuming it is post-shock material being redirected around the column. Indeed, we observe in our simulations the occurrence of an important mixing of plasma originating from the column and from the obstacle. Figure 9.6(e,f) shows at 22 and 40 ns the effect of the impact of the accretion flow on the obstacle material. The figure shows the isovolume of mass density from the obstacle, which is followed in the simulation by advecting, with the MHD velocity, a passive scalar tracer.

We observe that a large amount of obstacle material is ejected by the impacting accretion flow. Comparing these images with the one showing the total mass density (fig.9.6(a,b)) reveals the origin of the dense twisted "branches" observed early in the accretion process (fig.9.6(a)) and seen growing as time increases (fig.9.6(b)) from a height of $\sim 0.3\,mm$ to a height of $\sim 1.5\,mm$. These structures are in fact material of the obstacle set in motion and "lifted" by the accreting flow to form a kind of ring encircling, at first, the core and then a non negligible portion of the accretion column. We find for example that at $t = 40\,ns$ and at the altitude $z = 1.5\,mm$, the obstacle material account for roughly 23 % of the total mass

at this altitude, knowing that this ratio is even greater at as we look closer to the target surface. For potential direct comparisons with experimental results, we give in fig.9.6(c,d) the maps, corresponding to the two previous times (22 and 40 ns), of the integrated (along the y-axis) electron density. These should be directly comparable with Mach-Zehnder interferometric measurements frequently used as a diagnostic for the electron density [11; 12; 22]. As one can see, at $t = 22\,ns$ the relative good azimuthal symmetry of the ring structure (see fig.9.6(e)) is well visible in the line integrated density. However, at later times the obstacle ring is clearly deformed and the loss of symmetry means that the line integrated electron density map appears blurred, thus washing out the detectability of the ring structure (fig.9.6(f)).

In a previous paper [10], we have pointed out that the collimation of laser-produced plasmas by magnetic fields is subject to the growth of the Rayleigh-Taylor instability which develops on the plasma column outer surface, modulating these regions of the incoming flow into filaments with dimensions of the order of the column radius. These radial protrusions of matter out of the surface of the column, introduce inhomogeneities in both the local accretion rate $\rho|v_z|$ and the kinetic energy flux $\rho|v_z^3|$. For example, deviations of the local kinetic energy flux relative to the mean kinetic energy flux on at a given height of the accretion column can reach 70%. This aspect of the laboratory accretion columns structure represents a crucial difference with the perfectly homogeneous accreting flow assumed in the vast majority of 2D models [2]. We can however mention the recent work by Bonito et al. [23] where they performed simulations introducing a 2D accretion column with a density decreasing towards the edges. The goal was to investigate the effect of local absorption due to pre-shock material and surrounding chromosphere to resolve the discrepancies between observed X-ray luminosities and the higher values that are predicted by models [24]. Nevertheless, they still assumed a symmetry of the flow around the column main axis. We see here that inhomogeneities and filaments in the accretion flow result in large asymmetries developing in the shell (fig.9.6(f)).

The first important conclusion resulting from these observations is that adding a supplementary dimension when modeling the accretion problem, the shell observed in 2D simulations is still present despite the possible instabilities that can arise because of 3D effect (see below).

9.6 Temperatures and emission in the laboratory accretion process

We now address the question of the coupling of electron and ion temperatures in the laboratory accretion process. This point is of great importance if one wants to assess the astrophysically-relevance of an experiment like the one we present in this paper. We show in fig.9.7(a,b), at $t = 22\,ns$, two 2D slices of both the ion temperature (fig.9.7(a)) and the electron temperature (fig.9.7(b)). The three distinct parts of the accretion region are again clearly identifiable in these maps: (1) the accretion flow is seen as the relatively cold ($T_i \sim T_e \sim 100\,eV$, in blue in the images) column coming from the top of both images. We can however note that the center of the column is much hotter than its edges with in this region $T_i \sim 2-3\,keV$ and $T_e \sim 300-400\,eV$. These high temperatures come from the recollimation conical shock seen at $z \approx 2.4\,mm$ and $x = 0\,mm$ (also observed in the mass density map in fig.9.6(a)). This shock, which is an intrinsic feature of the magnetically-collimated laboratory jets [10], introduces in the column a supplementary

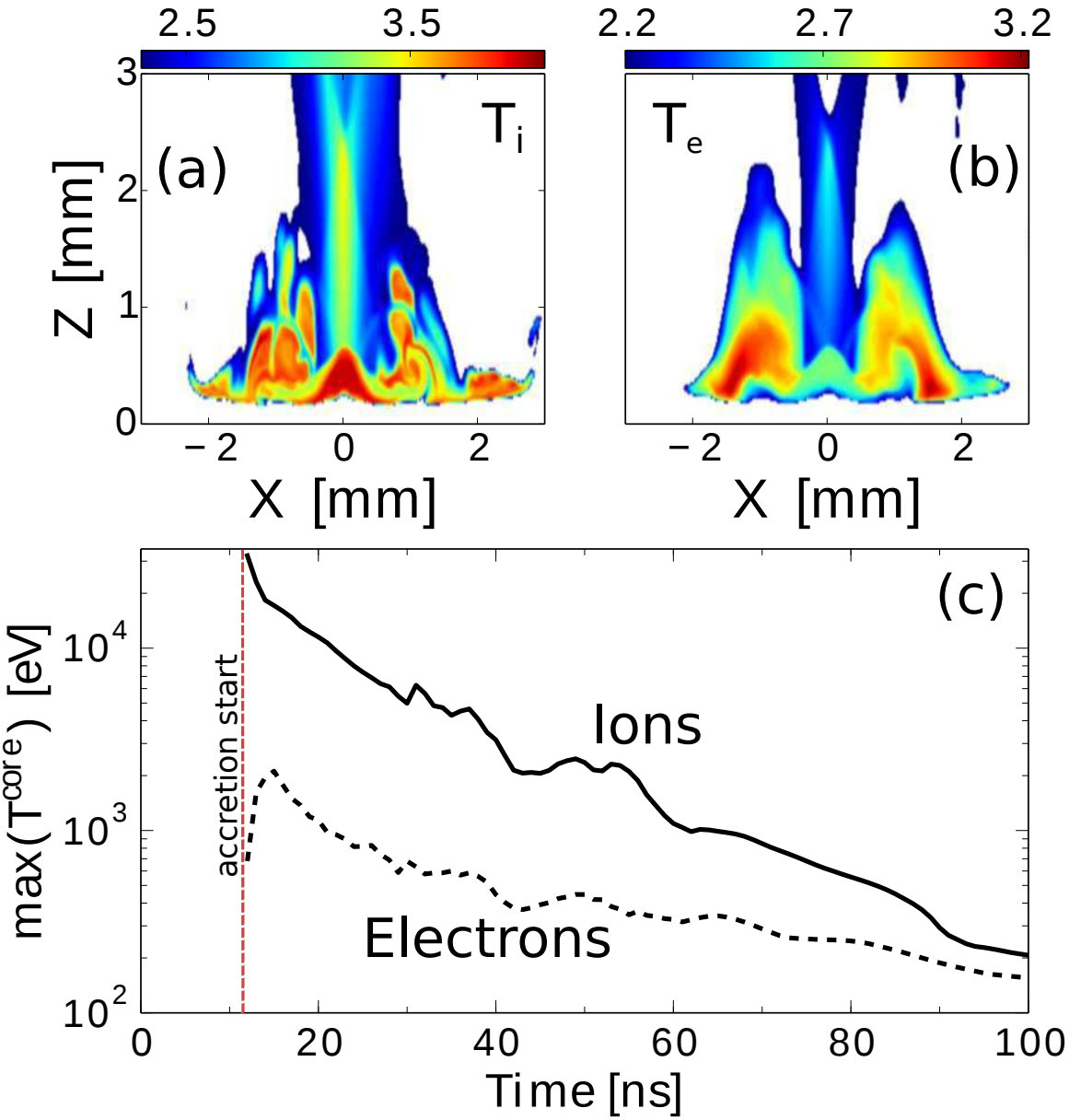

Figure 9.7: (a) 2D maps of the decimal logarithm of the ion temperature at $t = 22\,ns$ (corresponding to the density shown in fig.9.6(a)). (b) Same as (a) but for the electron temperature (same time). (c) Maximum ion (full line) and electron (dotted line) temperatures in the core as a function of time.

internal structure which is absent in the idealized 2D astrophysical accreting flows [2]. A consequence of the presence of the conical shock in the column above the obstacle is that when the plasma cross the accretion shock front (at $z \approx 0.6\,mm$) it is already in an post-shock state with ion temperatures much higher than electron temperatures. As we have seen in our chapter about laboratory supersonic jets, this point out an important aspect relevant for the experiments: when a longitudinal (z) magnetic field is used to generated supersonic jets [11; 12] or, equivalently, accretion flows [3] from an initially laser-produced expanding plasma, the collimation process is realized through successive compression and rarefaction regions (similar to the shock diamonds patterns observed in supersonic exhaust plumes of propulsion systems [25]) and thus, the distance chosen between the laser target and the obstacle must be beforehand carefully considered. In our simulation, we observed that if the obstacle is placed close after the first conical shock, this one degenerate into a Mach disk and thus breaks the collimation of the column. The conical shock seen in fig.9.6(a) and fig.9.7(a,b) is actually the second one and in this case does not degenerates into a Mach disk. The core temperatures show that the post-shock plasma is brought into a state very far from a thermal equilibrium with, at $t = 22\,ns$, $T_i \sim 10\,keV$ and $T_e \sim 500\,eV$ because the temperature gain is proportional to the mass of the shock particles and the equilibration time is $\sim 30\,ns$ in this region. We plot in fig.9.7(c) the maximum ion (full line) and electron (dashed line) temperatures inside the core as a function of time. The red vertical dashed line indicates the time when the incoming flow hit the obstacle surface ($\sim 12\,ns$). We see that during all the simulation duration ($100\,ns$) the ions and electrons never reach a total thermal equilibrium but as the time increases the temperature difference decreases from $\Delta T(t = 12\,ns) \approx 31\,keV$ to $\Delta T(t = 100\,ns) \approx 50\,eV$. The initial shock temperatures are $Ti \approx 32\,keV$ and $Te \approx 675\,eV$ whereas at the end we have $Ti \approx 207\,eV$ and $Te \approx 155\,eV$. These decreasing profiles of temperatures are a direct consequence of the velocity profile which is in our case very well approximated by $v_z = (z - z_{target})/t$ with $z_{target} = 12.0\,mm$ is the position of the laser target surface. This expression is valid for times greater than the laser pulse duration and for positions such that $z <= V_{max}t$ where $V_{max} \approx 1000\,km.s^{-1}$ is the velocity of the propagating front. Finally, in the shell we observe the result of the progressive equilibration between ions and electrons. Because the post-shock equilibration time ($\sim 30\,ns$) is much greater than the time needed by a fluid particle to exit the core region ($\sim 2\,ns$), the highest electrons temperatures ($\sim 1.4\,keV$ at $t = 22\,ns$) in the shell can be reached at more than $1\,mm$ away from the core. From energy conservation and neglecting the post-shock electron temperature, we can expect for an adiabatic and isochoric equilibration process the final temperature to be close to $T_{eq} \sim T_i/(1+Z)$ (Z been the mean degree of ionization taken to be close to its maximum value for carbon (Z=6)). Taking for T_i the maximum from 9.7(c), one would expect the electrons to reach, after equilibration, values up to $T_{eq} \sim 4.5\,keV$ (at early times). In fact we never observe electron temperatures as high as this idealized value and instead maximum values of $\sim 3.7\,keV$ at $t \approx 16\,ns$ that is $\sim 4\,ns$ after the column impact onto the target. These lower than expected temperatures are the result that both the adiabatic and the isochoric assumptions are non verified. Indeed, as soon ass the particles escape the core their density decreases because of their expansion and moreover they are cooled by radiations because of optically thin radiation losses.

Alongside the temperatures, our 3D simulations allow us to investigate the spatial distribution of where the radiated energy has been emitted during the accretion process. This spatial distribution is represented in fig.9.8 inside a cylinder of dimension ($r = 2.5\,mm, \Delta z = 6\,mm$) with the base of this cylinder anchored on the solid surface of the obstacle. The volume contained inside this cylinder thus includes all the regions of

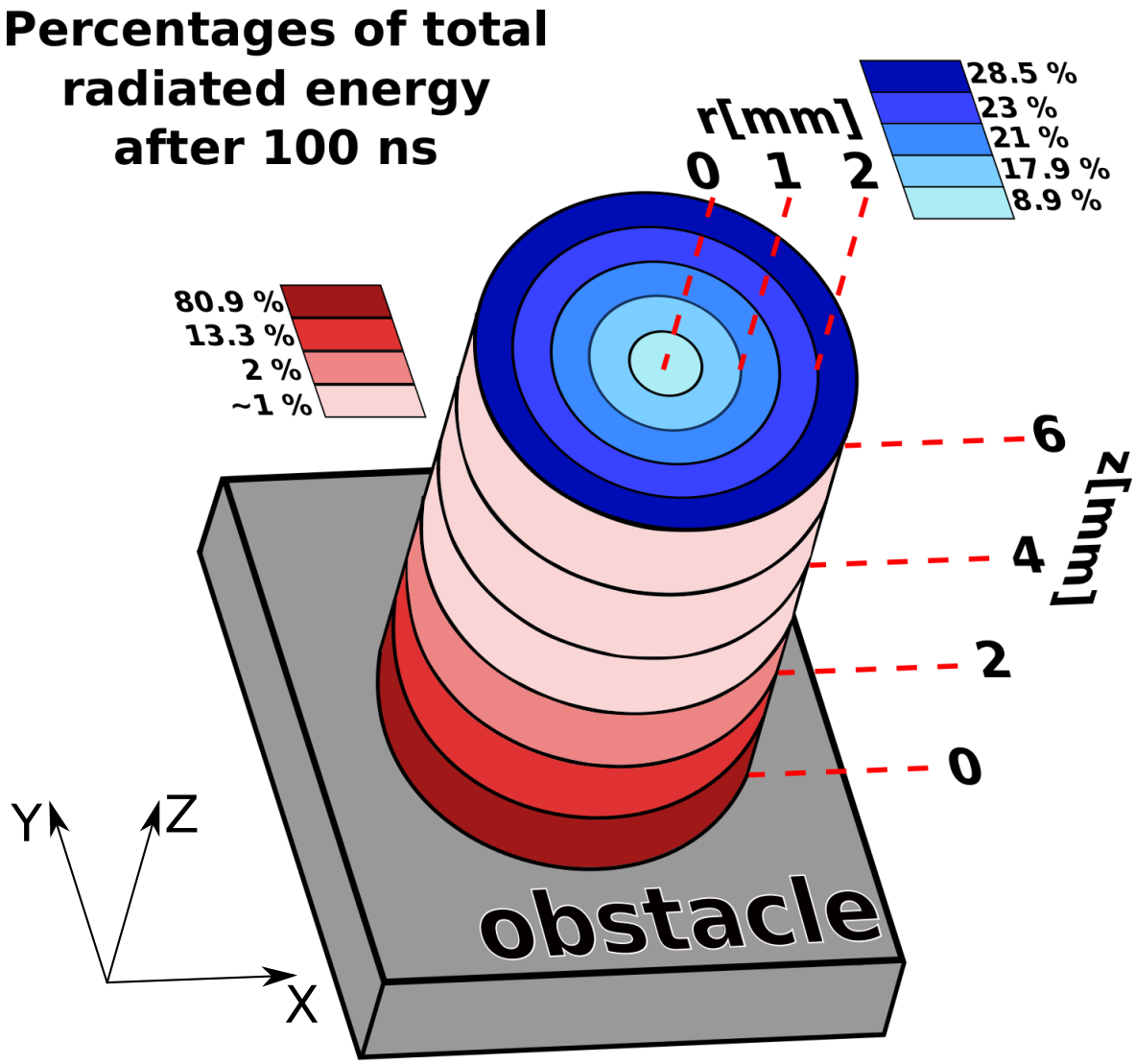

Figure 9.8: S
chematic representation of the spatial distribution of the total energy radiated during the first 100 ns. The volume containing the accretion region is cut into cylinders, both vertically (z) and radially (x/y). For the vertical cutting (red cylinders), each cylinder has a radius of 2.5 mm and a height of 1 mm. For the radial cutting (blue cylinders), each hollow cylinder has a thickness of 0.5 mm and a height of 6 mm. The percentages indicate the portion of the total energy radiated in each cylinder during the first 100 ns.

the accretion shock (column, shell and core) and we will call it V_{cyl}. In the azimuthal direction, we slice V_{cyl} in five smaller hollow cylinders of thickness $\Delta r = 0.5\,mm$ and heights $\Delta z = 6\,mm$ (the blue ones) and in the z direction we slice V_{cyl} in six smaller full cylinders of heights $\Delta z = 1\,mm$ and radius $r = 2.5\,mm$ (the red ones). Both colorbars indicates the percentages of the total radiated energy which has been emitted in each volume throughout the $100\,ns$ simulated. With this definitions, the sum of radiated energy in the red cylinders is thus equals to the sum of the radiated energy in the blue ones. As one can see from the longitudinal (z) distribution, almost all the energy ($\sim 95\,\%$) is lost in the first $2\,mm$ away from the obstacle surface and, looking closer, $\sim 81\,\%$ is lost below $1\,mm$. This region include the core and the base of the shell which is composed of plasma particles having, shortly before, been shocked at the temperatures described in the previous discussion. The conclusions drawn from the longitudinal direction is actually similar to what one could expect from a simple 1D accretion model since in this case the shock/post-shock regions are obviously where almost all the energy is emitted because of the conversion of kinetic energy into thermal energy. We now turn to a fundamental aspect concerning the radiative cooling in the laboratory system and deriving directly from the electron-ion temperature decoupling explained before. In typical astrophysical TTS accretion regimes [3], as previously mentioned, the post-shock electron population is sufficiently quickly heated after the shock to emit radiations inside the core itself. Because of the strong density in this region, the cooling is even more enhanced and thus one can expect, even in 2D/3D astrophysical models, that the core should be responsible for the vast majority of the radiative losses. In our laboratory configuration this situation is not true because electrons have the time to escape the core region before to be equilibrated through the electron-ion collisions. Therefore, they can radiate much farther in the azimuthal directions, far from the core, when they are traveling in the shell. This is seen in the blue volumes in fig.9.8 where only $\sim 9\,\%$ of the total energy is radiated inside the core itself whereas more of $50\,\%$ is lost outside the radius $r = 1.5\,mm$.

9.7 On the importance of the obstacle ablation

Astrophysical models and simulations of accretion shocks usually assume the shock to occur in the stellar chromosphere, where the incoming ram pressure equals the local thermal pressure [26]. Despite its large temperatures ($\sim 100\,eV$), the very low density corona ($\sim 10^8\,cm^{-3}$) is supposed to have basically no influence on the propagation of the accretion flow. Nevertheless it has been suggested that the accretion energy could be partially responsible for heating the corona to such high temperatures [27; 28].

We now address the crucial question of the influence of the solid carbon obstacle on the laboratory accretion dynamics. The obstacle "simulates" the atmosphere of TTS's, and we have seen that upon impact of the accretion flow its surface is strongly heated. It is ejected and recollimated by the magnetic field forming a dense and cold "ring" around the accretion shock and column (see fig.9.6(a)). This structure, as well as the mixing of plasma from the obstacle and the accretion flow have been observed experimentally, and the results are presented in our recent paper (see section 9.2 and [3]).

To assess the importance of correctly modeling the stream-obstacle interaction, we performed a simulation where the obstacle is replaced by reflective boundary conditions at $z = 0$ mm. This "perfect wall" essentially suppresses the effects of ablate obstacle material on the acretion dynamics. The results are shown in fig.9.9. The times pictured correspond to the same discussed in the previous sections ($22\,ns$ and $40\,ns$), the left column shows the "real" carbon target case, whereas the right column shows the "perfect wall"

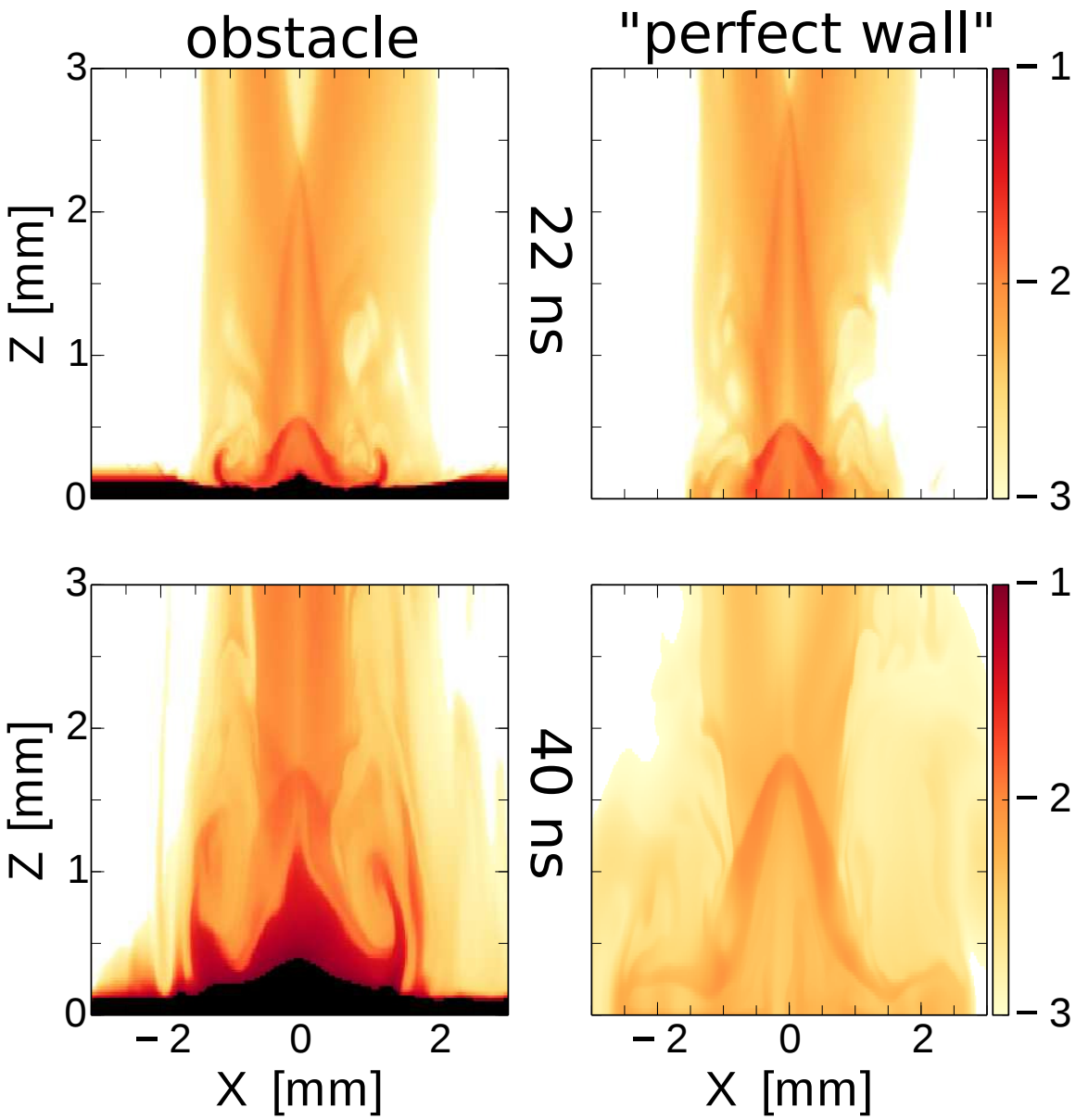

Figure 9.9: 2D maps of the decimal logarithm of the mass density $[kg.m^{-3}]$ at $t = 22\,ns$ and $t = 40\,ns$ for: **left panel:** the case of a "real" carbon obstacle and **right panel:** the case of a "perfect wall" obtained numerically by setting reflective boundary condition at $z = 0\,mm$.

case. At early times ($22\,ns$), we observe a similar shock structure for the two cases, however it is clear that the twisted ring, which has been discussed earlier, is almost entirely composed of obstacle material and thus is absent in the "perfect wall" case. At latter times ($40\,ns$), one can observe in the "perfect wall" case the development of a very tenuous shell and an accretion shock/column that is essentially unperturbed. This is in stark contrast with the more realistic obstacle case, where the column is largely disrupted by the back flowing plasma. Indeed, the head of the shock is at $z \approx 1.7\,mm$ in the "perfect wall" case, while it is hardly visible in the realistic obstacle simulations, because of the strong disturbances coming from the mixed shell. It should be noted that in the "perfect wall" case we took care to anchor the feet of the magnetic field lines at $z = 0\,mm$. If this condition is not set up and that instead the lines are free to move, the highly conductive plasma impacting the bottom surface will bring the field laterally without inducing much bending and consequently the feedback of the field on the post-shock dynamic will be much weaker.

The importance of correctly modeling the interaction of the accretion flow with the obstacle is highlighted in fig.9.5(a,b), where the mass accretion rate and the kinetic energy flux are plotted as a function of time. It is important to note that when computing these rates, we only consider the incoming accretion flow and not the backstreaming plasma. The incoming accretion flow is followed with a passive tracer and the rates are calculated for $v_z < 0$.

At early early times, $t \lesssim 22\,ns$, there is no substantial difference between the three cases; the shell is not fully formed and has had little or no influence on the accretion flow. After maxima in the profiles, we observe an increasing deviation from the free streaming case, with a decrease of the accretion rate for both the obstacle and the perfect wall. It is clearly more marked for the case where the carbon obstacle is present, with a rate equals to $\sim 0.1\,g.s^{-1}$ at $t = 100\,ns$, which represents a reduction of a factor ~ 27 compared to the rate without obstacle. In comparison, the perfect wall case shows a relatively small deviation with a reduction of only ~ 1.2. Looking at the accreting kinetic energy flux (fig.9.5(b)), we observe globally the same trends but because of the dependency on v_z^3, the deviations are strongly amplified. For the case with the obstacle, the final flux at $z = 2\,mm$ is ~ 2000 times lower than the maximum free streaming case. These results demonstrate that in the presence of a sufficiently developed shell composed of material coming from both the column and the obstacle, the luminosity in the shock region may be largely attenuated. We suggest in this regard the importance of obtaining experimental measurements of mass ablation from the obstacle in order to quantify the mixing and to constrain the numerical models.

9.8 Influence of the orientation

As a last point, we want to discuss the possibility to perform laboratory accretion experiments where the magnetic field is oriented at an angle with respect to the laser target and the obstacle. This configuration could be of interest to study the accretion dynamic in complex magnetic field topologies, as it may be the case in many TTS [29–32].

For example, it has been shown that when a significant transverse component of the magnetic field is present it can mitigate or even suppress cooling driven quasi-periodic oscillation [33]. The initial simulation setup with a tilted magnetic field is shown in fig.9.10(a). The laser target is still composed of carbon and the laser parameters are taken to be the same as in the previous cases. The only difference is the angle θ with which the magnetic field is inclined relative to the target normal and we note that the previous cases stud-

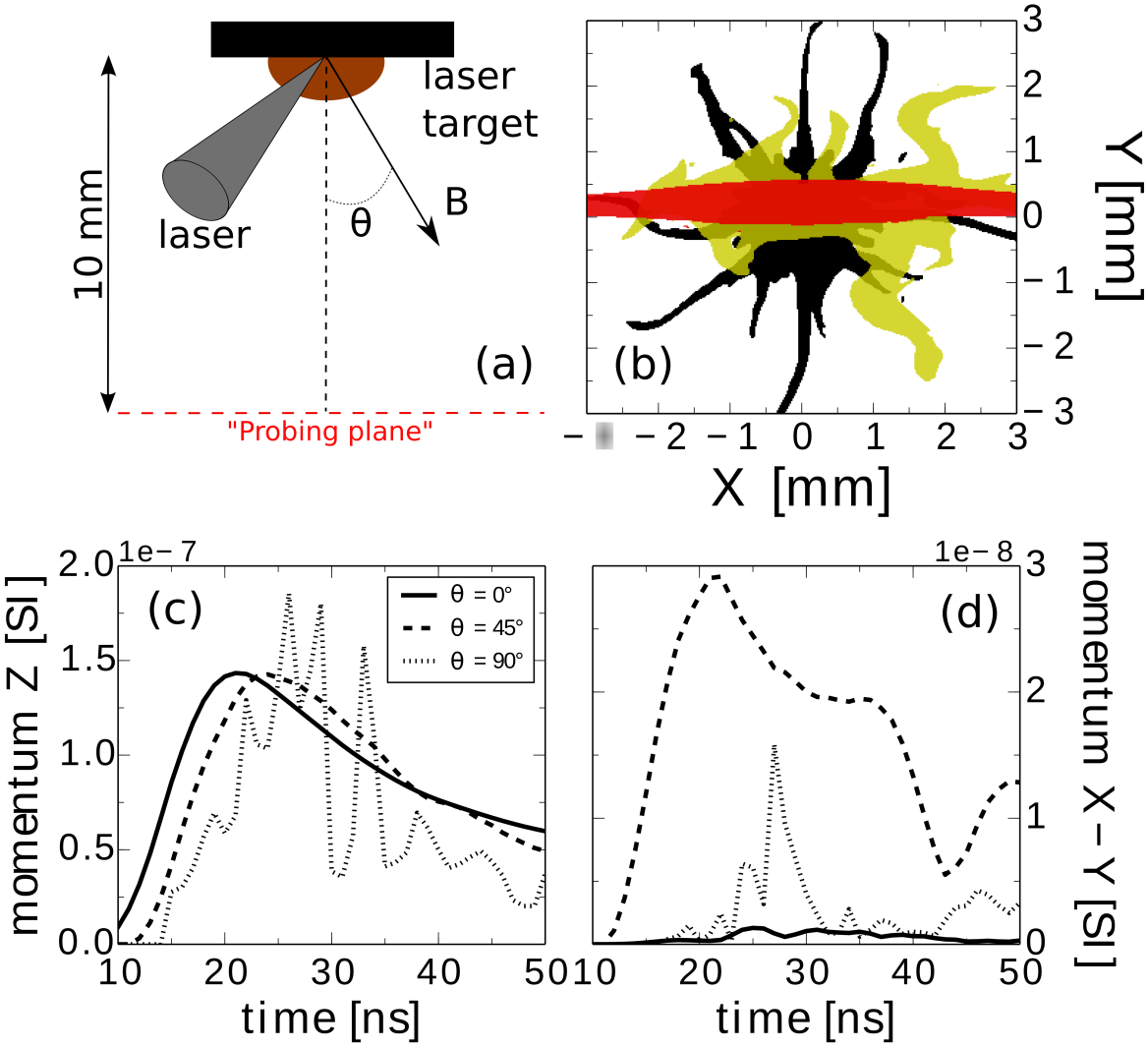

Figure 9.10: (a) Schema of the numerical setup used to study the influence of the field orientation. θ is the angle between the laser target normal and the magnetic field direction. The laser used is the same as in the previous sections (17 J, 0.5 ns). The "probing plane" (red dotted line) is where the quantities shown in (b-c-d) are analyzed. (b) "Shape" of the accretion column in the X-Y plane at the probing plane (see (a)) and at $t = 20\,ns$ for three different angles. The black cross section corresponds to the case θ = 0°, the yellow cross section to θ = 45° and the red cross section to θ = 90°. (c) Z momentum as function of time for the three tilt angle. (d) Radial (X-Y) momentum as function of time for the three tilt angle

ied were corresponding to $\theta = 0°$. Here we focus on the column generation and thus the obstacle is removed from the simulation and the flow is free to exit the domain (no reflective boundaries or obstacle). All the characterization given here is performed $10\,mm$ away from the laser target, a typical position for the introduction of a obstacle (the distance between the laser target and the obstacle is limited by both the necessary space required to let the laser pulse impact the target and the maximum dimension on which a current coil can produce an homogeneous magnetic field [12]). In fig.9.10(b), we show a slice of the column for three different inclinations: $\theta = 0°$ (black), $\theta = 45°$ (yellow) and $\theta = 90°$ (red). These images are given only to show the geometrical shape of the resulting flow and we do not provide informations about the density, which we observe to be highly inhomogeneous. As discussed earlier, the collimation of the laser-produced plasma is RT unstable, and produces azimuthal perturbations of the column surface that extend axially along most of the column surface. These can be clearly seen in the cross section of the column shown in fig.9.10(b) (black region). At the extreme case where $\theta = 90°$ (red) we see that the column has changed into a thin slab of thickness $\sim 500\,\mu m$ aligned with the magnetic field (along x) (we have studied in details this configuration in the dedicated chapter 7). We do not see the Rayleigh-Taylor (RT) filaments anymore but it could be misleading to think that this configuration is not subject to MHD instabilities. Indeed, first we observe also RT filaments in this case but because this instability is flutelike, the presence of these filaments is not seen when observing the column in a direction perpendicular to the magnetic field. Secondly, we observe that the plasma slab is strongly deformed by kink modes that can even be unstable and result in the break of the slab (7.5). The case at $\theta = 45°$ (yellow in fig.9.10(b)) is an intermediate case where we see the column is shrinked along the y-direction but where the RT filaments can still be observed. In fig.9.10(c-d) we present the integral over a plane at z=10 mm of the column z-momentum (fig.9.10(c)) and the azimuthal x/y-momentum (fig.9.10(d)) for all the three tilt angles. By showing these quantities we want to bring out the possibility to "imprint", on the accretion column, radial (x/y) momentum through magnetic forces feedback.

In fig.9.10(c), we can see that in the three cases, the z-momentum is of the same order of magnitude and more surprisingly the $\theta = 45°$ case is almost identical to the $\theta = 0°$ case, excepting for small shift in time ($\sim 2\,ns$) due probably to a small initial deceleration of the flow in the z-direction because of the existence of a x-y component of the magnetic field (here 10 T). Concerning the $\theta = 90°$, we now clearly see the effects of the presence of the RT instability that was mentioned earlier. Because the slab can be strongly kinked, the z-momentum is here a rapidly varying function of time with amplitude variations that can reach up to 80 % on $\sim 2\,ns$ (the big jump at $t \sim 30\,ns$). This behaviour could be of interest to study accretion dynamic under strongly non-steady conditions.

In fig.9.10(d), one can see the possibility to induce non negligible and relatively stable azimuthal momentum in the laser-produced plasma in the case where the field is tilted at $\theta = 45°$. At its maximum value, the azimuthal momentum of the column represents $\sim 16\,\%$ of its z-momentum. For the others cases ($\theta = 0°$ and $\theta = 90°$), the azimuthal momentum is globally less than $\sim 1\,\%$ of the longitudinal one with the exception of a peak value of $\sim 1.5 \cdot 10^{-8}\,kg.m.s^{-1}$ at $t \sim 27\,ns$, originating from the kink action.

9.9 Bibliography

[1] C. M. Johns-Krull, J. A. Valenti, and C. Koresko. Measuring the Magnetic Field on the Classical T Tauri Star BP Tauri. *ApJ*, 516:900–915, May 1999. 196

[2] S. Orlando, G. G. Sacco, C. Argiroffi, F. Reale, G. Peres, and A. Maggio. X-ray emitting MHD accretion shocks in classical T Tauri stars. Case for moderate to high plasma-β values. *aap*, 510:A71, February 2010. 196, 198, 206, 208

[3] G. Revet et al. Laboratory unravelling of matter accretion in young stars. *Science Advances*, 2017 (accepted). 196, 201, 203, 205, 208, 210

[4] M. M. Romanova, M. Long, F. K. Lamb, A. K. Kulkarni, and J.-F. Donati. Global 3D simulations of disc accretion on to the classical T Tauri star V2129 Oph. *mnras*, 411:915–928, February 2011. 196

[5] B Albertazzi, J Béard, A Ciardi, T Vinci, J Albrecht, J Billette, T Burris-Mog, SN Chen, D Da Silva, S Dittrich, et al. Production of large volume, strongly magnetized laser-produced plasmas by use of pulsed external magnetic fields. *Review of Scientific Instruments*, 84(4):043505, 2013. 197, 199, 205, XXXIV

[6] J P Zou, C L Blanc, P Audebert, S Janicot, A M Sautivet, L Martin, C Sauteret, J L Paillard, S Jacquemot, and F Amiranoff. Recent progress on luli high power laser facilities. *Journal of Physics: Conference Series*, 112(3):032021, 2008. 196

[7] A. Flacco T. Vinci. Neutrino. 2014. 197

[8] T. Pisarczyk, R. Arendzikowski, Z. Patron, and P. Parys. Polari interferometer with automatic images processing for laser plasma diagnostic. *Laser and Particle Beams*, 12:549, 1994. 197

[9] S. Atzeni, A. Schiavi, F. Califano, F. Cattani, F. Cornolti, D. Del Sarto, T. V. Liseykina, A. Macchi, and F. Pegoraro. Fluid and kinetic simulation of inertial confinement fusion plasmas. *Computer Physics Communications*, 169:153–159, July 2005. 199

[10] A. Ciardi, T. Vinci, J. Fuchs, B. Albertazzi, C. Riconda, H. Pépin, and O. Portugall. *Phys. Rev. Lett.*, 110:025002, 2013. 201, 206

[11] B. Albertazzi, A. Ciardi, M. Nakatsutsumi, T. Vinci, J. Béard, R. Bonito, J. Billette, M. Borghesi, Z. Burkley, S. N. Chen, T. E. Cowan, T. Herrmannsdörfer, D. P. Higginson, F. Kroll, S. A. Pikuz, K. Naughton, L. Romagnani, C. Riconda, G. Revet, R. Riquier, H.-P. Schlenvoigt, I. Yu. Skobelev, A.Ya. Faenov, A. Soloviev, M. Huarte-Espinosa, A. Frank, O. Portugall, H. Pépin, and J. Fuchs. Laboratory formation of a scaled protostellar jet by coaligned poloidal magnetic field. *Science*, 346(6207):325–328, 2014. 201, 206, 208

[12] DP Higginson, G Revet, B Khiar, J Béard, M Blecher, M Borghesi, K Burdonov, SN Chen, E Filippov, D Khaghani, et al. Detailed characterization of laser-produced astrophysically-relevant jets formed via a poloidal magnetic nozzle. *High Energy Density Physics*, 23:48–59, 2017. 201, 206, 208, 214

[13] DD Ryutov, RP Drake, and BA Remington. Criteria for scaled laboratory simulations of astrophysical mhd phenomena. *The Astrophysical Journal Supplement Series*, 127(2):465, 2000. 201

[14] Lee Hartmann, Gregory Herczeg, and Nuria Calvet. Accretion onto pre-main-sequence stars. *Annual Review of Astronomy and Astrophysics*, 54(1):135–180, 2016. 201

[15] Christopher M. Johns-Krull. *Wind and Accretion Variability in T Tauri Stars*, pages 153–159. Springer Berlin Heidelberg, Berlin, Heidelberg, 1998. 201

[16] H. Shang, Z.-Y. Li, and N. Hirano. Jets and Bipolar Outflows from Young Stars: Theory and Observational Tests. *Protostars and Planets V*, pages 261–276, 2007. 203

[17] R.P. Drake, F.W. Doss, R.G. McClarren, M.L. Adams, N. Amato, D. Bingham, C.C. Chou, C. DiStefano, K. Fidkowski, B. Fryxell, T.I. Gombosi, M.J. Grosskopf, J.P. Holloway, B. van der Holst, C.M. Huntington, S. Karni, C.M. Krauland, C.C. Kuranz, E. Larsen, B. van Leer, B. Mallick, D. Marion, W. Martin, J.E. Morel, E.S. Myra, V. Nair, K.G. Powell, L. Rauchwerger, P. Roe, E. Rutter, I.V. Sokolov, Q. Stout, B.R. Torralva, G. Toth, K. Thornton, and A.J. Visco. Radiative effects in radiative shocks in shock tubes. *High Energy Density Physics*, 7(3):130 – 140, 2011. 205

[18] J. E. Cross, G. Gregori, J. M. Foster, P. Graham, J.-M. Bonnet-Bidaud, C. Busschaert, N. Charpentier, C. N. Danson, H. W. Doyle, R. P. Drake, J. Fyrth, E. T. Gumbrell, M. Koenig, C. Krauland, C. C. Kuranz, B. Loupias, C. Michaut, M. Mouchet, S. Patankar, J. Skidmore, C. Spindloe, E. R. Tubman, N. Woolsey, R. Yurchak, and É. Falize. Laboratory analogue of a supersonic accretion column in a binary star system. *Nature Communications*, 7:11899, June 2016. 205

[19] Kazuki Matsuo, Hideo Nagatomo, Zhe Zhang, Philippe Nicolai, Takayoshi Sano, Shohei Sakata, Sadaoki Kojima, Seung Ho Lee, King Fai Farley Law, Yasunobu Arikawa, Youichi Sakawa, Taichi Morita, Yasuhiro Kuramitsu, Shinsuke Fujioka, and Hiroshi Azechi. Magnetohydrodynamics of laser-produced high-energy-density plasma in a strong external magnetic field. *Phys. Rev. E*, 95:053204, May 2017. 205

[20] Bo Ram Lee. *Study of a laser generated diamagnetic cavity and Alfvén waves in a large magnetized plasma*. PhD thesis, Technische Universität, Darmstadt, December 2015. 205

[21] J. D. Huba. Onset criteria for structure in magnetically confined plasma expansions. Technical report, July 1987. 205

[22] B. Khiar et al. D. Higginson. Enhancement of quasi-stationary shocks and heating via temporal-staging in a magnetized, laser-plasma jet. *PRL*, 2017 (submitted). 206

[23] R. Bonito, S. Orlando, C. Argiroffi, M. Miceli, G. Peres, T. Matsakos, C. Stehle, and L. Ibgui. Magnetohydrodynamic modeling of the accretion shocks in classical t tauri stars: The role of local absorption in the x-ray emission. *The Astrophysical Journal Letters*, 795(2):L34, 2014. 206

[24] C. Argiroffi, A. Maggio, G. Peres, J. J. Drake, J. López-Santiago, S. Sciortino, and B. Stelzer. X-ray optical depth diagnostics of T Tauri accretion shocks. *aap*, 507:939–948, November 2009. 206

[25] George P Sutton and Oscar Biblarz. *Rocket propulsion elements*. John Wiley & Sons, 2017. 208

[26] G. G. Sacco, C. Argiroffi, S. Orlando, A. Maggio, G. Peres, and F. Reale. X-ray emission from dense plasma in classical T Tauri stars: hydrodynamic modeling of the accretion shock. *aap*, 491:L17–L20, November 2008. 210

[27] S. R. Cranmer. Testing Models of Accretion-Driven Coronal Heating and Stellar Wind Acceleration for T Tauri Stars. *ApJ*, 706:824–843, November 2009. 210

[28] N. S. Brickhouse, S. R. Cranmer, A. K. Dupree, G. J. M. Luna, and S. Wolk. A Deep Chandra X-Ray Spectrum of the Accreting Young Star TW Hydrae. *ApJ*, 710:1835–1847, February 2010. 210

[29] Jeff A. Valenti and Christopher M. Johns-Krull. Observations of magnetic fields on t tauri stars. *Astrophysics and Space Science*, 292(1):619–629, Jul 2004. 212

[30] S. G. Gregory, M. Jardine, A. Collier Cameron, and J.-F. Donati. Rotationally modulated X-ray emission from T Tauri stars. *mnras*, 373:827–835, December 2006.

[31] J.-F. Donati, M. M. Jardine, S. G. Gregory, P. Petit, J. Bouvier, C. Dougados, F. Ménard, A. Collier Cameron, T. J. Harries, S. V. Jeffers, and F. Paletou. Magnetic fields and accretion flows on the classical T Tauri star V2129 Oph. *mnras*, 380:1297–1312, October 2007.

[32] M. Long, M. M. Romanova, and R. V. E. Lovelace. Accretion to stars with non-dipole magnetic fields. *mnras*, 374:436–444, January 2007. 212

[33] A. V. Koldoba, G. V. Ustyugova, M. M. Romanova, and R. V. E. Lovelace. Oscillations of magnetohydrodynamic shock waves on the surfaces of T Tauri stars. *mnras*, 388:357–366, July 2008. 212

Chapter 10

Conclusion and future prospects

The work performed during my three PhD years and presented in this manuscript has contributed to the field of High Energy Density Laboratory Astrophysics (HEDLA) through the study of several configurations coupling laser-produced plasmas with strong, eternally applied magnetic fields. The first natural work performed has been an extension of the study of hypersonic jets collimated by a poloidal magnetic fields. The underlying processes by which such jets are formed have been studied in details. One of the most important features is the generation of internal shocks which have been shown to be responsible for the redirection of the flow. Interestingly, through a numerical study of "idealized" supersonic jets propagating in medium (magnetized or not), we have been able to introduce general aspects of these objects especially concerning their stability. We have seen that in the absence of background, jets are extremely stable thanks to the absence of the Kelvin-Helmholtz instability. The jets produced with our setup are also, contrary to the ones produced using pulsed-power devices (plasma guns, pinches...), not kink unstable. As an extension of the work on magnetized jets, we also studied the effect introducing multiple laser pulses in our setup. Notably, we demonstrated the robustness of the jet generation when a precursor plasma is created by a low pulse energy. The life time of internal structures such that the first conical shock was observed to be increased with this modified configuration introducing the possibility to study strongly variable ejection rates in the laboratory.

We then presented results concerning the structure of a laser produced plasma expanding in a strong transverse magnetic field. We have shown, in remarkably good agreement with experimental results, that this configuration results in the formation of "magnetic slabs" or "magnetic pancakes" with omnipresent MHD instabilities. The slab, whose dimensions along the magnetic field can be dozens of times larger than perpendicular to it, were observed to be strongly sensible to MHD instabilities occurring at two different stages: in the collimating phase, the slab interfaces with vacuum see (as for the case of jets) the apparition of Rayleigh-Taylor filaments whereas in the expansion region far from the solid target, the slab can be kink unstable if the field is sufficiently strong. We suggest the potential interest to study this configuration in the context of magnetic structures present in stellar atmospheres.

In the last chapter we have presented state of the art modeling/experiments of laboratory magnetized accretion. The astrophysical context concerns the accretions shocks supposed to be responsible for the strong UV excess observed in almost every T Tauri stars systems. We have demonstrated the relevance of using our previously characterized jets as "accretion columns" and, by the addition of a second target to the original setup, we have observed for the first time in the laboratory typical plasma structures suggested in

the past by 2D MHD astrophysical simulations. One particularity of the presented work is that we have undertaken a full three dimensional numerical study of these laboratory shocks and found good agreement with the experimental results. Our work highlight the strongly non-asymmetric structure of what we have called the "shell" as well as the fundamental non-equilibrium (ions much hotter than electrons) state obtained in the shock region called here the "core". We also looked at the spatial distribution of the emitted radiations in this configuration and observed that the larger part of the energy losses is emitted far from the core region.

In term of the perspectives on the topic of accretion, since the vast majority of studies performed in the past have been focused on the case where the magnetic energy at the shock spot is much larger than the thermal energy (small betas), it will be very interesting to perform experiments with stronger fields and observe if the complete structure tends toward a one dimensional configuration. Notably, the presence of instabilities could strongly thwart this possibility. Numerically, more work need to be done concerning the modeling of the solid obstacle and the ablating which results from the accreting flow impact. As we have demonstrated, this point seems crucial in order to reproduce correctly the experimental structure observed. An interesting other point concerning the necessity to correctly model the column-obstacle interaction is linked to the fact that if dense and cold material from the obstacle is effectively lifted and mixed with the accreting material, there could be some important impacts on the radiative properties of the shell. This raises the necessity to perform in the future accretion simulations with radiative transfer included in order to quantify the impact of this mechanism.

Finally, our collaboration, as well as other experimental teams, have observed recurrent generation of high energy particles in these type of laboratory astrophysics experiments. We have notably observed energetic particles in the configuration of magnetized jets produced by external poloidal magnetic fields. As we have mentioned, these jets are relatively stable (at least there are no disruptive instabilities) by involved the generation of shocks. Therefore the physical mechanism producing these energetic particles needs to be identified and we have undertaken this work in our group by starting a project aiming to implement a Particle-In-Cell module to our MHD code. The question of the possibility to reproduce the observed spectra with our numerical tools is still open and is the topic of an ongoing PhD work.

Appendix A

Waves and instabilities

Sommaire

A.1 General formulation from the ideal MHD equations II

A.2 The case of motionless homogeneous unmagnetized compressible plasma: sound waves V

A.3 The case of motionless homogeneous magnetized compressible plasma: Alfven, slow and fast magnetoacoustic waves V

A.4 The case of discontinuously stratified plasma without magnetic field: the Raileygh-Taylor instability VIII

A.5 The case of a discontinuisly sheared velocity unmagnetized compressible plasma: the Kelvin-Helmoltz instability XIV

A.6 The case of a single magnetic stable interface XVII

A.7 The case of a magnetic slab XX

A.1 General formulation from the ideal MHD equations

We begin here with the ideal MHD set of equations:

$$\begin{cases} \dfrac{\partial \rho}{\partial t} + \nabla \cdot (\rho \mathbf{v}) = 0 & \text{(A.1)} \\ \rho(\dfrac{\partial \mathbf{v}}{\partial t} + (\mathbf{v} \cdot \nabla)\mathbf{v}) = -\nabla p + \dfrac{(\mathbf{B} \cdot \nabla)\mathbf{B}}{\mu_0} - \nabla(\dfrac{B^2}{2\mu_0}) + \rho \mathbf{g_{eff}} & \text{(A.2)} \\ \dfrac{\partial \mathbf{B}}{\partial t} = (\mathbf{B} \cdot \nabla)\mathbf{v} - (\mathbf{v} \cdot \nabla)\mathbf{B} - \mathbf{B}(\nabla \cdot \mathbf{v}) & \text{(A.3)} \\ \dfrac{\partial p}{\partial t} + (\mathbf{v} \cdot \nabla) p = -\gamma p \nabla \cdot \mathbf{v} & \text{(A.4)} \\ \nabla \cdot \mathbf{B} = 0 & \text{(A.5)} \end{cases}$$

Equation (1) describes the mass conservation, equation (2) the momentum conservation, equation (3) the magnetic induction, equation (4) the energy equation (since we suppose here $p = (\gamma - 1)\epsilon$, where p is the total pressure ($p = p_e + p_i$) and ϵ is the total internal energy density). The last equation (5) concerns the absence of magnetic monopoles. If true initially it will remain so.

Now we want to linearize the previous system of equations to explore the reaction of the magnetoplasma to a perturbation. The system is taken, at the zeroth-order, as a stationary equilibrium medium. The configuration studied here is shown in Fig.A.1. The plasma is structured along the x direction. The magnetic field is oriented in the z direction and we allow a velocity in the y direction. The equilibrium variables are thus given by:

$$\begin{cases} \rho_0 = \rho_0(x) & \text{(A.6)} \\ p_0 = p_0(x) & \text{(A.7)} \\ \mathbf{v_0} = v_0(x)\mathbf{e_y} & \text{(A.8)} \\ \mathbf{B_0} = B_0(x)\mathbf{e_z} & \text{(A.9)} \end{cases}$$

Furthermore, the effective acceleration is considered directed along x: $\mathbf{g_{eff}} = g_{eff}\mathbf{e_x}$

Now we consider first order perturbations as plane waves of wave vector $\mathbf{k} = k_y\mathbf{e_y} + k_z\mathbf{e_z}$ thus:

$$\begin{cases} \rho(\mathbf{r}, t) = \rho_0(x) + \rho_1(x)\exp(i\mathbf{k} \cdot \mathbf{r} - i\omega t) & \text{(A.10)} \\ p(\mathbf{r}, t) = p_0(x) + p_1(x)\exp(i\mathbf{k} \cdot \mathbf{r} - i\omega t) & \text{(A.11)} \\ \mathbf{v}(\mathbf{r}, t) = \mathbf{v_0}(x) + \mathbf{v_1}(x)\exp(i\mathbf{k} \cdot \mathbf{r} - i\omega t) & \text{(A.12)} \\ \mathbf{B}(\mathbf{r}, t) = \mathbf{B_0}(x) + \mathbf{B_1}(x)\exp(i\mathbf{k} \cdot \mathbf{r} - i\omega t) & \text{(A.13)} \end{cases}$$

with $\mathbf{r} = x\mathbf{e_x} + y\mathbf{e_y} + z\mathbf{e_z}$ The previous ideal MHD system of equations (eq (1)-(5)) is thus given at the first order by:

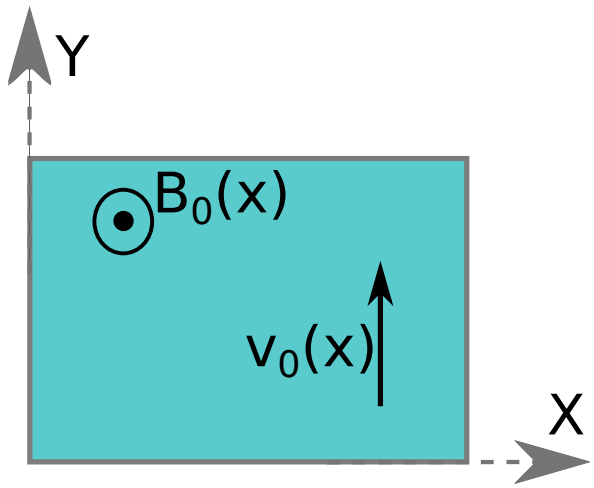

Figure A.1: Equilibrium plasma configuration used for our study

$$
\begin{cases}
i\rho_1(k_y v_0 - \omega) = -(\partial_x p_0) v_{1x} - \rho_0(\partial_x v_{1x} + i\mathbf{k}\cdot\mathbf{v_1}) & \text{(A.14)}\\
i\rho_0 v_{1x}(k_y v_0 - \omega) = i k_z \dfrac{B_0 B_{1x}}{\mu_0} - \partial_x(p_1 + \dfrac{B_0 B_{1z}}{\mu_0}) + \rho_1 g_{eff} & \text{(A.15)}\\
i\rho_0 v_{1y}(k_y v_0 - \omega) = i k_z \dfrac{B_0 B_{1y}}{\mu_0} - i k_y(p_1 + \dfrac{B_0 B_{1z}}{\mu_0}) - \rho_0(\partial_x v_0) v_{1x} & \text{(A.16)}\\
i\rho_0 v_{1z}(k_y v_0 - \omega) = i k_z \dfrac{B_0 B_{1z}}{\mu_0} - i k_z(p_1 + \dfrac{B_0 B_{1z}}{\mu_0}) + \dfrac{\partial_x B_0}{\mu_0} B_{1x} & \text{(A.17)}\\
B_{1x}(k_y v_0 - \omega) = k_z B_0 v_{1x} & \text{(A.18)}\\
i B_{1y}(k_y v_0 - \omega) = i k_z B_0 v_{1y} + (\partial_x v_0) B_{1x} & \text{(A.19)}\\
i B_{1z}(k_y v_0 - \omega) = i k_z B_0 v_{1z} - (\partial_x B_0) v_{1x} - B_0(\partial_x v_{1x} + i\mathbf{k}\cdot\mathbf{v_1}) & \text{(A.20)}\\
i p_1(k_y v_0 - \omega) = -(\partial_x p_0) v_{1x} - \gamma p_0(\partial_x v_{1x} + i\mathbf{k}\cdot\mathbf{v_1}) & \text{(A.21)}\\
\partial_x B_{1x} + i\mathbf{k}\cdot\mathbf{B_1} = 0 & \text{(A.22)}
\end{cases}
$$

The first equation corresponds to the mass conservation, the next three (15-16-17) are projections of the momentum equation. Equations (18-19-20) are projections of the induction equation. Equation (21) is the energy conservation equation and the last (22) is the magnetic divergence free equation. The system contains 8 unknown variables and 8 evolution equations plus the divergence free equation. With this system a very large panel of physical phenomena can be derived, from permitted modes in a homogeneous/structured magnetized medium (Alfven mode, fast and slow magnetoacoustic modes), to unstable modes like the Kelvin-Helmoltz or the Rayleigh-Taylor instabilities. It is also possible to switch to the incompressible limit ($\nabla\cdot\mathbf{v} = 0$) with this system. Indeed, the velocity divergence of the first order component is given by $\nabla\cdot(\mathbf{v_1}\exp(i\mathbf{k}\cdot\mathbf{r} - i\omega t)) = (\partial_x v_{1x} + i\mathbf{k}\cdot\mathbf{v_1})\exp(i\mathbf{k}\cdot\mathbf{r} - i\omega t)$ so to obtain the incompressible limit one has to take the above system of equations substituting the energy equation (21) by $\partial_x v_{1x} + i\mathbf{k}\cdot\mathbf{v_1} = 0$ (as discussed before, the energy equation (21) has no meaning in the incompressible limit).

Now we give, without detailing all the process, the solution of this system of equations. The method consists to write equation (15) only in term of the component x of the first order velocity v_{1x}. First we get the expressions of ρ_1, $p_1 + B_0 B_{1z}/\mu_0$ and B_{1x}:

$$\begin{cases} p_1 + \dfrac{B_0 B_{1z}}{\mu_0} = Z v_{1x} + W \partial_x v_{1x} & \text{(A.23)} \\ \rho_1 = -\dfrac{i}{\Omega^2}(K_1 v_{1x} + K_2 \partial_x v_{1x}) & \text{(A.24)} \\ B_{1x} = \dfrac{k_z B_0}{\Omega} v_{1x} & \text{(A.25)} \end{cases}$$

where:

$$\begin{cases} \Omega = k_y v_0 - \omega & \text{(A.26)} \\ Z = Z_1 \partial_x v_0 + Z_2 \partial_x p_{T0} & \text{(A.27)} \\ Z_1 = i\rho_0 \dfrac{k_y}{k^2} \dfrac{k_z^2 v_{A0}^2 - \Omega^2}{\Omega^2}(Z_3 - 1) & \text{(A.28)} \\ Z_2 = -i \dfrac{\Omega}{k^2(k_z^2 c_{s0}^2 - \Omega^2)}(Z_3 k_y^2 + k_z^2) & \text{(A.29)} \\ Z_3 = \dfrac{\Omega^4}{c_{ma0}^2 (k_z^2 c_{T0}^2 - \Omega^2)(m^2 + k_y^2)} & \text{(A.30)} \\ W = i \dfrac{\rho_0}{\Omega} \dfrac{k_z^2 v_{A0}^2 - \Omega^2}{m^2 + k_y^2} & \text{(A.31)} \\ m^2 = \dfrac{(k_z^2 c_{s0}^2 - \Omega^2)(k_z^2 v_{A0}^2 - \Omega^2)}{c_{ma0}^2 (k_z^2 c_{T0}^2 - \Omega^2)} & \text{(A.32)} \\ K_1 = i k^2 Z - \dfrac{\rho_0 k_y}{\Omega^2}(k_z^2 v_{A0}^2 - \Omega^2)\partial_x v_0 - \Omega \partial_x \rho_0 & \text{(A.33)} \\ K_2 = i k^2 W + \dfrac{\rho_0}{\Omega}(k_z^2 v_{A0}^2 - \Omega^2) & \text{(A.34)} \end{cases}$$

In these equations we used the following notations:

$$\begin{cases} c_{s0} = \sqrt{\dfrac{\gamma p_0}{\rho_0}} \, (sound\, speed) & \text{(A.35)} \\ v_{a0} = \dfrac{B_0}{\mu_0 \rho_0} \, (Alfven\, speed) & \text{(A.36)} \\ c_{ma0} = \sqrt{c_{s0}^2 + v_{a0}^2} \, (fast\, magnetoacoustic\, speed) & \text{(A.37)} \\ c_{T0} = \sqrt{\dfrac{c_{s0}^2 v_{a0}^2}{c_{s0}^2 + v_{a0}^2}} \, (to\, be\, named) & \text{(A.38)} \\ p_{T0} = p_0 + \dfrac{B_0^2}{2\mu_0} \, (total\, pressure) & \text{(A.39)} \end{cases}$$

Now we can write equation (15) only in terms of v_{1x}:

$$-\frac{i}{\Omega}(g_{eff}\frac{K_1}{\Omega} + \rho_0(k_z^2 v_{A0}^2 - \Omega^2))v_{1x} + \partial_x(Z v_{1x} + W \partial_x v_{1x}) - i g_{eff}\frac{K_2}{\Omega^2}\partial_x v_{1x} = 0 \qquad \text{(A.40)}$$

This last equation contains all the phenomena described before (when adding the proper boundary conditions). Of course there exist no universal analytical solution for this system and one has to apply it to specific cases. In the following parts we will present some of them.

A.2 The case of motionless homogeneous unmagnetized compressible plasma: sound waves

This case correponds to a situation where:

$$\begin{cases} v_0 = 0 & \text{(A.41)} \\ \Omega = -\omega & \text{(A.42)} \\ g_{eff} = 0 & \text{(A.43)} \\ \mathrm{B}_0 = 0 & \text{(A.44)} \\ v_{a0} = 0 & \text{(A.45)} \\ \mathrm{Z} = 0 & \text{(A.46)} \\ \mathrm{K}_1 = 0 & \text{(A.47)} \\ m^2 = \dfrac{k_z^2 c_{s0}^2 - \omega^2}{c_{s0}^2} & \text{(A.48)} \\ \mathrm{W} = i\rho_0 \dfrac{\omega c_{s0}^2}{k^2 c_{s0}^2 - \omega^2} & \text{(A.49)} \end{cases}$$

Thus, given the fact the medium is homogeneous, equation A.40 become:

$$c_{s0}^2 \partial_x^2 v_{1x} - (k^2 c_{s0}^2 - \omega^2) = 0 \tag{A.50}$$

where here $k^2 = k_y^2 + k_z^2$. In the case with no magnetic field, we can of course consider an isotropic form for the plane waves so we will assume that $v_{1x} \propto exp(ik_x x - i\omega t)$ and so in this case $\partial_x^2 v_{1x} = -k_x^2 v_{1x}$. We retrieve then the dispersion relation for sound waves:

$$\omega^2 = c_{s0}^2 k^2 \tag{A.51}$$

where in this isotropic case: $k^2 = k_x^2 + k_y^2 + k_z^2$. In the case of a bi-temperature model, the sound speed is given by: $c_{s0} = \sqrt{\gamma(p_e + p_i)/\rho}$. This is considering ions and electrons as ideal gases with the same adiabatic index γ.

A.3 The case of motionless homogeneous magnetized compressible plasma: Alfven, slow and fast magnetoacoustic waves

In this case we have the following set of conditions:

$$\begin{cases} v_0 = 0 & \text{(A.52)} \\ \Omega = -\omega & \text{(A.53)} \\ g_{eff} = 0 & \text{(A.54)} \\ Z = 0 & \text{(A.55)} \\ K_1 = 0 & \text{(A.56)} \\ m^2 = \dfrac{(k_z^2 c_{s0}^2 - \omega^2)(k_z^2 v_{A0}^2 - \omega^2)}{c_{ma0}^2 (k_z^2 c_{T0}^2 - \omega^2)} & \text{(A.57)} \\ W = -i \dfrac{\rho_0}{\omega} \dfrac{k_z^2 v_{A0}^2 - \omega^2}{m^2 + k_y^2} & \text{(A.58)} \end{cases}$$

With these values, the equation A.40 can be written:

$$(k_z^2 v_{a0}^2 - \omega^2)[(m^2 + k_y^2) v_{1x} - \partial_x^2 v_{1x}] = 0 \tag{A.59}$$

From this equation, one can see that this leads to two different possibilities:

$$\omega^2 = k_z^2 v_{a0}^2 \tag{A.60}$$

and

$$(m^2 + k_y^2) v_{1x} - \partial_x^2 v_{1x} = 0 \tag{A.61}$$

Equation A.60 describes the propagation of Alfven waves, also present in the limit of an incompressible plasma. The restoring force permitting their propagation is the magnetic tension arising when plasma fluid particles disturb the equilibrium magnetic field lines (consequence of a the ideal regime).

The second equation A.61 describes magnetoacoustic modes where effect of compressibility is present. Thus, they are no magnetoacoustic modes in a incompressible plasma. As in the previous case of sound waves, the fact that the medium is homogeneous allows us to suppose a normal wave behavior for the x component of the disturbed velocity: $v_{1x} \propto exp(ik_x x - i\omega t)$ and as previously: $\partial_x^2 v_{1x} = -k_x^2 v_{1x}$. So in this case, the non-trivial solution of equation A.61 simplifies to:

$$m^2 + k_y^2 + k_x^2 = 0 \tag{A.62}$$

Now using the expression (57) for m^2, we can write equation A.62 as:

$$\omega^4 - k^2 c_{ma0}^2 \omega^2 + k_z^2 k^2 c_{s0}^2 v_{A0}^2 = 0 \tag{A.63}$$

Solutions can be found rewriting this equation as a second order equation (posing $W = \omega^2$) and we get:

$$W_\pm = \omega_\pm^2 = \frac{1}{2}[k^2 c_{ma0}^2 \pm \sqrt{k^2(k^2 c_{ma0}^4 - 4k_z^2 c_{s0}^2 v_{A0}^2)}] \tag{A.64}$$

This last equation represents actually two different solutions: the slow (-) and the fast (+) magnetoacoustic modes. To retrieve the general behavior of these modes we analyse the case of perpendicular and parallel propagation (relative to the magnetic field orientation) for both slow and fast mode.

First, the slow magnetoacoustic mode, in perpendicular propagation ($k_z = 0$) gives the relation:

$$\omega^2_{slow,\perp} = 0 \tag{A.65}$$

So there is no propagation of the slow mode in perpendicular directions. In the case of parallel propagation ($k = k_z$), A.64 applied for the slow mode gives:

$$\omega^2_{slow,\parallel} = \frac{1}{2}k^2[c^2_{s0} + v^2_{A0} - \sqrt{(c^2_{s0} - v^2_{A0})^2}] \tag{A.66}$$

In this case, we see two different situations:

- if $c_{s0} > v_{A0}$, then $\omega^2_{slow,\parallel} = k_z^2 v^2_{A0}$
- if $c_{s0} < v_{A0}$, then $\omega^2_{slow,\parallel} = k_z^2 c^2_{s0}$

and we can summarize theses results by:

$$\omega^2_{slow,\parallel} = k_z^2 min(c^2_{s0}, v^2_{A0}) \tag{A.67}$$

Now, we look at the fast magnetoacoustic mode in perpendicular propagation ($k_z = 0$). In this case we get:

$$\omega^2_{fast,\perp} = k^2_\perp c^2_{ma0} \tag{A.68}$$

Here we see the meaning of the fast magnetoacoustic speed introduced before (equation 36): it is the speed of the fast magnetocacoustic mode in propagating in the perpendicular direction. For experiments of plasma flows propagating against the imposed magnetic field this speed is of great importance. Indeed, if in some regions the flow become faster than the fast magnetoacoustic speed of the local medium then shocks will be generated.

In the case of parallel propagation, the dispersion relation A.64 for the fast magnetoacoustic mode can be written:

$$\omega^2_{fast,\parallel} = \frac{1}{2}k^2[c^2_{s0} + v^2_{A0} + \sqrt{(c^2_{s0} - v^2_{A0})^2}] \tag{A.69}$$

Here we see, like in the case of the slow mode, two possibilities:

- if $c_{s0} > v_{A0}$, then $\omega^2_{fast,\parallel} = k_z^2 v^2_{s0}$
- if $c_{s0} < v_{A0}$, then $\omega^2_{fast,\parallel} = k_z^2 c^2_{A0}$

and we can summarize as:

$$\omega^2_{fast,\parallel} = k_z^2 max(c^2_{s0}, v^2_{A0}) \tag{A.70}$$

A first consequence from this analysis concerns the conditions to produce shocks in magnetized plasma. Indeed, two possibilities are available:

- in the case where the flow is propagating along the magnetic field, its speed V_{flow} (relative to the medium where we define the sound and alfven speeds) must be greater than $max(c_{s0}, v_{A0})$ and we can define an associated mach number: $M_\parallel = V_{flow}/max(c_{s0}, v_{A0})$. So in order to generated shocks in this configuration $M_\parallel > 1$, the flow has to be supersonic if $c_{s0} > v_{A0}$ and superalfvenic if $c_{s0} < v_{A0}$.

- in the case where the flow is propagating across the magnetic field, its speed V_{flow} (relative to the medium where we define the sound and alfven speeds) must be greater than c_{ma0} and we can define an associated mach number: $M_{\perp} = V_{flow}/c_{ma0}$.

An other interesting conclusion from this discussion is the fact that it is clear that there is no magnetoacoustic modes at all (in any direction) with phase speed between $min(c_{s0}, v_{A0})$ and $max(c_{s0}, v_{A0})$.

A.4 The case of discontinuously stratified plasma without magnetic field: the Raileygh-Taylor instability

The condition to see the growth of the Rayleigh-Taylor (RT) instability: in the frame of the interface the effective acceleration MUST be opposite to the density gradient.

As a consequence, if we now look from the laboratory frame a interface delimiting two regions of different density, the growth of the RT instability will be observed if,

- in the case of a accelerating interface, the density gradient is in the same direction than the acceleration.

- in the case of a decelerated interface , the density gradient is also in the same direction than the deceleration.

The first step when trying to describes the Rayleigh-Taylor instability is to correctly pose the initial equilibrium configuration. It has been known for a long time that generally the Rayleigh-Taylor instability is mathematically an ill-posed problem and the dependence on initial conditions is still a topic of discussions (see D. Livescu, 2013), in particular when we consider this instability in the general case of a compressible medium. The first step is to apply our general equation A.40 to the Rayleigh-Taylor configuration. For the main variables and characteristic speeds associated we have:

$$\begin{cases} v_0 = 0 & \text{(A.71)} \\ \Omega = -\omega & \text{(A.72)} \\ B_0 = 0 & \text{(A.73)} \\ v_{a0} = 0 & \text{(A.74)} \\ c_{ma0} = c_{s0} & \text{(A.75)} \\ c_{T0} = 0 & \text{(A.76)} \\ & \text{(A.77)} \end{cases}$$

Then we derive all the terms for this configuration needed for the main equation A.40:

$$\begin{cases} m^2 = k_z^2 - \dfrac{\omega^2}{c_{s0}^2} & \text{(A.78)} \\ m^2 + k_y^2 = \dfrac{k^2 c_{s0}^2 - \omega^2}{c_{s0}^2} & \text{(A.79)} \\ Z_3 = -\dfrac{\omega^2}{k^2 c_{s0}^2 - \omega^2} & \text{(A.80)} \\ Z_2 = i\dfrac{\omega}{k^2 c_{s0}^2 - \omega^2} & \text{(A.81)} \\ Z = i\dfrac{\omega}{k^2 c_{s0}^2 - \omega^2}\partial_x p_0 & \text{(A.82)} \\ W = i\omega\dfrac{\rho_0 c_{s0}^2}{k^2 c_{s0}^2 - \omega^2} = i\dfrac{\omega}{k^2}\alpha & \text{(A.83)} \\ K_1 = \omega\partial_x\rho_0 - \dfrac{k^2\omega}{k^2 c_{s0}^2 - \omega^2}\partial_x p_0 & \text{(A.84)} \\ K_2 = \rho_0\omega - \omega k^2\dfrac{\rho_0 c_{s0}^2}{k^2 c_{s0}^2 - \omega^2} = \rho_0\omega - \omega\alpha & \text{(A.85)} \end{cases}$$

In these expressions we used the notation $\alpha = \rho_0/(1-\omega^2/(k^2 c_{s0}^2))$. Now, as previously, we need to apply our main equation A.40 to our problem. First we lightly rewrite this equation:

$$\partial_x(W\partial_x v_{1x}) + (Z - i g_{eff}\frac{K_2}{\omega^2})\partial v_{1x} + (\partial_x Z - i g_{eff}\frac{K_1}{\omega^2} - i\rho_0\omega)v_{1x} = 0 \tag{A.86}$$

Now we must write the initial equilibrium condition for the first order variables p_0, ρ_0 are:

$$\frac{\partial p_0}{\partial x} = -\rho_0 g_{eff} \tag{A.87}$$

It is important that this last relation implies the continuity of the pressure since the density ρ_0 is finite. Indeed, if we integrate equation A.87 around the interface, between $x = -\epsilon$ and $x = +\epsilon$, we get:

$$\int_{-\epsilon}^{+\epsilon}\partial_x p_0 dx = p_{0,+} - p_{0,-} = -g_{eff}\int_{-\epsilon}^{+\epsilon}\rho_0 dx = 0 \tag{A.88}$$

This expresses the continuity of p_0 because $p_{0,+} = p_{0,-} = p_{0,s}$. Here the indeces + and - corresponds to values of quantities at $\pm\epsilon$ for $\epsilon \to 0$. Then using relation A.87, we have:

$$\begin{cases} Z - i g_{eff}\dfrac{K_2}{\omega^2} = 0 & \text{(A.89)} \\ \partial_x Z - i g_{eff}\dfrac{K_1}{\omega^2} - i\rho_0\omega = -i\partial_x(\dfrac{\omega g_{eff}}{k^2 c_{s0}^2}\alpha) - i\dfrac{g_{eff}^2}{\omega c_{s0}^2}\alpha - i\rho_0\omega - i\dfrac{g_{eff}}{\omega}\partial_x\rho_0 & \text{(A.90)} \end{cases}$$

After some arrangements, equation A.86 become:

$$\partial_x(\alpha\partial_x v_{1x}) - (\rho_0 k^2 + \frac{k^2}{\omega^2}g_{eff}\partial_x\rho_0 + \frac{g_{eff}^2 k^2}{\omega^2 c_{s0}^2}\alpha + g_{eff}\partial_x(\frac{\alpha}{c_{s0}^2}))v_{1x} = 0 \tag{A.91}$$

Also, concerning the equilibrium configuration, we can deduce the expression for ρ_0 and p_0 if we assume that each region of the plasma (1/2) is isothermal (and iso-ionized) with the temperatures defined by:

$$\begin{cases} (1+Z_0^*)T_0(x) = (1+Z_{0,1}^*)T_{0,1} \ (x<0) & \text{(A.92)} \\ (1+Z_0^*)T_0(x) = (1+Z_{0,2}^*)T_{0,2} \ (x>0) & \text{(A.93)} \end{cases}$$

The discontinuity of the temperature at the interface is a consequence of the discontinuity in density at the interface between the two plasmas 1/2. Indeed, in our model, we choose as the equation of state linking the density and the pressure the ideal gas law, for electrons and ions:

$$p_0 = R\rho_0(1+Z_0^*)T_0 \tag{A.94}$$

with $R = k_B/m_i$ where k_B is the Boltzmann constant and m_i the ion mass. Thus if we write the relation expressing the jump of temperature at the interface, we get:

$$(1+Z_{0,2}^*)T_{0,2} - (1+Z_{0,1}^*)T_{0,1} = p_{0,s}(\frac{1}{R_2\rho_{0,+}} - \frac{1}{R_1\rho_{0,-}}) \tag{A.95}$$

We can see that the continuity of T_0 will be realized only if $R_1\rho_{0,-} = R_2\rho_{0,+}$. In our model we assume the temperature to be homogeneous in each medium 1/2 and this, associated to the equation of state A.94 leads to a plasma under what is called the barotropy assumption: the pressure is a function only of the density. In this case, as it has been noticed by (REF Plesset and Prosperetti), the constant density assumption coupled with the constant sound speed (or the constant temperature) is inconsistent. Indeed, from equation A.87 and equation A.94 we can deduce a relation expressing the variation of the density with x:

$$\frac{\partial\rho_0}{\partial_x} = -\frac{\gamma g_{eff}\rho_0}{c_{s0}^2} \tag{A.96}$$

We highlight the fact of this non-homegenous density inside each medium since in numerous previous works (Vanderwoort), the authors assume the density to be constant in each side. With the constant speed of sound, equation A.96 leads to:

$$\rho_{0,m}(x) = C_{1,m}\exp(-\frac{\gamma_m g_{eff}}{c_{s0,m}^2}x) \tag{A.97}$$

where m=1 refers to the medium 1 where $x<0$ and m=2 to the medium 2 where $x>0$. $C_{1,m}$ are the densities near the interface at x=0 for each medium (and from our previous notations we have: $C_{1,1} = \rho_{0,-}$ and $C_{1,2} = \rho_{0,+}$). Then we can write the expression for the pressure p_0 using equation A.87:

$$\rho_{0,m}(x) = \frac{c_{s0,m}^2 C_{1,m}}{\gamma_m}\exp(-\frac{\gamma_m g_{eff}}{c_{s0,m}^2}x) + C_2 \tag{A.98}$$

As discussed before, the pressure is continuous at x=0 (the interface) and we note its value at this position P_I, then we have $C_2 = 0$ and $C_{1,m} = \gamma_m P_I/c_{s0,m}^2$ and this results in:

$$\begin{cases} \rho_{0,+} = \dfrac{\gamma_2 P_I}{c_{s0,2}^2} & \text{(A.99)} \\ \rho_{0,-} = \dfrac{\gamma_1 P_I}{c_{s0,1}^2} & \text{(A.100)} \end{cases}$$

Before deriving the jump relation at the interface we want to justify a little bit more the assumption of the constant value of $(1+Z_0^*)T_0$ in each medium. In real gases, thermal conduction processes (among others) have to be taken into account, and in this case we need to add a term in the energy equation (or the pressure equation). In the zero order equation, we can thus write:

$$\frac{\partial p_0}{\partial t} = (\gamma - 1)\frac{\partial}{\partial x}(\lambda \frac{\partial T_0}{\partial x}) \tag{A.101}$$

where λ is the thermal conduction coefficient. In order to have an equilibrium (stationary) configuration we thus must have $\partial_t p_0 = \partial_x(\lambda \partial_x T_0) = 0$. It means that the fourier heat flux $q_{heat} = \lambda \partial_x T_0$ has to be constant in the domain. If for example we consider a infinite domain in both x directions, physically the flux should be taken to be null in each medium and obviously it corresponds to two medium of constant temperatures. At the interface There can exist a thermal flux but it will be constant. Another possibility is the existence of perfectly adiabatic walls in each of the medium at a certain distance of the interface. In this case the thermal flux at these walls has to be zero and thus null in all both mediums. Here again it corresponds to constant temperatures in these medium.

Now we derive the jump relation at the interface using the main equation A.91. To do that we integrate, has done previously, each term between $-\epsilon$ and $+\epsilon$ and then we take the limit $\epsilon \to 0$. The first gives:

$$\int_{-\epsilon}^{+\epsilon} \partial_x(\alpha \partial_x v_{1x})dx = \alpha_+ \partial_x v_{1x}|_{x=+\epsilon} - \alpha_- \partial_x v_{1x}|_{x=-\epsilon} \tag{A.102}$$

where $\alpha_\pm = \rho_{0,\pm}/(1-\omega^2/k^2 cs_{0,\pm})$.

Here we see the need to find the solution of equation A.91 in order to compute the derivatives in both sides of the interface. We will do that after expressing the integration of the other terms.

Since the second term consists of an integration of a finite quantity, when taking the limit $\epsilon \to 0$ is value is given by:

$$\int_{-\epsilon}^{+\epsilon} (\rho_0 k^2 v_{1x})dx = 0 \tag{A.103}$$

The third term can be evaluated using the theory of distribution, in the context of the integration and the small limit of ϵ, we can write $\partial_x \rho_0 = (\rho_{0,+} - \rho_{0,-})\delta(x)$ where $\delta(x)$ is the dirac distribution. Thus in the integral we get:

$$\int_{-\epsilon}^{+\epsilon} (\frac{k^2}{\omega^2} g_{eff}(\partial_x \rho_0) v_{1x})dx = \frac{k^2}{\omega^2} g_{eff}(\rho_{0,+} - \rho_{0,-}) v_{1x}(0) \tag{A.104}$$

Then the fourth term can considered as the second one, that is to say an integration of a quantity of finite value and so we get:

$$\int_{-\epsilon}^{+\epsilon} (\frac{g_{eff}^2 k^2}{\omega^2 c_{s0}^2} \alpha v_{1x})dx = 0 \tag{A.105}$$

Finally the last and fifth term can be treated as the third one with: $\partial_x(\alpha/c_{s0}) = (\alpha_+/c_{s0,2} - \alpha_-/c_{s0,1})\delta(x)$ and we get:

$$\int_{-\epsilon}^{+\epsilon} (g_{eff} \frac{\alpha}{c_{s0}^2} v_{1x})dx = g_{eff}(\frac{\alpha_+}{c_{s0,2}} - \frac{\alpha_-}{c_{s0,1}}) v_{1x}(0) \tag{A.106}$$

Now we can rewrite equation A.91 as a jump condition at the interface by bringing together all the terms and noting that the sum of the third and the fifth terms gives:

$$\frac{k^2}{\omega^2} g_{eff}(\rho_{0,+} - \rho_{0,-}) v_{1x}(0) + g_{eff}(\frac{\alpha_+}{c_{s0,2}} - \frac{\alpha_-}{c_{s0,1}}) v_{1x}(0) = g_{eff}\frac{k^2}{\omega^2}(\alpha_+ - \alpha_-) v_{1x}(0) \tag{A.107}$$

Finally the global jump relation is given by (and very importantly valid for $\epsilon \to 0$):

$$\alpha_+ \partial_x v_{1x}|_{x=+\epsilon} - \alpha_- \partial_x v_{1x}|_{x=-\epsilon} = g_{eff}\frac{k^2}{\omega^2}(\alpha_+ - \alpha_-) v_{1x}(0) \tag{A.108}$$

So now, as explained before we need to find the solution of equation A.91 in order to get the derivatives present in the jump relation A.108. Noting that for each region 1/2 (in which c_{s0} is constant) we have $\partial_x \alpha = -g_{eff}\gamma\alpha/c_{s0}^2$ and furthermore, since we are looking for only unstable modes, we have $\omega = in$ where n is the growth rate, we can rewrite equation A.91 as:

$$\partial_x^2 v_{1x} - \frac{\gamma g_{eff}}{c_{s0}^2}\partial_x v_{1x} - k^2(1 + \frac{n^2}{k^2 c_{s0}^2} + (\gamma - 1)\frac{g_{eff}^2}{n^2 c_{s0}^2}) v_{1x} = 0 \tag{A.109}$$

This is a second order differential equation. We write the general solution of A.109 as: $v_{1x} = \mathrm{A}\exp(r_1 x) + \mathrm{B}\exp(r_2 x)$ where r_1 and r_2 are the solutions of the associated characteristic equation:

$$r^2 - \frac{\gamma g_{eff}}{c_{s0}^2} r - k^2(1 + \frac{n^2}{k^2 c_{s0}^2} + (\gamma - 1)\frac{g_{eff}^2}{n^2 c_{s0}^2}) = 0 \tag{A.110}$$

The constants A and B are to be determined by boundary conditions. It is a very important point and a misinterpretation of the variables that must be continuous can be at the source of errors in the derivation of the dispersion relation. The most important, physical quantity that must be continuous at the interface is the variable representing the displacement of the interface. We call it $\delta_x(x)$ and it is of course a first order quantity (considered as small). Saying that this variable must be continuous at x=0 is equivalent to enforce the unicity of the interface. The equation describing the evolution of $\delta_x(x)$ is given by:

$$\frac{\partial \delta_x}{\partial t} + (\mathbf{v_0} \cdot \nabla)\delta_x = v_{1x} \tag{A.111}$$

Using the same convention as in equation (10,11,12,13), this equation gives:

$$\delta_x = -i\frac{v_{1x}}{k_y v_0 - \omega} \tag{A.112}$$

As we can see, the continuity of δ_x implies the continuity of $\frac{v_{1x}}{k_y v_0 - \omega}$ so of course if there is no velocity v_0 in the plasma (as in our present case) or a uniform velocity field then the continuity of the displacement is strictly equivalent to the continuity of v_{1x} at x=0 and we must have for our general solution: A=B. However, we cant to highlight the fact that if there exist a shear of velocity at the interface we must be careful of considering the correct continuity condition because otherwise we will not retrieve the valid dispersion relation for example, the Kelvin-Helmholtz instability.

The delta associated to the characteristic equation A.110 is given by:

$$\Delta = 4k^2(1 + \frac{n^2}{k^2 c_{s0}^2} + (\gamma - 1)\frac{g_{eff}^2}{n^2 c_{s0}^2} + \frac{\Upsilon^2 g_{eff}^2}{4k^2 c_{s0}^2}) \tag{A.113}$$

And thus the solutions of the characteristic equation are:

$$r_\pm = \frac{\Upsilon g_{eff}}{2c_{s0}^2} \pm \sqrt{1 + \frac{n^2}{k^2 c_{s0}^2} + (\gamma - 1)\frac{g_{eff}^2}{n^2 c_{s0}^2} + \frac{\Upsilon^2 g_{eff}^2}{4k^2 c_{s0}^2}} \tag{A.114}$$

We clearly see that $r_+ > 0$ and $r_- < 0$ and so in order to have vanishing values of v_{1x} for $x \to \pm\infty$ we write solutions of the first order velocity (with A = B = v_S the velocity at x=0) as:

$$v_{1x}(x) = \begin{cases} v_S \exp(r_- x) & \text{if } x > 0 \\ v_S \exp(r_+ x) & \text{if } x < 0 \end{cases} \tag{A.115}$$

and for the derivatives which of interest for our jump relation A.108:

$$\partial_x v_{1x}(x) = \begin{cases} r_- v_{1x} & \text{if } x > 0 \\ r_+ v_{1x} & \text{if } x < 0 \end{cases} \tag{A.116}$$

To be explicit we write the expressions for r_+ and r_-:

$$\begin{cases} r_- = \frac{\Upsilon g_{eff}}{2c_{s0,2}^2} - \sqrt{1 + \frac{n^2}{k^2 c_{s0,2}^2} + (\gamma_2 - 1)\frac{g_{eff}^2}{n^2 c_{s0,2}^2} + \frac{\Upsilon_2^2 g_{eff}^2}{4k^2 c_{s0,2}^2}} & \text{(A.117)} \\ r_+ = \frac{\Upsilon g_{eff}}{2c_{s0,1}^2} + \sqrt{1 + \frac{n^2}{k^2 c_{s0,1}^2} + (\gamma_1 - 1)\frac{g_{eff}^2}{n^2 c_{s0,1}^2} + \frac{\Upsilon_1^2 g_{eff}^2}{4k^2 c_{s0,1}^2}} & \text{(A.118)} \\ & \text{(A.119)} \end{cases}$$

Now we can write the derivatives involved in the jump relation A.108 by taking the limit $\epsilon \to 0$:

$$\partial_x v_{1x}(x) = \begin{cases} r_- v_{1x}(0) & \text{for } x = +\epsilon, \epsilon \to 0 \\ r_+ v_{1x}(0) & \text{for } x = -\epsilon, \epsilon \to 0 \end{cases} \tag{A.120}$$

By inserting these expressions in A.108 and excluding the trivial solution $v_{1x}(0) = 0$ we get:

$$\alpha_+ r_- - \alpha_- r_+ = g_{eff}\frac{k^2}{\omega^2}(\alpha_+ - \alpha-) \tag{A.121}$$

By noting $\mu_+ = r_-/k$ and $\mu_- = r_+/k$ we can simplify equation A.121 in:

$$\omega^2 = \frac{g_{eff} k(\alpha_+ - \alpha_-)}{\alpha_+ \mu_+ - \alpha_+ \mu_+} \tag{A.122}$$

A.5 The case of a discontinuisly sheared velocity unmagnetized compressible plasma: the Kelvin-Helmoltz instability

Now consider a configuration where there exist a velocity shear at an interface and initially the plasma is in equilibrium. Here we don't consider the effect of an effective acceleration. We thus have the following set of variables:

$$\begin{cases} \Omega = k_y v_0 - \omega & \text{(A.123)} \\ g_{eff} = 0 & \text{(A.124)} \\ \mathrm{B}_0 = 0 & \text{(A.125)} \\ v_{a0} = 0 & \text{(A.126)} \\ c_{ma0} = c_{s0} & \text{(A.127)} \\ c_{\mathrm{T}0} = 0 & \text{(A.128)} \\ & \text{(A.129)} \end{cases}$$

Furthermore, the equilibrium configuration is very simple with:

$$\partial_x p_0 = 0 \tag{A.130}$$

it corresponds to a plasma with uniform pressure. Accordingly with this condition, we can just consider the plasma as two regions of constant density and constant velocity defined using the Heaviside function $\theta(x)$:

$$\begin{cases} \rho_0 = rho_{0,1}\theta(-x) + rho_{0,2}\theta(x) & \text{(A.131)} \\ v_0 = v_{0,1}\theta(-x) + v_{0,2}\theta(x) & \text{(A.132)} \\ & \text{(A.133)} \end{cases}$$

The terms needed for the main equation A.40:

$$\begin{cases} m^2 = k_z^2 - \dfrac{\Omega^2}{c_{s0}^2} & \text{(A.134)} \\ m^2 + k_y^2 = \dfrac{k^2 c_{s0}^2 - \Omega^2}{c_{s0}^2} & \text{(A.135)} \\ \mathrm{Z}_1 = i\rho_0 \dfrac{k_y c_{s0}^2}{k^2 c_{s0}^2 - \Omega^2} & \text{(A.136)} \\ \mathrm{Z}_3 = -\dfrac{\Omega^2}{k^2 c_{s0}^2 - \Omega^2} & \text{(A.137)} \\ \mathrm{Z} = i\rho_0 \dfrac{k_y c_{s0}^2}{k^2 c_{s0}^2 - \Omega^2} \partial_x v_0 & \text{(A.138)} \\ \mathrm{W} = i\Omega \dfrac{\rho_0 c_{s0}^2}{k^2 c_{s0}^2 - \Omega^2} & \text{(A.139)} \\ & \text{(A.140)} \end{cases}$$

In this configuration the main equation A.40 take the form:

$$\partial_x(\mathrm{W}\partial_x v_{1x}) + \partial_x(\mathrm{Z} v_{1x}) + i\rho_0 \Omega v_{1x} = 0 \tag{A.141}$$

As in the case of the Rayleigh-Taylor instability, we now derive the jump relation integrating equation A.141 across the interface:

For the first term we get:

$$\int_{-\epsilon}^{+\epsilon} \partial_x(\mathrm{W}\partial_x v_{1x})dx = \mathrm{W}_2\partial_x v_{1x}|_{x=+\epsilon} - \mathrm{W}_1\partial_x v_{1x}|_{x=-\epsilon} \tag{A.142}$$

the second term gives:

$$\int_{-\epsilon}^{+\epsilon} \partial_x(\mathrm{Z}v_{1x})dx = [\mathrm{Z}v_{1x}]_{-\epsilon}^{+\epsilon} = 0 \tag{A.143}$$

because in each region 1/2 the velocity is constant and thus $\mathrm{Z}(x=+\epsilon) = \mathrm{Z}(x=-\epsilon) = 0$. The last and third term is zero because of the finitude of the variable v_{1x}:

$$\int_{-\epsilon}^{+\epsilon} \partial_x(i\rho_0\Omega v_{1x})dx = 0 \tag{A.144}$$

Thus finally we can write the jump relation for this configuration:

$$\mathrm{W}_2\partial_x v_{1x}|_{x=+\epsilon} - \mathrm{W}_1\partial_x v_{1x}|_{x=-\epsilon} = 0 \tag{A.145}$$

which has to be considered for $\epsilon \to 0$.

Now, in the same way as in the case the Raileygh-Taylor instability, we must find the expression for v_{1x} in order to express the derivatives present in the jump relation A.145. We consider the propagation equation A.141 for each region 1/2 of the plasma, where Z=0 because of the constant velocity field and W is constant. We thus have:

$$\mathrm{W}\partial_x^2 v_{1x} + i\rho_0\Omega v_{1x} = 0 \tag{A.146}$$

which can be, using the expression for W, rewritten as:

$$\partial_x^2 v_{1x} - (k^2 - \frac{\Omega^2}{c_{s0}^2})v_{1x} = 0 \tag{A.147}$$

First we look for the incompressible limit of this equation. To do that we consider that $c_{s0} \to 0$ and thus we have $\Omega^2/c_{s0} \to 0$ and equation A.147 gives:

$$\partial_x^2 v_{1x} - k^2 v_{1x} = 0 \tag{A.148}$$

Since we need to have evanescent waves for $x = \pm\infty$, the solutions for our configuration are:

$$v_{1x}(x) = \begin{cases} \mathrm{A}\exp(-kx) & \text{for } x > 0 \\ \mathrm{B}\exp(kx) & \text{for } x < 0 \end{cases} \tag{A.149}$$

Now we need to express a continuity condition to find the relation between the constants A and B. As discussed for the Rayleigh-Taylor instability, the most physically-obvious quantity that must be continuous at the interface is the displacement δ_x of the latter. Using equation A.112, we must have:

$$\frac{\mathrm{A}}{\Omega_2} = \frac{\mathrm{B}}{\Omega_1} \tag{A.150}$$

and thus: $\mathrm{B} = \Omega_1\mathrm{A}/\Omega_2$. With this relation we can obtain the expression for the derivatives of v_{1x} in both regions 1/2:

$$\partial_x v_{1x}(x) = \begin{cases} -k\mathrm{A}\exp(-kx) & \text{for } x > 0 \\ \frac{\Omega_1}{\Omega_2}\mathrm{A}\exp(kx) & \text{for } x < 0 \end{cases} \tag{A.151}$$

Still considering the incompressible limit we can simplify the expression of W: $\mathrm{W} \approx -i\rho_0\Omega/k^2$ and the resulting jump relation A.145 become (with $\epsilon \to 0$):

$$i\rho_{0,2}\frac{\Omega_2}{k}\mathrm{A} + i\rho_{0,1}\frac{\Omega_1^2}{k\Omega_2}\mathrm{A} = 0 \tag{A.152}$$

And after a little bit of math, we can rewrite this expression:

$$\omega^2 - 2\omega k_y\frac{\rho_{0,1}v_{0,1} + \rho_{0,2}v_{0,2}}{\rho_{0,1} + \rho_{0,2}} + \frac{\rho_{0,1}v_{0,1}^2 + \rho_{0,2}v_{0,2}^2}{\rho_{0,1} + \rho_{0,2}} = 0 \tag{A.153}$$

We recognize a second order equation so we first find the delta:

$$\Delta = -4k^2\frac{\rho_{0,1}\rho_{0,2}}{(\rho_{0,1} + \rho_{0,2})^2}(v_{0,2} - v_{0,1})^2 \tag{A.154}$$

As we can see the delta is always less than zero so the txo solutions are:

$$\omega_\pm = k_y\frac{\rho_{0,1}v_{0,1} + \rho_{0,2}v_{0,2}}{\rho_{0,1} + \rho_{0,2}} \pm ik\sqrt{\rho_{0,1}\rho_{0,2}}\frac{|v_{0,2} - v_{0,1}|}{\rho_{0,1} + \rho_{0,2}} \tag{A.155}$$

From this equation we see the existence of a imaginary part of the pulsation and regardless of the sign of both velocities, if they are different there exist a unstable solution and we recognize the Kelvin-Helmholtz growth rate for an incompressible plasma. For example if we consider the two regions to have the same density then the growth rate is very simply given by : $n = k\Delta\mathrm{V}/2$ where $\Delta\mathrm{V}$ is the absolute value of the velocity shear.

Next we investigate the case of a compressible plasma and thus the propagation equation A.147. The jump relation is sill given by A.145. In order to have evanescent modes in both regions 1/2 now we need to have:

$$k^2 - \frac{\Omega^2}{c_{s0}^2} = k^2 - k_y^2\mathrm{M}^2(1 - \frac{\omega}{k_y v_0})^2 > 0 \tag{A.156}$$

where $\mathrm{M} = v_0/c_{s0}$ is the sonic mach number. In discussing condition A.156, we may without loss of generality consider an antisymmetric velocity profile for which the real part of ω is zero. Furthermore we do make the approximation $n/k_y v_0 << 1$. At the zero order, we thus rewrite relation A.156 as:

$$k^2 - k_y^2\mathrm{M}^2 > 0 \tag{A.157}$$

Interestingly, if we consider modes such as $k_z = 0$, then this last condition transforms to $k_y^2(1 - \mathrm{M}^2)$ and finally to:

$$\mathrm{M} < 1 \tag{A.158}$$

One can see that in order to have evanescent modes the flow, in both sides, has to be subsonic.

A.6 The case of a single magnetic stable interface

Here we consider a situation where there is no effective (de-)acceleration, not velocity field but an interface delimiting two regions of plasma with different parameters in the presence of a magnetic field. This configuration is of interest for example in the solar atmosphere where strong structuring can exist because of the magnetic field. Here we have the following values:

$$\begin{cases} v_0 = 0 & \text{(A.159)} \\ \Omega = -\omega & \text{(A.160)} \\ g_{eff} = 0 & \text{(A.161)} \\ & \text{(A.162)} \end{cases}$$

then we use again the same main equation A.40 and considering that in each regions on both sides of the interface, the plasma parameters (ρ_0, B_0, c_{s0}... are homogeneous we get:

$$(k_z v_{a0}^2 - \omega^2)(\partial_x^2 v_{1x} - (m^2 + k_y^2) v_{1x}) = 0 \tag{A.163}$$

This is the equation describing the propagation of waves at a single magnetized interface in the compressible case. The first obvious solution can be directly retrieved with the left term which corresponds to incompressible Alfven waves:

$$\omega^2 = k_z^2 v_{A0} \tag{A.164}$$

Thus one can see that this configuration allows the propagation of completely decoupled Alfven waves on both sides of the interface. The Alfven waves propagating, for example, on the right of the interface "don't see" the Alfven waves propagating on the left. Next the other solution is:

$$\partial_x^2 v_{1x} - (m^2 + k_y^2) v_{1x} = 0 \tag{A.165}$$

It represents the propagation of compressible magnetoacoustic waves. Now we see that two cases are possible:

$$\begin{cases} m^2 + k_y^2 > 0 \text{(surface waves)} & \text{(A.166)} \\ m^2 + k_y^2 < 0 \text{(body waves)} & \text{(A.167)} \\ & \text{(A.168)} \end{cases}$$

Here we use the same nomenclature that in the paper of **(PAPIER SCOTLAND)** where by "surface wave" we mean that the energy of the wave stay confined near the location of the interface. It corresponds in fact to the traditional evanescent waves. On this opposite, by "body waves", we mean that the energy is not localized and the interface actually acts like an "radiator" of waves (**REF**). Here we focus our discussion on the case of surface waves, that is to say, waves such as $m^2 + k_y^2 > 0$. In this case, the solution of equation A.165 is given by:

$$v_{1x}(x) = \begin{cases} A\exp(-\sqrt{m^2 + k_y^2}x) & \text{for } x > 0 \\ B\exp(\sqrt{m^2 + k_y^2}x) & \text{for } x < 0 \end{cases} \tag{A.169}$$

Using again the same condition for the continuity of the displacement (see relation A.112), we must have A = B (absence of velocity field).

Now, contrary to the case of the instabilities, here we use an second continuity relation to express the link between both regions 1/2. We use the continuity of the first order total pressure $p_1 + B_0 B_{1z}/\mu_0$ at the interface (x=0). We already have expressed this pressure in Eq.(23). Here since in both regions we have homogeneous pressure and no velocity (Z = 0), the last equation write:

$$p_1 + \frac{B_0 B_{1z}}{\mu_0} = W \partial_x v_{1x} \tag{A.170}$$

and in our case we have:

$$W = -i \frac{\rho_0}{\omega} \frac{k_z^2 v_{A0}^2 - \omega^2}{m^2 + k_y^2} \tag{A.171}$$

and for the derivatives of v_{1x} we have:

$$\partial_x v_{1x}(x) = \begin{cases} -\sqrt{m^2 + k_y^2} A \exp(-\sqrt{m^2 + k_y^2} x) & \text{for } x > 0 \\ \sqrt{m^2 + k_y^2} A \exp(\sqrt{m^2 + k_y^2} x) & \text{for } x < 0 \end{cases} \tag{A.172}$$

Using A.170 and A.171, the continuity of the total first order pressure is thus given by:

$$-i \frac{\rho_{0,1}}{\omega} \frac{k_z^2 v_{A0,1}^2 - \omega^2}{m_1^2 + k_y^2} A \sqrt{m_1^2 + k_y^2} = i \frac{\rho_{0,2}}{\omega} \frac{k_z^2 v_{A0,2}^2 - \omega^2}{m_2^2 + k_y^2} A \sqrt{m_2^2 + k_y^2} \tag{A.173}$$

the term on the left side been the total pressure in the region 1 ($x < 0$) and the right side been the total pressure in the region 2 ($x > 0$). After some manipulations one can obtain a simpler expression:

$$\rho_{0,1}(k_z^2 v_{A0,1}^2 - \omega^2)\sqrt{m_2^2 + k_y^2} + \rho_{0,2}(k_z^2 v_{A0,2}^2 - \omega^2)\sqrt{m_1^2 + k_y^2} = 0 \tag{A.174}$$

This last expression is the final dispersion relation for a single magnetized interface in a compressible plasma. This relation can be expressed in two others forms which can be more easily interpreted if we want to know the phase speed of waves along the magnetic field direction (z):

$$\begin{cases} \dfrac{\omega^2}{k_z^2} = v_{A0,1}^2 + \dfrac{1}{1+R}(v_{A0,2}^2 - v_{A0,1}^2) & \text{(A.175)} \\ \dfrac{\omega^2}{k_z^2} = v_{A0,2}^2 - \dfrac{R}{1+R}(v_{A0,2}^2 - v_{A0,1}^2) & \text{(A.176)} \\ & \text{(A.177)} \end{cases}$$

with R defined by:

$$R = \frac{\rho_{0,1}}{\rho_{0,2}} \sqrt{\frac{m_2^2 + k_y^2}{m_1^2 + k_y^2}} \tag{A.178}$$

from the two variant (175,176), one can deduce bounds for the parallel phase speed of waves allowed in the single magnetized interface:

$$min(v_{A0,1}^2, v_{A0,2}^2) \leq \frac{\omega^2}{k_z^2} \leq max(v_{A0,1}^2, v_{A0,2}^2) \tag{A.179}$$

thus, the parallel phase speed of waves on a magnetized interface is necessarily greater than the minimum Alfven speed of both mediums and lower than the maximum Alfven speed of these mediums. Now, to obtain a maximum of information without numerical resolution of A.174 we look at specific simpler situations.

First we consider shear waves, that is to say waves such as their propagation is mainly perpendicular to the magnetic field ($k_y >> k_z$). Furthermore, if we consider that $m_{1/2}^2 << k_y$ then we can say that $R \sim \rho_{0,1}/\rho_{0,2}$ and thus inserting that in expression (175) we get:

$$\frac{\omega^2}{k_z^2} = \frac{\rho_{0,1} v_{A0,1}^2 + \rho_{0,2} v_{A0,2}^2}{\rho_{0,1} + \rho_{0,2}} \tag{A.180}$$

This dispersion relation corresponds to the propagation of waves with parallel phase speed equals to the averaged (by densities) alfven speeds. If one medium is much more dense than the other then it "imposes" its speed to the surface waves on the interface.

An other interesting case concerns the situation where the thermal beta is low everywhere, in both regions 1/2. In this case we have:

$$\beta \approx \frac{c_{s0}^2}{v_{A0}^2} << 1 \tag{A.181}$$

We can thus simplify several expressions as:

$$\begin{cases} c_{T0}^2 = \dfrac{c_{s0}^2 v_{A0}^2}{c_{s0}^2 + v_{A0}^2} \approx c_{s0}^2 & \text{(A.182)} \\ c_{ma0}^2 = c_{s0}^2 + v_{A0}^2 \approx v_{A0}^2 & \text{(A.183)} \\ m^2 = \dfrac{(k_z^2 c_{s0}^2 - \omega^2)(k_z^2 v_{A0}^2 - \omega^2)}{c_{ma0}^2 (k_z^2 c_{T0}^2 - \omega^2)} \approx k_z^2 - \dfrac{\omega^2}{v_{A0}^2} & \text{(A.184)} \\ & \text{(A.185)} \end{cases}$$

with these simplified expressions we know can rewrite the main dispersion relation A.174 in the low beta case as:

$$\rho_{0,1}(k_z^2 v_{A0,1}^2 - \omega^2)\sqrt{k^2 - \frac{\omega^2}{v_{A0,2}^2}} + \rho_{0,2}(k_z^2 v_{A0,2}^2 - \omega^2)\sqrt{k^2 - \frac{\omega^2}{v_{A0,1}^2}} = 0 \tag{A.186}$$

As we can, see, since if the two terms inside the square roots are positive (and they have to be since we are looking only at surface waves), there exist solutions (and thus waves) to this equation because one term is negative and the other positive (a consequence of the bounding of the parallel phase velocity, see A.179). Now in the particular case where we are looking only at waves propagating along the magnetic field ($k_y = 0$), the dispersion equation A.186 transforms to:

$$\rho_{0,1}(k_z^2 v_{A0,1}^2 - \omega^2)\sqrt{k_z^2 - \frac{\omega^2}{v_{A0,2}^2}} + \rho_{0,2}(k_z^2 v_{A0,2}^2 - \omega^2)\sqrt{k_z^2 - \frac{\omega^2}{v_{A0,1}^2}} = 0 \tag{A.187}$$

In this case it is not possible to have both terms inside the square roots positives, still because of the parallel phase speed bounding. Thus, the conclusion is that in a low-beta

single magnetized interface there exist no surface waves propagating only along the magnetic field. There must be a non-zero component k_y in order to allow waves to propagate.

An other interesting situation can be analyzed with the case of one side (let's say region 2) to be field-free, that is to say $B_0 = 0$, $v_{A0,2} = 0$ and considering only parallel modes ($k_y = 0$). In this case we have:

$$m_2^2 = k_z^2 - \frac{\omega}{c_{s0,2}^2} \tag{A.188}$$

and the general dispersion relation A.174 becomes:

$$\rho_{2,1}(k_z^2 v_{A0,1}^2 - \omega^2)\sqrt{m_2^2} - \rho_{0,2}\omega^2\sqrt{m_1^2} = 0 \tag{A.189}$$

This last equation can be rewritten as:

$$\omega^2 = \frac{k_z^2 v_{A0,1}^2}{1 + \frac{\rho_{0,2}}{\rho_{0,2}}\sqrt{\frac{m_1^2}{m_2^2}}} \tag{A.190}$$

So of course, in coherence with the bounding on the phase speed established before (see A.179), the phase speed of surface waves in the case where one side is field-free is lower than the alfven speed in the magnetized medium. Also, since the stationary equilibrium configuration is defined by $\partial_x p_{T0} = 0$ where p_{T0} is the total pressure (sum of thermal and magnetic pressure), we must have the following relation:

$$\frac{\rho_{0,1}}{\gamma} c_{s0,1}^2 + \frac{\rho_{0,1}}{2} v_{A0,1}^2 = \frac{\rho_{0,2}}{\gamma} c_{s0,2}^2 \tag{A.191}$$

where we used the fact that the thermal pressure is given by $p = \rho c_s/\gamma$ where γ is the adiabatic index (and we supposed the same index in both regions) and the magnetic pressure by $p_{mag} = \rho v_A^2/2$. Now we assume that the sound speed is the same in both regions 1/2, that is to say that they both have the same temperature. Then the equilibrium relation A.191 can be rewritten:

$$v_{A0,1}^2 = \frac{2}{\gamma}\left(\frac{\rho_{0,2}}{\rho_{0,1}} - 1\right) c_{s0}^2 \tag{A.192}$$

As we can see, in order to be physical, this relation implies that $\rho_{0,2} > \rho_{0,1}$. Furthermore, the ratio m_1^2/m_2^2 is given in this case by:

$$\frac{m_1^2}{m_2^2} = \frac{c_{s0}^2}{c_{ma0,1}^2}\frac{k_z^2 v_{A0,1}^2 - \omega^2}{k_z^2 c_{T0,1}^2 - \omega^2} \tag{A.193}$$

(TO BE CONTINUED WITH NUMERICAL CALCULATIONS)

A.7 The case of a magnetic slab

The configuration consists here of a slab embedded in an external medium. We note quantities related to the external medium with the index "e", whereas in the slab we use the index "s". The dimensions of the slab in the x direction, where there exist inhomogeneities in terms of density, magnetic field and temperature, are noted $\pm x_0$. In the y and z directions we consider an infinite slab. Here the general equation describing the propagation of waves is exactly the same that in the case of the single magnetized interface. So we come back to the equation A.163. For convenience purpose, we recall this equation:

$$(k_z v_{a0}^2 - \omega^2)(\partial_x^2 v_{1x} - (m^2 + k_y^2) v_{1x}) = 0 \tag{A.194}$$

Here again we see that alfven waves can still propagates independently in each domain: external"e" and inside the slab "s". Concerning compressible waves, that is to say magnetoacoustic waves, we have to deal with basically two regions:

- In the external medium ($|x| > x_0$), we want the physical solution corresponding to evanescent waves so it corresponds to the case where $m_e^2 + k_y^2 > 0$ and thus the general solutions:

$$v_{1x}(x) = \begin{cases} \mathrm{A}_e \exp(-\sqrt{m_e^2 + k_y^2}(x - x_0)) & \text{for } x > 0 \\ \mathrm{B}_e \exp(\sqrt{m_e^2 + k_y^2}(x + x_0)) & \text{for } x < 0 \end{cases} \tag{A.195}$$

  where A_e and B_e are constants depending on the boundaries conditions.

- Inside the slab, we allow for solutions with both $m_s^2 + k_y^2 > 0$ and $m_s^2 + k_y^2 < 0$. The first case to corresponds to "surface waves" whereas the second case corresponds to "body waves". The general solution for waves allowed inside the slab can be written:

$$v_{1x}(x) = \mathrm{A}_s cosh(\mathrm{M}_s x) + \mathrm{B}_s sinh(\mathrm{M}_s x) \tag{A.196}$$

  where:

$$\mathrm{M}_s = \begin{cases} \sqrt{m_s^2 + k_y^2} & \text{for } m_s^2 + k_y^2 > 0 \\ i\sqrt{|m_s^2 + k_y^2|} & \text{for } m_s^2 + k_y^2 < 0 \end{cases} \tag{A.197}$$

Now, to go further, we need to use continuity/boundary conditions. Here we first use as in all previous cases, the continuity of the displacement δ_x and thus in the case of no velocity field, the continuity of the velocity v_{1x} on both interfaces $x = \pm x_0$. The continuity in $x = -x_0$ gives:

$$\mathrm{B}_e = \mathrm{A}_s cosh(-\mathrm{M}_s x_0) + \mathrm{B}_s sinh(-\mathrm{M}_s x_0) \tag{A.198}$$

whereas at $x = x_0$, we get:

$$\mathrm{A}_e = \mathrm{A}_s cosh(\mathrm{M}_s x_0) + \mathrm{B}_s sinh(\mathrm{M}_s x_0) \tag{A.199}$$

Then, as in the previous case of a magnetic single interface, we use the continuity of the first order pressure $p_1 + \mathrm{B}_0\mathrm{B}_{1z}/\mu_0 = \mathrm{W}\partial_x v_{1x}$ (given by expression (23) with here Z=0 in each medium). First we express $p_1 + \mathrm{B}_0\mathrm{B}_{1z}/\mu_0$ in the external medium for $|x| = x_0$:

$$(p_1 + \mathrm{B}_0\mathrm{B}_{1z}/\mu_0)|_{"e"} = \begin{cases} i\mathrm{A}_e \frac{\rho_e}{\omega} \frac{k_z^2 v_{\mathrm{A}e}^2 - \omega^2}{\sqrt{m_e^2 + k_y^2}} & \text{for } x = x_0 \\ -i\mathrm{B}_e \frac{\rho_e}{\omega} \frac{k_z^2 v_{\mathrm{A}e}^2 - \omega^2}{\sqrt{m_e^2 + k_y^2}} & \text{for } x = -x_0 \end{cases} \tag{A.200}$$

and inside the slab, the total first order pressure is given by:

$$(p_1 + \mathrm{B}_0\mathrm{B}_{1z}/\mu_0)|_{"e"} = -i\mathrm{M}_s \frac{\rho_s}{\omega} \frac{k_z^2 v_{\mathrm{A}s}^2 - \omega^2}{m_s^2 + k_y^2} (\mathrm{A}_s sinh(\mathrm{M}_s x) + \mathrm{B}_s cosh(\mathrm{M}_s x)) \tag{A.201}$$

Thus we can now write the continuity of the total first order pressure on both interfaces $x = \pm x_0$:

$$\rho_e \mathrm{B}_e \frac{k_z^2 v_{\mathrm{A}e}^2 - \omega^2}{\sqrt{m_e^2 + k_y^2}} = \rho_s \mathrm{M}_s \frac{k_z^2 v_{\mathrm{A}s}^2 - \omega^2}{m_s^2 + k_y^2} (\mathrm{B}_s cosh(\mathrm{M}_s x_0) - \mathrm{A}_s sinh(\mathrm{M}_s x_0)) \tag{A.202}$$

for $x = -x_0$

$$\rho_e \mathrm{A}_e \frac{k_z^2 v_{\mathrm{A}e}^2 - \omega^2}{\sqrt{m_e^2 + k_y^2}} = -\rho_s \mathrm{M}_s \frac{k_z^2 v_{\mathrm{A}s}^2 - \omega^2}{m_s^2 + k_y^2} (\mathrm{B}_s cosh(\mathrm{M}_s x_0) + \mathrm{A}_s sinh(\mathrm{M}_s x_0)) \tag{A.203}$$

for $x = x_0$

then, in order to get an easier understanding of these dispersion relations, we split the solutions into two different kind: "sausage" modes and "kink" modes. The first ones correspond to the case where the first order velocity v_{1x} given by A.196 is an odd function of x and of course it corresponds to solutions associated with the hyperbolic sinus. Thus, for "sausage" modes, we assume that $\mathrm{A}_s = 0$. Concerning the "kink" modes, it corresponds to the case where the first order velocity A.196 is a pair function of x so this is associated to the presence of the hyperbolic cosinus and thus in this case we will assume that we have $\mathrm{B}_s = 0$.

First we deduce the dispersion relation for the sausage modes. From the fact that we have here $\mathrm{A}_s = 0$, we get, from A.198 and A.199, the equality $\mathrm{A}_e = -\mathrm{B}_e$. Also, we have $\mathrm{B}_e = -\mathrm{B}_s sinh(\mathrm{M}_s x_0)$ so, injecting this expression in A.202 leads to the equation:

$$\rho_e \frac{k_z^2 v_{\mathrm{A}e}^2 - \omega^2}{\sqrt{m_e^2 + k_y^2}} tanh(\mathrm{M}_s x_0) + \rho_s \mathrm{M}_s \frac{k_z^2 v_{\mathrm{A}s}^2 - \omega^2}{m_s^2 + k_y^2} = 0 \tag{A.204}$$

This last equation is the dispersion relation for "sausage" body/surface waves allowed in a magnetic slab of dimension $2x_0$. One can note that if we use the relation A.203 instead of A.202, we get exactly the same result because we are looking here separately to the "sausage" and the "kink" modes.

Then for the case of "kink" modes, using the fact that $\mathrm{B}_s = 0$, we have , from A.198 and A.199 the equality $\mathrm{A}_e = \mathrm{B}_e$. We also have, from A.199 in this case $\mathrm{A}_e = \mathrm{B}_e = \mathrm{A}_s cosh(\mathrm{M}_s x_0)$. Thus, injecting theses relations in A.202 or A.203, we obtain:

$$\rho_e \frac{k_z^2 v_{\mathrm{A}e}^2 - \omega^2}{\sqrt{m_e^2 + k_y^2}} coth(\mathrm{M}_s x_0) + \rho_s \mathrm{M}_s \frac{k_z^2 v_{\mathrm{A}s}^2 - \omega^2}{m_s^2 + k_y^2} = 0 \tag{A.205}$$

Equation A.205 is the general dispersion relation for "kink" body/surface waves allowed in a magnetic slab of dimension $2x_0$.

One of the first question that one can ask with this system concerns the stability of the slab. Are they unstable modes in this configuration ? To answer this question, we first look at the case of "surface" waves, that is to say when $m_s^2 + k_y^2 > 0$ and $\mathrm{M}_s = \sqrt{m_s^2 + k_y^2} > 0$. This leads to have $tanh(\mathrm{M}_s x_0) > 0$ and $coth(\mathrm{M}_s x_0) > 0$. Furthermore, we have (because

we want evanescent modes for $x \to \pm\infty$) $m_e^2 + k_y^2 > 0$. Thus, if we are looking for purely unstable modes, such that $\omega^2 < 0$, we see that it is not possible to satisfy both dispersion relation A.204 and A.205. The conclusion is that there exist no unstable surface sausage/kink modes in a magnetic slab, regardless of the parameters in both the external medium and the slab.

Now in the case of body waves, the situation is even simpler to analyze. Indeed, if we have an unstable mode with $\omega^2 < 0$, then, from relation (32), one can see that we must have $m_s^2 > 0$ and thus $m_s^2 + k_y > 0$. This last inequality is precisely the opposite of the condition for the existence of a body waves. Thus, also in the case of body waves, it is no possible to see, from this configuration, unstable sausage/kink modes.

Now we ask the question of the possibility to obtain from this configuration purely shear waves, that is to say waves such that $k_z = 0$. In this case, we can write for the slab and the external medium:

$$\begin{cases} m_e^2 = -\dfrac{\omega^2}{c_{mae}^2} & \text{(A.206)} \\ m_s^2 = -\dfrac{\omega^2}{c_{mas}^2} & \text{(A.207)} \\ & \text{(A.208)} \end{cases}$$

thus, using these expressions, we get the dispersion relation for shear sausage(tanh)/kink(coth) waves:

$$\frac{\rho_e}{\sqrt{k_y^2 - \frac{\omega^2}{c_{mae}^2}}} \begin{cases} tanh(\mathrm{M}_s x_0) \\ coth(\mathrm{M}_s x_0) \end{cases} + \mathrm{M}_s \frac{\rho_s}{k_y^2 - \frac{\omega^2}{c_{mas}^2}} = 0 \tag{A.209}$$

Since, we are only looking at evanescent modes, we must always have $m_e^2 + k_y^2 > 0$ and thus, using (206), we have the condition:

$$\frac{\omega}{c_{mae}} < c_{mae} \tag{A.210}$$

It means that shear waves always propagate at speeds lower than the fast magnetoacoustic speed of the external medium. Now we can precise the conditions for shear waves in both the case of surface waves and body waves. First, if we look at surface waves, we must have $k_y^2 - \omega^2/c_{mas}^2 > 0$ and $\mathrm{M}_s > 0$. It follows that it is not possible verify the dispersion relation A.209, for sausage as well as kink modes. Thus, there exist no shear ($\mathbf{k} \cdot \mathbf{B} = 0$) surface waves in a magnetic slab.

In the case of shear body waves, we must have $k_y^2 - \omega^2/c_{mas}^2 < 0$ and $\mathrm{M}_s = i\sqrt{\omega^2/c_{mas}^2 - k_y^2}$ is complex. It leads to the condition $\omega/k_y > c_{mas}$. Thus, there can be shear body waves with the following bounds on the phase speed:

$$c_{mas} < \frac{\omega}{c_{mae}} < c_{mae} \tag{A.211}$$

We thus see that if the fast magnetoacoustic speed in the slab c_{mas} is higher that the one in the external medium c_{mae} then shear body waves can't exists.

The dispersion relation for shear waves A.209 can be developed more easily if we look at the case of a "slender" slab, such that $k_y x_0 << 1$. If in addition it is supposed that $|\mathrm{M}_s| x_0$ then we have for the sausage and the kink modes:

$$\begin{cases} tanh(\mathrm{M}_s x_0) \approx \mathrm{M}_s x_0 & \text{(A.212)} \\ coth(\mathrm{M}_s x_0) \approx \dfrac{1}{\mathrm{M}_s x_0} & \text{(A.213)} \end{cases}$$

For the shear sausage body waves, we get the dispersion relation from A.209:

$$\frac{\rho_e x_0}{\sqrt{k_y^2 - \frac{\omega^2}{c_{mae}^2}}} + \frac{\rho_s}{k_y^2 - \frac{\omega^2}{c_{mas}^2}} = 0 \tag{A.214}$$

This last equation can be rewritten as a fourth order equation:

$$(\frac{\rho_e x_0}{\rho_s c_{mas}^2})^2 \omega^4 + (\frac{1}{c_{mae}^2} - 2(\frac{\rho_e k_y x_0}{\rho_s c_{mas}})^2)\omega^2 + k_y^2((\frac{\rho_e}{\rho_s})^2 (x_0 k_y)^2 - 1) = 0 \tag{A.215}$$

Defining $\mathrm{W} = \omega^2$, this equation can be written as a second order equation and we get the associated delta:

$$\Delta = \left(\frac{\rho_e}{\rho_s}\right)^2 \frac{(k_y x_0)^2}{c_{mas}^4} \left[\left(\frac{\rho_s}{\rho_e}\right)^2 \left(\frac{c_{mas}}{c_{mae}}\right)^4 \frac{1}{(k_y x_0)^2} + 4\left(1 - \left(\frac{c_{mas}}{c_{mae}}\right)^2\right)\right] \tag{A.216}$$

And since for body waves we must have the condition A.211 and thus $c_{mas}/c_{mae} < 1$, we have $\Delta > 0$. The two possible solutions are thus:

$$\omega_\pm^2 = c_{mas}^2 \left[k_y^2 - \left(\frac{\rho_s c_{maes}^2}{\sqrt{2}\rho_e c_{mae} x_0}\right)^2 \pm \frac{\rho_s k_y c_{mas}^2}{2\rho_e x_0} \sqrt{\left(\frac{\rho_s c_{mas}^2}{\rho_e c_{mae}^2 x_0 k_y}\right)^2 + 4(1 - \frac{c_{mas}^2}{c_{mae}^2})}\right] \tag{A.217}$$

This last equation can be rewritten in a somewhat more readable form:

$$\omega_\pm^2 = c_{mas}^2 \left[k_y^2 + \frac{1}{2}\frac{\rho_s}{\rho_e}\frac{1}{x_0}\left(\pm k_y \sqrt{\mathrm{K}} - \left(\frac{c_{mas}}{c_{mae}}\right)^2 \frac{1}{x_0}\right)\right] \tag{A.218}$$

with K defined by:

$$\mathrm{K} = \left(\frac{\rho_s c_{mas}^2}{\rho_e c_{mae}^2 x_0 k_y}\right)^2 + 4(1 - \frac{c_{mas}^2}{c_{mae}^2}) \tag{A.219}$$

Equation A.218 is the dispersion relation of shear body sausage waves in the case of a slender slab ($k_y x_0 << 1$). As an particular case, we look at the case where the fast magnetoacoustic speed is the same in both regions: $c_{mas} = c_{mae}$. In this case we have:

$$\omega_\pm^2 = k_y^2 c_{mas}^2 + \frac{1}{2}\frac{\rho_s}{\rho_e}\frac{c_{mas}^2}{x_0^2}\left[\pm\frac{\rho_s}{\rho_e} - 1\right] \tag{A.220}$$

As a safety check of our expression, we can see that in the case where there is an uniform medium (no slab) such that $\rho_s = \rho_e$ then we have the two following solutions:

$$\begin{cases} \omega_+^2 = k_y^2 c_{mas}^2 & \text{(A.221)} \\ \omega_-^2 = \dfrac{c_{mas}^2}{x_0^2}\left(k_y^2 x_0^2 - 1\right) & \text{(A.222)} \end{cases}$$

the first solution corresponds to the already seen fast magnetic acoustic waves in a uniform medium whereas the second solution is actually not possible since to obtain this solution we have supposed that $k_y x_0 << 1$ so that the second solution would lead to a imaginary pulsation, which is not possible in this case.

List of Figures

1.1 Schematic representation of the main addressed topics in this manuscript. 5

2.1 Spatial localization of the GORGON variables used to perform the numerical scheme 41

2.2 48

2.3 Left: Z position of the ray as a function of time. The full black line corresponds to the solution 2.250 whereas the dotted red line corresponds the ray trajectory obtained in GORGON using the model described in the previous section. Right: same as previously but here the plotted quantity is the ray energy as a function of time. 51

2.4 Mass flux (in SI units) of a hemispherical blast expansion created by a plasma "ball" of 100 eV with center in (x=0,y=0,z=0). Field lines represents the velocity. Without electronic thermal conduction. 55

2.5 Convergence with the spatial resolution of maximal value of the self-generated magnetic field in the case of a hemispherical expansion of a 100 eV plasma blast. Without electronic thermal conduction 56

2.6 For a fixed resolution dx=0.46 um, evolution, as a function of the plasma "ball" temperature, of the maximal value of the self-generated magnetic field in the case of a hemispherical expansion. Without electronic thermal conduction 56

3.1 Graph showing the history of maximum laser pulse intensity throughout the past 40 years. From [2]. 63

3.2 Schematic picture of the different regions established during the interaction of a laser pulse with a solid target. Region 1: Unperturbed solid target. Region 2: Part of the solid target been shocked. Region 3: conductive zone, delimited on the left by the ablation front and on the right by the critical surface. The laser energy can not be deposited directly in this region but instead is transported through thermal conduction up to the ablation front. Region 4: Expanding plasma, represented in this schema as been isothermal but, as explained in the main text, in some condition and far form the critical surface, the expansion can be closer to an adiabatic regime. 66

3.3 Crater produced in copper by a focused Nd laser beam of an energy of 10 J and a duration of 10 ns. From [36] 68

3.4 Electron temperature of a lucite plasma (C_5,O_2,H_8) as a function of the laser intensity. Temperatures were deduced from soft x-ray continuum. From [51] 70

3.5 Schematic picture of initial configuration studied for the plasma expansion. The region located on the left of piston ($x < 0$) is considered to be vacuum whereas on the right ($x > 0$) we consider a infinite reservoir filled of plasma with mass density ρ_0, electron/ion temperature $T_{e/i0}$ and ionization Z_0^*. At $t = 0$, the piston is pulled back with the constant velocity U_{piston} and an rarefaction wave begins to propagate inside the reservoir. 72

3.6 Graphs of the mass density at a given time ($t = 20\,ns$) computed using eq.3.41 with four different piston velocity: (a) in this case the piston goes sufficiently slowly such that the characteristic point X_0 (from where the fluid velocity equals the piston velocity) is "pushed" on the right, inside the reservoir. (b) Here the piston has exactly the velocity ($2c_0/(\gamma+1)$) at which the point X_0 is stationary and stay at the initial position of the piston (i.e. $x = 0$). (c) Here the piston goes slightly faster than in the previous case and thus the point X_0 is also pulled back. (c) In the extreme case where the piston has an velocity greater of equal to the maximum adiabatic velocity $|u_{max}| = 2c_0/(\gamma-1)$ then the plasma behaves exactly as if the the piston was absent: this situation is equivalent to a vacuum expansion. 77

3.7 Profiles of mass density, velocity, "temperature" and pressure for: (blue) a $T_i = 100\,eV$ plasma with cold electrons ($T_e = 0\,eV$ and no electron-ion energy exchange), (red) a $T_i = T_e = 100\,eV$ plasma with electrons treated as being a perfect gas (no energy going in ionization) and (green) a $T_i = T_e = 100\,eV$ plasma with the ionization energy taken into account in the electron energy. 79

3.8 Schematic (and very simplified) representation of a laser-produced plasma expanding in front of a solid target (black). We consider two main regions: an accelerating region (in red) where the pressure forces are still important and fluid particles are being accelerated (subsonic flow or weakly supersonic). The second region can be called the "propagation region" (in blue) and is composed of plasma in hypersonic regimes ($M \gtrsim 4$) where the fluid particles behave as ballistic particles. The two regions are delimited by the important point called x_s which, as shown in the main text, does not correspond to the sonic point (where $M = 1$) 84

3.9 Mass density profiles (at $t = 50\,ns$) for both the adiabatic expansion (red full lines) and the free-streaming expansion proposed here (black dotted lines). The adiabatic expansion is supposed to come from the expansion of a plasma reservoir at an ion and electron temperature of 300 eV and a density of $10^{-2}\,kg.m^{-3}$. The join between the adiabatic and the free-streaming solutions is realized at the point x_s which is varied in each of the graphs presented here ($x_s = 1, 4, 8, 12\,mm$). We see that as this point is shifted away from the origin (where the adiabatic flow is sonic, i.e $M = 1$), the two solution converges because the fluid particles crossing this point have effectively higher Mach numbers and are so well described by the Burger's equation. . 87

4.1 (a) Self-steepening of a finite amplitude sound wave. The situation a $t = t_3$ is not physical because of the multi-valued function that the pressure would become. Instead, dissipative processes create the situation represented at $t = t_4$, where the front shock separating the regions 1 and 2 is established on a distance of few mean free path. (b) Cartoon representing the process by which a shock is formed, in this case a receding reverse/accretion) shock. The skiers which are going faster than the speed at which they can receive informations from skiers downstream, just hit the stack in front of them before being able to slow down. From "Supersonic flow and Shock waves", R.Courant and K. O. Friedrichs, 1948 [4]. 95

4.2 (a) Photograpic image of the bow shock in front of a projectile embedded in a supersonic flow. From Ernst Mach, "Uber Erscheinungen an fliegenden Projectilen". 1898. (b) Schematic, from Mach himself, of what he observed in his experiment. In front of the projectile is represented the bow shock whereas at the back turbulence is represented 96

4.3 From [2]. Idealized supersonic slightly underexpanded jet ($P_{jet} > P_{background}$). Conical shocks are formed at regular steps as a consequence of the action of the background on the jet material. 97

4.4 Quasar 3C 175 pictured in radio wavelengths. The jet extend far into intergalactic space and its most visible part consists of the head, where there exist the strongest conversion of kinetic energy into thermal energy, re-radiated subsequently. From Brotherton, Nature, (2014) [12] 98

4.5 Schematic of the head of a supersonic jet expanding in a external medium. From [2] 98

4.6 Images of the supergiant elliptical galaxy Messier 87 (M87), also known as "the Smoking Gun". Images – X-ray: H. Marshall (MIT), et al., CXC, NASA Radio: F. Zhou, F. Owen (NRAO), J. Biretta (STScI) Optical: E. Perlman (UMBC), et al., STScI, NASA 100

4.7 Schema showing the configuration at a constriction along the jet, both in the external frame (left) and the frame of the constriction (right). From [2]. 101

4.8 Schema of the simulation domain used in the GORGON code to simulate idealized supersonic jets. In all simulations presented in this chapter we will use $\theta = 0°$ meaning that the jet enters in the domain with a null opening angle. 104

4.9 2D maps of the decimal logarithm of the mass density at t=0.15, 0.35, 0.45, 0.5, 1 and 2 μs. The jet is injected at $z = 0$ with a zero opening angle. The internal Mach number of the jet is 3, the density ration η is 0.1 and the jet is pressure-matched with the background. The corresponding ion temperature maps are shown in fig.4.10 and the pressure maps in fig.4.11 105

4.10 2D maps of the decimal logarithm of the ion temperature at t=0.15, 0.35, 0.45, 0.5, 1 and 2 μs. The jet is injected at $z = 0$ with a zero opening angle. The internal Mach number of the jet is 3, the density ration η is 0.1 and the jet is pressure-matched with the background. The corresponding densities map are shown in fig.4.9 and the pressure maps in fig.4.11 107

4.11 2D maps of the decimal logarithm of the total pressure (ionic + electronic) at t=0.15, 0.35, 0.45, 0.5, 1 and 2 μs. The jet is injected at $z = 0$ with a zero opening angle. The internal Mach number of the jet is 3, the density ration η is 0.1 and the jet is pressure-matched with the background. The corresponding densities map are shown in fig.4.9 and the corresponding ion temperature maps in fig.4.10 108
4.12 2D maps of the decimal logarithm of the mass density for pressure-matched jets. Are shown four different Mach number jets: M=0.5, M=1, M=6 and M=9. The jets are injected at $z = 0$ with a zero opening angle. The density ratio η is 0.1 for all cases. The corresponding ion temperature maps are shown in fig.4.13. 110
4.13 2D maps of the decimal logarithm of the ion temperature for pressure-matched jets. Are shown four different Mach number jets: M=0.5, M=1, M=6 and M=9. The jets are injected at $z = 0$ with a zero opening angle. The density ratio η is 0.1 for all cases. The corresponding mass density maps are shown in fig. 112
4.14 2D maps of the decimal logarithm of the mass density for a pressure-matched jet. The background pressure is the sum of the thermal background pressure and the magnetic pressure. In the left panel, the field ($B_z = 6.97$ T) accounts for ≈ 35% of the total pressure whereas in the right panel the field ($B_z = 10.23$ T) accounts for ≈ 75% of the total pressure. The jets are injected in both cases at $z = 0$ with a zero opening angle. The density ratio η is 0.1 in both cases. 113
4.15 2D maps of the magnetic field magnitude at $t = 1\,\mu s$ for the case where the initial field is of 10.23 T (≈ 35% of the total background pressure). The corresponding mass density maps is the middle one in the right panel of fig.4.14. 115
4.16 2D maps of the mass density at t=0.05, 0.15, 0.25 and 2 μs for "magnetically" pressure-matched supersonic jets (M = 3, $T_{jet} = 100\,eV$ and $\rho_{jet} = 0.01\,kg.m^{-3}$). Here the jet is propagating in vacuum. 116

5.1 a) Top view schematic of the Helmholtz coil system. The “laser bore” (left-right axis) of the coil would allow a maximum of 27° full-angle beam for a laser beam at normal incidence. The “diagnostic bore” (up-down axis) is of constant 11 mm diameter. b) Photograph of the Helmholtz coil in the chamber looking into the “laser-bore”. Motorized stages are not shown. c) Magnetic field profiles along the coil central axes. The target is recessed along the longitudinal (laser bore) axis which is parallel to the field lines. Dotted and dashed lines show the extent of the coil bore and the maximum distance over which the target was recessed. 121
5.2 Pseudo-color images of electron density taken via interferometry showing jet propagation from 6 to 70 ns as indicated in the plots. The jet was created by a $2\,10^{13}$ W.cm^{-2} laser irradiating a CF_2 target in a 20 T ambient magnetic field. The dotted vertical lines indicate the edges of the individual images. The gray background indicates a region where no data was taken or the fringes were not of sufficient quality to be unwrapped properly. The central ±5 pixels (±55 μm) have been removed due to the uncertainty of the Abel inversion on axis. Note that many of the fine structured features are due to noise in the fringes of the interferometer and thus are non-physical. From [3].122

5.3 Simulated configuration with the GORGON code. The solid target is composed of carbon, the laser pulse impacts this target with an intensity of ≈ $7.7\,10^{12}\,\mathrm{W}.cm^{-2}$ (the laser-solid-plasma interaction is performed using the DUED code [15]). The magnetic field is initialized as been perpendicular to the surface target (it corresponds to the z-direction) and its magnitude is 20 T. The left image shows, at $t = 8\,ns$, an isovolume rendering of the mass density of the jet resulting from the dynamic described in the main text. The right image shows the same jet but seen from above. 124

5.4 2D slices of the decimal logaristm of the electron density at t=2,10 and 30 ns. The carbon target is located on the left of each images (between $x = \pm 1\,mm$) and the laser pulse is coming from the left. The magnetic field lines are represented in green. 125

5.5 1D profiles from GORGON simulations of the velocity (v_z) on the z-axis at t=2,10 and 15 ns. Dotted lines represent the solution of Eq.5.2, $v_z = z/t$. . . 126

5.6 Full lines: simulation profiles of mass density (as a function of z) averaged around the z-axis over a radius of 700 µm. Dotted lines: solution computed from the adiabatic expression 5.4 129

5.7 (a): 2D maps of the plasma betas: the thermal beta (thermal pressure over magnetic pressure) is shown with the red colormap while the dynamic beta (ram pressure over magnetic pressure) is represented using the blue colormap. (b):2D map of the decimal logarithm of the electrical current density taken in a x/y slice at $z = 3\,mm$ (see the vertical line in (b)). Both images are taken at $t = 8\,ns$. 130

5.8 Plasma flow kinetic energy at z=0.6 mm and cavity radius time behavior . . 132

5.9 (a) 2D x/z maps of the decimal logarithm of electronic density at t=20 ns. (b/c) 2D x/y slices of (a) at z=4mm and z=9 mm showing the Rayleigh-Taylor filaments developing around the jet. (d/e) Mode amplitudes of the azimuthal perturbations (at z=4mm (d) and z=9 mm (e)) obtained from discrete Fourier transform (f) Full line:Amplitude of the most developed mode as a function of z. Dotted line: m value of the maximum mode. (5.13) 137

5.10 Left: Cavity maximum radius as a function of the laser energy (for 0.5 ns pulses) for three different magnetic fields (5, 10 and 20 T). Dots are taken from simulations whereas full lines are computed from 5.14. Right: Maximum cavity radius as a function of the target material atomic number for a 3 J pulse and a 5 T field. 139

5.11 Above: 3D iso-volumes of mass density when changing the orientation of the magnetic field at θ = 10°, 30° and 45°. The three pictures correspond to a time t=14 ns. Curve: Mean total impulsion in the direction of the magnetic field as a function of tilt angle. The initial laser energy is the same in all cases: 17 J (for a 0.5 ns pulse). 141

5.12 (a)2D maps of the decimal logarithm of the mass density for the case where a gas background, in addition to the magnetic field of 20 T, fills the simulation domain. It corresponds to $t = 20\,ns$(b) Time-averaged (on the first 30 ns) of the maximum mode amplitude as a function of z. (c) 2D x/y slice of the decimal logarithm of the mass density at z=9 mm. 143

5.13 2D maps of the decimal logarithm of the emissivity integrated along the line of sight at t=10 ns. 145

5.14 **(a,b,c,d)** X/Y slices of the decimal logarithm of the electron density at $t = 20\,ns$ for four different resolutions: $dx = 10\,\mu m$ (a), $dx = 30\,\mu m$ (2),$dx = 40\,\mu m$ (c),$dx = 50\,\mu m$ (d). **(e)** Time-averaged (on the first 30 ns) amplitude of the maximum mode as a function of z. 146

6.1 Schematic of the experimental setup and 3D MHD simulations of the overall plasma dynamics. The volume rendering shows the simulated mass density at 22 ns, for the case of a single 17 J pulse, with a 1/4 of the volume removed to show the internal structure of the flow. Two co-linear laser pulses (3/17 J), that are temporally-offset by either 9 or 19 ns, irradiate a CF_2 target embedded in a 20 T magnetic field. The diagnostic observation axis is also shown. 153

6.2 Plasma electron density measured via interferometry, and analyzed using Abel inversion[9; 10], in pseudo-color with identical colorscales as shown on the right. The central pixels are removed due to the uncertainty of the Abel inversion on-axis. Notice that the images appear very symmetric. The three columns show different times, measured from the beginning of the main pulse irradiation. The times highlight: cavity formation (10 ns), conical shock development (42 ns) and shocks and jet persistence over long times (70 ns). 154

6.3 X-ray spectrometry measurements of T_e from the FSSR. Lines with circles (and X's) represent the main pulse alone with (and without) an applied 20 T B-field. Lines with diamonds and squares show cases with a precursor of 9 and 19 ns delay, respectively. 154

6.4 Streaked optical emission profiles along the center of the plasma expansion axis (smoothed with a 5-pixel Gaussian) plotted with the same linear color scale for (a) the main pulse alone and (b)/(c) the precursor and main pulses with a 9/19 ns delay between them. Time is measured from the beginning of the main pulse. Notice the small signal from the precursor interaction in (b), at -9 ns, and in (c), at -19 ns. The profiles in (a) and (b) were taken over successive shots and with the exact same detector settings. Profile (c) was taken at a later time and thus was slightly scaled and shifted for comparison with the previous profiles. Note that the thin streak in (c) at $t = -15$ ns, $z = -2.25$ mm is from the probe used for interferometry. 155

6.5 3D MHD simulations results. (a,b,c) Pseudo-color maps of electron density in the temporally-staged configuration with a 19 ns delay. Times shown are measured from the main-pulse arrival. Arrows represent fluid velocity (not scaled in magnitude) and magnetic field lines are shown. Panel (a) shows the plasma created by the low energy precursor at a time just before the arrival of the main pulse. The white dashed line corresponds to the iso-contour at $0.1 n_c$. (d) Profiles of n_e, averaged over the laser focal spot, for a case of precursor-only irradiation at 9, 19, and 39 ns after *precursor* irradiation. Cases with (solid) and without (dashed) magnetic field are shown. (e) Ratio of longitudinal ($K_z = 0.5\rho v_z^2$) to radial ($K_{xy} = 0.5\rho(v_x^2 + v_y^2)$) kinetic energy integrated over the entire plasma volume, for the main pulse only (M), and the temporally-staged cases (P+M). 156

7.1 (a-b-c) 3D isovolumes of the decimal logarithm mass density at t=8, 0 and 48 ns after the laser pulse. The external magnetic field of 20 T is oriented along the x-axis. (d-e-f) Decimal logarithm of the integrated electron density along the y-direction (perpendicular to the external magnetic field) at the same times. 164
7.2 (a) Zoom of the plasma/vacuum interface at t=8 ns. The colormap corresponds to the decimal logarithm of the electron density. (b) Faraday rotation numerical diagnostic when looking in the y-direction (c) Temperature dependence of the wavelength (in millimeters) and the corresponding growth time (in nanoseconds) of the fastest growing mode for the MHD Rayleigh-Taylor instability in presence of resistivity and viscosity. At low temperatures the resistive damping dominates whereas at high temperatures the viscous dissipation predominant. 166
7.3 2D slices of the decimal logarithm of the electron density. The top three images represent three different fields (5, 10 and 100 T) at the same time (20 ns). The three bottom images are for the same field (100 T) but at three different times (8, 30 ,50 ns). 170
7.4 2D maps of the of the integrated electron density, showing the plasma dynamic at different times and for two perpendicular probing lines of sight. (a)-(c) Three different times, 3 ns, 8ns and 29 ns respectively, coming from the Elfie campaign, i.e. the 20 T magnetic field being perpendicular to the figure plane. (d) and (e) two different times, 2.5 ns and 12 ns respectively, coming from the TITAN campaign, i.e. the 20 T magnetic field being in the figure plane. 172

8.1 Schematic view a classical T Tauri star (from Hartmann L, et al., 2016. [1]). The disk rotating around its pre-main sequence star exchanges both matter and angular momentum through the existence of the stellar magnetic field (here represented as been dipolar). The coupling is done in the inner part of the disk where the gas is heated and ionized by the stellar radiations. The funneling of the disk material by the magnetic field to form the accretion flows leads to the generation of the polar accretions shocks which radiate in X-ray, UV and optical domains. 179
8.2 Schematic view of an accretion shock on the stellar surface (from Hartmann L, et al., 2016.). The infalling accreting material impact the star chromosphere and forms, where its ram pressure is comparable to the local thermal pressure, a shock. Temperature produced by this shock are of the order of few millions of kelvins and thus a large amount of X-rays are emitted. These radiations are then reprocessed by the preshock, the postshock and the ambient environment into larger wavelengths which creates the features observed on the TTS spectra. 183
8.3 Schematization of the distribution of the total radiated energy by the accretion shock. All percentages indicates the portion of this total energy. The flux is first absorbed roughly equally by the preshock and the postshock/heated atmosphere whereas then the preshock radiates ~ 50% of it outside the accretion region (mainly in UV band) and the other ~ 50% are reabsorbed and then re-radiated (in otpical, near-Ir and UV bands) by the postshock/heated atmosphere which is then finally responsible for emitting ~ 75% of the initial shock radiation flux. 184

8.4 Table presenting stelar parameters for sixteen TTS (from C.M. Johns-Krull, 1999 ([39]). The main point regarding our discussion in the main text concerns the fact that surface magnetic field strengths spread over three order of magnitude (from 190 G TO 10,4 Kg) and thus one can expect a large range of plasma betas for the accretion process. The assumption of a 1D, 2D or 3D accretion dynamic relies heavily on the assumed value for this plasma beta. 187

8.5 Density and temperatures maps of 2D MHD simulations of accretion shocks using the PLUTO code ([44]). On the left is shown the case where the gravity is included in the simulation whereas the right panel shows the case were it is artificially removed. The accreting column is coming from the top of the images, on each images, the left part represents the decimal logarithm of the number density whereas the right part shows the decimal logarithm of the temperature. It can be seen that in both cases, the dynamic reveals the development of a "shell" surrounding the accreting flow. It is important to remark that this shell develops with or without gravity included, indicating that the expulsion of material on the column sides is mainly pressure-driven. Courtesy of S. Orlando 190

9.1 Cartoon showing the top view of the central coil-region of the experimental set-up and the diagnostics paths. The grey rectangle represents the Helmholtz coil, inside the airtight structure, delivering a magnetic field in the central region up to 20 T [5]. The conical apertures allow the insertion of the stream-source target as well as the main laser beam to reach the stream-source target without clipping the obstacle target. The obstacle target is inserted from the bottom of the coil through a vertical aperture. The probe beam travels along the coil following the perpendicular aperture, going through the interaction region. 197

9.2 2D maps of the decimal logarithm of electron density inferred from interferograms which have been Abel inverted (assuming axisymmetric distribution of the plasma). Times refer to the start of the accretion process when the head of the column hit the obstacle. (see G.Revet, PhD thesis, 2017) . . . 198

9.3 Profile of the decimal logarithm of electron density inferred from interferograms (green) which have been Abel inverted (assuming axisymmetric distribution of the plasma). Also shown is the density very close to the target (black dotted line) measured from x-rays absorption. The blue curve is the best interpolation obtained and corresponds to a decrease of the density in front of the obstacle inversely proportional to the distance. Here times refer to the start of the laser pulse. (see G.Revet, PhD thesis, 2017) 199

9.4 Left: 3D iso-volume of the decimal logarithm of the mass density at $t = 8\,ns$. The laser target is located at the top whereas the collimated laser-produced plasma, forming our laboratory accretion column, is propagating towards the obstacle at the bottom of the image. The blue tubes represent the magnetic field lines. On the right, the top table gives the relevant laser parameters used to generate the expanding plasma whereas the second table gives a comparison of the important parameters for both the laboratory column and the TTS column. 200

9.5 (a) Time-dependence of the mass accretion rate of the laboratory column computed at the altitude $z = 2\,mm$ (the point P in fig.9.4) and integrated over the column cross section: $\dot{M}_{acc} = \int \Phi_{mass} dS$ with $\Phi_{mass} = \rho|v_z|$. (b) Time-dependence of the accretion kinetic energy flux of the laboratory column computed at the altitude $z = 2\,mm$ (the point P in fig.9.4) and integrated over the column cross section: $1/2\dot{M}_{acc} v_z^2 = \int \Phi_{energy} dS$ with $\Phi_{energy} = 1/2\rho|v_z^3|$. For each quantity, we plot the case where the obstacle is removed, when it is present as well as when it is replaced by a "perfect wall" (i.e. reflecting boundary condition). 202
9.6 (a-b) Iso-volume of the decimal logarithm of the mass density near the obstacle (in a volume of 6mm x 6mm x 3mm). The gray slab is the solid obstacle material. The left image corresponds to $t = 22\,ns$ whereas the right to $t = 40\,ns$. (c-d) 2D maps of the decimal logarithm of the integrated (along y-direction) electron density. Both images correspond to the times indicated above (left:22 ns, right:40 ns). (e-f) Iso-volume of the decimal logarithm of the obstacle mass density for the same times indicated above. The material from the obstacle is followed in GORGON using a tracer. 204
9.7 (a) 2D maps of the decimal logarithm of the ion temperature at $t = 22\,ns$ (corresponding to the density shown in fig.9.6(a)). (b) Same as (a) but for the electron temperature (same time). (c) Maximum ion (full line) and electron (dotted line) temperatures in the core as a function of time. 207
9.8 S 209
9.9 2D maps of the decimal logarithm of the mass density $[kg.m^{-3}]$ at $t = 22\,ns$ and $t = 40\,ns$ for: **left panel:** the case of a "real" carbon obstacle and **right panel:** the case of a "perfect wall" obtained numerically by setting reflective boundary condition at $z = 0\,mm$. 211
9.10 (a) Schema of the numerical setup used to study the influence of the field orientation. θ is the angle between the laser target normal and the magnetic field direction. The laser used is the same as in the previous sections (17 J, 0.5 ns). The "probing plane" (red dotted line) is where the quantities shown in (b-c-d) are analyzed. (b) "Shape" of the accretion column in the X-Y plane at the probing plane (see (a)) and at $t = 20\,ns$ for three different angles. The black cross section corresponds to the case θ = 0°, the yellow cross section to θ = 45° and the red cross section to θ = 90°. (c) Z momentum as function of time for the three tilt angle. (d) Radial (X-Y) momentum as function of time for the three tilt angle 213

A.1 Equilibrium plasma configuration used for our study III

List of Tables

3.1 Scaling laws for the maximum temperature T_{max}, the ablation pressure P_a and the ablation rate $\dot{m}_a$ assuming both the deflagration model and the self-regulating model 71

5.1 Plasma parameters in the cavity at three different times. Values taken near the center of the cavity (z=1 mm at t=2 ns, z= 3 mm at t=10 ns and z=1.5 mm at t=15 ns). 133